An investigation of contact laws for coated pharmaceutical particles using the finite element method.

Cheong, Su Sam

School of Engineering
University of Wales Swansea

An Investigation of Contact Laws for Coated Pharmaceutical Particles Using the Finite Element Method

by

Su Sam Cheong

Submitted to the University of Wales in fulfilment of the requirements for the Degree of Doctor of Philosophy.

September 2006

ProQuest LLC.
789 East Eisenhower Parkway
P.O. Box 1346
Ann Arbor, MI 48106 – 1346

Summary

This research is inspired by the use of combined finite-discrete element method to model the compaction of coated drug particles during the tableting process. The use of extremely thin finite elements to represent the coatings proves to be inefficient as the use of explicit integration scheme in the simulation requires that each time step to be less than the critical time step that is determined from the smallest element size used in the simulation. Therefore, this research aims to overcome the problem of computational cost by formulating empirical interaction/contact laws (force-penetration relation) for coated particles to be incorporated into the simulation so that there is no need to model the coatings physically in the simulation. The contact between two coated particles is studied with the aid of finite element simulation by using a FE software package *ELFEN*. Elastic and plastic coatings are investigated, and adhesion is also included at the contact between plastic coatings. The formulated contact laws have made use of the material factor that successfully uncouple the influence of the coating material properties from the determination of other parameters, and provides a straightforward formulation that relates the contact force and the penetration. Comparisons between the formulated contact laws and the FE results show that the contact laws are able to approximate the contact behaviour of coated particles with good accuracy.

DECLARATION

This work has not previously been accepted in substance for any degree and is not being concurrently submitted in candidature for any degree.

Signed .....(candidate)

Date .....30/09/2006.....

STATEMENT 1

This thesis is the result of my own investigations, except where otherwise stated. Where correction services have been used, the extent and nature of the correction is clearly marked in a footnote(s).

Other sources are acknowledged by footnotes giving explicit references. A bibliography is appended.

Signed .....(candidate)

Date .....30/09/2006.....

STATEMENT 2

I hereby give consent for my thesis, if accepted, to be available for photocopying and for inter-library loan, and for the title and summary to be made available to outside organisations.

Signed .....(candidate)

Date .....30/09/2006.....

Contents

Acknowledgement

The author would like to thank her research supervisors, Dr. Y. Feng and Prof. R.W. Lewis, for their constructive suggestions and opinions throughout the course of the research. Besides, the help from Prof. D. Gethin, Dr. X. Yang, Dr. L. Dong and Dr. C. Lin are also very much appreciated. The author would also like to thank her family and friends who have been supportive throughout. Sponsorship from Astra Zeneca is greatly appreciated.

Chapter 1

Introduction

The application of discrete numerical modelling has received great interest from industrial processes such as metal powder forming. Lately, the application has also been extended to the process of pharmaceutical tablet forming to study the behaviour of tablets prior to production. Knowing the impact of numerical modelling, many researchers have dedicated their work to the development and improvement of numerical modelling techniques in the hope for better simulation performance.

In this chapter, some aspects of tablet compaction are pointed out as a preliminary study to the numerical modelling of powder compaction for pharmaceutical tableting. To conclude this chapter, the objective of the research is mentioned and the scope of the thesis is introduced in brief.

1.1 Introduction to Pharmaceutical Tableting

Tablets are the most commonly used oral dosage form in pharmaceutical preparation thanks to their many advantages. Not only are they easy and cheap to manufacture, they are also easy to administer while efficiently delivering drugs to patients. The technology of tablet preparation started when pharmacists pressed the medicines using a tablet triturate mould or an apparatus for compression [1] as shown in Figure 1.1 and Figure

1.2. As the demand on pressed tablets increased in the later days, small machines with adjustable compression dies were used. These machines were able to introduce the medicines automatically into the die in a measured dose and to control the compression of the tablet. Nowadays, more advanced tablet press machines are used worldwide to produce pharmaceutical tablets on a large scale, and the manufacturing process involves three different stages starting from die filling followed by compaction and ejection (decompression) [2].

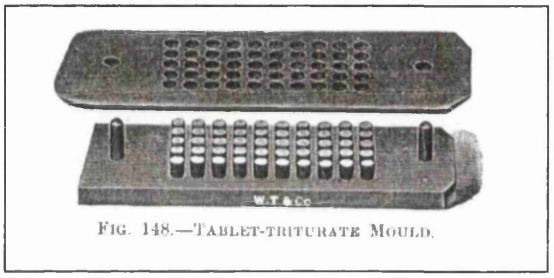

Figure 1.1: The tablet triturate mould. (Image credit: *Practical Pharmacy,* 1908)

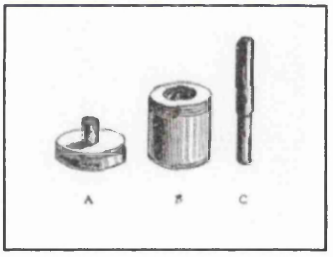

Figure 1.2: A simple press apparatus for the production of a compressed tablet - A: a base die; B: a sleeve; and C: a punch. (Image credit: *Art of Dispensing,* 1926)

1.2 Tablet Compaction

Pharmaceutical tablets are formed by uniaxial compaction of drug powders consisting of materials from inorganic to organic chemicals [3]. A successful compaction of a pharmaceutical tablet depends greatly on the mechanical properties of the powders, i.e. the deformation behaviour [4]. Excipients such as binders, diluents, or lubricants are usually added to the active drug ingredients to achieve the desired properties without altering the function of the drug. This is because the excipients chosen are normally

intended to deform plastically or undergo fragmentation around the active drug ingredients which exist mostly in crystalline or amorphous solids, and thus provide a good compact [5,6]. For example, starch has been used widely in pharmaceutical tableting as binders to improve the compression properties of paracetamol which is highly elastic [7]. Besides, excipients also provide volume to the powder mix for tablet compaction. Due to the occurance of particles of different size, shape and material behaviour in the powder mix, a tablet that is formed under uniaxial compaction is anisotropic and inhomogeneous [6].

During powder compaction, the powder bulk undergoes particle rearrangement and initial packing. With the increased pressure on the powder, the bulk will go through elastic deformation, plastic deformation, and possibly fracture for brittle particles which will lead to bulk deformation [7]. A sketch of the stages that the powder particles undergo during compaction is shown below [7].

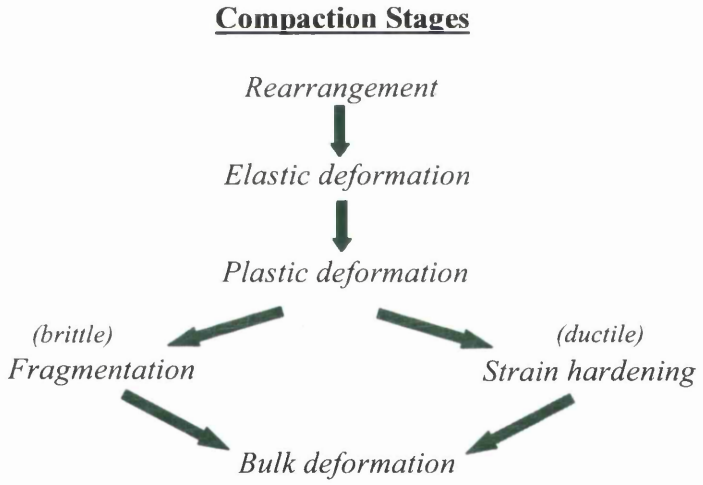

Figure 1.3: A flow chart of the compaction process.

Elastic deformation is a time independent and reversible deformation. The release of the stored elastic energy during unloading is the cause of the springback phenomenon, and is one of the factors that cause cracks or fracture in the powder compact [2]. The one dimensional stress-strain relation for elastic deformation is [5]:

$$\sigma_d = \varepsilon E \tag{1.1}$$

where σ_d is the deformation stress; ε is the deformation strain; E is the Young's modulus of elasticity.

Plastic deformation, on the other hand, causes a permanent change of shape on a solid upon unloading [9]. The amount of the plastic deformation is dependent on the overall time of compaction, the rate at which the compression force is applied, the contact time, and the time during which the powder bulk is subjected to the maximum force [4]. Due to this deformation, permanent particle-particle contact is formed during powder compaction. The plastic deformation stress is given by [5]:

$$\sigma_{d_{plastic}} = \sigma_y \tag{1.2}$$

where σ_y is the yield stress of the material, i.e. the stress at which the material will start to deform plastically. There are many criteria that determine the yielding of solids, and the von Mises yield criterion is normally adopted for pharmaceutical materials [9].

For material that undergoes brittle fracture, the deformation stress is given by [5]:

$$\sigma_{d_{brittle}} = \frac{AK_{ic}}{\sqrt{d}} \tag{1.3}$$

where K_{ic} is the stress intensity factor of material that indicates the stress required to produce crack propagation; A is a constant depending on the geometry and stress application; d is the particle size diameter.

A sketch of the different types of deformation is shown in Figure 1.4.

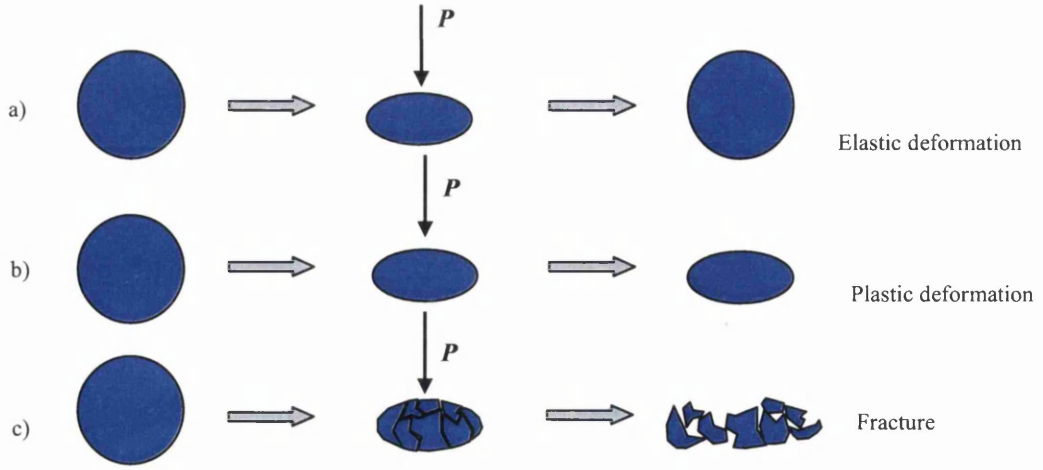

Figure 1.4: Different types of deformation due to compression force *P*: a) Elastic deformation; b) Plastic deformation; c) Fracture.

1.3 Evaluation of Tablet Compaction

The understanding of the deformation behaviour of the powder can provide information about the compressibility of the material, i.e. the ability of the material to undergo volume reduction due to the application of stress [4]. This is particularly important so that a successful tablet compaction can be achieved. In order to assess the compressibility of the powders, many techniques were introduced, and these include measuring the change of density during compression, stress transmission during compression, work involved in compaction, and so on [4]. However, none of these techniques alone can provide a complete understanding of the mechanism due to the complexity of the powders being compacted [4].

One of the most popular methods to study the compression process during tablet compaction is by the use of a force-displacement relation measured from the punch force and displacement [11]. A typical graph of the punch force versus punch displacement is shown in Figure 1.5.

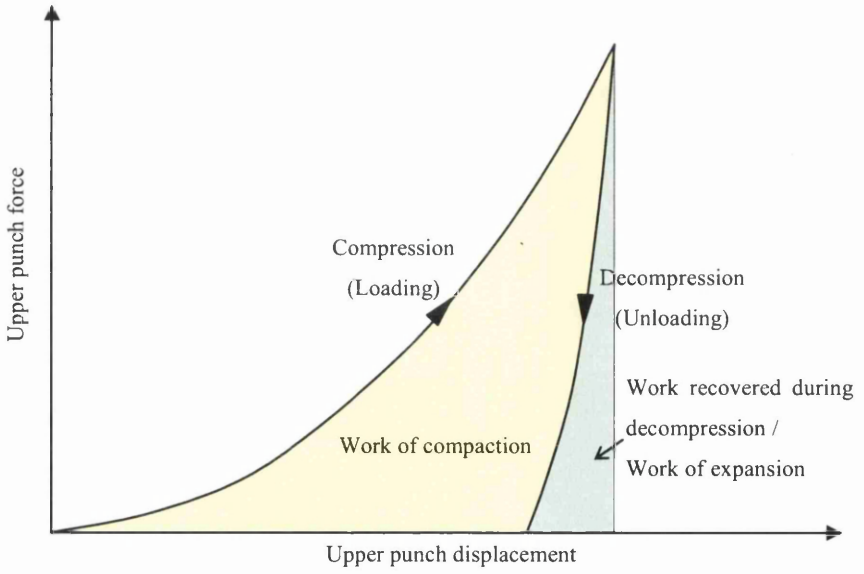

Figure 1.5: A typical graph of the punch force versus punch displacement during the compression and decompression.

Referring to the figure above, the area shaded with yellow is the net work used to form the compact and also the work required to overcome the die wall friction, and the area shaded with green represents the work recovered when the punch is removed.

Besides, this also represents the work of expansion, where it can be obtained from the measurement of the axial expansion of the tablet during decompression. In fact, the deformation and binding properties of the materials used in the tablet are said to affect the extent of these areas. For example, for elastic materials, the compression work will fully recover during decompression and so there is no net work used in the formation of the compact. On the other hand, materials that deform plastically will yield a net work input, and the extent of the net work increases with increasing deformation. Hence, the influence of particulate interactions during compression is significant [11].

The compactibility of powders is defined as the ability of the powders to form a compact. This feature is important for the assessment of tablet strength and is affected by the bonding mechanism between particles and particles shape, size and surface texture [6]. The bonding mechanisms are classified into five main types as mentioned in [6] and are listed in Table 1.1.

Table 1.1: Classification of bonding mechanisms.

Type of Bonding Mechanism	Mechanism	Sketch
Solid Bridges	Sintering, melting, chemical reaction, crystallisation, hardened binders	
Bonding due to movable liquids	Capillary force, surface tension force	
Non-freely-movable binder bridges	Viscous binders, adsorption layers	
Attraction between solid particles	Molecular force, electrostatic force	
Shape-related bonding	Mechanical interlocking	

For the compaction of dry and crystalline powders, solid bridges, attraction forces and mechanical interlocking are the three main mechanisms that are said to affect the tablet strength [6]. Solids bridges are strong bonds due to activities such as melting, recrystallisation of soluble materials and so on, where a true contact is established between the particles. Attraction forces are weaker bonds acting over distances, such as van der Waals forces, electrostatic forces, and hydrogen bonding. Mechanical interlocking is the hooking and twisting together between particles and is dependent on the shape and surface structure of the particles. However, the presence of liquid or moisture in a compact might be of significance to the tablet strength [6]. Porous materials often contain moisture trapped between the pores which causes capillary forces to form liquid bridges between the adhering surfaces. During this contact, the liquid pressure is less than the air pressure and thus a state of tension is created [3].

1.4 Particle Coating

Often, the properties and/or the functionality of the powders are altered with the use of a particle coating [12]. For example, film coating is normally used in the pharmaceutical industry to produce controlled-release drugs [12]. Besides, the application of polymeric coating on harder core particles can also improve the compactibility of the core powder particle by acting as a viscous binder, or adsorption layer, such as the one shown in Table 1.1 to improve the bonding mechanism between the powder particles.

By using the method of wet or dry coating, the surface properties of the particles, such as flowability, solubility, particle shape and so on, can be improved or modified. However, wet coating has become less desirable recently due to the environmental concerns over the resulting waste stream and dry coating has become a new alternative approach for powder particle coating [12].

The process of dry coating involves the coating of the micron-sized host particles with submicron-sized guest particles to produce value-added composite particulate materials [12]. Mechanical forces are used to bring the guest particles into close contact with the host particle and since the guest particles are very small, they are attached to the host particle under the influence of the van der Waals forces [12].

In the dry coating process, either a discrete or continuous coating can be formed depending on the operating conditions such as the processing time, weight ratio between the guest and host particles and the particles' properties [12]. A continuous coating can be either a porous particle layer or a continuous film coating that is generally non-porous. Although preference is generally on the continuous coating, discrete coatings are sometimes required to modify the surface properties of the particle while keeping the host particle's properties exposed on the surface [12]. A schematic explanation of the dry coating process is shown in Figure 1.6.

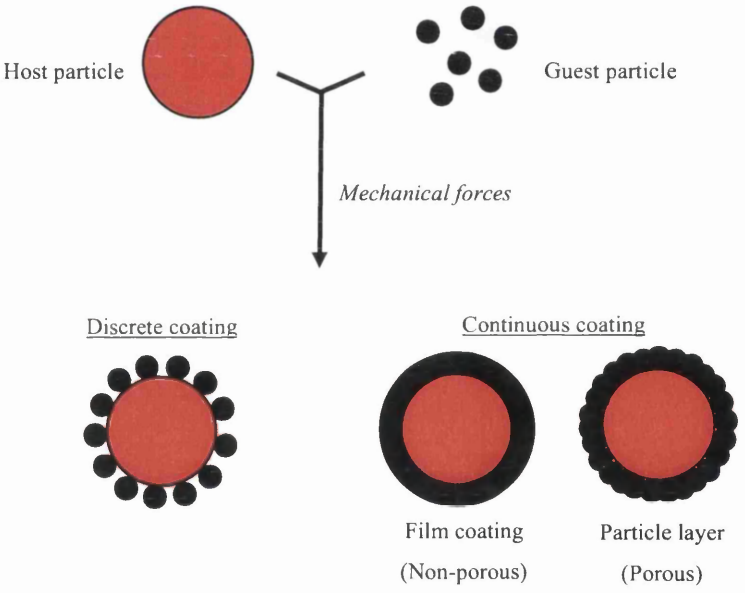

Figure 1.6: Process of dry particle coating.

Some of the commonly used binders in tableting are microcrystalline cellulose, starch and lactose. These materials are highly plastic, and undergo plastic deformation during compaction to provide larger contact surface that increase the bonding between the particles [13].

1.5 Particle Adhesion and Models to Describe Adhesion Forces

Particle adhesion is formed due to the force that exists at the contact of two particles or between the contact of a particle and a solid surface. The major factor to be considered in this contact is the influence of adhesion, which is defined as the free energy change required to separate unit areas of two surfaces from contact to infinity in a vacuum. For surfaces of different materials the term 'work of adhesion' is used, and for surfaces of the same materials the term 'work of cohesion' applies.

The work of adhesion/cohesion, $\Delta\gamma_a$ or $\Delta\gamma_c$, can be calculated from the surface free energy. For solids, this is generally denoted as γ_s, and has units of mJm^{-2}. For the work of cohesion between two surfaces of similar material then,

$$\Delta\gamma_c = 2\gamma_s \tag{1.4}$$

For work of adhesion between surfaces of dissimilar materials, the so-called "Dupré-equation" [3] is followed:

$$\Delta\gamma_a = \gamma_{s1} + \gamma_{s2} - \gamma_{s1,s2} \tag{1.5}$$

where γ_{s1} and γ_{s2} are the surface energy of material 1 and 2, and $\gamma_{s1,s2}$ is the interfacial energy. As it is assumed that the work of adhesion needed to separate the two surfaces is equal to the energy released when the two surfaces are brought into contact, then these two equations are often used to approximate the separation as well as the adhesion energies [3].

A typical force-separation graph, taking into account adhesion, is shown in Figure 1.7, where the shaded area is equivalent to the work required to separate the surfaces from the equilibrium distance, d_0 to infinity, d_∞ [14].

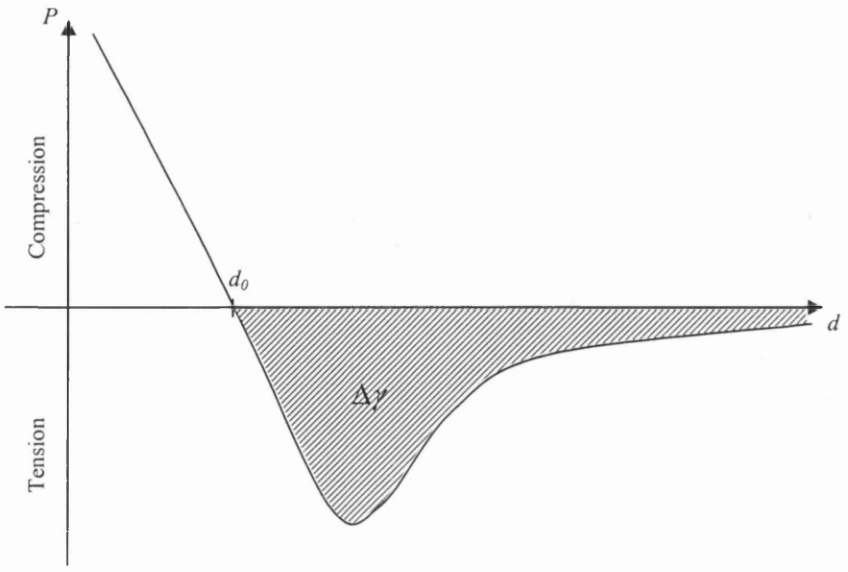

Figure 1.7: Force-separation graph with showing work of adhesion.

Many models have been developed to describe the adhesion forces and the model that is most used to date is the Johnson-Kendall-Roberts (JKR) theory [3,15,16]. This model assumed the contact of two perfectly elastic spheres with smooth surfaces and the adhesion force follows the relation

$$F_{JKR} = \frac{3}{2}\pi R^* \Delta\gamma \tag{1.6}$$

where $R^* = \frac{R_1 R_2}{(R_1 + R_2)}$ is the effective radius of the two surfaces, with particle radii R_1 and R_2. Besides, Deryaguin, Muller and Toporov also developed a theory that describes the adhesion forces, which is known as the Deryaguin-Muller-Toporov (DMT) theory. This model predicts a slightly higher adhesion force of

$$F_{DMT} = 2\pi R^* \Delta\gamma \tag{1.7}$$

These two models assume that the separation forces are independent of the elastic material properties, but are a linear function of the particle radius and surface energy. However, it was found that these models are limiting cases, where the JKR model works well for large, soft particles with high surface energy and the DMT model should be used for small, hard solid particles with low surface energy [3,16,17].

1.6 The Application of Numerical Modelling to Powder Compaction

Due to a lack of knowledge and theory that describe the compaction of pharmaceutical powders [5], numerical simulation has become a more promising tool in understanding the powder compaction process [18]. In addition, the use of numerical modelling is also able to reduce the cost and time involved in the production of powder compact as any possible defects in the powder compact could be determined using numerical simulation without the need of experiments, which sometimes involve costly raw materials and time consuming setting-up.

In general, there are several methods to model the powder compaction process: macromechanical and micromechanical approaches. The macromechanical, also called a continuum approach, idealises the powder mass as an equivalent continuum material, where the powder compact is modelled as a whole without taking into account the deformation at particle levels. Many researchers have carried out simulation on powder compaction using this method: Lewis and Khoei [19,20] utilised a large deformation finite element method to simulate metal powder forming, Khoei [21] performed an inelastic finite element analysis on metal powder during the cold compaction process, Coube and Riedel [18] utilised finite elements to predict the green density distribution and cracks in the compact during metal powder pressing and ejection, Cunningham, Sinka and Zavaliangos [22,23] examined the compaction of tablet with the use of finite elements and experimental data, Michrafy, Ringenbacher and Tchoreloff [24] used the elastic-plastic finite element method to compute the stresses and density change in the tablet, etc. However, while a continuum analysis is so widely used for powder compaction simulation, the major draw back of this method is the requirement of the experimental characterisation of each powder mix prior to simulation and constitutive relations are needed for the stress- strain variation for the continuum model [25].

The micromechanical approach, on the other hand, takes into account the discrete nature of the powder particles and the particle interactions, such as contact, sliding and rolling. This is the main feature of this method. The discrete element method that utilises this concept was originally introduced for the analysis of rock mechanics problem by

Cundall [26]. This method treats each particle as a rigid disc and the force-displacement law is used to update the contact forces from a knowledge of the displacements. The behaviour of granular assemblies can thus be simulated based on the contacting particle pairs without the need of developing constitutive laws that involves a large amount of parameters and assumptions [27]. Nowadays, this method has been improved to allow for deformation in order to obtain more precise modelling of individual elements [28]. The application of this method is also extended by many researchers to industrial processes such as modelling of powder compaction. For example, Rendanz and Fleck [29] have carried out an investigation on the cold compaction of a random distribution of metal cylinders using this method.

A third approach, using the combination of finite and discrete element methods, was introduced by Munjiza [28] to simulate the deformation of particle systems. This technique focuses on the deformation of particles that are each mapped with finite elements using a continuum approach, and discrete element algorithms are used to model the inter-particle interaction [30]. Hence, this method has an advantage over both the finite element and discrete element method as it can be easily used to model the compaction of a mixture of particles of any shape, size and material. An analysis was carried out employing this method on the compression of a ductile matrix and a matrix comprising ductile and brittle particles by Ransing et al. [31]. In addition, Gethin et al. [32] have also demonstrated the applicability of the combined finite and discrete element method for powder compaction. They carried out comparison of combined finite and discrete element analysis with continuum analysis through two case studies, and found a consistent pattern on the force displacement curve between these two analyses. Cameron and Gethin [33] looked into the friction mechanisms between powders and rough surfaces with the aid of combined finite and discrete element method. Gethin et al. [25] also studied the application of the deformable discrete element modelling to explore the influence of particulate behaviour on the yield characteristics of the powder bulk. Nevertheless, these simulations are limited to spherical particles or cylindrical rods, as contact detection on interacting particles is a very time consuming procedure [34,35,36,37,38], and nearly two third of the computing time is used on the contact detection algorithm [38]. Hence, abundant researches have been focused on developing

new techniques to improve the efficiency of contact detection and interaction procedures for different particle size and geometry, such as, to name but a few, the works of [30,34,35,36,38,39].

Lewis et al. [39] carried out a combined finite and discrete element simulation on the compaction of pharmaceutical tablet that consists of powder particles of irregular shape and found that the particle shape and size can highly affect the particle deformation and stress distribution during compaction.

1.7 Issues on Numerical Modelling Using Combined Finite and Discrete Element Method

A pharmaceutical tablet normally consists of more than one type of powder and therefore is an inhomogeneous compact due to the mixture of powder particles of different material properties, shape and size. The use of a combined finite and discrete element simulation on the compaction of pharmaceutical tablet has an edge over a finite element simulation as it allows the inhomogeneous nature of the tablet to be modelled directly without having to work out the effective properties of the compact beforehand. Furthermore, the representation of a tablet by a powder particles compact in the combined finite and discrete element simulation also allows the stress and deformation to be calculated at the particle level.

During the compaction simulation, the powder particles displace due to the movement of the punch and hence form a network of contacts between the particle pairs. As the compaction process continues, a compression force is produced at the contact between each particle pair. The contact force between the particles is governed by a contact law that relates the amount of penetration/approach between the particles to the force produced due to the penetration. This can then be used to update the stress and deformation in each particle. The choice of contact law between particles is dependent on the nature and material of the contacting particles and one of the most popular contact laws is the classical Hertz Theory.

Although the combined finite and discrete element simulation has an edge over a finite element simulation in tablet compaction, the compaction of a large amount of

powder particles faces challenges as the time required for the simulation is enormous. The situation is worse when coated particles are included in the compaction process which results in the use of very small finite elements for representing the particle coating. A dynamic analysis, especially an explicit analysis where the simulation time step size is governed by the smallest element size, will require a very long time to converge to the desired solution.

1.8 Objective and Method of the Research

As coated drug particles are important in improving the quality of pharmaceutical tableting, the currently available contact analysis models (mainly for elastic half-space) are not suitable for the coated nature of the particles. The purpose of this research is to explore the contact behaviour of coated particles and to develop a contact model for coated particles that can be used in the tableting simulation in pharmaceutical industry.

This research is inspired by the use of the combined finite-discrete element method to model the compaction of coated drug particles. The use of extremely thin finite elements to represent the coating proves to be inefficient as the use of an explicit integration scheme will require that each time step be less than the critical time step as governed by the smallest element size. Extremely intensive computation is therefore required to carry out the simulation. The situation is worse when the system consists of thousands or even millions of coated particles, when the size of the problem becomes huge.

The aim of this research is to overcome the problem of computational cost by formulating empirical interaction/contact laws for coated particles to be incorporated into the simulation so that there is no need to physically model the coatings in the simulation. Instead, the coated particles are represented by 'representative particles' that can be meshed with coarser finite elements which have the properties of coated particles, and the contact between the 'representative particles' is governed by the formulated contact law. In some cases, the coated particles can even be represented by single particle elements if the deformation is very small (i.e. the particles are hard). A schematic of the idea of

representative particles, with the use of the formulated contact law in the compaction simulation, is shown in Figure 1.8.

The contact between two coated particles will be studied with the aid of a finite element simulation by using a FE software package *ELFEN* as it benefits from built-in adaptive mesh update ability for the modelling of nonlinear (large deformation) behaviour that will be encountered very often in this research. In the analyses, elastic and plastic coatings of a certain range of thickness will be investigated and the adhesion between plastic coatings under tension will also be studied. From the observed relation between some important parameters in the analyses, a general force-displacement law will be formulated for coating of different materials and the compliance of the analytical formulations with the contact behaviour of the coated particles will be examined via comparison with the simulation results.

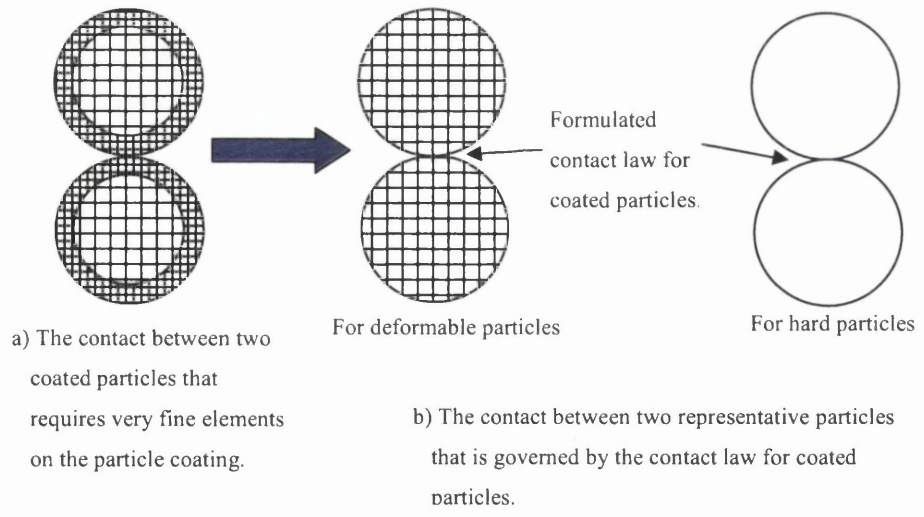

Figure 1.8: The idea of representative particles with the use of formulated contact law for coated particles in the compaction simulation.

As the contact between coated particles has received very little attention from other researchers in the past, the novelty in this research is that the contact behaviour of coated particles is studied leading to the derivation of simple contact laws to approximate the contact behaviour of coated particles. Since elastic materials and plastic materials

behave differently, the research work is separated into two main parts: the contact between elastic coatings and the contact between elastic-plastic coatings. In the elastic coating analysis, assumption on contact strains has been made to allow for weighting factors to be applied to the models to arrive at a simple contact law. For the analysis of elastic-plastic coating, a modified Hertz law together with material factor are employed to arrive at a simple contact law. In order to extend the simple law for elastic-plastic coating to include contact adhesion, the contact between the coatings are modelled as a continuum in the FE analysis to create a state of tension when subject to pulling. This simple continuum model of representing the contact adhesion benefits from avoiding the use of complicated contact model set-up such as spring and/or dashpot or even more complicated combination to represent the adhesive contact between two coated particles.

1.9 Layout of the Thesis

The layout of the thesis is outlined as follows:

In the next chapter, some aspects of numerical modelling methods that are related to the research are mentioned in brief. Continuum modelling such as the finite element method is discussed with issues focus on the modelling of material nonlinearity and topics such as iterative solution methods, time integration methods for dynamic simulations and adaptive mesh refinement. Besides, the discrete element method is also mentioned, with discussion focusing on the contact detection and motion updates. The chapter closes with discussion on an improved modelling method that combines the features of both the finite element and discrete element methods.

Some aspects of contact mechanics are covered in Chapter 3, with discussion on the Hertz theory for the contact of elastic spheres and the non-Hertzian contact of layered solids. A comparison between the finite element analyses results of contact between two elastic spheres and also the compression of plane strain elastic layer will be compared to the available theories.

In Chapter 4, finite element simulations of the axi-symmetric normal compression of an incompressible elastic coating are presented in order to study the relation between the contact force and the penetration. A comparison between the simulation results with analytical solutions is also shown. In addition, a modification which allows nonlinear

behaviour to the existing analytical solution (i.e. large deformation) for better accuracy is also shown.

In Chapter 5, finite element simulations of the axi-symmetric normal compression of plastic coatings are presented. A contact law that relates the contact force to the penetration is formulated semi-empirically to approximate the behaviour of the contact between two particles coated with a plastic coating. A comparison between the finite element results and the formulated contact law is also presented.

Further to the work in Chapter 5, Chapter 6 aims to develop a contact law for the plastic coatings that includes adhesion at the contact. Hence, finite element simulations of the axi-symmetric normal compression of plastic coating with the effect of adhesion due to tensile forces are carried out and a comparison is made between the simulation results and the formulated contact law.

Finally, conclusions based on the discussions made in the previous chapters are drawn in Chapter 7, and some suggestions for further work regarding the existing findings are also made.

Chapter 2

Numerical Modelling Methods

In general, numerical modelling can be categorised into continuum and discrete modelling. Continuum modelling, such as the finite element method, models the behaviour of the body as a whole when subject to loading, while discrete modelling, such as the discrete element method, captures the behaviour of separate bodies that are interacting with each other.

In this chapter, modelling methods such as the finite element and discrete element methods are briefly presented. Also, the combined finite and discrete element method which is an improved method for simulating discrete bodies with deformation is discussed. Only the numerical aspects that relate to the modelling of coated particles are considered.

2.1 Finite Element Method

The finite element method was first introduced to solve problems associated with structural mechanics [40]. It is now widely used in engineering analysis such as solids and structural mechanics, heat transfer, fluids etc [41]. Recently, with the advancement of computer technology, the use of finite element analysis has become more important in solving engineering problems as it can be used to analyse complex structures. A brief history on the development of this method can be found in [41], [42] and [43].

As previously mentioned, the finite element method is used to solve engineering problems. Hence, it involves the idealisation of a physical problem to a mathematical model that governs all the assumptions made in the problem. An appropriate mathematical model is therefore important to give insight into the physical problem. Also, the model should be reliable and yield the required answer to a sufficient accuracy with least cost.

The analysis of a problem by the finite element method involves the discretisation of the region to be analysed into many smaller regions called finite elements, where nodal points are used to connect the elements together. There are various types of element shapes, and the most commonly used shapes in two-dimensional analyses are triangles or quadrilaterals, with straight or curve sides. Within each element, the nodal loads associated with all element deformation states that are allowed are determined. The assembly of all the elements into a global system is then carried out, with the assignment of suitable boundary conditions and any known applied loads to the global system. Having determined the global loadings, simultaneous algebraic equations are solved at this level to determine the nodal responses such as the displacements, and hence the determination of element strains and stresses (by using relevant constitutive relations). These results can be analysed or visualised graphically in the output programs called post-processors.

2.1.1 Type of Analysis

If a force that is applied to a system is assumed to vary very slowly with time, the effect of inertia can be neglected, and the problem can be treated as quasistatic or static.

Otherwise, the problem requires a dynamic analysis and the effect of inertia and damping, if important, will have to be taken into account.

In the static linear finite element analysis, the displacements of the finite element assemblage are (infinitesimally) small, and the material behaves linearly elastic [41]. The boundary conditions remain unchanged during the course of loading and the finite element equilibrium equation follows the form

$$\mathbf{KU} = \mathbf{F} \tag{2.1}$$

where $\mathbf{K}$ is the stiffness matrix, $\mathbf{F}$ is the applied load vector, and $\mathbf{U}$ is the displacement vector. Both $\mathbf{K}$ and $\mathbf{F}$ are independent of $\mathbf{U}$ in a linear analysis. The solution to this problem is straight forward, and there are many types of direct or iterative method to choose from. The direct methods are normally favoured in practice for small scale problems [42], and one of them is the Gauss Elimination method; while iterative solvers have to be used for very large scale problems particularly in 3D cases.

However, real life engineering practical problems often involve nonlinearity such as material nonlinearity or geometric nonlinearity. Material nonlinearity is related to the change in material properties, i.e. plasticity and so on; and geometric nonlinearity is related to the change in configuration, i.e. large deformation or rotation. Another type of nonlinearity is the contact problem that involves a change in boundary conditions. A classification of analyses can be found in Figure 2.1 [41]. When any of these nonlinearities appear in the problem considered, the matrix $\mathbf{K}$ and/or vector $\mathbf{F}$ are no longer independent of $\mathbf{U}$ but a function of $\mathbf{U}$, and a nonlinear analysis is therefore essential. Iterative procedures such as Newton-Raphson Schemes are required to solve the equilibrium conditions.

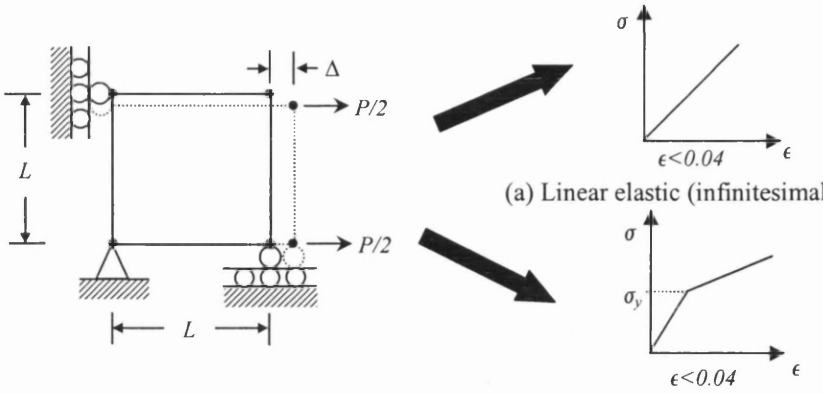

(a) Linear elastic (infinitesimal displacements)

(b) Materially-nonlinear-only (infinitesimal displacements, but nonlinear stress-strain relation)

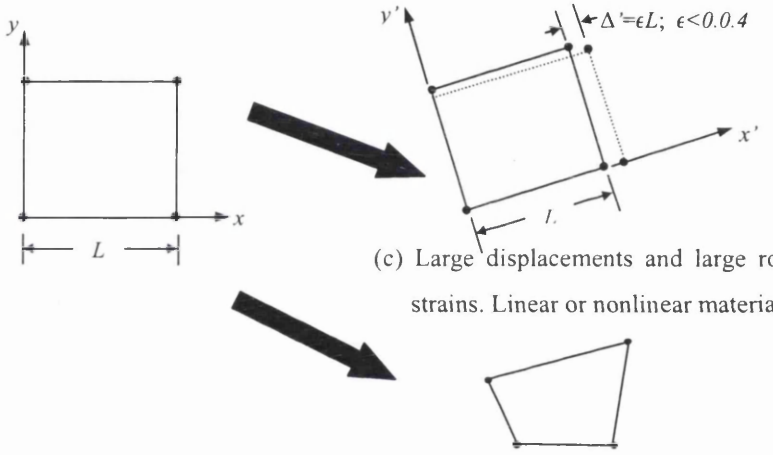

(c) Large displacements and large rotations but small strains. Linear or nonlinear material behaviour.

(d) Large displacements, large rotations and large strains. Linear or nonlinear material behaviour.

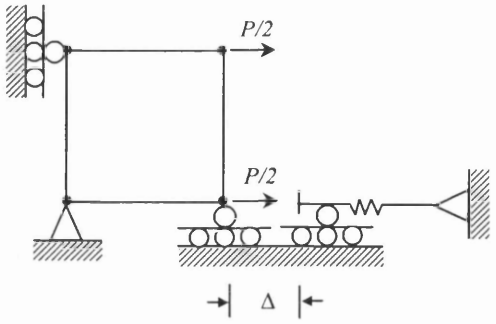

(e) Change in boundary condition at displacement Δ. Contact problems.

Figure 2.1: Classification of analysis.

In a dynamic analysis, the equilibrium equation governing the linear/nonlinear response of a system is expressed as

$$\mathbf{M}\ddot{\mathbf{U}} + \mathbf{C}\dot{\mathbf{U}} + \mathbf{K}\mathbf{U} = \mathbf{F} \tag{2.2}$$

where $\mathbf{M}, \mathbf{C}$ and $\mathbf{K}$ are the mass, damping and stiffness matrices; $\mathbf{U}, \dot{\mathbf{U}}$ and $\ddot{\mathbf{U}}$ are the displacement, velocity and acceleration vectors; and $\mathbf{F}$ is the vector of applied loads. $\mathbf{M}\ddot{\mathbf{U}}, \mathbf{C}\dot{\mathbf{U}}$ and $\mathbf{K}\mathbf{U}$ are the inertia forces, damping forces and elastic forces respectively, and all of them are time-dependent. Therefore, the principle of dynamic analysis is to carry out a time-history analysis to seek for the response of the system within a time period. The solution to the equations can be evaluated using direct time integration methods such as an explicit or implicit integration method. Similarly, for nonlinear dynamic problems, direct time integration methods can be used to solve for the response.

2.1.2 Material Nonlinearity: Elasto-Plastic Material [44]

2.1.2.1 Mathematical Model of 1-D Elasto-Plasticity

In general, the one-dimensional deformation of elasto-perfectly-plastic solids at small strain can be written as the additive decomposition of the total strain into elastic and plastic parts as

$$\varepsilon = \varepsilon^e + \varepsilon^p \tag{2.3}$$

and the constitutive equation for the stress can be written as

$$\sigma = E\varepsilon^e = E\left(\varepsilon - \varepsilon^p\right) \tag{2.4}$$

The material is said to experience plastic strain when the stress in the material is equal to the yield stress σ_y. In other words, the yield criterion for the material is satisfied, i.e.

$$f(\sigma) = |\sigma| - \sigma_y = 0 \tag{2.5}$$

When the yield criterion is met, the material will start to flow plastically and the flow of the material is governed by the flow rule written as

$$\dot{\varepsilon}_p = \dot{\lambda} sign[\sigma] \tag{2.6}$$

where $\dot{\varepsilon}_p$ is the plastic slip in the material that may be expressed as

$$\begin{aligned} \dot{\varepsilon}_p &= \dot{\lambda}, \qquad \text{if } \sigma = \sigma_y \\ \dot{\varepsilon}_p &= -\dot{\lambda}, \qquad \text{if} \sigma = -\sigma_y \end{aligned} \tag{2.7}$$

For elasto-plastic materials that experience isotropic hardening during plastic deformation, experimental evidences suggest that the elastic domain Ξ_σ of the material is evolving. The evolution of the elastic domain is described by a hardening parameter $\alpha > 0$, and the material is assumed to expand with its centre being fixed in $\sigma - \alpha$ space as shown in Figure 2.2.

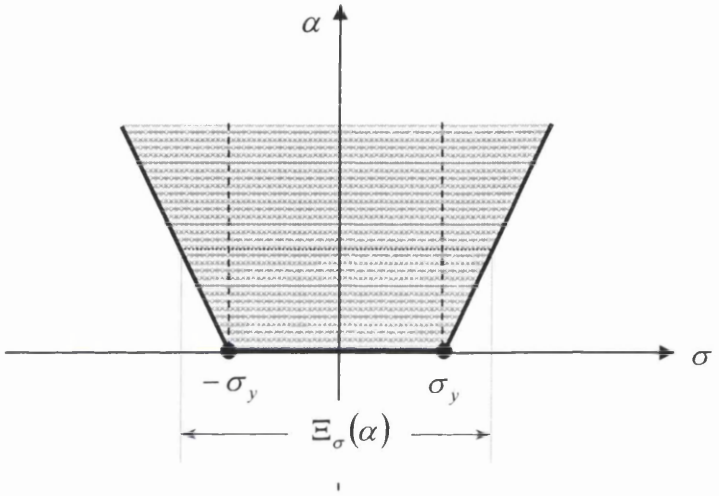

Figure 2.2: Isotropic hardening of the elastic domain Ξ_σ.

The yield criterion for isotropic hardening can be represented by a simple mathematical expression of the form

$$f(\sigma,\alpha) = |\sigma| - (\sigma_y + H\alpha) \leq 0 \tag{2.8}$$

There are several choices for the hardening parameter and the most widely used hardening laws are

$$\dot{\alpha} = |\dot{\varepsilon}_p| \tag{2.9}$$

and

$$\dot{\alpha} = \sigma|\dot{\varepsilon}_p| \tag{2.10}$$

which are called the strain and work hardening laws respectively.

To obtain the tangent elastoplastic modulus $\hat{T}$ as shown in Figure 2.3, the consistency condition as shown below is employed.

$$\dot{\lambda}\dot{f}(\sigma,\alpha)=0 \tag{2.11}$$

By evaluating $\dot{f}(\sigma,\alpha)$ as

$$\begin{aligned}\dot{f}(\sigma,\alpha)&=\frac{\partial f(\sigma,\alpha)}{\partial\sigma}\dot{\sigma}+\frac{\partial f(\sigma,\alpha)}{\partial\alpha}\dot{\alpha}\\&=sign[\sigma]E(\dot{\varepsilon}-\dot{\varepsilon}_p)-H\dot{\alpha}\\&=sign[\sigma]E\dot{\varepsilon}-\dot{\lambda}(E+H)\end{aligned} \tag{2.12}$$

the parameter $\dot{\lambda}$ can be solved for using the consistency condition in (2.11)as

$$\dot{\lambda}=\frac{sign[\sigma]E}{(E+H)}\dot{\varepsilon} \tag{2.13}$$

The tangent modulus can then be evaluated using (2.13) and (2.6) in (2.4) as

$$\begin{aligned}\hat{T}&=\frac{d\sigma}{d\varepsilon}\\&=\frac{EH}{(E+H)}\qquad \text{for } \dot{\lambda}>0\end{aligned} \tag{2.14}$$

A schematic of the tangent elasto-plastic modulus is shown in the figure below.

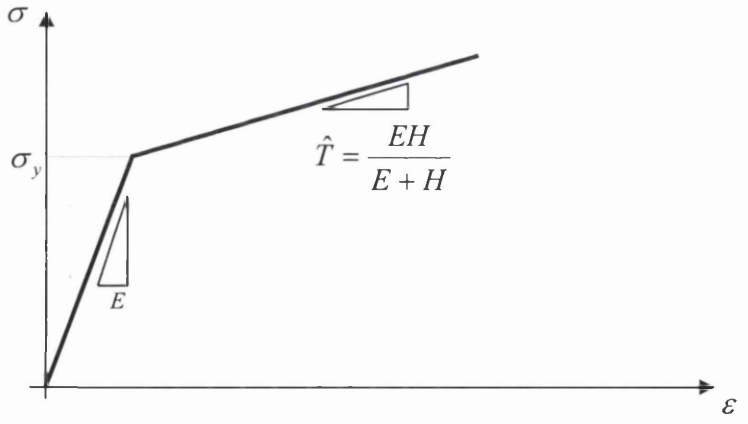

Figure 2.3: The tangent elastoplastic modulus $\hat{T}$.

2.1.2.2 Computational Aspect of 1-D Elasto-Plasticity

The analysis of a problem is usually supplied with the incremental strain $\Delta\varepsilon_{n+1}$ at time t_{n+1}, and hence the strain ε_{n+1} at t_{n+1} is known. However, for elasto-plastic problems, the updating of the variables from time t_n to t_{n+1} is not straight forward, and the process of prediction-and-correction is required. This is normally done by a trial value at time t_{n+1}, called the elastic predictor and the correction of the value called a plastic corrector.

In the process of the elastic predictor, the trial values for the stress σ, internal variable α and yield function f at time t_{n+1} are sought. To do this, the plastic strain during the time increment from t_n to t_{n+1} is kept constant so that

$$\varepsilon_{n+1}^{p,trial} = \varepsilon_n^p \tag{2.15}$$

and

$$\alpha_{n+1}^{trial} = \alpha_n \tag{2.16}$$

Thus, the trial stress at t_{n+1} is obtained as

$$\begin{aligned} \sigma_{n+1}^{trial} &= E\left(\varepsilon_{n+1} - \varepsilon_n^p\right) \\ &= \sigma_n + E\Delta\varepsilon_{n+1} \end{aligned} \tag{2.17}$$

and the trial yield function can be evaluated as

$$f_{n+1}^{trial} = \left|\sigma_{n+1}^{trial}\right| - \left(\sigma_y + H\alpha_n\right) \tag{2.18}$$

According to the Kuhn-Tucker loading/unloading condition,

$$\Delta\lambda \geq 0, \qquad \Delta\lambda f_{n+1} = 0 \tag{2.19}$$

where $\Delta\lambda = \dot{\lambda}\Delta t$, the trial yield function can be used to determine whether an elastic or elasto-plastic step is required. If

$$f_{n+1}^{trial} \leq 0 \Rightarrow \Delta\lambda = 0 \tag{2.20}$$

the system has not yielded and an elastic step is required;

If, $$f_{n+1}^{trial} \geq 0 \Rightarrow \Delta\lambda > 0 \tag{2.21}$$

an elasto-plastic step is required and a plastic corrector is needed.

To evaluate the plastic corrector, the parameter $\Delta\lambda$ is obtained after some manipulation as

$$\Delta\lambda = \frac{f_{n+1}^{trial}}{E+H} \tag{2.22}$$

and the solution for the variables at time t_{n+1} is evaluated as

$$\sigma_{n+1} = \sigma_{n+1}^{trial} - \Delta\lambda E sign\left[\sigma_{n+1}^{trial}\right] \tag{2.23}$$

$$\varepsilon_{n+1}^{p} = \varepsilon_{n}^{p} + \Delta\lambda sign\left[\sigma_{n+1}^{trial}\right] \tag{2.24}$$

$$\alpha_{n+1} = \alpha_n + \Delta\lambda \tag{2.25}$$

A schematic representation of the elastic predictor and plastic corrector steps is shown in Figure 2.4.

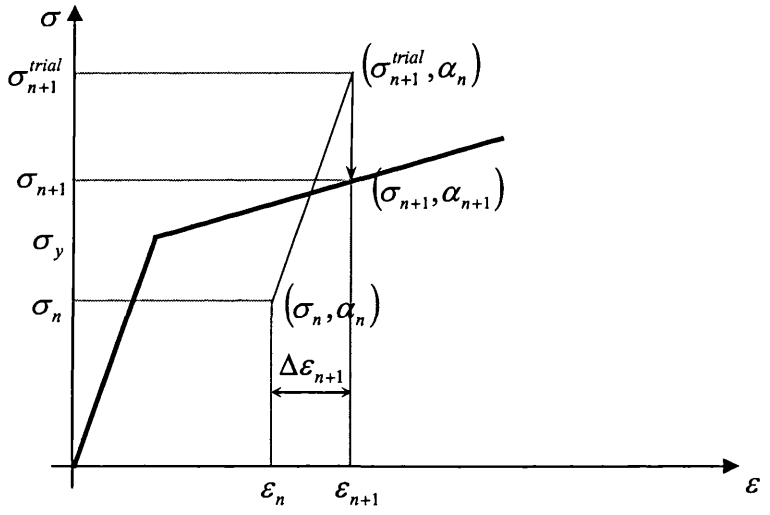

Figure 2.4: The elastic predictor and plastic corrector steps.

2.1.2.3 General Elasto-Plasticity Problems

In general, the computational aspect of a multi-dimensional elasto-plastic problem is similar to a 1-D elasto-plastic problem except that a generalisation of the mathematical model from one dimensional to multi-dimensional is required. As a multi-dimensional response is required, the evaluation of the updated plastic responses involves the solution of a system of nonlinear algebraic equations for the plastic variables. The most effective method of achieving this is the Newton-Raphson method.

The modification in the model is that the constitutive law used in the problem is replaced by a constitutive matrix that describes the response of the material in different axes. Also, the yield criterion that determines the onset of plastic flow is replaced by yield criteria such as the Tresca yield criterion, von Mises yield criterion and so on. When plastic strain takes place, a flow rule that can be categorised into either an associative (normal) flow rule or a non-associative (general) flow rule is employed.

At the point of yielding in simple tension, the von Mises criterion assumes that the yield condition has the form [10]

$$\frac{1}{2}\left[(\sigma_1-\sigma_2)^2+(\sigma_2-\sigma_3)^2+(\sigma_3-\sigma_1)^2\right]=\sigma_y^2 \tag{2.26}$$

where σ_1, σ_2 and σ_3 are the principal stresses, and $\sigma_1 > \sigma_2 > \sigma_3$. In terms of biaxial case $(\sigma_2 = \sigma_3)$, the yield condition can be written as

$$\sigma_1^2-\sigma_1\sigma_2+\sigma_2^2=\sigma_y^2 \tag{2.27}$$

For perfect elasto-plasticity, the associative flow rule has the form

$$\dot{\varepsilon}^p=\dot{\lambda}\frac{\partial f(\sigma)}{\partial \sigma} \tag{2.28}$$

while the non-associative flow rule has the form

$$\dot{\varepsilon}^p=\dot{\lambda}g(\sigma) \tag{2.29}$$

where g is a prescribed function.

For isotropic hardening elasto-plasticity, the hardening rule used together with the associative flow rule has the form

$$\dot{q}=-\dot{\lambda}D\frac{\partial f(\sigma,q)}{\partial q} \tag{2.30}$$

where q is a single parameter that describes the evolution of the elastic domain, and D is the generalised hardening modulus. For a non-associative flow rule, the hardening rule is expressed as

$$\dot{q}=-\dot{\lambda}h(\sigma,q) \tag{2.31}$$

where h is a prescribed function.

2.1.3 Iterative Methods

For a nonlinear system, the stiffness, $\mathbf{K}$, and the applied force, $\mathbf{F}$, are not independent of the deformation. Considering a one-dimensional problem for simplicity, the spring stiffness is composed of a constant k_0 and k_N that is a function of displacement. The equation describing the problem can be written as

$$(k_0 + k_N)u = P \tag{2.32}$$

where $k_N = f(u)$, and u is the displacement caused by load P. To determine u from a given P, iterative methods are needed and the most commonly used scheme is the Newton-Raphson (N-R) method.

When using the N-R method, let us assume that there is an applied load, P_0, and the corresponding displacement is determined as being u_0. The equation above will become

$$(k_0 + k_{N0})u_0 = P_0 \tag{2.33}$$

where $k_{N0} = f(u_0)$. Now, if the load is increased to P_A, the purpose of the N-R method is to seek for the corresponding displacement, u_A, by carrying out an iterative procedure.Tthe tangent stiffness, k_T, is evaluated corresponding to u_0 as

$$(k_T)_0 = \left(\frac{dP}{du}\right)_0 \tag{2.34}$$

Using a Taylor series expansion of $P = f(u)$ about u_0,

$$\begin{aligned} f(u_0 + \Delta u_1) &= f(u_0) + \left(\frac{dP}{du}\right)_0 \Delta u_1 \\ &= P_0 + (k_T)_0 \Delta u_1 \end{aligned} \tag{2.35}$$

For $f(u_0 + \Delta u_1) = P_A$, the equation becomes

$$(k_T)_0 \Delta u_1 = P_A - P_0 \tag{2.36}$$

where $P_A - P_0$ is the imbalance force which needs to be minimised as the iteration procedure progresses and Δu_1 is used to update the displacement estimate to $u_1 = u_0 + \Delta u_1$.

In the next iteration, a new tangent stiffness, $(k_T)_1$, is obtained at u_1, and the new imbalance force is evaluated as $P_A - P_1$, where P_1 is obtained from equation (2.33) by replacing u with u_1. Δu_2 is then obtained from equation (2.36) by solving $(k_T)_1 \Delta u_2 = P_A - P_1$, and the displacement can be updated to $u_2 = u_1 + \Delta u_2$ for the next iteration. This process keeps repeating itself until the imbalance force and Δu are eventually reduced to the tolerance value set in the numerical procedure.

Although this procedure is represented for a one dimensional problem, it can be easily extended to multi degrees of freedom by solving equations $[\mathbf{K}_T]_i \{\Delta \mathbf{D}\}_{i+1} = \{\Delta \mathbf{R}\}_{i+1}$, where $[\mathbf{K}_T], \{\Delta \mathbf{D}\}$ and $\{\Delta \mathbf{R}\}$ are the tangent stiffness matrix, displacement-increment vector and the imbalance force vector respectively. The solution process using this method is shown in Figure 2.5 [42].

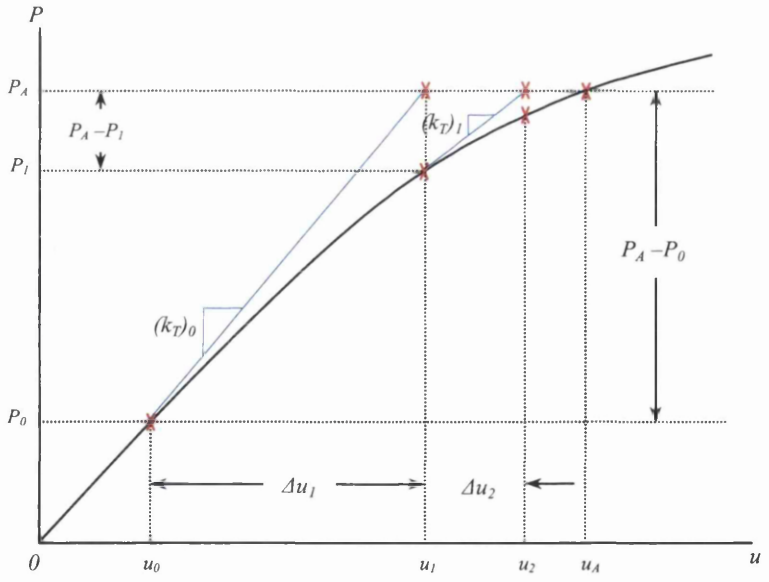

Figure 2.5: Newton-Raphson solution for u_A starting from u_0.

2.1.4 Direct Time Integration Methods

Direct integration methods, also called step-by-step methods, utilise the finite difference approximation to replace the time derivatives that appear in the equation of motion, i.e.

the accelerations and velocities are represented by the differences of displacement at various time instances [42]. There are many methods of direct integration and they can be classified into explicit and implicit methods in general. The explicit integration scheme is a forward marching method that computes the variables from the known quantities, while the implicit integration scheme requires iterative techniques to obtain the solution of coupled sets of equations that define the variables [45].

2.1.4.1 Explicit Direct Integration Method

The central-difference method is a popular explicit method used in numerical solution method [42]. In the method, the acceleration and velocity terms are approximated by

$$\dot{\mathbf{U}}_n = \frac{1}{2\Delta t}\left(\mathbf{U}_{n+1} - \mathbf{U}_{n-1}\right) \tag{2.37}$$

and

$$\ddot{\mathbf{U}}_n = \frac{1}{\Delta t^2}\left(\mathbf{U}_{n+1} - 2\mathbf{U}_n + \mathbf{U}_{n-1}\right) \tag{2.38}$$

Substituting these into equation (2.2), a system of linear algebraic equations is formed as below, and $\mathbf{U}_{n+1}$ can be obtained without the need for solving simultaneous equations.

$$\left[\frac{1}{\Delta t^2}\mathbf{M} + \frac{1}{2\Delta t}\mathbf{C}\right]\mathbf{U}_{n+1} = \mathbf{F}_n - \mathbf{K}\mathbf{U}_n + \mathbf{M}\left(2\mathbf{U}_n - \mathbf{U}_{n-1}\right) + \frac{1}{2\Delta t}\mathbf{C}\mathbf{U}_{n-1} \tag{2.39}$$

Besides, this method is also well suited for the treatment of material nonlinearity as the strain of the material at time $n\Delta t$ can be easily evaluated from $\mathbf{U}_n$ [42]. However, this equation, as for all explicit methods, is conditionally stable, which requires that the time step size Δt be smaller than the critical time step

$$\Delta t_{cr} = \frac{l}{c} \tag{2.40}$$

where $c \approx \sqrt{\frac{E}{\rho}}$, is the wave speed; E is the Young's Modulus; ρ is the density; and l is the effective length of the smallest element used in the analysis.

If $\Delta t > \Delta t_{cr}$, the solution will grow unboundedly and causes erroneous time-history solutions. As a result, this method could be computationally expensive due to this restriction. However, providing that the stability criterion is satisfied, a satisfactory accuracy is usually guaranteed [42].

2.1.4.2 Implicit Direct Integration Methods

One of the popular implicit integration methods used is the trapezoidal rule or the average acceleration method [42]. This method relates the accelerations, velocities, and displacements in the following form:

$$\mathbf{U}_{n+1} = \mathbf{U}_n + \frac{\Delta t}{2}\left(\dot{\mathbf{U}}_n + \dot{\mathbf{U}}_{n+1}\right) \tag{2.41}$$

$$\dot{\mathbf{U}}_{n+1} = \dot{\mathbf{U}}_n + \frac{\Delta t}{2}\left(\ddot{\mathbf{U}}_n + \ddot{\mathbf{U}}_{n+1}\right) \tag{2.42}$$

Alternatively, $\dot{\mathbf{U}}_{n+1}$ and $\ddot{\mathbf{U}}_{n+1}$ can be solved for to give

$$\dot{\mathbf{U}}_{n+1} = \frac{2}{\Delta t}\left(\mathbf{U}_{n+1} - \mathbf{U}_n\right) - \dot{\mathbf{U}}_n \tag{2.43}$$

$$\ddot{\mathbf{U}}_{n+1} = \frac{4}{\Delta t^2}\left(\mathbf{U}_{n+1} - \mathbf{U}_n\right) - \frac{4}{\Delta t}\dot{\mathbf{U}}_n - \ddot{\mathbf{U}}_n \tag{2.44}$$

Substituting these into equation (2.2) at time $(n+1)\Delta t$ yields a system of coupled linear algebraic equations

$$\left(\frac{4}{\Delta t^2}\mathbf{M} + \frac{2}{\Delta t}\mathbf{C} + \mathbf{K}\right)\mathbf{U}_{n+1} = \left\{\begin{array}{l} \mathbf{F}_{n+1} + \mathbf{M}\left(\frac{4}{\Delta t^2}\mathbf{U}_n + \frac{4}{\Delta t}\dot{\mathbf{U}}_n + \ddot{\mathbf{U}}_n\right) \\ + \mathbf{C}\left(\frac{2}{\Delta t}\mathbf{U}_n + \dot{\mathbf{U}}_n\right) \end{array}\right\} \tag{2.45}$$

or

$$\mathbf{K}^{\text{eff}}\mathbf{U}_{n+1} = \mathbf{F}^{\text{eff}}{}_{n+1} \tag{2.46}$$

where $\mathbf{K}^{\text{eff}}$ is the effective stiffness matrix, and $\mathbf{F}^{\text{eff}}{}_{n+1}$ is the effective load vector.

For a linear problem, $\mathbf{K}^{\text{eff}}$ needs to be formed and factored only once at the beginning, and subsequently the time-stepping can be carried out by a forward- and backward-substitution. Alternatively, if the problem involves material nonlinearity then $\mathbf{K}$ and thus $\mathbf{K}^{\text{eff}}$ are functions of the unknown $\mathbf{U}_{n+1}$. A prediction of $\mathbf{K}$ is hence needed to solve for $\mathbf{U}_{n+1}$, and this is done by using iterative procedures. As a result, the implicit method will have to alternate between substitution and iterative procedures to converge to a solution.

Unlike the explicit method, most implicit methods have the advantage of being unconditionally stable. This means the time step size chosen for the integration can be

large for a faster convergence. However, with the use of a large time step size the accuracy of the solution could be poor. Furthermore, the implicit method is more difficult to implement than the explicit method, especially for nonlinear problems and also requires more computer storage [42].

2.1.5 Adaptive Finite Element Mesh Refinement

Many industrial operations, such as forming operations often experience deformation that significantly changes the geometry and material characteristic during the course of the process [46]. The mesh configuration used in the finite element simulation of such problems is required to vary continually throughout the deformation process so that an accurate response can be captured. Therefore, the use of adaptive mesh refinement for the solution is essential to attain a reasonable solution accuracy while maintaining the local details of deformation, especially in large scale industrial problems [46, 47].

Self-adaptive mesh refinement strategies for linear elastic finite element analyses are now well developed and can be performed routinely in modern finite element computations. Nevertheless, an adaptive analyses for nonlinear problems, such as plasticity, are still ongoing research [46, 48]. An adaptive strategy in a finite element simulation requires procedures such as defining a re-meshing criterion, specification of error estimation criterion, the strategy for mesh adaptation based on the error distribution, and automatic mesh generation tools.

In general, there are three sources of error that are present in a nonlinear finite element analysis [48]:

- Error due to finite element discretisation
- Error due to step sizes used in the incremental (dynamic) analysis
- Error due to iterative solutions of nonlinear system of equations

Error estimators based on the constitutive relation of the problem, on the plastic work rate, on the effective stress, on the energy dissipation rate or on the effective plastic strain rate are used to control the quality of the mesh discretisation, whereas the plastic strain increment error estimator controls the load increments [48]. The result of an adaptive re-meshing strategy requires that the relative error computed from the error estimator in the

analysis be within a specified tolerance. When the criterion is violated, mesh refinement is carried out.

There are several ways in which mesh refinement can be done: by introducing smaller elements of the same type (h-refinement), by using the same elements with increased order of polynomials that involves the use of additional nodes on the elements (p-refinement) or by a combination of both [40]. After re-meshing is carried out, variables such as displacements, deformations, and stresses as determined from the previous mesh are then transferred to the refined mesh using some transfer operators.

2.1.5.1 Error Norms and Error Estimators

To measure the error in a finite element analysis, norms that represent some integral values are introduced. For instance in elasticity problems, the 'energy norm' has the form [40]

$$\begin{aligned}\|e\| &= \left[\int_\Omega (\boldsymbol{\varepsilon}-\hat{\boldsymbol{\varepsilon}})^T \mathbf{D}(\boldsymbol{\varepsilon}-\hat{\boldsymbol{\varepsilon}})d\Omega\right]^{1/2} \\ &= \left[\int_\Omega (\boldsymbol{\varepsilon}-\hat{\boldsymbol{\varepsilon}})(\boldsymbol{\sigma}-\hat{\boldsymbol{\sigma}})d\Omega\right]^{1/2} \\ &= \left[\int_\Omega (\boldsymbol{\sigma}-\hat{\boldsymbol{\sigma}})\mathbf{D}^{-1}(\boldsymbol{\sigma}-\hat{\boldsymbol{\sigma}})d\Omega\right]^{1/2}\end{aligned} \tag{2.47}$$

where $\mathbf{D}$ is the elasticity matrix; $\boldsymbol{\varepsilon}$ and $\hat{\boldsymbol{\varepsilon}}$ are the exact and approximated strains; $\boldsymbol{\sigma}$ and $\hat{\boldsymbol{\sigma}}$ are the exact and approximated stresses; and Ω is the domain of the model.

Also, there are also other scalar norms such as the so called L_2 norm of displacement or stress error [40]. For the displacement error, the norm has the form

$$\|e_u\|_{L_2} = \left[\int_\Omega (\mathbf{u}-\hat{\mathbf{u}})^T(\mathbf{u}-\hat{\mathbf{u}})d\Omega\right]^{1/2} \tag{2.48}$$

and for a stress error, the norm is written as

$$\|e_\sigma\|_{L_2} = \left[\int_\Omega (\boldsymbol{\sigma}-\hat{\boldsymbol{\sigma}})^T(\boldsymbol{\sigma}-\hat{\boldsymbol{\sigma}})d\Omega\right]^{1/2} \tag{2.49}$$

Any of these errors can be evaluated on individual elements or over the whole domain, where

$$\|e\|^2 = \sum_{i=1}^{m} \|e\|_i^2 \tag{2.50}$$

, with i representing an individual element up to a total number of m elements in the domain.

2.1.5.2 Adaptive Strategy Using Error Estimator

In the finite element analysis, error estimators are used to represent the global and local energy norm of the error. For example, in elasticity problems, the error estimator has the form [40]

$$\|\varepsilon_\sigma\| = \|\boldsymbol{\sigma}^* - \hat{\boldsymbol{\sigma}}\| \tag{2.51}$$

where $\hat{\boldsymbol{\sigma}}$ is the approximate or discontinuous stress and $\boldsymbol{\sigma}^*$ is the smoothed or continuous stress obtained from averaging or 'projection' of the approximate stresses which satisfies

$$\int \Pi(\boldsymbol{\sigma}^* - \hat{\boldsymbol{\sigma}}) d\Omega = 0 \tag{2.52}$$

where Π is the projection matrix. If this error has exceeded the specified tolerance set by the analyst, a mesh refinement is necessary.

The simplest way to assess the requirement for re-meshing is by measuring the relative energy norm percentage error η, which has to be less than some prescribed value $\overline{\eta}$, so that

$$\eta \leq \overline{\eta} \tag{2.53}$$

For elasto-plastic problems, the generalised stress error estimator for an element i and global error may be obtained as [46]

$$\|\varepsilon_\Sigma\|_i^2 = \|\boldsymbol{\Sigma}^* - \boldsymbol{\Sigma}^h\|_i^2 = \|e_\Sigma\|_i^2 \tag{2.54}$$

$$\|\varepsilon_\Sigma\|^2 = \sum_i \|\varepsilon_\Sigma\|_i^2 \tag{2.55}$$

where Σ^* and Σ^h are the smoothed and approximate generalised stress values.

The relative energy norm error can then be defined as [46]

$$\eta_\Sigma = \frac{\|e_\Sigma\|}{\boldsymbol{\Sigma}} \approx \frac{\|\varepsilon_\Sigma\|}{\boldsymbol{\Sigma}} \tag{2.56}$$

2.1.5.3 Transfer Operation

When a new mesh is created, the variables from the previous mesh are transferred to the new mesh so that the analysis is able to proceed. The transfer of the variables is a crucial operation and some important issues that need consideration are [46]:

- Consistency with the constitutive equations
- Equilibrium requirements
- Compatibility of the state transfer with the displacement field on the new mesh
- Compatibility with the boundary conditions that are changing
- Minimisation of the numerical diffusion of the state fields

For a typical elasto-plastic material, whose behaviour is described by a set of internal variables, the mapping of the variables between the old and new finite element mesh, say h and $h+1$, is an essential part of an adaptive strategy. Besides, the transfer of the displacement field between the meshes is also necessary. To carry out the transfer of the variables and displacement field, transfer operators are used [46].

The mapping of internal variables between meshes h and $h+1$ are carried out using the transfer operator T_1 defined by [46]

$$\left({}^{h+1}\varepsilon_n^p, {}^{h+1}A_n\right) = T_1\left[{}^{h}\varepsilon_n^p, {}^{h}A_n\right] \tag{2.57}$$

where ε_n^p and A_n are the plastic strain tensor and internal variables vector at time t_n. The operator can be constructed in different ways, e.g. by taking constant values over the area associated with every quadrature point or by a continuous solution using a least-square method or a suitable projection of ${}^{h}\varepsilon_n^p$.

In the transfer operation, the continuous values for ${}^{h}\varepsilon_n^{p*}$ and ${}^{h}A_n^*$ are obtained by projecting the Gauss point components ${}^{h}\varepsilon_{n,G}^p$ and ${}^{h}A_{n,G}$ to nodal points by using shape functions, hence resulting in ${}^{h}\varepsilon_{n,N}^p$ and ${}^{h}A_{n,N}$. The averaging of the projected values on the nodal points are then performed to give ${}^{h}\varepsilon_{n,N}^{p\,*}$ and ${}^{h}A_{n,N}^*$. These values are then transferred to the nodes of the new mesh $h+1$ and followed by interpolation using the shape functions of the finite element to obtain the Gauss point components.

In addition, the mapping of the displacement field between meshes h and $h+1$, in the context of an implicit analysis, can be performed using a transfer operator T_2 defined by [46]

$$^{h+1}u_{n+1}^{trial} = T_2\left[^{h}u_{n+1}\right] \tag{2.58}$$

The transferred displacement is used on the new mesh as an initial guess for the displacements in the first iteration of the iterative procedure. Also, the transfer operator T_2 for the displacement field can be constructed easily since the nodal displacement values and finite element shape functions prescribe the displacement field completely.

2.2 Discrete Element Method

The discrete or distinct element method was originally developed by Cundall for the analysis of rock assemblies [26]. In this method, the equilibrium contact forces and displacements of a particle assembly is found through a series of calculations (using time integration method as discussed in section 2.1.4) that trace the movement of the particles as a consequence of a dynamic process, i.e. propagation. The velocities and accelerations are assumed to be constant over the time step intervals and the time steps chosen are so small that in each step the disturbance cannot propagate through its immediate neighbours. The resultant forces on any particle are therefore determined exclusively from the interaction with the neighbouring particles that are in contact only.

In the discrete element method, the particles are treated as rigid bodies. The overlap between particles (or the relative displacement at the contact) is used to represent the deformation and the magnitude of the overlap is relatively small compared to the dimension of the particles. From the overlap calculated, a force-displacement law is used to obtain the contact force and the motion of the particles, such as velocities and positions, are updated using Newton's second law.

When the discrete element method was first introduced, the simulation only allowed assemblies of disks to be analysed [26]. This method has now been improved to model discrete particles of other shapes such as ellipses/ellipsoids and polygons/polyhedra [49]. Furthermore, many works have been focused on improving the contact detection among the particles during the simulation as this step forms the most

crucial part in the discrete element method in determining the interacting forces among the particles.

2.2.1 Contact Detection

The most important part of the discrete element method is the determination of the interaction forces among the discrete particles. The detection of contact during the simulation is therefore a crucial procedure in order to make sure an accurate force is obtained.

The contact detection procedure generally consists of three phases: spatial search (global), interaction or contact resolution (local) and interaction force computation [37,49]. The spatial search is a step for detecting potential contact pairs among the discrete particles, whereas a local interaction resolution is carried out on the identified potential contacting pairs with non-interacting pairs excluded. In the global spatial search, the various shape objects are represented by simple geometries, such as disks(2D)/spheres(3D) or rectangles(2D)/boxes(3D), that bound the target objects for a rough detection. Many very effective algorithms have been developed for the purpose of global contact search, for examples, references [36,50,51]. On local contact resolution, the geometric details of the objects are considered.

After the local contact resolution, the interaction force between the actual contacting pairs is determined using a constitutive relationship or physical interaction laws. The interaction law describes the relation between the overlap and the repulsive force at the contact. An example of interaction law is the Hertz contact model for normal contact between two elastic spheres. For contact between particles of other material, e.g. plastic spheres with or without adhesion/cohesion at the contact, then other interaction laws are needed. In addition, other contact conditions such as friction can also be incorporated into the contact interaction law by using the appropriate choice of friction model according to the purpose of the simulation.

2.2.2 2D Shape Descriptors for Non-circular Particles

The shape representation used for a particular object is important not only to control the accuracy of the geometrical modelling, but also to determine the type and accuracy of the

contact detection algorithm that can be used [37]. The most commonly used 2D shape descriptors in the modelling of non-circular granular particles are:

- Polygons
- Continuous function representations such as ellipses or superquadrics
- Discrete function representations

2.2.2.1 Polygon

The geometry of polygonal objects is represented in terms of corners, edges and the cosine directions of the local axes [37]. The types of contact between polygonal objects are categorised into: corner-to-edge, edge-to-edge, and corner-to-corner. These are shown in the following figure [37].

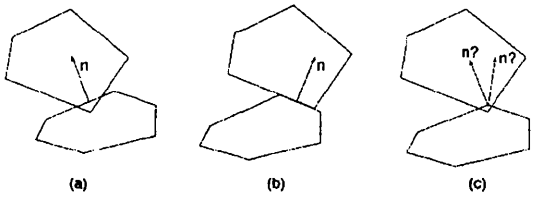

Figure 2.6: Types of contact between polygonal objects: a) corner-to-edge; b) edge-to-edge; and c) corner-to-corner.

For the contact corner-to-edge and edge-to-edge, the contact normal is easily determined, i.e. perpendicular to the edge. However, the contact normal for corner-to-corner is difficult to determine.

The contact detection between two co-planar polygons can be done in a number of ways. For example, the edge of one polygon can be tested to check if it crosses with another polygon. Alternatively, as proposed by Muller and Liebling (according to [37]), triangulation method can be used to join the corners of all the polygons with their adjacent neighbours. If the triangle becomes flat, a contact is found. However, the disadvantage of using polygonal representation for a non-circular object is that the mixture of polygonal objects with smooth objects cannot be easily investigated in a simulation. Although smooth objects can be represented by polygons with a large number of corners, the contact detection efficiency is decreased proportionally.

Feng and Owen [52] addressed the issue of the contact between the corners of polygons and proposed a method based on the contact energy to determine the normal

contact force uniquely for the corner to corner contact between polygons. Furthermore, the method can also be extended to treat normal contact of any shaped convex objects

2.2.2.2 Continuous Function Representations

To model smooth non-circular shape objects, the surface of the object can be represented by a continuous function $f(x,y)$, i.e. ellipses or 2D superquadrics. Although the geometry and position for elliptical objects can be easily defined (i.e. by the length and orientation of the principal axes), the contact between two ellipses with a small overlap that approaches a single point can produce ill-conditioning of the resulting equation. A more general continuous function representation, such as the 'superquadric' or 'superellipse' curve, can be used for a greater variety of shapes. However, the nonlinearity of the equations for the two contacting superquadric curves can be computationally expensive [53].

In general, the contact normal for a continuous function representation is straightforward and is represented by the direction perpendicular to the curve at the intersection point. This allows the contact normal to be determined at the beginning of the simulation.

A robust algorithm was proposed by Han et al [53] for the contact of 2D superquadrics, where the superquadrics are represented by convex polygons. When the contact between the polygons is detected, the contact model derived by Feng and Owen [52] is used to determine the contact forces and directions between the convex polygons.

2.2.2.3 Discrete Function Representations

A discrete function representation in 2D is defined as a discretised representation of the boundary of an object by a function at each interval which produces an array of nodes for the object [54]. An example is the polar descriptor, used by Hogue and Newland [55], where each node is defined by a radius R and angle θ from a datum. This representation is not restricted to convex shapes only and is straightforward for common granular material shapes.

The contact detection between discrete function representation bodies can be performed in multi stages where a rough search can be done by using bounding boxes, or

spheres, to check for any overlap. If overlap is detected, the search is then refined to the overlapping area between the bounding boxes or spheres.

Many contact detection methods have been devised, such as the two-stage process for particles represented by polar coordinates [37] or the Cartesian coordinates and trapezoidal strips proposed by Williams and O'Connor [54] for the contact between two particles represented by discrete function representation. The contact normal for these methods cab be found analytically if the particle shapes are generated from one or more functions, where it can be computed at the start of the simulation. Otherwise, the determination of the contact normal depends on the type of contact.

Another type of contact search suitable for large scale problem is the direct evidence search for discrete representation objects used by Munjiza et al [28]. In this method, a circular search represented by regularly spaced grid points, centred at the centre of mass of the target object, is used to search for grid points that lie inside both of the target and neighbouring object. Normal vectors are determined at each node and edge as part of the boundary description of the object so that the contact normal can be determined.

In general, the discrete function representations enjoys the benefit of being able to handle various shapes, whether they are smooth, sharp edges, compact or elongated, within a single simulation.

2.2.3 Illustration on Motion Update Calculation

In the discrete element method proposed by [26], the contact between the particles is represented by a linear spring and the contact force between the particles is determined from the amount of overlap between the particles. The calculation alternates between the linear spring equation (which is a special case for interaction law) and Newton's second law to update the position and the forces between the particles.

To illustrate the way forces and displacements are updated during the calculation cycle, consider the vibration of two disks between a pair of moving rigid walls as shown in the following figure. Point A and C are the contacts between the discs and the walls, and x and y have positive directions as shown.

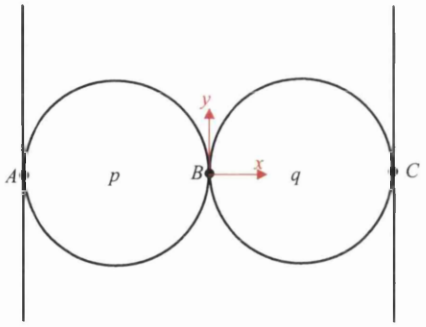

Figure 2.7: Two discs in contact at $t = t_0$.

After a time interval Δt, the walls are moved towards each other with a velocity v. As the disturbance cannot travel beyond a single disc during one time step, as mentioned previously, discs p and q remain in their original position during the time interval. Thus, the amount of overlap at contacts A and C at time $t_1 = t_0 + \Delta t$ is

$$(\Delta n_A)_{t_1} = (\Delta n_C)_{t_1} = v\Delta t \tag{2.59}$$

and the contact at A and C lies halfway between $A' - A''$ and $C' - C''$. This can be visualised in the following figure.

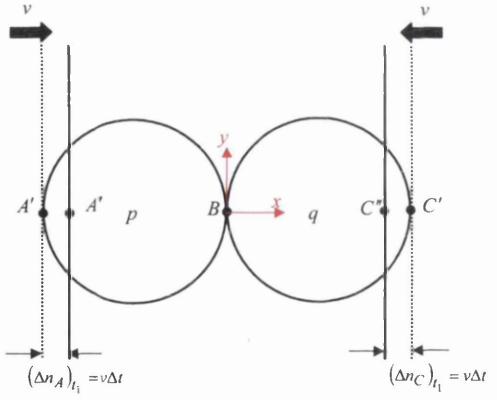

Figure 2.8: Two discs compressed between the walls at time $t_1 = t_0 + \Delta t$.

The force-displacement relation has the form

$$\Delta F_n = k_n (\Delta n)_{t1} = k_n v \Delta t \tag{2.60}$$

where k_n is the normal stiffness and ΔF_n is the normal force increment. The sum of the forces on liscs p and q at time $t_1 = t_0 + \Delta t$ hence becomes,

$$F_{(p)x} = k_n(\Delta n)_{t1} \tag{2.61}$$

$$F_{(q)x} = k_n(\Delta n)_{t1} \tag{2.62}$$

Using Newton's second law, the accelerations can be found as

$$\ddot{x}_p = \frac{F_{(p)x}}{m_p} \tag{2.63}$$

$$\ddot{x}_q = \frac{F_{(q)x}}{m_q} \tag{2.64}$$

where $\ddot{x}_p$ and $\ddot{x}_q$ are the accelerations of discs p and q in x direction, and m_p and m_q are the masses of discs p and q. Assuming constant acceleration over the time interval from $t_1 = t_0 + \Delta t$ to $t_2 = t_0 + 2\Delta t$, the velocities can be integrated from the accelerations as

$$(\dot{x}_p)_{t2} = \left(\frac{F_{(p)x}}{m_p}\right)\Delta t \tag{2.65}$$

$$(\dot{x}_q)_{t2} = \left(\frac{F_{(q)x}}{m_q}\right)\Delta t \tag{2.66}$$

Hence, the relative displacements increment, taking positive for compression at A, B and C, can be obtained as

$$(\Delta n_A)_{t2} = \left[v - \left(\frac{F_{(p)x}}{m_p}\right)\Delta t\right]\Delta t \tag{2.67}$$

$$(\Delta n_B)_{t2} = \left[\left(\frac{F_{(p)x}}{m_p}\right)\Delta t - \left(\frac{F_{(q)x}}{m_q}\right)\Delta t\right]\Delta t \tag{2.68}$$

$$(\Delta n_C)_{t2} = \left[\left(\frac{F_{(q)x}}{m_q}\right)\Delta t - (-v)\right]\Delta t \tag{2.69}$$

The overlap at the contacts is illustrated in the following figure.

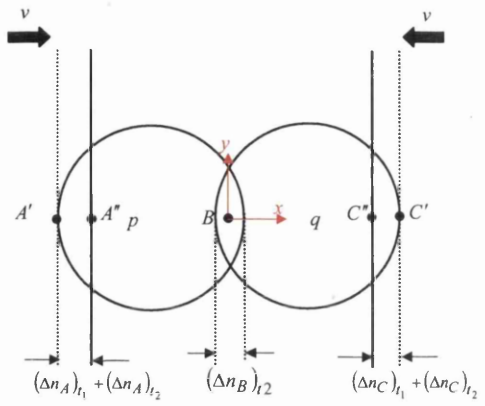

Figure 2.9: Two discs compressed between the walls at time $t_2 = t_0 + 2\Delta t$.

This cycle can be repeated again and again, alternating between the force-displacement law and Newton's second law to update the forces and displacements.

For a general assembly of discs, the force-displacement law is applied at each contact and the vectorial sum of the forces is calculated to give the resultant force acting on a particular disc. In this case, two discs are said to be in contact if the distance between the centres of the discs is less than the sum of the two particles' radius, i.e. $D < R_1 + R_2$, where D is the distance between the centres and R_1, R_2 are the radius of disc 1 and 2 respectively.

2.3 Combined Finite-Discrete Element Method

The combined finite-discrete element method obtained its name from the idea of meshing each discrete particle with finite elements in the simulations. It is an evolution from the discrete element method where the deformation kinematics is incorporated into the discrete element formulation to improve the accuracy of particle modelling. This method is particularly suitable for modelling problems with progressive fracturing such as missile impact simulations and composite fracture/delamination [46].

In the context of the explicit time integration scheme, this method typically performs the following procedure at each time step [34]:

1. Compute the internal forces of the finite element meshes and evaluate material failure criterion, if any.

2. Search for potential contacting pairs and determine the actual interacting pairs.
3. Compute the interaction forces between the actual interacting pairs by using appropriate interaction laws.
4. Compute the velocities and displacements of all nodes.
5. Update the coordinate of all finite element nodes and the location of all discrete particles.

Chapter 3

Contact Analyses

As mentioned in the previous chapter, the modelling of discrete particles requires contact interaction laws to update the forces and positions of the particles during the simulation. Hence, the use of an appropriate interaction law (which is referred to as contact mechanics in general) is crucial in the analysis in order to capture with reasonable accuracy the response of the discrete particles upon loading.

The study of contact mechanics will not be complete without reference being made to the very famous Hertz theory. Hence, the purpose of this chapter is to discuss Hertz theory for elastic contact and also, with further relaxation on the assumptions made in the theory, the non-Hertzian analysis that focuses on the contact of layered solids. In addition, the results obtained from finite element simulation on the contact between two solids and the contact of layered solids will also be shown and compared with the theoretical values. To make this chapter more complete, some topics on the contact between two bodies and two-dimensional plane analysis will be mentioned briefly before going into the discussion on the theories.

3.1 Stress-Strain Relations

3.1.1 Hooke's Law

The stress-strain relations for linear elastic isotropic materials are usually known as Hooke's Law [56]. If a cubic element with the sides parallel to the coordinate axes is subjected to uniformly distributed normal stresses σ_x, σ_y, σ_z and shear stresses γ_{xy},

γ_{xz}, γ_{yz} over the sides as shown in Figure 3.1, the stress-strain relations according to Hooke's Law are

$$\begin{aligned}
\varepsilon_x &= \frac{1}{E}\left[\sigma_x - \nu(\sigma_y + \sigma_z)\right] \\
\varepsilon_y &= \frac{1}{E}\left[\sigma_y - \nu(\sigma_x + \sigma_z)\right] \\
\varepsilon_z &= \frac{1}{E}\left[\sigma_z - \nu(\sigma_x + \sigma_y)\right] \\
\gamma_{yz} &= \frac{\tau_{yz}}{G}; \gamma_{xz} = \frac{\tau_{xz}}{G}; \gamma_{xy} = \frac{\tau_{xy}}{G}
\end{aligned} \tag{3.1}$$

where E is the Young's modulus, ν is the Poisson's ratio, and $G = \frac{E}{2(1+\nu)}$ is the shear modulus of the material.

The strain components are related to the displacements as shown:

$$\begin{aligned}
\varepsilon_x &= \frac{\partial u}{\partial u}; \varepsilon_y = \frac{\partial v}{\partial y}; \varepsilon_z = \frac{\partial w}{\partial z} \\
\gamma_{xy} &= \frac{\partial u}{\partial y} + \frac{\partial v}{\partial x}; \gamma_{xz} = \frac{\partial u}{\partial z} + \frac{\partial w}{\partial x}; \gamma_{yz} = \frac{\partial v}{\partial z} + \frac{\partial w}{\partial y}
\end{aligned} \tag{3.2}$$

where u, v, and w are the displacements in x, y and z directions respectively.

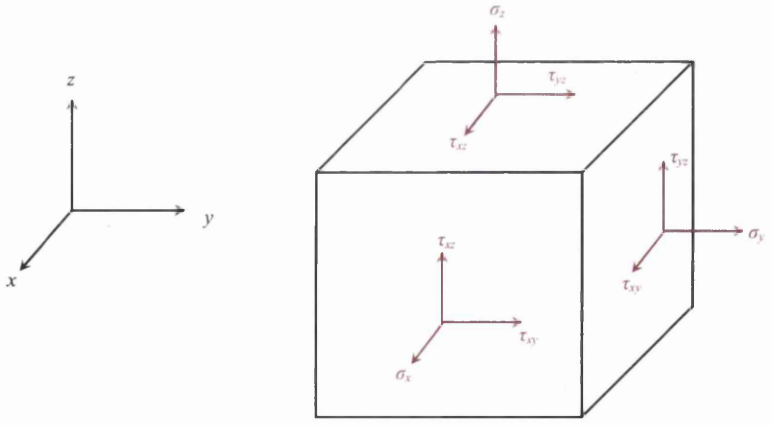

Figure 3.1: Stresses acting on an element.

3.1.1.1 Two Dimensional Problems in Rectangular Coordinates

If the problem to be analysed is reduced to a two-dimensional rectangular coordinate system, only the stresses acting on the square element shown in Figure 3.2 are considered.

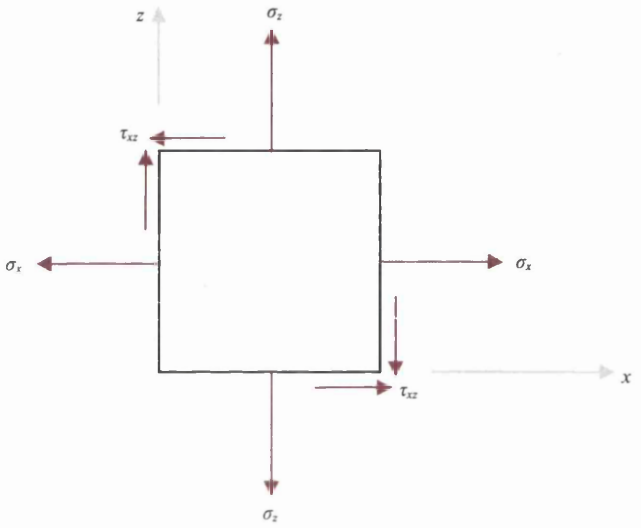

Figure 3.2: Two-dimensional stresses in rectangular coordinates.

If the size of the element is so small that the sides of the element are close to zero, the equilibrium equations to be satisfied at this point are

$$\frac{\partial \sigma_x}{\partial x} + \frac{\partial \tau_{xz}}{\partial z} = 0$$
$$\frac{\partial \sigma_z}{\partial z} + \frac{\partial \tau_{xz}}{\partial x} = 0 \tag{3.3}$$

and the strains are reduced to

$$\varepsilon_x = \frac{\partial u}{\partial u}; \varepsilon_z = \frac{\partial w}{\partial z}; \gamma_{xz} = \frac{\partial u}{\partial z} + \frac{\partial w}{\partial x} \tag{3.4}$$

3.1.1.2 Two-Dimensional Problems in Polar Coordinates

Sometimes, due to the nature of the problems, the use of cylindrical polar coordinates is more convenient in the analysis. This coordinate system consists of axes r, θ, and y in the radial, circumferential and normal directions respectively, as shown in Figure 3.3.

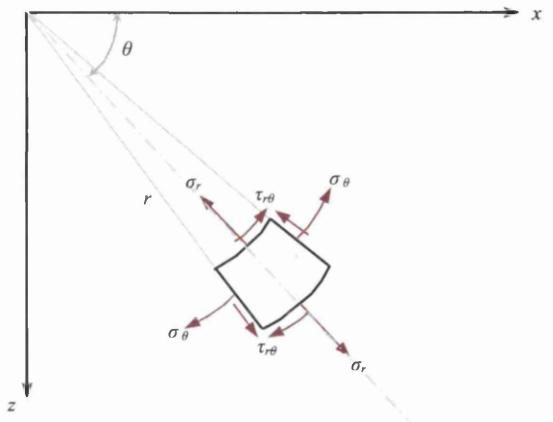

Figure 3.3: Two-dimensional stresses in polar coordinates.

If the size of the element is so small that the sides of the element are close to zero, the equilibrium equations to be satisfied at this point are

$$\frac{\partial \sigma_r}{\partial r} + \frac{1}{r}\frac{\partial \tau_{r\theta}}{\partial \theta} + \frac{\sigma_r - \sigma_\theta}{r} = 0$$
$$\frac{1}{r}\frac{\partial \sigma_\theta}{\partial \theta} + \frac{\partial \tau_{r\theta}}{\partial r} + \frac{2\tau_{r\theta}}{r} = 0 \tag{3.5}$$

The strain components are related to the displacements as follows:

$$\varepsilon_r = \frac{\partial u_r}{\partial r}; \varepsilon_\theta = \frac{u_r}{r} + \frac{1}{r}\frac{\partial u_\theta}{\partial \theta}; \gamma_{r\theta} = \frac{1}{r}\frac{\partial u_r}{\partial \theta} + \frac{\partial u_\theta}{\partial r} - \frac{u_\theta}{r} \tag{3.6}$$

Where u_r and u_θ are the displacements in the radial and circumferential directions respectively.

3.1.2 Plane Stress and Strain Analyses

A 2D problem can be classified into either a plane stress or a plane strain analysis depending on the state of affairs considered. If the problem consists of a thin plate loaded with forces at the boundary along the plane of the plate and an even distribution of the force is assumed throughout the thickness of the plate, the situation can be treated as a plane stress problem. The stresses σ_z, τ_{xz} and τ_{yz} are assumed to be zero throughout the plate, and σ_x, σ_y and τ_{xy} are independent of z, i.e. constant throughout the thickness of the plate [56]. This situation is illustrated in Figure 3.4.

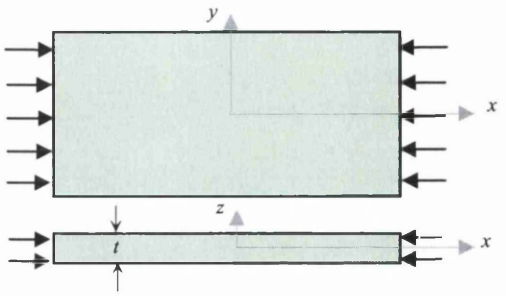

Figure 3.4: Plane stress analysis.

A plane strain analysis, conversely, is applied to a problem which consists of a long body subjected to forces acting constantly all along and perpendicular to the longitudinal direction. The longitudinal displacement, *w*, and hence the strains and stresses, γ_{xz}, γ_{yz}, τ_{xz} and τ_{yz}, are assumed to be zero. The stresses σ_x, σ_y and τ_{xy} are to be determined, and the longitudinal stress σ_z can be obtained from Hooke's Law as

$$\frac{1}{E}\left[\sigma_z - \nu\left(\sigma_x + \sigma_y\right)\right] = 0$$
$$\sigma_z = \nu\left(\sigma_x + \sigma_y\right) \tag{3.7}$$

Figure 3.5 shows an example of plane strain analysis.

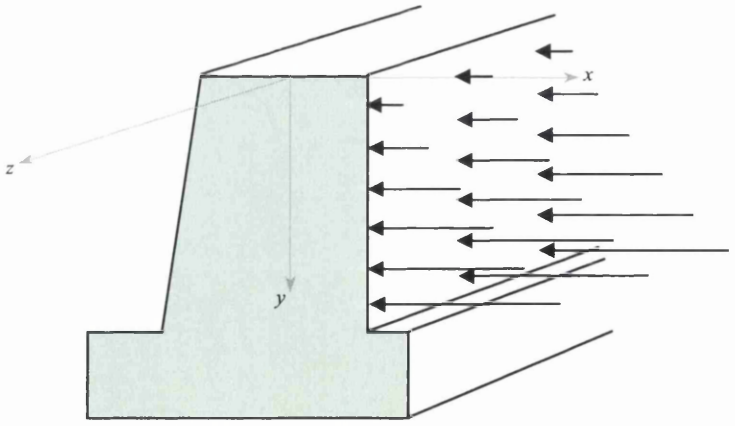

Figure 3.5: Plane strain analysis.

3.2 Contact between Two Bodies

The contact between two bodies can be categorised as conforming or non-conforming contact. If the two bodies fit closely without deformation, the contact is said to be conforming. In contrast, if the two bodies are having dissimilar profiles, the contact is said to be non-conforming. When brought into contact, the two bodies will touch at a point (point contact) or along a line (line contact) [14]. Examples of non-conforming contacts are shown in Figure 3.6.

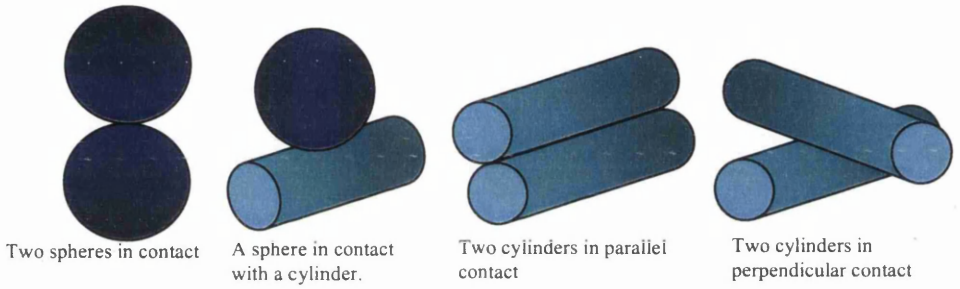

Figure 3.6: Examples of non-conforming contact.

When two non-conforming surfaces are brought into contact at a point, the interaction can be represented using rectangular coordinate with axes *Oxyz*, where *O* is the origin of the coordinate. The *Oz* axis is chosen to match with the common normal of the two surfaces at *O*, and the *x*-*y* plane is the tangent plane to the two surfaces. This representation is illustrated in the figure below.

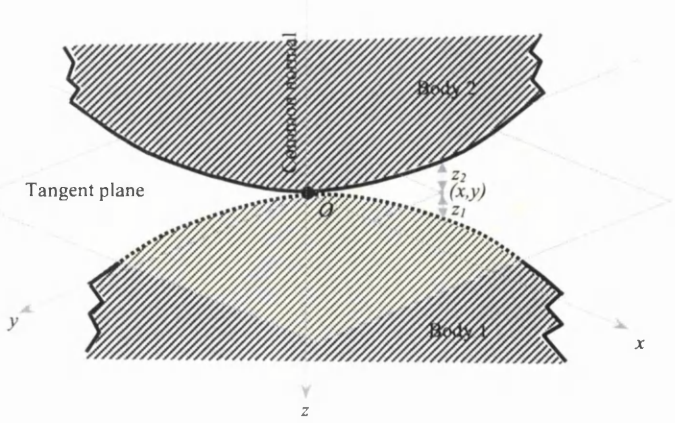

Figure 3.7: Reference frame for a point contact at *O*.

For two surfaces that are brought into contact along a line, i.e. the case of two cylinders in contact with their axes in parallel, non-conforming contact is observed in the plane of cross-section, while conforming line contact occurs in the plane that contains the axes of the cylinders. This can be treated by choosing one of the coordinate axes to lie in the cross section plane and the other lies in the axis that is parallel to the axes of the cylinders. An example of this representation is shown in Figure 3.8.

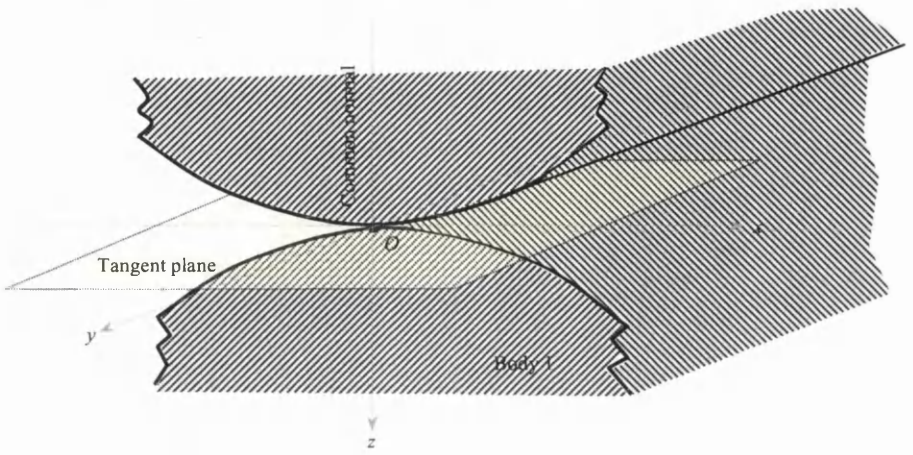

Figure 3.8: Reference frame for the contact of two parallel cylinders.

In Figure 3.7, the undeformed shape of the surfaces are specified by the functions

$z_1 = f_1(x, y)$

$z_2 = f_2(x, y)$

and hence the separation between the surfaces before loading can be written as

$$h = z_1 + z_2 = f(x, y) \tag{3.8}$$

The resultant force transmitted from one surface to another at the point of contact can be resolved into a normal compressive force P acting along the common normal and a tangential force Q acting in the tangential plane, which can be resolved into Qx and Qy along the Ox and Oy axes respectively. The magnitude of Q must be less than or equal to the limiting friction, i.e.

$$Q \leq \mu P \tag{3.9}$$

where μ is the coefficient of limiting friction.

3.3 Elastic Half-Space

The deformation caused by the contact between two non-conforming elastic bodies has to be sufficiently small for the theory of small strain linear elasticity to be applicable. The contact area formed due to the deformation is relatively small compared with the radii of curvature of the undeformed surfaces, and the contact stresses are highly concentrated around the region of the contact. As the stresses decrease rapidly with distance from the contact, and provided that the contact area is small compared with the dimensions of the bodies, the shapes of the bodies far-away from the contact and the way the bodies are supported have no effect on the stresses at the contact interface. Thus, interest only lies around the contact interface, and a good stress approximation can be calculated by treating each body as a semi-infinite solid bounded by a plane surface, i.e. an elastic half-space [14].

3.4 Hertz Theory for Elastic Contact [14]

The first satisfactory stress analysis at the contact of two elastic solids is due to the work of Hertz [14]. A simplification of the local deformation calculation was made by idealising each loaded body as an elastic half-space loaded over a small region of its plane surface. The high stress concentration around the contact region is assumed to be neither affected by the shape of the body nor the way the body is supported a distance from the contact. In order for this simplification to be justifiable, two conditions must be fulfilled:

1. The dimension of the contact area must be small compared with the dimension of each body.
2. The dimension of the contact area must be small compared with the relative radii of curvature of the surfaces.

The first condition is necessary to make sure that the stresses calculated are not seriously affected by the proximity of the boundary, i.e. the solids are of an infinite extent. The second condition is essential so that the strains in the contact region are sufficiently small to fulfil the theory of linear elasticity, and also to ensure that the surfaces outside the contact region are roughly a plane surface of a half-space.

Further, the surfaces are also assumed to be frictionless so that there is only normal pressure transmitted between the surfaces. The normal tractions are taken to act parallel to the common normal of the two surfaces at the point of contact and the tangential tractions, q_x and q_y, which act in the x-y plane, are ignored.

Metallic solids loaded within their elastic limit are found to comply well with this theory. However, for materials with a low modulus such as rubber, caution must be taken when applying this theory as the deformation of such materials could exceed the small strain restriction [14].

3.4.1 Geometry of Non-conforming Surfaces in Contact

The non-conforming surfaces of elastic solids in contact are considered to be topographically smooth on both the micro and macro scales. This means that the microscopic surface irregularities, which would lead to discontinuous contact or high local contact pressure, are ignored and the macroscopic profile of the surfaces is continuous up to the second derivative in the contact region [14]. Thus, as mentioned in section 3.2, and with the use of the reference frame in Figure 3.7, the profile of each surface close to the point of contact can be approximated by an expression of the form (higher order terms in x and y are neglected)

$$z = Ax^2 + By^2 + Cxy + \ldots \tag{3.10}$$

By choosing the appropriate orientation of the x and y axes so that the term xy disappears, the expression can be written as

$$z_1 = \frac{1}{2R_1'}x_1^2 + \frac{1}{2R_1''}y_1^2 \tag{3.11}$$

for surface 1, and as

$$z_2 = -\left(\frac{1}{2R_2'}x_2^2 + \frac{1}{2R_2''}y_2^2\right) \tag{3.12}$$

for surface 2, where $R_{1,2}'$ and $R_{1,2}''$ are the minimum and maximum principal radii of curvature of the surface at the origin (point of contact) for surfaces 1 and 2 respectively. The separation between the two surfaces is then given by $h = z_1 - z_2$, and can be written as

$$h = Ax^2 + By^2$$
$$= \frac{1}{2R'}x^2 + \frac{1}{2R''}y^2 \tag{3.13}$$

where A and B are positive constants and R' and R'' are defined as the principal relative radii of curvature.

For the contact between solids of revolution, the minimum and maximum principal radii of curvature are the same (i.e. $R'_{1,2} = R''_{1,2} = R_{1,2}$), and the contact area between the two surfaces upon loading are circular. For the contact between two cylinders with their axes parallel, $R'_{1,2} = R_{1,2}$ and $R''_{1,2} = \infty$, and the contact area extents from a line to a narrow strip parallel to their axes upon loading.

3.4.2 Geometry of Deformation

When a normal load P is applied to two curved shaped solids, the deformation at the contact is as shown in the figure below.

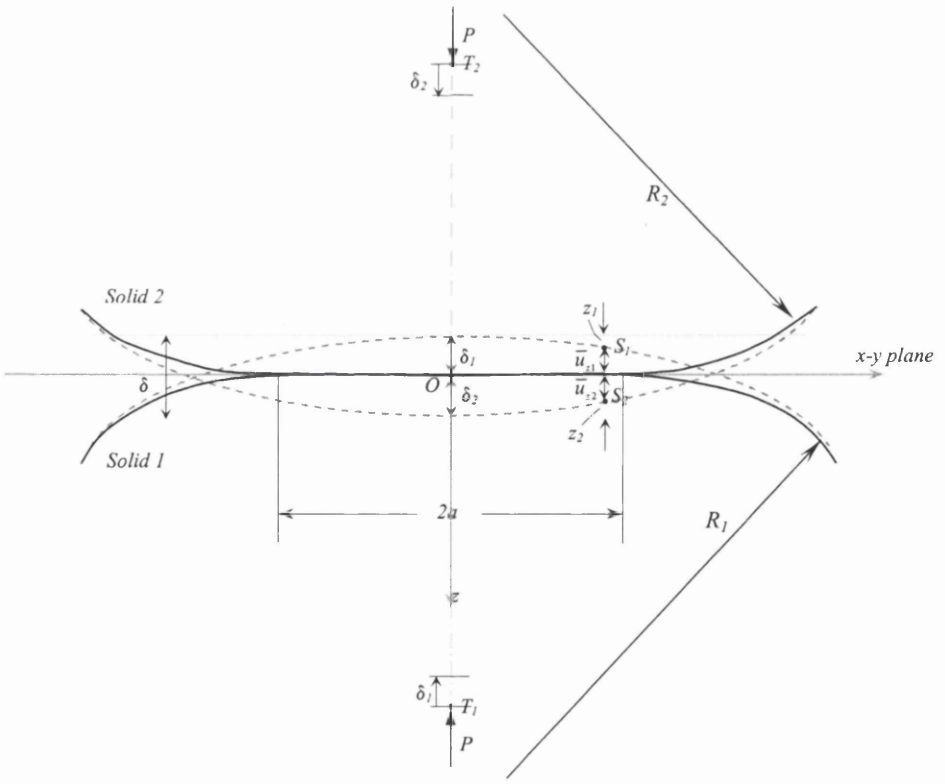

Figure 3.9: Deformation at the contact between two solids subjected to applied normal load P.

During compression, the distant points T_1 and T_2 move towards O, parallel to the z-axis, by displacements of δ_1 and δ_2 respectively. This causes an overlap between the undeformed solids where the profiles are shown by dotted lines. However, due to the contact pressure, the surface of the solids is displaced parallel to the z-axis by an amount of $\bar{u}_{z1}$ and $\bar{u}_{z2}$ respectively into the body. The surface points S_1 and S_2 are given by equation (3.13), and will coincide within the contact surface after deformation when

$$\bar{u}_{z1} + \bar{u}_{z2} + h = \delta_1 + \delta_2 = \delta \tag{3.14}$$

Making use of the expression in equation (3.13), this can be written as

$$\bar{u}_{z1} + \bar{u}_{z2} = \delta - Ax^2 - By^2 \tag{3.15}$$

If the surface points S_1 and S_2 lie outside the contact area after deformation, i.e. they do not touch, it follows that

$$\bar{u}_{z1} + \bar{u}_{z2} > \delta - Ax^2 - By^2 \tag{3.16}$$

Therefore, when solving for normal elastic displacements on the surface of the solids, Equations (3.15) and (3.16), formulated by Hertz, need to be satisfied within and outside the contact area [14].

3.4.3 Elastic Contact between Solids of Revolution

The geometry of a solid of revolution is generated by revolving a plane figure about an axis, namely the z-axis, and is axially symmetric. It is normally expressed by cylindrical coordinates with axes r, θ, and z. If the geometry, support conditions, loading and material properties are independent of θ, the displacements and stresses are independent of θ, and the circumferential displacement u_θ is zero. There will only be radial displacement u_r, axial displacement u_z, and non-zero stresses $\sigma_z, \sigma_r, \sigma_\theta$ and τ_{zr} [14,42].

For the case of solids of revolution, the minimum and maximum principal radii of curvature of the solids are equal, i.e. $R_1' = R_1'' = R_1$ and $R_2' = R_2'' = R_2$. When brought into contact by an applied normal load P, a circular contact area is formed with radius a. Therefore, it can be seen from equation (3.13) that $A = B = \frac{1}{2}\left(\frac{1}{R_1} + \frac{1}{R_2}\right)$. For the

condition within the contact region to be satisfied, the expression in Equation (3.15) can be written as

$$\bar{u}_{z1} + \bar{u}_{z2} = \delta - \left(\frac{1}{2R}\right) r^2 \tag{3.17}$$

where $\frac{1}{R} = \frac{1}{R_1} + \frac{1}{R_2}$ is the relative radii of curvature.

The pressure exerted between two contacting frictionless elastic solids of revolution is given by Hertz as

$$p(r) = p_0 \left\{ 1 - \left(\frac{r}{a}\right)^2 \right\}^{\frac{1}{2}} \tag{3.18}$$

where p_0 is the maximum pressure, and produces normal displacements

$$\bar{u}_z = \frac{1-\nu^2}{E} \frac{\pi p_0}{4a} \{2a^2 - r^2\}; \qquad \text{for r} \le a \tag{3.19}$$

As the pressure acting on the second body is the same as the pressure acting on the first body, by writing the effective modulus for the two bodies as

$$\frac{1}{E^*} = \frac{1-\nu_1^2}{E_1} + \frac{1-\nu_2^2}{E_2} \tag{3.20}$$

and by substituting the expressions for $\bar{u}_{z1}$ and $\bar{u}_{z2}$ into equation (3.17), the following expression is obtained

$$\frac{\pi p_0}{4aE^*} \left(2a^2 - r^2\right) = \delta - \left(\frac{1}{2R}\right) r^2 \tag{3.21}$$

By assigning zero to r (correspond to the centre of the contact) in equation (3.21) , the total overlap between the two bodies is given by

$$\delta = \frac{\pi p_0 a}{2E^*} \tag{3.22}$$

and the contact radius can be written as

$$a = \frac{\pi p_0 R}{2E^*} \tag{3.23}$$

The total compressive force acting on the solids can be obtained by integrating the contact pressure from *0* to *a* as

$$P = \int_0^a p(r) 2\pi r dr$$
$$= \frac{2}{3} p_0 \pi a^2 \tag{3.24}$$

Therefore, the contact force P and contact radius a can also be expressed in terms of the total force (for practical use) as

$$P = \frac{4}{3} R^{1/2} E^* \delta^{3/2} \tag{3.25}$$

and

$$a = \left(\frac{3PR}{4E^*} \right)^{1/3} \tag{3.26}$$

3.5 Non-Hertzian Contact for Elastic Bodies

The assumptions and restrictions made in the Hertz theory are that the profiles of the bodies in contact are non-conforming, continuous, and frictionless, with each body represented by an elastic half-space. When one or more of these restrictions is relaxed in the contact analysis between two elastic bodies, then Hertz theory is no longer applicable, and some other methods of analysis are needed. Examples of non-Hertzian contacts are [14]:

- Discontinuous profiles such as the contact of a wedge or cone with a plane surface.
- Conforming surfaces in contact such as the case of a pin in a hole.
- Friction at the interface between two non-conforming bodies.
- Adhesion between elastic bodies where the tensile force is required to separate them.
- Line contact of cylindrical bodies.
- Inhomogeneous materials such as contact between foundations built on stratified soils.
- Layered solids where the elastic property of the surface layer is different from that of the substrate.

The contact between layered solids will be discussed further in the following section and other topics of non-Hertzian contact are beyond the scope of this research.

3.5.1 Elastic Contact between Layered Solids [14]

When two layered solids are brought into contact, where one or both of the layers are of different elastic properties than the underlying solid, the contact analysis based on Hertz theory will be unsuitable. Figure 3.10 illustrates an example of a solid which is brought into contact with another layered solid under normal force P.

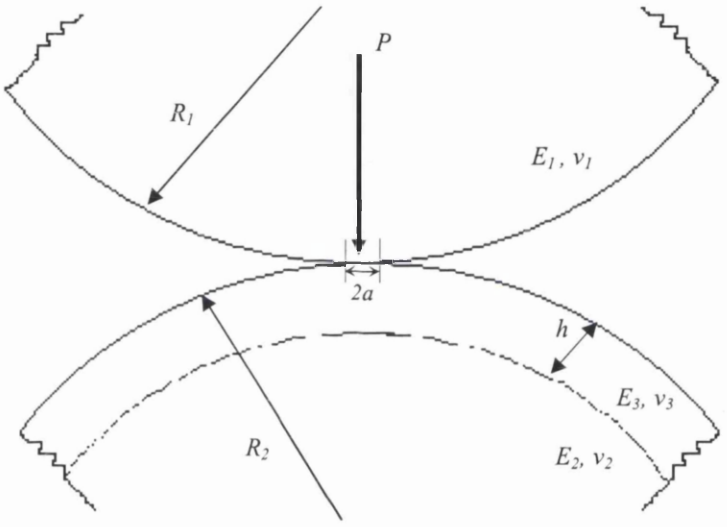

Figure 3.10: Contact between a layered solid and another solid.

If the thickness, h, of the layer is large compared to the contact size, $2a$, the substrate has negligible influence and the contact stresses can be solved for using Hertz theory. However, when the thickness of the layer is comparable with or less than the contact size, Hertz theory will no longer hold and the contact behaviour of the compression depends on the behaviour at the interface between the layer and the substrate. Possible forms of behaviour at the interface are as follow [14]:

- The layer is free to slip, but remains in contact with the substrate (no friction at the interface).
- The layer is perfectly bonded to the substrate.
- Slip may occur when the shear traction at the interface exceeds the frictional limit.
- The layer that is initially in complete contact with the substrate may be partially lifted from the substrate due to the applied load.

If the contact size is small compared to the radii of curvature of the bodies, the curvature of the layer can be ignored and the solids can be treated as elastic half-spaces. In most analyses, contact friction is ignored, and the studies are restricted to a plane strain analysis of the line contact or an axi-symmetry analysis of a solid of revolution, where the contact area is circular [14].

In this section, plane strain analysis will be discussed and the axi-symmetry analysis for the indentation of incompressible layer by the work of Matthewson [57] will be discussed in the next chapter.

3.5.1.1 Plane Strain Analysis of the Compression of an Elastic Layer

As mentioned earlier, the contact behaviour of the compression of a thin layer resting on a rigid substrate, in this case, by a rigid frictionless cylinder, is dependent on the behaviour at the interface between the layer and the substrate. Two types of layer-substrate interface are considered here and they are:

- No friction at the layer-substrate interface, i.e. the layer is free to slip along the substrate.
- Perfect bonding between the layer and the substrate.

When the thickness of the layer h is small compared to the contact radius a, the situation can be analysed in an elementary way [14]. The deformation of the layer is assumed to be homogeneous, and plane sections remain plane after deformation. This is shown in Figure 3.11. However, this is not the case for an incompressible material, where the Poisson's ratio, ν, is equal or close to 0.5. This is because the deformation of the section does not remain plane, but is a parabolic shape as shown in Figure 3.12. Incompressible materials will not be looked into in plane strain analysis, but will be studied as axi-symmetry analyses.

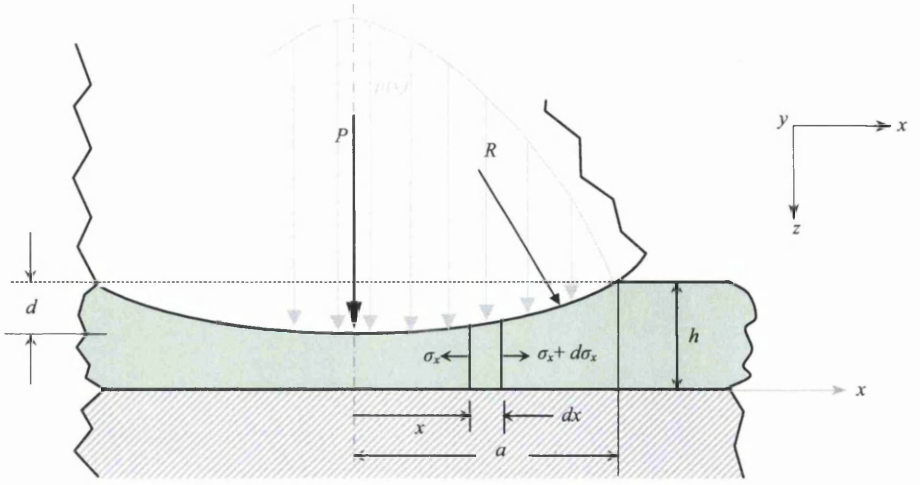

Figure 3.11: The compression of a compressible elastic layer ($\nu < 0.45$) by a rigid cylinder.

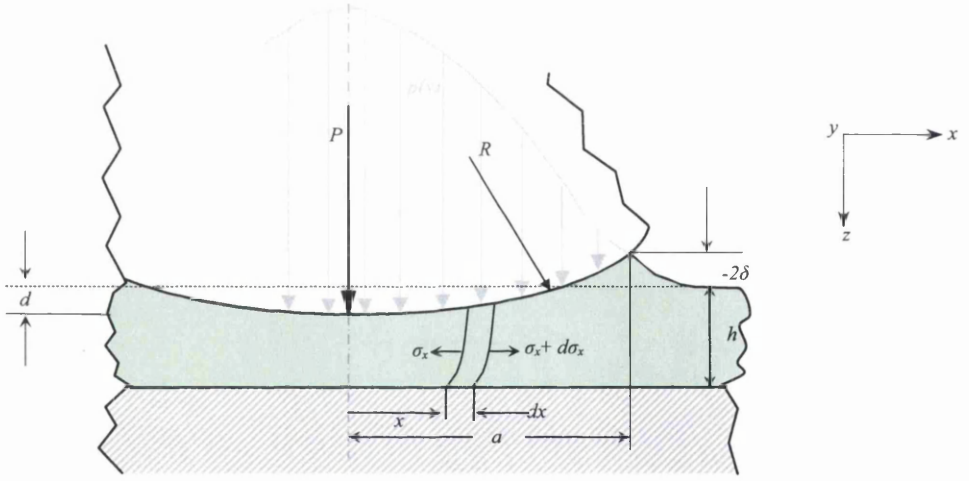

Figure 3.12: The compression of an incompressible elastic layer by a rigid cylinder.

Before going into the derivation of the formulae for two layer-substrate contact conditions, it is worth mentioning Hooke's Law for a linear elastic stress-strain relation in a plane strain analysis. Refer to the reference frame used in both Figure 3.11 and Figure 3.12, all strains in the normal direction to the plane, say ε_y, are zero. Hence, ε_x and ε_z can be written as

$$\varepsilon_x = \frac{1}{E}\left[(1-\nu^2)\sigma_x - \nu(1+\nu)\sigma_z\right]$$
$$\varepsilon_z = \frac{1}{E}\left[(1-\nu^2)\sigma_z - \nu(1+\nu)\sigma_x\right] \quad (3.27)$$

When a pressure is applied onto the thin layer by the rigid cylinder, the magnitude of the vertical stress, σ_z, is equal to the applied pressure, *-p(x)*. The geometry of deformation thus gives

$$\varepsilon_z = -\frac{\left(d - \frac{x^2}{2R}\right)}{h} \quad (3.28)$$

3.5.1.1.1 Frictionless Layer-Substrate Interface

For the case where there is no friction at the interface between the layer and the substrate, σ_x is zero throughout. This reduces, ε_z, to

$$\varepsilon_z = \frac{1}{E}(1-\nu^2)\sigma_z$$
$$= -\frac{1}{E}(1-\nu^2)p(x) \quad (3.29)$$

By equating (3.28) and (3.29), the penetration *d* is obtained as

$$d = \frac{h}{E}(1-\nu^2)p(x) + \frac{x^2}{2R} \quad (3.30)$$

which will be reduced to

$$d = \frac{a^2}{2R} \quad (3.31)$$

at $x = \pm a$, where the pressure drops to zero.

Hence, the pressure *p(x)* can be written as

$$p(x) = \frac{E}{(1-\nu^2)}\frac{a^2 - x^2}{2Rh} \quad (3.32)$$

By integrating *p(x)* over the region from *–a* to *+a*, the total applied force *P* can be obtained as

$$\begin{aligned} P &= \int_{-a}^{+a} p(x)dx \\ &= \int_{-a}^{+a} \frac{E}{(1-\nu^2)} \frac{a^2}{2Rh}\left(1-\frac{x^2}{a^2}\right)dx \\ &= \frac{2}{3}\frac{E}{1-\nu^2}\frac{a^3}{Rh} \end{aligned} \tag{3.33}$$

3.5.1.1.2 Perfect Bonding between the Layer and the Substrate

When the layer is bonded to the substrate, ε_x is zero throughout. Therefore, from equation (3.27) we obtain

$$\frac{1}{E}\left[(1-\nu^2)\sigma_x + \nu(1+\nu)p(x)\right] = 0 \tag{3.34}$$

and from which σ_x can be obtained as

$$\sigma_x = -\frac{\nu}{(1-\nu)}p(x) \tag{3.35}$$

Substituting this into the expression for ε_z in (3.27) yields

$$\varepsilon_z = \frac{1}{E}\left[-(1-\nu^2)p(x) + \frac{\nu^2(1+\nu)}{(1-\nu)}p(x)\right] \tag{3.36}$$

The expression for pressure *p(x)* can then be obtained by equating (3.36) with (3.28) as

$$p(x) = \frac{(1-\nu)^2 E}{(1-2\nu)(1-\nu^2)}\frac{a^2}{2Rh}\left(1-\frac{x^2}{a^2}\right) \tag{3.37}$$

Finally, the applied force P can be obtained by integrating equation (3.37) over the whole contact size as shown below

$$\begin{aligned} P &= \int_{-a}^{+a} p(x)dx \\ &= \int_{-a}^{+a} \frac{(1-\nu)^2 E}{(1-2\nu)(1-\nu^2)}\frac{a^2}{2Rh}\left(1-\frac{x^2}{a^2}\right)dx \\ &= \frac{2}{3}\frac{(1-\nu)^2 E}{(1-2\nu)(1-\nu^2)}\frac{a^3}{Rh} \end{aligned} \tag{3.38}$$

3.6 Numerical Analysis of Contact Problems

When contact problems are involved in a finite element analysis, the impenetrability condition on the contact interface, i.e. the condition that the two bodies cannot penetrate each other, is added to the governing equations in the analysis [43]. The constraints imposed on the contact interface can be treated using several methods:

1. The Lagrange multiplier method
2. The penalty method
3. The augmented Lagrangian method
4. The perturbed Lagrangian method

An analysis that involves contact is among the most difficult of nonlinear problems as the contact forces that arise from the constraints at the contact are unknowns. Furthermore, the contact area and the deformation status of the bodies are also unknown [43].

The contact between two bodies, denoted by Ω^A and Ω^B, is shown in Figure 3.13. The boundaries of the bodies are denoted by Γ^A and Γ^B and the contact interface (i.e. the intersection of the two surface) is denoted by Γ^C:

$$\Gamma^C = \Gamma^A \cap \Gamma^B \tag{3.39}$$

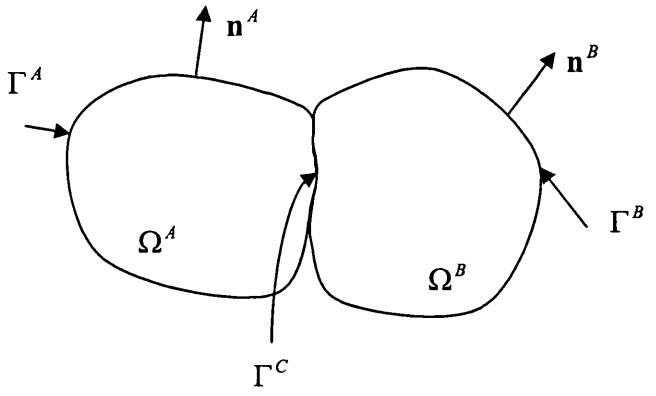

Figure 3.13: Contact between two bodies.

At the contact interface, the normal of the two bodies are in opposite direction, i.e.

$$\mathbf{n}^A = -\mathbf{n}^B \tag{3.40}$$

By choosing surface A as the master surface, the normal velocities are written as

$$V_N^A = \mathbf{v}^A \cdot \mathbf{n}^A; \qquad V_N^B = \mathbf{v}^B \cdot \mathbf{n}^A \tag{3.41}$$

Apart from satisfying the impenetrability condition at the contact (i.e. the surfaces cannot penetrate each other), the normal traction across the contact interface must also satisfy the conservation of momentum [43]. Also, they cannot be tensile.

3.6.1 Impenetrability Condition

The impenetrability condition for a pair of bodies in contact can be written as [43]

$$\Omega^A \cap \Omega^B = 0 \tag{3.42}$$

i.e. the two bodies do not intersect or overlap. This condition is highly nonlinear for large displacement problems, and due to the difficulty in anticipating the points of the two bodies that will be in contact under an arbitrary motion, this condition cannot be expressed as a differential equation in terms of displacement. Instead, it is expressed in a rate or incremental form at each step of the process [43].

The rate form of the impenetrability condition for the points on the contact surface Γ^C is written as

$$\gamma_N = \mathbf{v}^A \cdot \mathbf{n}^A + \mathbf{v}^B \cdot \mathbf{n}^A = \left(\mathbf{v}^A - \mathbf{v}^B\right) \cdot \mathbf{n}^A \equiv v_N^A - v_N^B \leq 0 \tag{3.43}$$

where γ_N is termed the rate of interpenetration of the two bodies. This condition ensures that the bodies in contact either remain in contact $(\gamma_N = 0)$ or separate $(\gamma_N < 0)$.

For the tangential direction, the impenetrability condition is written as

$$\gamma_T = v_T^A - v_T^B \tag{3.44}$$

3.6.2 Traction Condition

Considering the balance of momentum across the contact interface, the sum of the tractions of the two bodies at the interface must vanish [43], i.e.

$$\mathbf{t}^A + \mathbf{t}^B = 0 \tag{3.45}$$

The normal tractions are defined as

$$t_N^A = \mathbf{t}^A \cdot \mathbf{n}^A; \qquad t_N^B = \mathbf{t}^B \cdot \mathbf{n}^A \tag{3.46}$$

and the tangential tractions are defined as

$$\mathbf{t}_T^A = \mathbf{t}^A - t_N^A \cdot \mathbf{n}^A; \qquad \mathbf{t}_T^B = \mathbf{t}^B - t_N^B \cdot \mathbf{n}^A \tag{3.47}$$

The momentum balance requires that in the normal direction

$$t_N^A + t_N^B = 0 \tag{3.48}$$

and in the tangential direction

$$\mathbf{t}_T^A + \mathbf{t}_T^B = 0 \tag{3.49}$$

For the condition that the normal tractions cannot be tensile (i.e. they are compressive)

$$t_N \equiv t_N^A = -t_N^B \leq 0 \tag{3.50}$$

For frictionless contact, the tangential tractions vanish, and so

$$\mathbf{t}_T^A = \mathbf{t}_T^B = 0 \tag{3.51}$$

3.6.3 Unitary Condition

The unitary contact condition on the contact surface states that [43]

$$t_N \gamma_N = 0 \tag{3.52}$$

This implies that when the bodies are in contact and remain in contact, $\gamma_N = 0$; whereas when they are not in contact, although $\gamma_N \leq 0$, the normal traction vanishes.

3.6.4 Surface Description and the Measure of Interpenetration

Consider the situation shown in Figure 3.14 where point P has penetrated body A. The distance l_{AB} between point P which has coordinates $x^B(\zeta^B, t)$ and any point on the surface of A is given by [43]

$$l_{AB} = \left\| \mathbf{x}^B(\zeta^B, t) - \mathbf{x}^A(\zeta^A, t) \right\| \equiv \left[(x^B - x^A)^2 + (y^B - y^A)^2 + (z^B - z^A)^2 \right]^{1/2} \tag{3.53}$$

where ζ^A and ζ^B are the curvilinear coordinates that describe the surface of the contacting bodies.

The minimum of equation (3.53) is represented by the interpenetration $g_N(\zeta^B, t)$ defined as

$$g_N(\zeta^B, t) = \min_{\zeta^A} \alpha l_{AB}; \qquad \alpha \begin{cases} 1 \text{ if} (\mathbf{x}^B - \mathbf{x}^A) \cdot \mathbf{n}^A \leq 0 \\ 0 \text{ if} (\mathbf{x}^B - \mathbf{x}^A) \cdot \mathbf{n}^A > 0 \end{cases} \tag{3.54}$$

This value is nonzero only when point P is inside body A, i.e. $\left(\mathbf{x}^B - \mathbf{x}^A\right)\cdot \mathbf{n}^A \leq 0$.

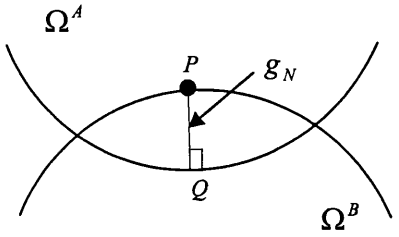

Figure 3.14: The closest point on body A (point Q) to point P.

3.6.5 The Penalty Method

One method of treating the constraint on the contact interface is referred to as the penalty method. In this method, a penalty normal traction along the contact surface is used to impose the impenetrability constraints. It allows some interpenetration at the contact and is widely used [43].

There are two types of penalty methods [43]:

1. A penalty that is proportional to the square of the interpenetration rate γ_N, i.e. velocity-dependent.
2. A penalty which is an arbitrary function of the interpenetration and its rate.

For nonlinear problems, the second method is more useful, as the velocity-dependent penalty in the first method allows too much penetration.

In the penalty method, the discontinuous nature of the contact problem is introduced by the Heaviside step function which has the form [43]

$$\mathrm{H}(\gamma_N) = \begin{cases} 1 & \text{if } \gamma_N > 0 \\ 0 & \text{if } \gamma_N < 0 \end{cases} \tag{3.55}$$

For the interpenetration-dependent penalty method, the normal traction is also a function of the interpenetration. Thus, an interface pressure is introduced defined by [43]

$$p = \bar{p}(g_N, \gamma_N)\mathrm{H}(\bar{p}) \tag{3.56}$$

where $\bar{p}(g_N, \gamma_N)$ is a penalty function. Besides, this method also ensures that the tractions are always compressive and that the momentum balance is satisfied at the contact interface, giving [43]

$$t_N^A + p = 0; \quad t_N^B - p = 0 \quad \text{on } \Gamma^C \tag{3.57}$$

and

$$t_N^A = -t_N^B = -p = -\bar{p}(g_N, \gamma_N)\mathrm{H}(\bar{p}) \tag{3.58}$$

i.e. the tractions are functions of interpenetration, g_N, and the rate of interpenetration γ_N.

An example of a penalty function is [43]

$$\bar{p} = \beta_1 g_N + \beta_2 \gamma_N \tag{3.59}$$

or

$$\bar{p} = \beta_1 g_N \mathrm{H}(g_N) + \beta_2 \gamma_N \mathrm{H}(\gamma_N) \tag{3.60}$$

where β_1 and β_2 are the penalty parameters to be specified by the analyst.

However, the disadvantage of using the penalty method is that its effectiveness depends on the choice of the penalty parameter. If the values chosen are too big, ill-conditioning will be observed when the off-diagonal matrix elements are affected by a large penalty number [41]. On the other hand, if the values chosen are too small, the interpenetration will be excessive [43]. Therefore, the determination of the correct penalty parameter forms a challenge in the analysis. In fact, some trial-and error process is needed sometimes in order to look for a suitable penalty number.

3.6.6 Time Integration Method for Dynamic Contact Analysis

For dynamic contact problems, the explicit time integration scheme is a more suitable method. Due to the restriction on the time step size for stability criterion, the problems of discontinuities caused by the contact are reduced by the use of this method; whereas the unconditionally stable implicit method is not efficient in capturing the discontinuous response at the contact as a result of the use of large time steps. Furthermore, the discontinuities introduced also hinder the convergence of Newton's method in an implicit scheme.

3.7 Finite Element Analysis of Contact Problems

The finite element analysis of contact mechanics are carried out using the FE software package *ELFEN*. In order to validate the settings used in the contact analyses, such as the dynamic simulation scheme, the contact penalty method and the adaptive re-meshing procedures, a simple finite element analysis of the contact between two solids of revolution is carried out and validated against the well established Hertz theory. Also, the compression of an elastic layer is analysed and compared to the non-Hertzian solution.

The contact mechanics between two bodies is analysed quasi-statically using an *explicit dynamic simulation scheme*, where the load applied (in terms of displacement in this context) varies slow enough for the behaviour of the contact at each time instant in the analysis to be treated as a static response. The contact between the bodies is treated using the *penalty method*, where trial and error is used to choose the correct/optimum penalty number.

Linear rectangular elements are used to mesh the bodies throughout the simulations and finer elements are assigned to the contact region to give a better approximation for the analyses. Where element distortions are great, due to the deformation, then an adaptive mesh refinement scheme is used. The quality of the mesh is assessed at every 10000 steps, and the criterion for re-meshing is based on the percentage of element area distortion. A limit of 10% is used in the assessment.

3.7.1 Contact between Two Solids of Revolution

The analysis of the contact between two solids of revolution is carried out using an axi-symmetry analysis as shown in Figure 3.15, with the solids touching at a point without load as the initial configuration of the simulation. Due to the symmetry of the spheres, only a hemisphere is used to represent each solid. Also, for the sake of convenience in the later simulations of the contact between coated particles in subsequent chapters, a layer is modelled around each solid to a represent thin coating. By assigning the same material properties to the coating and the solid, the influence of the coating will disappear and the model will resemble two solids in contact. However, it should be noted that this is only applicable if the layer is assumed to be fully bonded to the underlying solid.

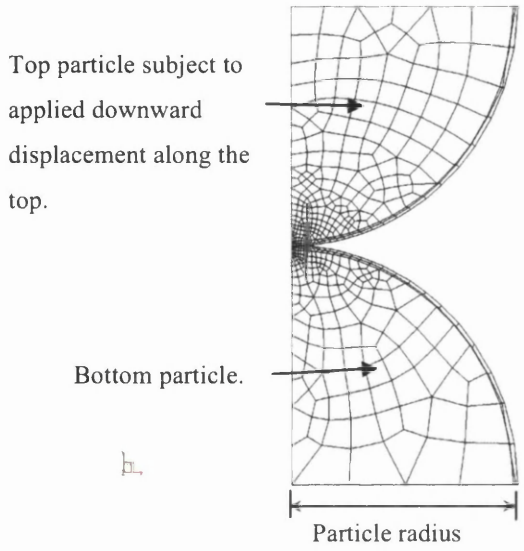

Figure 3.15: Axi-symmetry model for the contact between two solids of revolutions.

In order to retain the behaviour of the solids as spherical bodies, constraints are applied in the horizontal direction along the vertical axis and a vertical constraint is applied along the bottom of the hemisphere to avoid rigid movement of the system upon loading. This can be seen in the following figure.

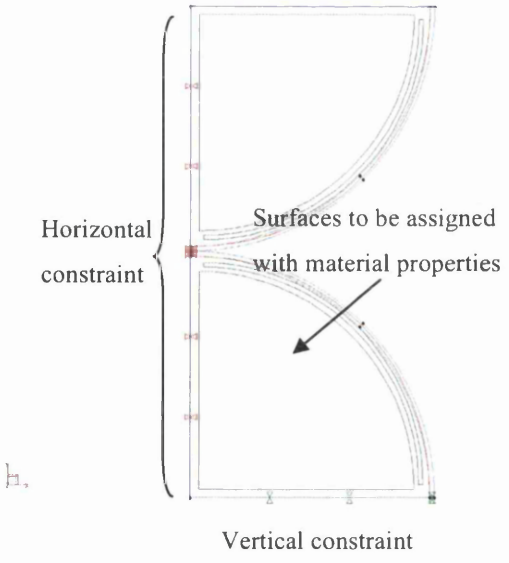

Figure 3.16: Constraints applied to the model: Red markers represent horizontal constraints; Green markers represent vertical constraints.

In the analysis, a downward displacement is applied along the top of the model with a speed of *0.02m/s*. The radius of the solids is *0.0102m*, and the material properties used are as follow:

Table 3.1: Material properties used in the analysis.

	Young's Modulus, E (N/m^2)	*Poisson's Ratio, v*
Case 1	$3x10^{10}$	0.49
Case 2	$1x10^{6}$	0.49

In this analysis, as $\nu = 0.5$ will produce singularity in the numerical analysis, a value of $\nu = 0.49$ is used instead to study the effect of material incompressibility. This assumption provides a guide to the later analysis of an incompressible layer which will be discussed in the next chapter.

3.7.1.1 Finite Element Analysis Results and Discussion

The comparisons between the results from the FE simulation and Hertzian theory are shown in the following graphs in terms of a force-penetration (P-d) relation for the two cases.

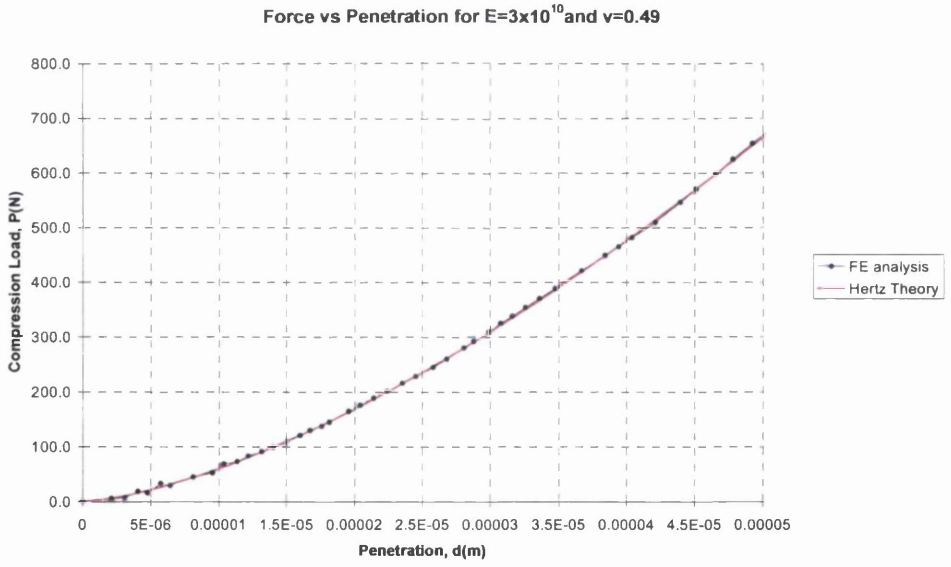

Figure 3.17: Force versus penetration for $E=3x10^{10}N/m^2$ and $v=0.49$.

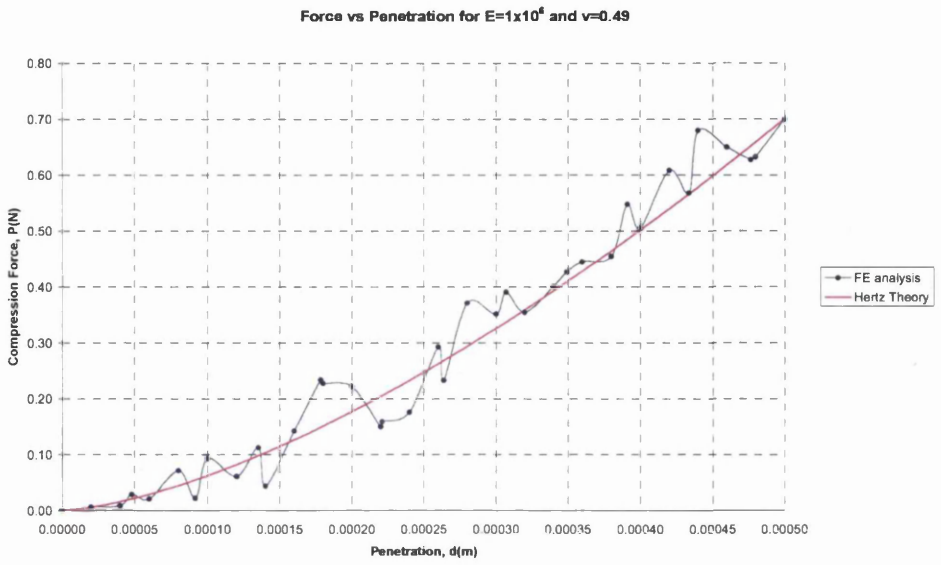

Figure 3.18: Force versus penetration for $E=1x10^6 N/m^2$ and $v=0.49$.

It can be seen from the graphs that the FE results match well with the Hertz theory, especially for the case of $E=3x10^{10} N/m^2$. However, when the Young's modulus reduces (i.e. the material becomes softer), oscillations are observed along the curve, as can be seen in Figure 3.18. This phenomenon is due to the load application which is not slow enough to produce a quasi-static state, and causes an unsteady response during the load application. In order to have a closer look at this problem, another simulation was carried out on the softer material ($E=1x10^6 N/m^2$) subjected to half the original speed. The result of the analysis is shown in the following figure.

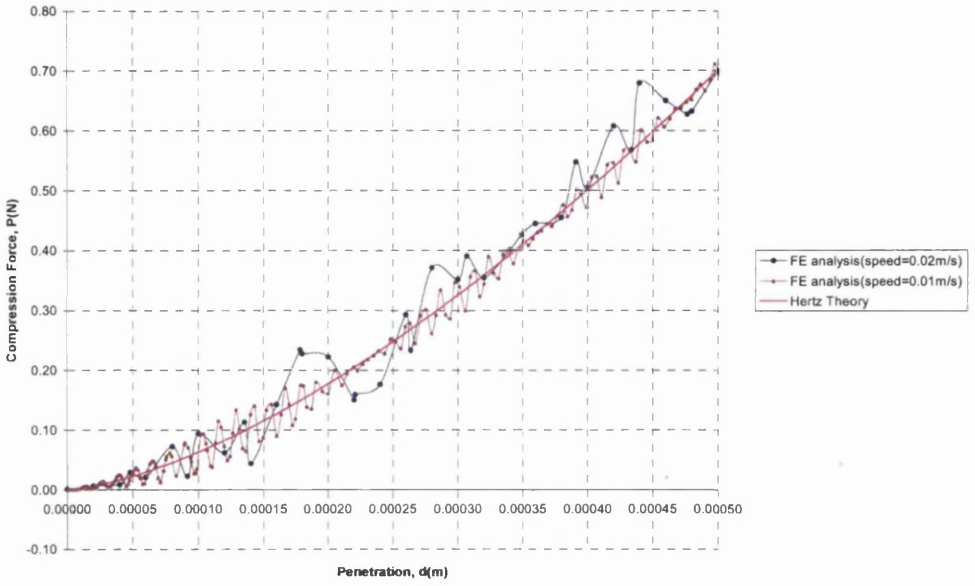

Figure 3.19: Comparison between different loading speed for $E=1x10^6$ and $v=0.49$.

It can be seen from the graph in Figure 3.19 that the oscillations formed in the FE analysis which uses a lower rate of load application (*0.01m/s*) are more frequent and smaller in magnitude when compared to the oscillations which occurred in the analysis subjected to a speed of *0.02m/s*. The oscillations are slightly greater at the beginning of the contact and die down as the loading progresses. The reason for the greater oscillations observed in the early stage is found to be due to the 'shock' that is produced when the two bodies are brought into contact. Hence, provided that the loading speed is low enough, the oscillations will decrease in magnitude as the simulation progresses. Also, it is anticipated that the oscillations will decrease in size if the loading speed is further reduced. However, the simulation time could be enormous to reach the desired amount of penetration, especially when an explicit integration scheme (restricted by the critical time step) is used.

3.7.2 The Compression of an Elastic Layer

The compression of an elastic layer by a rigid cylinder is analysed using plane strain analysis. As high stresses only occur around the point of contact, the cost of computation can be saved by modelling only half the cylinder. As the layer is assumed to rest on a rigid substrate, only the layer is modelled and proper constraints are assigned to the boundary of the layer to resemble the interface behaviour between the layer and the

substrate. The cylinder is assumed to rest on the layer at a point in the beginning of the simulation. This is shown in Figure 3.20.

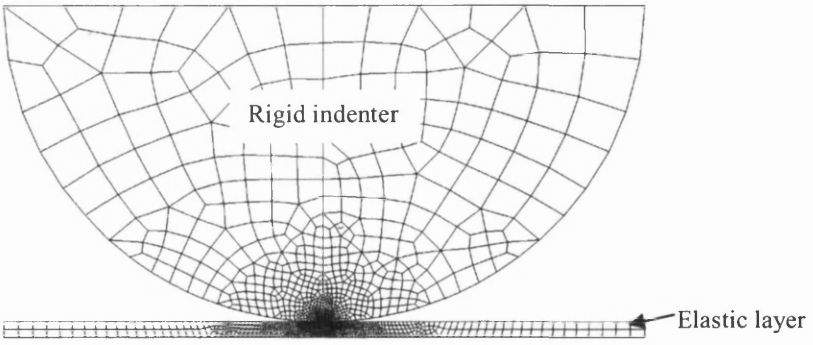

Figure 3.20: Plane strain analysis of the compression of an elastic layer by a rigid cylinder.

In order to model frictionless contact between the layer and the substrate, the bottom of the layer is constrained in the vertical direction to avoid rigid movement of the whole system, and is free to move in the horizontal direction as shown in Figure 3.21. Whereas for the case where the layer is perfectly bonded to the substrate, the bottom of the layer is constrained in both the vertical and horizontal directions as shown in Figure 3.22.

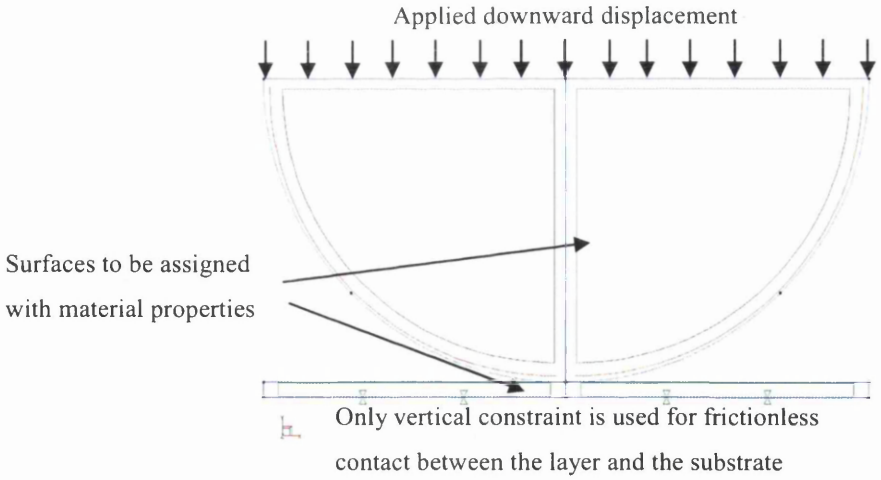

Figure 3.21: Constraints applied to the layer for frictionless contact between the layer and the substrate. (Green markers represent vertical constraints)

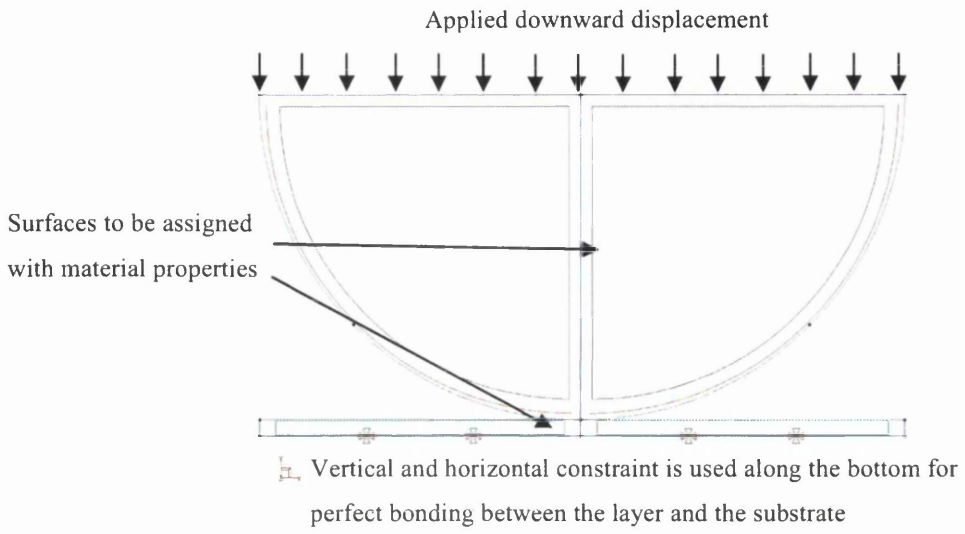

Figure 3.22: Constraints applied to the layer for perfect bonding between the layer and the substrate. (Green markers represent vertical constraints; Red markers represent horizontal constraints)

To model the compression from the cylinder, a downward displacement was applied along the top of the cylinder with a speed of $0.005m/s$. The radius of the cylinder R used in the analysis was $0.001m$, and the thickness of the layer h is $\frac{R}{20} = 0.00005m$.

The material properties used for the layer and the cylinder are as follow:

Table 3.2: Material properties used for the layer and the cylinder.

	Young's Modulus, E (N/m^2)	***Poisson's Ratio, v***
Layer	$1x10^5$	0.3
Cylinder	$1x10^{10}$	0.3

3.7.2.1 Finite Element Analysis Results and Discussion

The comparisons between the results from the FE simulation and theoretical values are plotted in terms of a force-penetration (P-d) relation in Figure 3.23 for the case where the contact between the layer and the substrate is frictionless and in Figure 3.24 for the case where the layer is perfectly bonded to the substrate. It can be seen that the FE results and the theoretical values are almost identical.

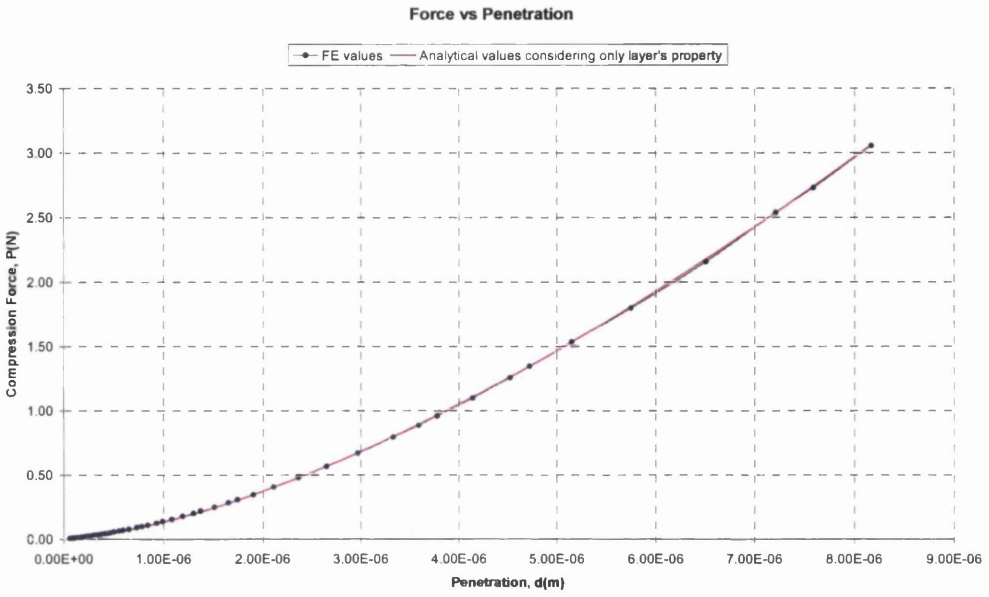

Figure 3.23: Force versus penetration for frictionless layer-substrate interface.

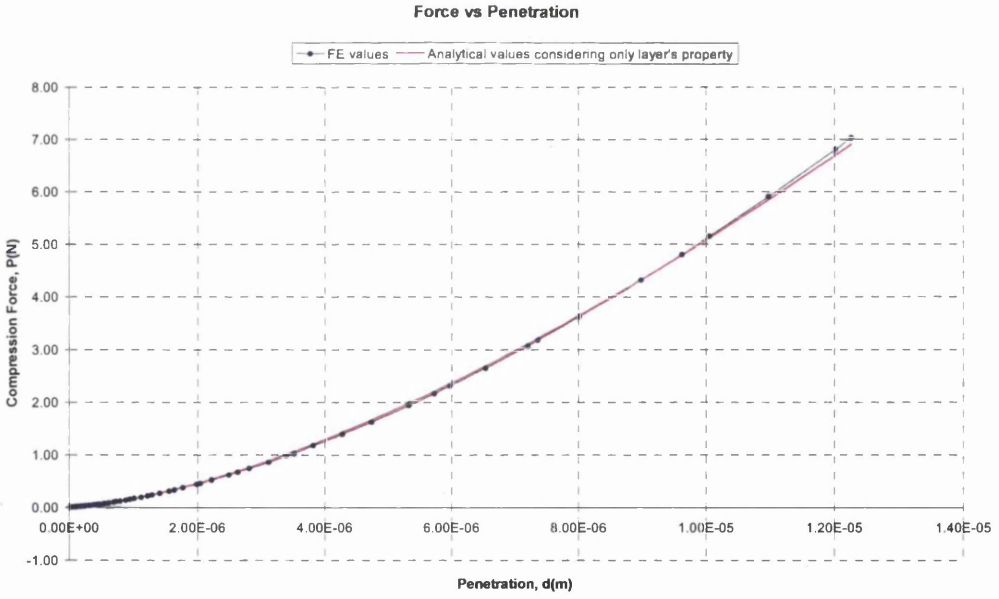

Figure 3.24: Force versus penetration for perfect bonding between the layer and the substrate.

It can be seen from the graphs that the FE results and the theoretical values are almost identical, and there is no oscillation occurring in the FE results as obtained in the previous analyses. This shows that the speed of the load application is low enough to

resemble a quasi-static response at each time instant and thus produce good FE approximations that match well with the theoretical values.

The comparisons between the FE results and the theoretical values indicate that the force required to penetrate into the layer by a certain amount, for the case where the layer is bonded to the substrate, is higher than where the layer is free to slip along the substrate, i.e. frictionless interface. This can be seen in the figure below which compares the f-d relation between these two cases.

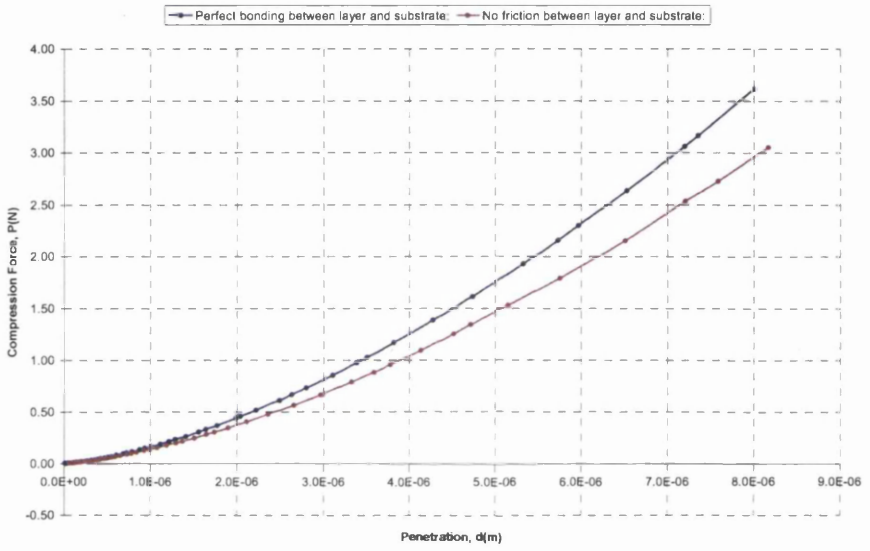

Figure 3.25: Comparison on the F-d relation between the two layer-substrate interface condition assumptions.

A frictionless layer-substrate interface allows the layer to slip when subjected to a compression load, while the perfect bonding between the layer and the interface hinders the movement of the layer upon loading. Thus, the load required to penetrate into the layer by a certain amount is expected to be higher for the case of perfect bonding.

Chapter 4

Axi-symmetric Contact of Elastic Layer

In this chapter, the solution to the compression of a thin and incompressible elastic coating, derived by Matthewson based on the theory of linear elasticity, is presented. A modification to Matthewson's equation using a semi-empirical approach which allows for nonlinear behaviour in the coating (i.e. large deformation) is also presented. To assess the validity of the equations, finite element simulations of the problems are also carried out and the results are compared with the approximations obtained from the equations.

4.1 Some Research Works on the Elastic Contact of Layered Object

Problems that involve axi-symmetric contact of layered materials have been studied by a number of researchers using various methods and assumptions. The stresses caused by the indentation of a rigid frictionless sphere on an elastic layer of finite thickness lying on an undeformable foundation was analysed by Aleksandrov [58,59] by employing asymptotic methods. Whereas for the contact stresses on an elastic layer subjected to a rough and rigid spherical indenter, Conway and Engel [60] have made use of numerical methods such as the incremental method and the direct method. Also, Ogilvy [61] developed a parametric model to predict the contact radius and penetration caused by the indentation of a rigid sphere on an elastic thin film bonded to a substrate, where either the

film or the substrate can be a soft material. Matthewson [57], on the other hand, formulated an analytical solution from the differential equations that describe the deformation of a linearly elastic incompressible thin coating which was bonded to a rigid substrate and subjected to spherical indenter. The method used by Matthewson to solve for the deformation of an elastic incompressible coating is presented in the following section and comparisons with the results obtained from the FE simulations will be made in section 4.3.

4.2 The Compression of a Thin Elastic Coating by a Rigid Indenter

An analytical approximation for the indentation of a thin coating by a rigid body was presented by Matthewson in [57] with the following assumptions:

- The coating behaves linearly elastic, and fully bonded to a rigid semi-infinite substrate;
- The elastic modulus of the coating material, E, is small compared to that of the indenter and substrate, i.e. softer than both indenter and substrate;
- The thickness of the coating, h, is small compared to the contact radius, a;
- The contact radius is small compared to the characteristic linear dimension of the indenter; and
- The contact between the coating and the indenter is frictionless.

Using the above assumptions, the differential equations that describe the deformation of the coating can be found for arbitrary indenter profiles. The solution for the indentation by a sphere is found explicitly for general values of Poisson's ratio for the coating.

4.2.1 The Formulation of Stress and Strain Components in the Coating

The geometry of the indentation of a thin coating by a rigid indenter of parabolic profile can be seen in the following figure.

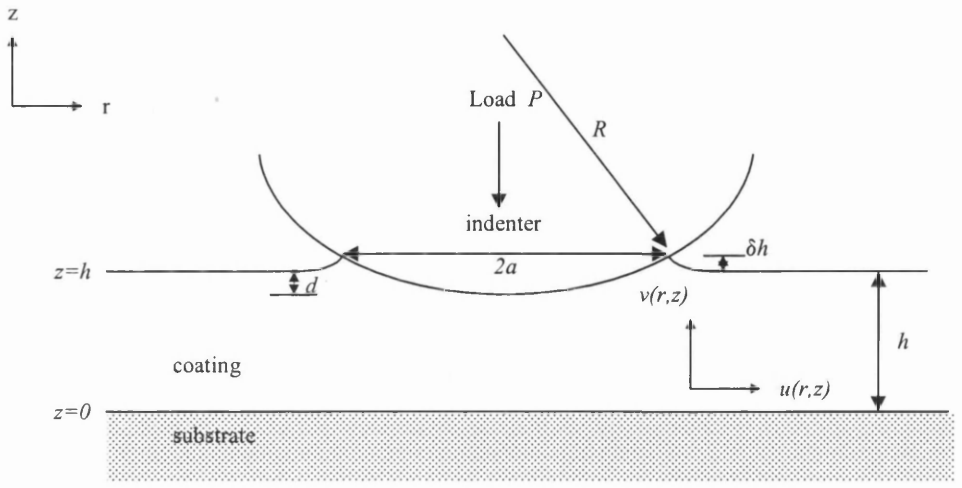

Figure 4.1: Geometry of the indenter in contact with a coating b substrate.

The movement of the coating material is described by horizontal and vertical displacements, *u(r,z)* and *v(r,z)*, and are approximated by a finite power series in *z* as:

$$\begin{aligned} u(r,z) &= A(r) + B(r)z + C(r)z^2 \\ v(r,z) &= D(r) + E(r)z \end{aligned} \tag{4.1}$$

As the coating is rigidly bonded to a semi-infinite substrate, $u(r,0) = v(r,0) = 0$, and hence $A(r)$ and $D(r)$ will naturally become zero. This reduces equation (4.1) to

$$\begin{aligned} u(r,z) &= B(r)z + C(r)z^2 \\ v(r,z) &= E(r)z \end{aligned} \tag{4.2}$$

where the functions $B(r)$ and $C(r)$ are to be found, and $E(r)$ is determined from the indenter profile.

The strain components for linear elastic materials are as follow:

$$\varepsilon_r = \frac{\partial u}{\partial r};\ \varepsilon_\theta = \frac{u}{r};\ \varepsilon_z = \frac{\partial v}{\partial z} \tag{4.3}$$

where ε_r = radial strain

ε_θ =circumferential strain

ε_z = strain in *z* direction

Hence, the average strain values through the coating thickness can be evaluated as:

$$\begin{aligned}\bar{\varepsilon}_r &= \frac{1}{h}\int_0^h \varepsilon_r dz \\ &= \frac{1}{h}\int_0^h \left[\frac{d}{dr}\{B(r)\}z + \frac{d}{dr}\{C(r)\}z^2\right]dz \\ &= \frac{1}{h}\left[\frac{d}{dr}\{B(r)\}\frac{z^2}{2} + \frac{d}{dr}\{C(r)\}\frac{z^3}{3}\right]_0^h \\ &= \frac{1}{2}h\frac{d}{dr}\{B(r)\} + \frac{1}{3}h^2\frac{d}{dr}\{C(r)\}\end{aligned} \tag{4.4}$$

$$\begin{aligned}\bar{\varepsilon}_\theta &= \frac{\bar{u}}{r} = \frac{1}{h}\int_0^h \left[\frac{B(r)z}{r} + \frac{C(r)z^2}{r}\right]dz \\ &= \frac{1}{h}\left[\frac{B(r)z^2}{2r} + \frac{C(r)z^3}{3r}\right]_0^h \\ &= \frac{1}{2}h\frac{B(r)}{r} + \frac{1}{3}h^2\frac{C(r)}{r}\end{aligned} \tag{4.5}$$

$$\begin{aligned}\bar{\varepsilon}_z &= \frac{\partial \bar{v}}{\partial z} \\ &= \frac{v(r,h)}{h} \\ &= E(r)\end{aligned} \tag{4.6}$$

The elasticity equations for averaged direct stresses and strains can then be written as [56]

$$\begin{aligned}\bar{\sigma}_r &= \frac{2\nu G}{1-2\nu}(\bar{\varepsilon}_r + \bar{\varepsilon}_\theta + \bar{\varepsilon}_z) + 2G\bar{\varepsilon}_r \\ \bar{\sigma}_\theta &= \frac{2\nu G}{1-2\nu}(\bar{\varepsilon}_r + \bar{\varepsilon}_\theta + \bar{\varepsilon}_z) + 2G\bar{\varepsilon}_\theta \\ \bar{\sigma}_z &= \frac{2\nu G}{1-2\nu}(\bar{\varepsilon}_r + \bar{\varepsilon}_\theta + \bar{\varepsilon}_z) + 2G\bar{\varepsilon}_z\end{aligned} \tag{4.7}$$

where G and ν are the shear modulus and Poisson's ratio of the coating.

Given that $a/h >> 1$, the radial equilibrium equation becomes

$$\frac{d\bar{\sigma}_r}{dr} + \frac{\bar{\sigma}_r - \bar{\sigma}_\theta}{r} = \frac{\tau_0 - \tau_1}{h} \tag{4.8}$$

where $\bar{\sigma}_r$ = averaged radial stresses

$\bar{\sigma}_\theta$ = averaged circumferential stresses

τ_0 = shear stress acting on the lower surface of the coating

τ_1 = shear stress acting on the upper surface of the coating

As the friction between the indenter and the coating is ignored,

$$\tau_1 = 0 \quad \text{for all } r. \tag{4.9}$$

The shear strain is written as

$$\begin{aligned} \gamma_{rz} &= \frac{\partial u}{\partial z} + \frac{\partial v}{\partial r} \\ &= B(r) + 2C(r)z + \frac{\partial v(r,z)}{\partial r} \end{aligned} \tag{4.10}$$

which gives

$$\tau_0 = G(\gamma_{rz})_{z=0} = GB(r) \tag{4.11}$$

and

$$\tau_1 = G(\gamma_{rz})_{z=h} = 0 \tag{4.12}$$

4.2.2 Analysis Within the Contact Region (r<a)

For analysis within the contact region (r<a), $\bar{\varepsilon}_z$ is written as

$$\bar{\varepsilon}_z = E(r) = \frac{f(r)}{h} + \delta \tag{4.13}$$

where $f(r)$ is the function that describe the indenter profile.

By using equations (4.6), (4.10), (4.12) and (4.13), τ_1 can be written as

$$\begin{aligned} \tau_1 &= 0 \\ &= G(\gamma_{rz})_{z=h} \\ &= G\left(B(r) + 2hC(r) + \frac{\partial v(r,z)}{\partial r} \right) \\ &= G\left(B(r) + 2hC(r) + \frac{dE(r)}{dr} h \right) \\ &= G\left(B(r) + 2hC(r) + \frac{df(r)}{dr} \right) \end{aligned} \tag{4.14}$$

By substituting the strain components from equations (4.4), (4.5) and (4.13) into the elasticity equations in (4.7), the normal stresses in terms of $B(r)$ and $C(r)$ can be

obtained. The normal stresses are then substituted into the equilibrium equation in (4.8), and after eliminating τ_0 and τ_1 as given in (4.11) and (4.12), to yield

$$\frac{2(1-\nu)}{1-2\nu}\nabla\left\{\frac{1}{2}hB(r)+\frac{1}{3}h^2C(r)\right\}+\frac{2\nu}{1-2\nu}\frac{1}{h}\frac{df}{dr}=\frac{B(r)}{h}, \qquad 0\le r<a \tag{4.15}$$

where ∇ is the differential operator, defined as

$$\nabla\{g\}=\frac{d^2g}{dr^2}+\frac{1}{r}\frac{dg}{dr}-\frac{g}{r^2} \tag{4.16}$$

By rearranging the terms in equation (4.14), *C(r)* can be written as

$$C(r)=-\frac{1}{2h}\left(B(r)+\frac{df(r)}{dr}\right) \tag{4.17}$$

Hence, a differential equation for $B(r)$ is formed as follows

$$\nabla\left\{B(r)-\frac{1}{2}\frac{df}{dr}\right\}-\frac{3}{2h^2}\frac{(1-2\nu)}{(1-\nu)}B(r)+\frac{3\nu}{h^2(1-\nu)}\frac{df}{dr}=0, \qquad 0\le r<a \tag{4.18}$$

4.2.3 Analysis Outside the Contact Region (r>a)

From equations (4.10) and (4.12)

$$B(r)+2hC(r)+\frac{\partial v(r,h)}{\partial r}=0 \tag{4.19}$$

As $\bar{\sigma}_z = 0$ for $r>a$, from the elasticity equations in (4.7)

$$\begin{aligned}\frac{2\nu G}{1-2\nu}(\bar{\varepsilon}_r+\bar{\varepsilon}_\theta+\bar{\varepsilon}_z)+2G\bar{\varepsilon}_z&=0\\ \frac{2\nu G}{1-2\nu}(\bar{\varepsilon}_r+\bar{\varepsilon}_\theta+\bar{\varepsilon}_z)&=-2G\bar{\varepsilon}_z\\ \bar{\varepsilon}_z&=-\frac{\nu}{1-\nu}(\bar{\varepsilon}_r+\bar{\varepsilon}_\theta)\end{aligned} \tag{4.20}$$

Referring to equation (4.6), $\bar{\varepsilon}_z$ can also be rewritten as

$$v(r,h)=h\bar{\varepsilon}_z \tag{4.21}$$

Thus,

$$\frac{dv(r,h)}{dr}=-\frac{\nu h}{1-\nu}\left\{\frac{d\bar{\varepsilon}_r}{dr}+\frac{d\bar{\varepsilon}_\theta}{dr}\right\} \tag{4.22}$$

Hence, by equating (4.19) and (4.22), the following is obtained

$$B(r)+2hC(r)=\frac{\nu h}{1-\nu}\left\{\frac{d\bar{\varepsilon}_r}{dr}+\frac{d\bar{\varepsilon}_\theta}{dr}\right\} \tag{4.23}$$

Substituting the strain components from equations (4.4) and (4.5) then yields

$$\nabla\left\{\frac{1}{2}hB(r)+\frac{1}{3}h^2C(r)\right\}=\frac{1-\nu}{\nu h}\{B(r)+2hC(r)\}, \qquad r>a \tag{4.24}$$

Concurrently, by substituting $\bar{\varepsilon}_z$, $\bar{\varepsilon}_r$ and $\bar{\varepsilon}_\theta$ from equations (4.4)-(4.6) into the elasticity equation (4.7), followed by substitution into the equilibrium equation with the use of the definition of shear stresses in (4.11) and (4.12), the resulting equation is obtained

$$\nabla\left\{\frac{1}{2}hB(r)+\frac{1}{3}h^2C(r)\right\}=\frac{1-\nu}{2h}B(r), \qquad r>a \tag{4.25}$$

It can be seen that the left hand side of equations (4.24) and (4.25) are of the same form. Hence, by equating the right hand side of these two equations the relation between $B(r)$ and $C(r)$ is obtained as follows,

$$C(r)=-\frac{2-\nu}{4h}B(r) \tag{4.26}$$

This, when substituted into equation (4.24) or (4.25), will give

$$\nabla\{B(r)\}-\frac{6-(1-\nu)}{4+\nu}\frac{B(r)}{h^2}=0, \qquad r>a \tag{4.27}$$

which is independent of the indenter profile.

The general solution of this equation is given as

$$B(r)=\alpha_1 K_1\left\{\sqrt{\frac{6(1-\nu)}{4+\nu}}\frac{r}{h}\right\}+\alpha_2 I_1\left\{\sqrt{\frac{6(1-\nu)}{4+\nu}}\frac{r}{h}\right\}, \qquad \text{r > a} \tag{4.28}$$

where α_1 and α_2 are constants, and $I_1(x)$ and $K_1(x)$ are the first-order modified Bessel functions. The graph of $I_1(x)$ and $K_1(x)$ can be found in Chapter 9 in [62].

It is shown in (4.11) that *GB(r)* can be treated as the shear stress acting across the coating/substrate interface and therefore must approach zero for large values of $r.I_1(x)$. This can be seen from the graph in [62], where the value is bounded for finite $x \geq 0$ but unbounded when x approaches infinity. Hence, α_2 is zero. Equation (4.28) is therefore reduced to the form

$$B(r) = \alpha_1 K_1\left\{\sqrt{\frac{6(1-\nu)}{4+\nu}}\frac{r}{h}\right\}, \qquad \text{r > a} \tag{4.29}$$

4.2.4 Indentation Caused by Spherical Profile

Although the differential equations discussed in the previous section can be used for the analysis of coating deformation under an arbitrary indenter profile, only a spherical indenter is considered here. The results of indentation by a different indenter profile, such as a blunt cone, can be found in [57].

If the radius of the indenter, R, is much larger than the contact radius, a, the profile of a spherical indenter can be approximated by the following equation

$$f(r) = \frac{r^2 - a^2}{2R} \tag{4.30}$$

Substituting this into (4.18), a differential equation for $B(r)$ within the contact radius, a, can be obtained as

$$\nabla\{B(r)\} - \frac{3}{2h^2}\frac{(1-2\nu)}{(1-\nu)}B(r) + \frac{3\nu r}{(1-\nu)h^2 R} = 0, \qquad 0 \le r < a \tag{4.31}$$

and the solution to this is

$$B(r) = \frac{2\nu}{1-2\nu}\frac{r}{R} + \beta_1 I_1\left\{\sqrt{\frac{3(1-2\nu)}{2(1-\nu)}}\frac{r}{h}\right\} + \beta_2 K_1\left\{\sqrt{\frac{3(1-2\nu)}{2(1-\nu)}}\frac{r}{h}\right\}, \quad 0 \le \text{r} < \text{a} \tag{4.32}$$

where β_1 and β_2 are constants.

The above expression contains two singularities, one at r=0, where K_1 is unbounded, and another when ν=0.5. These singularities have to be removed as $B(r)$ must be finite. To overcome this problem, the first singularity is removed by simply making β_2 equal to zero. In order to balance the singularity produced in the first term when ν=0.5, β_1 is selected so that the second term has the same singularity and their sum remains finite. The evaluation of $B(r)$, with or near to ν=0.5, may then be carried out by expressing $I_1(x)$ in the form of an analytical power series and combine with the diverging terms in r to yield a finite expression that satisfies the symmetry condition at r=0. Matthewson adopted an empirical procedure by imposing continuity on the three strains and found a simplified solution for the case when ν is precisely 0.5.

When ν=0.5, $B(r)$ reduces to

$$B(r)=\begin{cases}\beta_3\dfrac{r}{a}+\dfrac{3a^3}{8h^2R}\left[1-\left(\dfrac{r}{a}\right)^2\right]\left(\dfrac{r}{a}\right) & 0\le r<a\\ \alpha_1 K_1\left\{\sqrt{\dfrac{2}{3}}\dfrac{r}{h}\right\} & r>a\end{cases} \tag{4.33}$$

For $0\le r<a$, substituting $B(r)$ into the expression for strains in equations (4.4), (4.5) and (4.6) gives

$$\begin{aligned}\bar{\varepsilon}_r &= \frac{1}{2}h\frac{d}{dr}\left\{\beta_3\frac{r}{a}+\frac{3a^3}{8h^2R}\left[1-\left(\frac{r}{a}\right)^2\right]\left(\frac{r}{a}\right)\right\}+\frac{1}{3}h^2\frac{d}{dr}\left\{-\frac{1}{2h}\left[B(r)+\frac{df}{dr}\right]\right\}\\ &=\frac{h\beta_3}{3a}+\frac{\left(a^2-3r^2\right)}{8hR}-\frac{h}{6R},\end{aligned} \tag{4.34}$$

$$\begin{aligned}\bar{\varepsilon}_\theta &= \frac{h}{2r}\left\{\beta_3\frac{r}{a}+\frac{3a^3}{8h^2R}\left[1-\left(\frac{r}{a}\right)^2\right]\left(\frac{r}{a}\right)\right\}+\frac{h^2}{3r}\left\{-\frac{1}{2h}\left[B(r)+\frac{df}{dr}\right]\right\}\\ &=\frac{h\beta_3}{3a}+\frac{\left(a^2-r^2\right)}{8hR}-\frac{h}{6R}\end{aligned} \tag{4.35}$$

$$\bar{\varepsilon}_z=\frac{r^2-a^2}{2Rh}+\delta \tag{4.36}$$

For $r>a$,

$$\begin{aligned}\bar{\varepsilon}_r &= \frac{1}{2}h\frac{d}{dr}\left[\alpha_1 K_1\left\{\sqrt{\frac{2}{3}}\frac{r}{h}\right\}\right]+\frac{1}{3}h^2\frac{d}{dr}\left[-\frac{1.5}{4h}\alpha_1 K_1\left\{\sqrt{\frac{2}{3}}\frac{r}{h}\right\}\right]\\ &=\frac{3}{8}h\alpha_1\frac{d}{dr}\left[K_1\left\{\sqrt{\frac{2}{3}}\frac{r}{h}\right\}\right]\end{aligned} \tag{4.37}$$

$$\begin{aligned}\bar{\varepsilon}_\theta &= \frac{h}{2r}\alpha_1 K_1\left\{\sqrt{\frac{2}{3}}\frac{r}{h}\right\}+\frac{h^2}{3r}\left\{-\frac{1.5}{4h}\alpha_1 K_1\left\{\sqrt{\frac{2}{3}}\frac{r}{h}\right\}\right\}\\ &=\frac{3}{8}h\frac{1}{r}\alpha_1 K_1\left\{\sqrt{\frac{2}{3}}\frac{r}{h}\right\}\end{aligned} \tag{4.38}$$

$$\bar{\varepsilon}_z=-\left(\bar{\varepsilon}_r+\bar{\varepsilon}_\theta\right) \tag{4.39}$$

When meeting at $r = a$, these equations will give

$$\alpha_1 = \frac{2a^3}{3h^2 R(K - K'a)} \tag{4.40}$$

$$\beta_3 = \frac{9\alpha_1 K}{8} + \frac{a}{2R} \tag{4.41}$$

$$\delta = \frac{a^2}{4Rh} + \frac{h}{3R} - \frac{2h\beta_3}{3a} \tag{4.42}$$

4.2.4.1 The determination of the Contact Force and Penetration

When ν=0.5, the stresses in (4.7) will reduce to

$$\begin{aligned} \bar{\sigma}_r &= \bar{\sigma}_0 + 2G\bar{\varepsilon}_r \\ \bar{\sigma}_\theta &= \bar{\sigma}_0 + 2G\bar{\varepsilon}_\theta \\ \bar{\sigma}_z &= \bar{\sigma}_0 + 2G\bar{\varepsilon}_z \end{aligned} \tag{4.43}$$

where $\bar{\sigma}_0$ is the averaged hydrostatic pressure.

As $\bar{\sigma}_z$=0 and $\bar{\varepsilon}_z = \delta$ at r=a, then

$$\bar{\sigma}_0 = -2G\delta \tag{4.44}$$

On substituting the stresses from (4.43) and the strains from equations (4.34)-(4.36) into the equilibrium equation (4.8), a differential equation for $\bar{\sigma}_0$ is obtained. By using the boundary condition in (4.44), $\bar{\sigma}_0$ is obtained as below:

$$\frac{\bar{\sigma}_0}{G} = \left(r^2 - a^2\right)\left[\frac{\beta_3}{2ah} + \frac{1}{hR} - \frac{3}{32h^3 R}\left(r^2 - a^2\right)\right] - 2\delta \tag{4.45}$$

The normal stresses can therefore be obtained by substituting equation (4.45) back into equation (4.43), and $\bar{\sigma}_z$ is obtained as follows,

$$\bar{\sigma}_z = \left(r^2 - a^2\right)G\left[\frac{\beta_3}{2ah} + \frac{1}{hR} - \frac{3}{32h^3 R}\left(r^2 - a^2\right)\right] + G\frac{r^2 - a^2}{Rh} \tag{4.46}$$

The total compression load can then be found by integrating $\bar{\sigma}_z$ over the contact area as shown:

$$\begin{aligned} P &= \int 2\pi r \bar{\sigma}_z dr \\ &= 2\pi G \int r \left(\left(r^2 - a^2\right) \left[\frac{\beta_3}{2ah} + \frac{1}{hR} - \frac{3}{32h^3 R}\left(r^2 - a^2\right) \right] + \frac{r^2 - a^2}{Rh} \right) dr \\ &= \pi a^2 G \left[\frac{a\beta_3}{4h} + \frac{a^2}{hR} + \frac{a^4}{32h^3 R} \right] \end{aligned} \tag{4.47}$$

The penetration, d, into the coating by the indenter is given as

$$\begin{aligned} d &= -h\bar{\varepsilon}_{z(r=0)} \\ &= \frac{a^2}{2R} - \delta h \end{aligned} \tag{4.48}$$

The variation of the compression load P with the penetration d is shown in the following figures for:

a) A coating thickness h of 1mm with various values of shear modulus G; and

b) A shear modulus G of 50kN/m^2 with various coating thicknesses h.

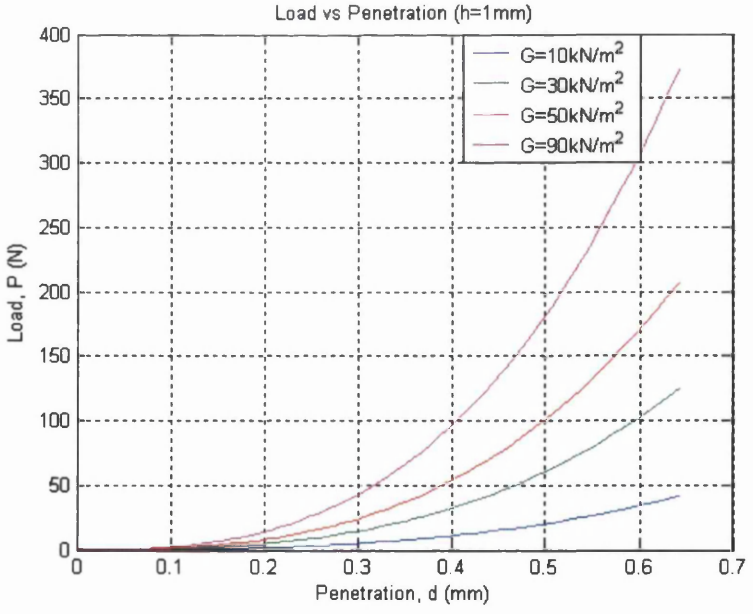

Figure 4.2: Variation of P with d for different G. (h = 1mm)

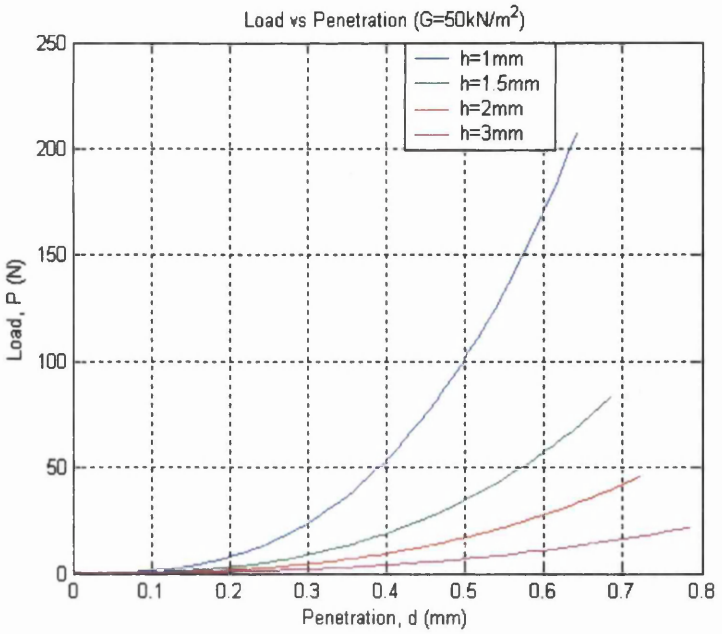

Figure 4.3: Variation of P with d for different h. (G = 50kN/m^2)

It can be seen that, for a certain thickness of the coating, as the shear modulus increases, the force required to reach a certain amount of penetration is increased. Whereas, for a certain value of shear modulus for the coating, the force required to reach a certain amount of penetration increases with the reduction in coating thickness.

Furthermore, it is worth mentioning that, by referring to equation (4.47) and (4.48), it can be seen that the contact force and penetration are both functions of the contact radius and the substitution of a with d in the force equation is not straight forward as $d = f(a,\delta)$ and $\delta = g(a,\beta_3)$, which requires the use of Bessel Functions. Therefore, the force equation can not be related to penetration independently.

4.3 Finite Element Analysis of the Compression of an Elastic Layer

A finite element model was set up using *ELFEN* to model the indentation of a thin elastic coating by a rigid spherical indenter. By taking advantage of the symmetric nature of the spherical indenter, only a quadrant of the sphere is modelled. The central line of the indenter and the coating is constrained horizontally to preserve the symmetric behaviour.

In order to simulate the bonding between the coating and the rigid substrate, the bottom part of the coating is constrained in both directions. The boundary conditions used in the model can be seen in the following figure, where the green markers represent constraints in the vertical direction and the red markers represent constraints in the horizontal direction.

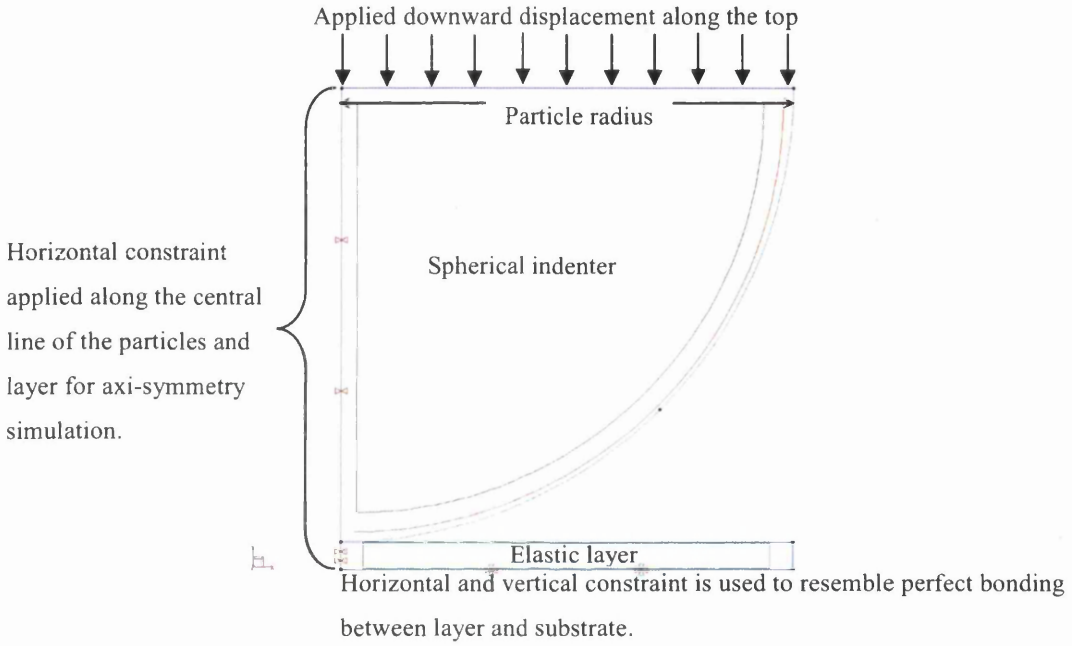

Figure 4.4: Boundary constraints used in the FE model for the compression of an elastic layer.

The model is meshed with unstructured linear rectangular elements, with smaller elements assigned to the region of contact. To model the compression of the layer, a downward displacement is applied along the top of the sphere with a loading speed of *0.02m/s*. Different values of thickness, h, and shear modulus, G, are used for the coating in the analyses, while the radius, R, of the spherical indenter is kept constant at *0.047m* in all cases.

A value of *0.49* was used to model the incompressibility of the elastic layer, as a Poisson's ratio of *0.5* will produce a singularity in the numerical analysis. The results produced between these two values are indistinguishable as can bee seen in the following figure, where the solution approximated by Matthewson using $\nu=0.49$ and $\nu=0.5$ are identical.

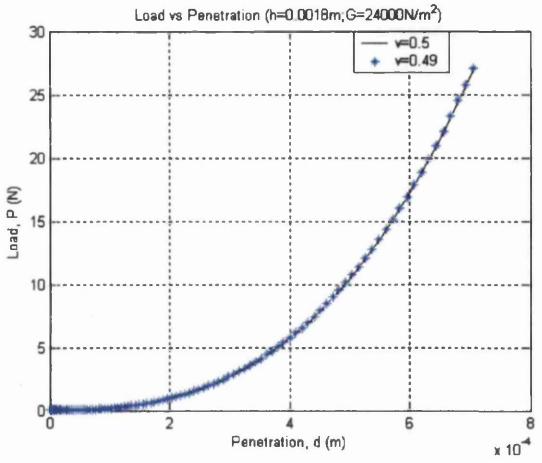

Figure 4.5: Comparison between solutions using $v=0.49$ and $v=0.5$.

4.3.1 FE Results and Comparisons

The relation between the compression force P and penetration d is shown in the graphs below for different cases of coating thickness and shear modulus. The black curves are the approximation derived by Matthewson which involves the use of Bessel Functions while the red dots are the FE results obtained from the simulations.

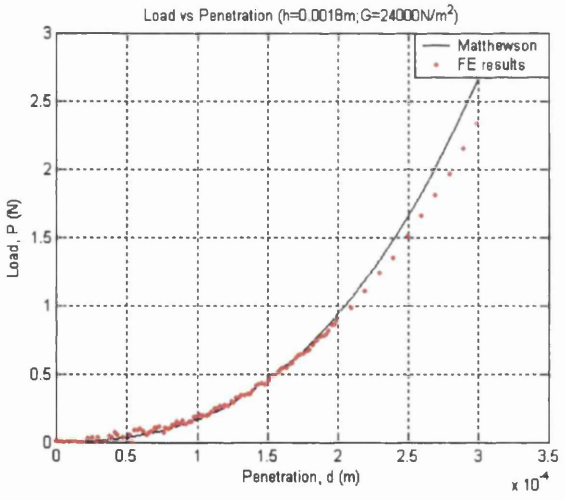

Figure 4.6: Comparisons between FE results and theoretical values obtained by Matthewson ($G=24000N/m^2$; $h=0.0018m$)

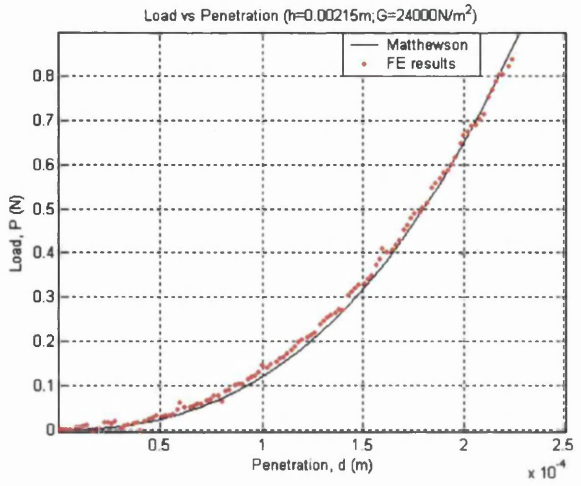

Figure 4.7: Comparisons between FE results and theoretical values obtained by Matthewson ($G=24000N/m^2$; $h=0.00215m$)

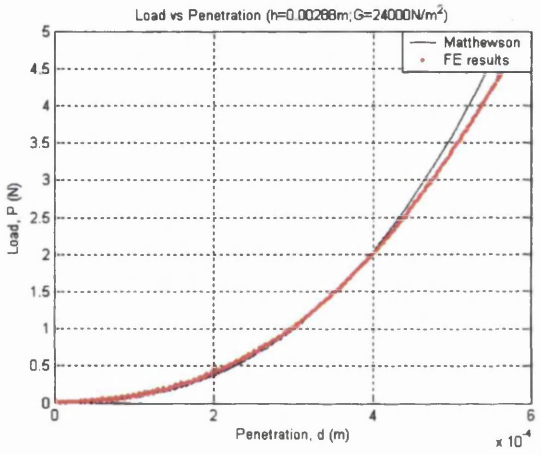

Figure 4.8: Comparisons between FE results and theoretical values obtained by Matthewson ($G=24000N/m^2$; $h=0.00288m$)

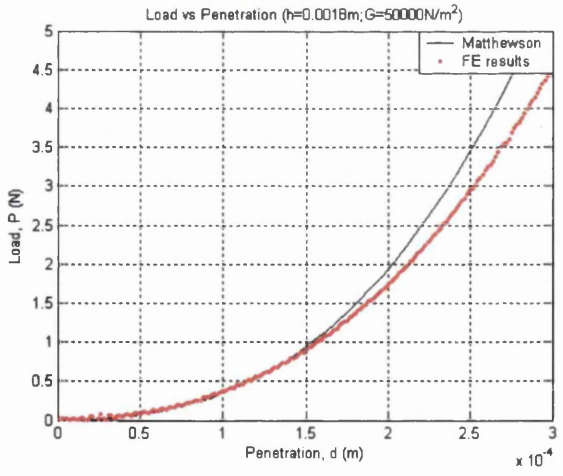

Figure 4.9: Comparisons between FE results and theoretical values obtained by Matthewson ($G=50000N/m^2$; $h=0.0018m$)

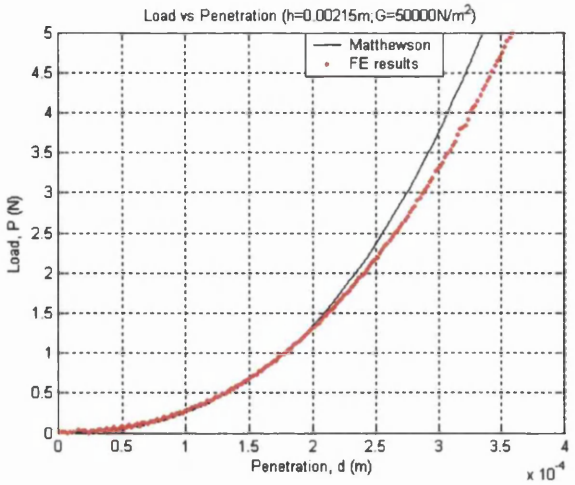

Figure 4.10: Comparisons between FE results and theoretical values obtained by Matthewson ($G=50000N/m^2$; $h=0.00215m$)

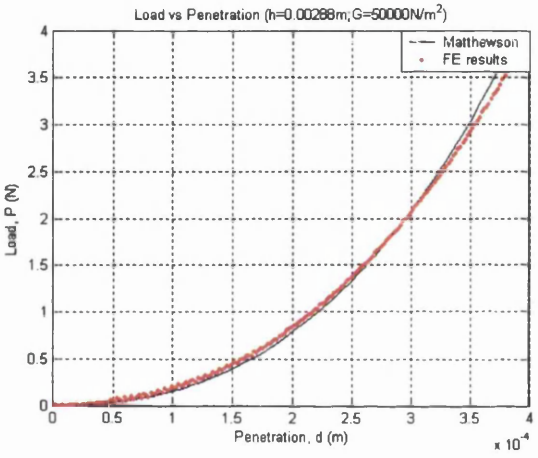

Figure 4.11: Comparisons between FE results and theoretical values obtained by Matthewson ($G=50000N/m^2$; $h=0.00288m$)

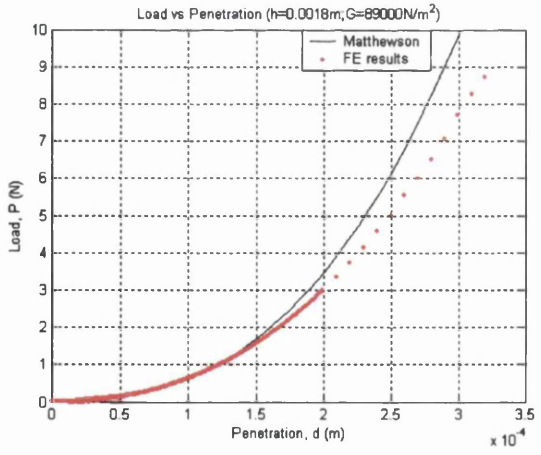

Figure 4.12: Comparisons between FE results and theoretical values obtained by Matthewson ($G=89000N/m^2$; $h=0.0018m$)

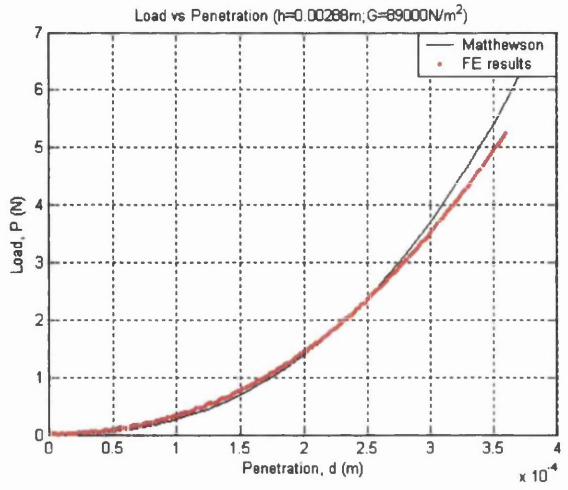

Figure 4.13: Comparisons between FE results and theoretical values obtained by Matthewson ($G=89000N/m^2$; $h=0.00288m$)

It can be seen from the figures that the FE results match closely with the approximation derived by Matthewson at the beginning of the contact. However, the results from the simulation deviate from the approximation at later stages of the compression, where the approximated force is higher than the one obtained from the FE analysis. This, from observation, mainly happens when the depth of penetration is about 10% of the coating thickness. The reason for this is due to the nonlinearity caused by the large deformation in the layer, hence causing the discrepancy between the approximated values and the FE results.

As the use of a combined finite-discrete element simulation to model the compaction of pharmaceutical powder usually involves extensive deformation, a force-displacement relation is used as the interaction law at the contact of the particles which allows large deformation of the material. This is necessary in order to obtain sensible results in the simulations. The use of Matthewson's theory would be inappropriate in this case as it is only able to model small deformation in the layer. Furthermore, the contact force can not be written independently in terms of the penetration. Hence, an approximation that takes into consideration the nonlinearity, i.e. large deformation in the layer and related to the penetration directly, is necessary in order to model the deformation of powder particles. This, as will be shown in the next section, can be done by modifying some of the terms in Matthewson's equations based on certain assumptions and observations.

4.4 Modification to Matthewson's Equation

As mentioned in [57], Matthewson adopted empirical procedure to impose continuity at the boundary $r=a$ for the normal strain terms $\bar{\varepsilon}_z, \bar{\varepsilon}_r, \bar{\varepsilon}_\theta$. The reason for the success of this was still unclear. However, the approximation is only for linear elasticity and does not take into account the nonlinear behaviour in the coating at the later stage of the compression. Hence, Matthewson's equation is only suitable for small deformation analysis, and is not applicable when the coating material experiences large deformation. Furthermore, the contact force is related to the contact radius, and the substitution of the contact radius by the penetration is not straight forward as it involves the use of Bessel Functions, which will cause singularities in the analysis when the function becomes unbounded. A modification to the present equations is performed in the following sub-sections to allow for the nonlinear deformation in the layer to be approximated.

4.4.1 Modification of Radial and Circumferential Strains

Since Matthewson adopted empirical procedure on the strain terms to impose continuity at the boundary $r=a$ in the solutions, the modification to the equations can be tackled from the strain equations for $\bar{\varepsilon}_r$ and $\bar{\varepsilon}_\theta$.

In the modification, the incompressible coating is assumed to behave in two extreme situations when subjected to compression. First, the radial strain at $r=a$ is assumed to be zero $\left((\bar{\varepsilon}_r)_{r=a} = 0\right)$, and second, the circumferential strain is assumed to be zero at $r=a$ $\left((\bar{\varepsilon}_\theta)_{r=a} = 0\right)$. When $(\bar{\varepsilon}_r)_{r=a} = 0$ during compression, the contact radius remains constant while the circumferential strain causing the movement of material around the contact and hence no heaving formed around the contact. However, when $(\bar{\varepsilon}_r)_{r=a} \neq 0$ during compression, the increase of contact radius without the flow of circumferential strain forms a deep heave around the contact. These situations can be visualised in the following figure.

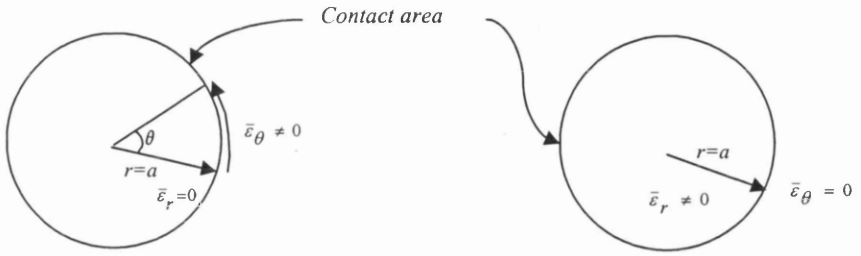

Figure 4.14: Two extreme assumptions: a) $(\bar{\varepsilon}_r)_{r=a} = 0$; b) $(\bar{\varepsilon}_\theta)_{r=a} = 0$.

First assumption: $(\bar{\varepsilon}_r)_{r=a} = 0$

For the region $0 \le r < a$, the radial strain in the layer is as shown in equation (4.34). If the strain is assumed to be zero at $r = a$, the equation can be written as

$$\frac{h\beta_3}{3a} - \frac{a^2}{4hR} - \frac{h}{6R} = 0 \tag{4.49}$$

, and by rearranging the equation, β_3 can be written as

$$\beta_3 = \frac{3a^3}{4Rh^2} + \frac{a}{2R} \tag{4.50}$$

Substituting this into equation (4.35) gives

$$\bar{\varepsilon}_\theta = \frac{a^2}{4Rh} + \frac{\left(a^2 - r^2\right)}{8hR} \tag{4.51}$$

Hence, at $r = a$,

$$\frac{a^2}{4Rh} = \frac{3}{8}h\frac{1}{a}\alpha_1 K_1\left\{\sqrt{\frac{2}{3}}\frac{a}{h}\right\}$$

$$\alpha_1 = \frac{2a^3}{3Rh^2}\frac{1}{K_1\left\{\sqrt{\frac{2}{3}}\frac{a}{h}\right\}} \tag{4.52}$$

and by equating the vertical strain at $r = a$, the heave around the contact (referring to the geometry of the contact shown in Figure 4.1) can be written as

$$\delta = -\left(\bar{\varepsilon}_r + \bar{\varepsilon}_\theta\right)$$

$$= -\frac{a^2}{4Rh} \tag{4.53}$$

which is without the use of Bessel Functions.

Second assumption: $(\bar{\varepsilon}_\theta)_{r=a} = 0$

For the region $0 \le r < a$, the circumferential strain has the form shown in equation (4.35). For this to be zero at $r = a$, then

$$\frac{h\beta_3}{3a} - \frac{h}{6R} = 0 \tag{4.54}$$

Hence, β_3 can be written as

$$\beta_3 = \frac{a}{2R} \tag{4.55}$$

Substituting this into the radial strain equation gives

$$\bar{\varepsilon}_r = \frac{\left(a^2 - 3r^2\right)}{8hR} \tag{4.56}$$

Thus, at $r = a$,

$$\begin{aligned} \frac{-a^2}{4hR} &= \frac{3}{8} h\alpha_1 \frac{d}{da}\left[K_1\left\{\sqrt{\frac{2}{3}}\frac{a}{h}\right\}\right] \\ \alpha_1 &= \frac{-2a^2}{3Rh^2} \frac{1}{\frac{d}{da}\left[K_1\left\{\sqrt{\frac{2}{3}}\frac{a}{h}\right\}\right]} \end{aligned} \tag{4.57}$$

Equating the vertical strains at $r = a$, the heave around the contact is obtained as

$$\begin{aligned} \delta &= -\left(\bar{\varepsilon}_r + \bar{\varepsilon}_\theta\right) \\ &= \frac{a^2}{4Rh} \end{aligned} \tag{4.58}$$

The variation of $\bar{\varepsilon}_r$ and $\bar{\varepsilon}_\theta$ with respect to the ratio $\frac{r}{a}$ can be seen in the following figures. Also, the graphs obtained from [57] are also shown for comparison. The values are only dependent on $\frac{a}{h}$ and Poisson's ratio ν, and the ratio of $\frac{a}{h} = 5$ is chosen for the comparison.

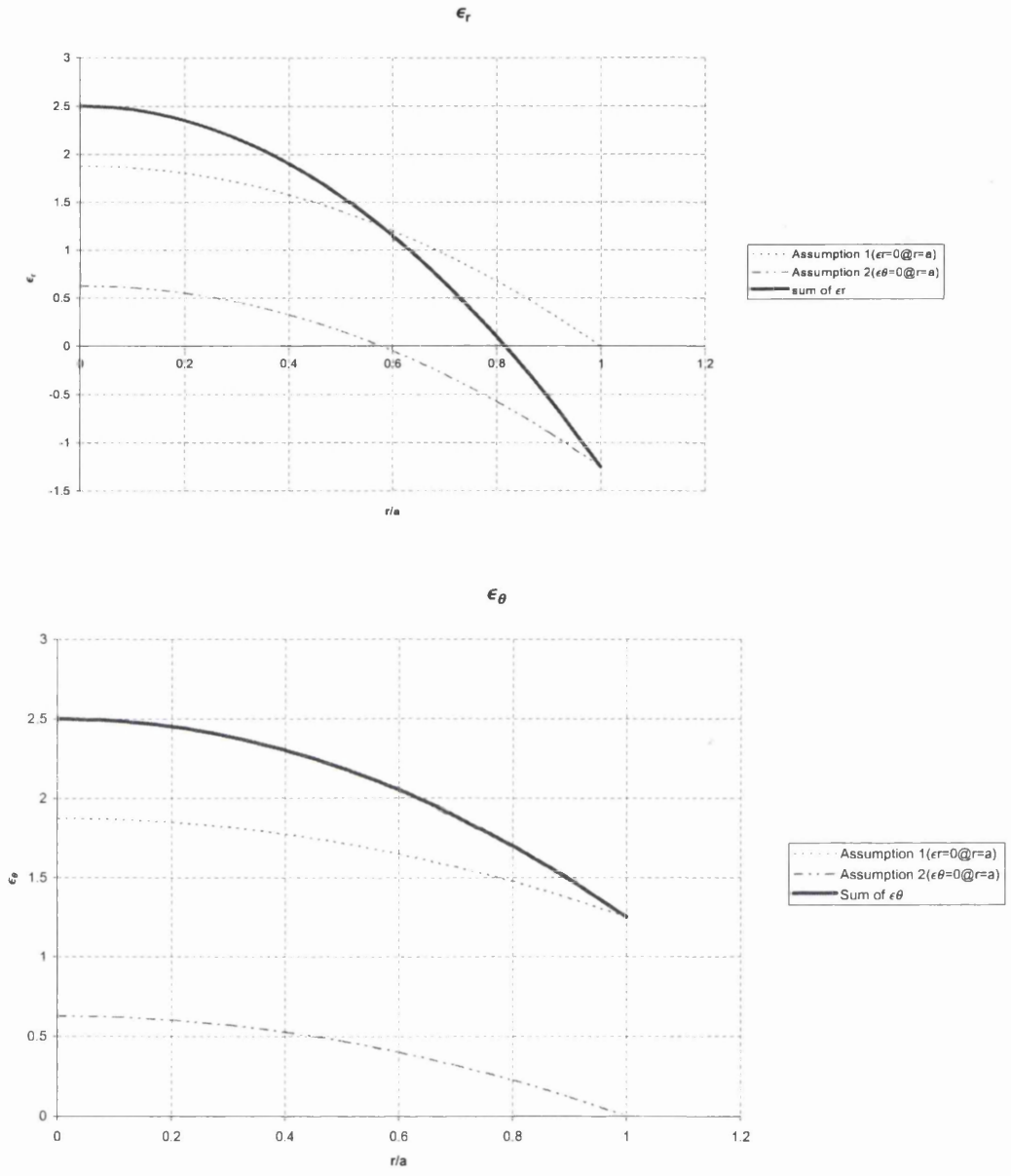

Figure 4.15: The variation of $\bar{\varepsilon}_r$ and $\bar{\varepsilon}_\theta$ with respect to $\frac{r}{a}$ for v=0.5 (Based on assumptions).

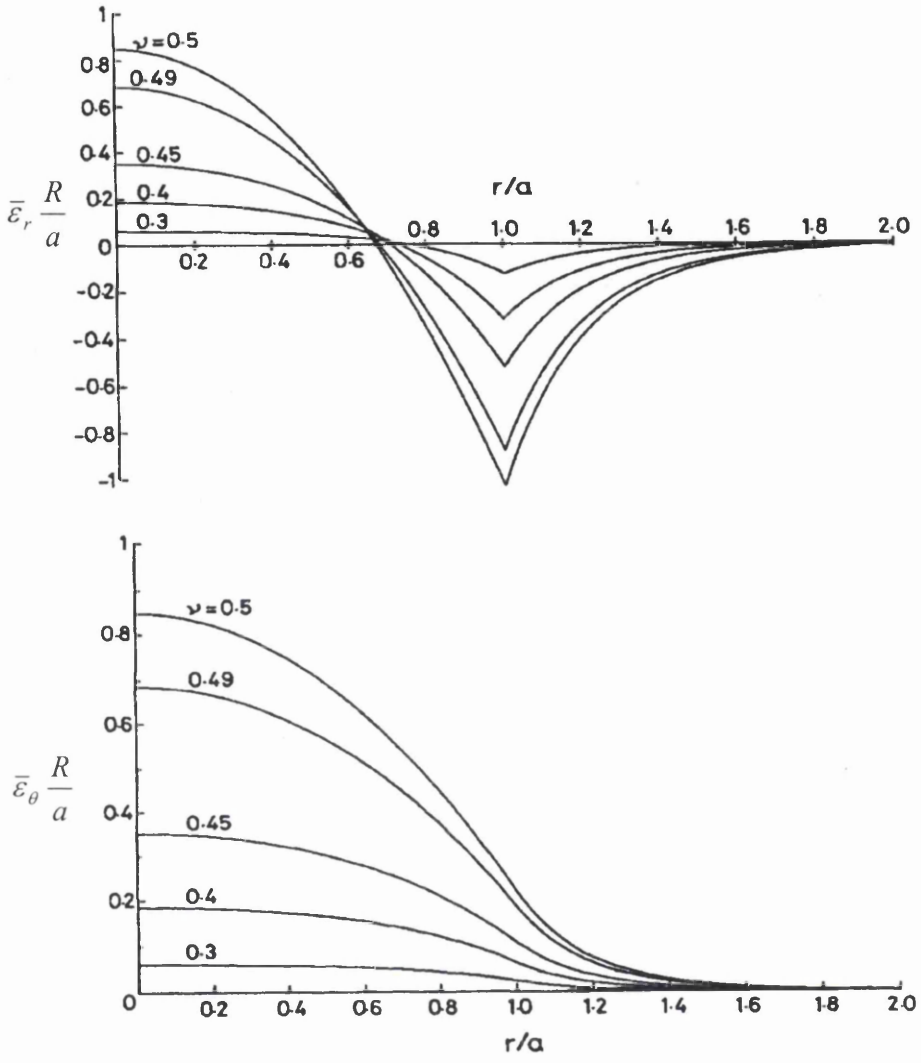

Figure 4.16: The variation of $\bar{\varepsilon}_r$ and $\bar{\varepsilon}_\theta$ with respect to $\frac{r}{a}$ for v=0.5 (Obtained by Matthewson [57]).

It can be seen from the graphs that, although the magnitude of the response is different from the ones obtained by Matthewson in [57], the general trends obtained for the sum of the two assumptions are similar.

4.4.2 Relation between Penetration and Contact Radius

From [57], the pile-up around the contact radius for elastomeric coating is assumed to be approximately

$$\delta = \frac{a^2}{6Rh} \tag{4.59}$$

which gives the relation between the penetration and contact radius as

$$d_m = \frac{a_m^{\,2}}{3R} \tag{4.60}$$

or

$$a_m = \sqrt{3d_m R} \tag{4.61}$$

where the subscript m corresponds to the contact radius and penetration obtained based on the assumed value of δ in [57].

However, as the relation between the penetration and the contact radius in equation (4.48) is related to the pile-up around the contact radius, the relation is now changed due to the change of δ as determined in section 4.4.1. Based on the first assumption $\left((\bar{\varepsilon}_r)_{r=a} = 0\right)$, the relation between the penetration and the contact radius is now

$$\begin{aligned} d_1 &= -h\bar{\varepsilon}_{z(r=0)} \\ &= \frac{a_1^{\,2}}{2R} + \frac{a_1^{\,2}}{4R} \\ &= \frac{3a_1^{\,2}}{4R} \end{aligned} \tag{4.62}$$

or, writing in terms of contact radius

$$a_1 = \sqrt{\frac{4}{3} d_1 R} \tag{4.63}$$

Whereas for the second assumption $\left((\bar{\varepsilon}_\theta)_{r=a} = 0\right)$, the relation can be written as

$$\begin{aligned} d_2 &= -h\bar{\varepsilon}_{z(r=0)} \\ &= \frac{a_2^{\,2}}{2R} - \frac{a_2^{\,2}}{4R} \\ &= \frac{a_2^{\,2}}{4R} \end{aligned} \tag{4.64}$$

or

$$a_2 = \sqrt{4d_2 R} \tag{4.65}$$

where the subscript 1 and 2 correspond to the 1st and 2nd assumptions respectively.

Comparing (4.63) and (4.65) with (4.61), it can be seen that $a_1 < a_m$ and $a_2 > a_m$. The difference between a_1 and a_2 with a_m is shown in the figure below.

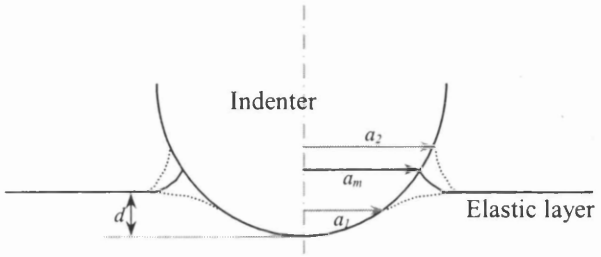

Figure 4.17: Diagram showing the difference between a_1, a_2 and a_m.

From Figure 4.17, it can be seen that both of the two assumptions show the extreme situations and will not give sensible responses individually. However, if a factor is applied to each assumption and an average between these two is sought for, the response will be close to the realistic behaviour. To do this, the force-penetration (*P-d*) response will be obtained for each assumption and the factors to be applied to each assumption will be determined semi-empirically based on observation. This is shown in the next section.

4.4.3 Force-Penetration Relations

Having found the relation for β_3 and d using the assumptions, the force equation determined by Matthewson which is dependent on the contact radius can now be expressed in terms of the penetration without the need for Bessel Functions.

For the first assumption, by substituting β_3 and d from equations (4.50) and (4.63) into the force equation (4.47), the force-penetration can be written as

$$P_1 = \frac{2}{9}\frac{\pi G R d^2}{h}\left(\frac{7}{3}\frac{Rd}{h^2} + 9\right) \tag{4.66}$$

where the subscript 1 indicates the force derived from assumption 1.

For the second assumption, by substituting β_3 and d from equations (4.55) and (4.65) into the force equation in (4.47), the force-penetration relation is obtained as

$$P_2 = \frac{2\pi G R d^2}{h}\left(\frac{Rd}{h^2} + 9\right) \tag{4.67}$$

where the subscript 2 indicates the force derived from assumption 2.

Finally, the resultant force that can approximate the force-penetration relation for the nonlinear deformation in the coating can be obtained by averaging the factored forces based on assumption 1 and 2. This can be done as below

$$P_{res} = \frac{\alpha P_1 + \frac{1}{\gamma} P_2}{2} \tag{4.68}$$

where α and γ are to be determined from observations.

The reason that P_1 is multiplied by α and P_2 is divided by γ can be justified by referring to Figure 4.17. The first assumption is found to underestimate the contact radius while the second assumption is found to overestimate the contact radius at certain penetration. Therefore, in order to neutralise these, αP_1 and $\frac{1}{\gamma} P_2$ are used. To have a more accurate approximation, the two force-penetration assumptions are averaged up. By using curve-fitting method, the factors to be applied to each assumption for a particular coating shear modulus can be determined.

4.4.4 Determination of the α and γ Factors

The modification to the contact strains in section 4.4.2 gives rise to two extreme responses. This is because the modification has excluded the influence of material properties to the contact behaviour by eliminating the Bessel Functions, and hence produces response based purely from the manipulation of the geometry of the contact. In order to complement this, each of the two extreme cases needs to be corrected using a factor that is determined from the observation based on the influence of the material properties.

The following figure shows the comparison between the FE results and the curves based on the first and second assumptions prior to factorisation. The thickness of the coating h is $0.00288m$ and the shear modulus G for the coating is $24000N/m^2$.

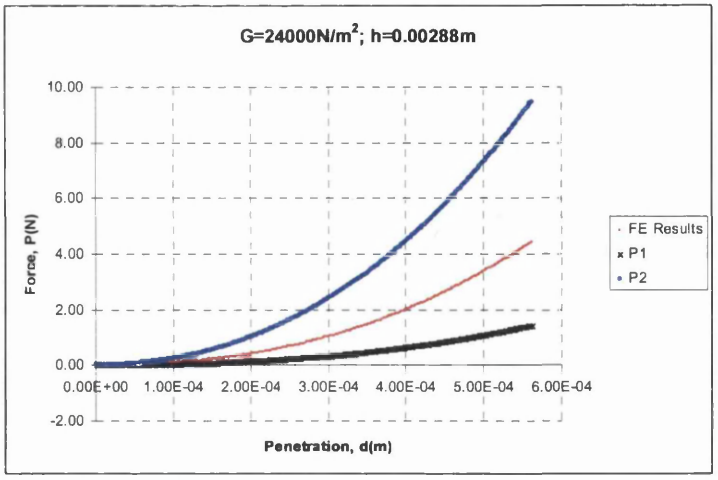

Figure 4.18: Comparison between the FE results and the unfactored forces determined from assumptions 1 and 2.

It can be seen from the graph above that P_1 produces a much softer response as compared to the FE results. Conversely, P_2 produces a much stiffer response compared to that of the FE results. Although it can be said that modification needs only be applied to one of these responses, it is however shown from observation that the rate of growth of the penetration due to the contact force for these two extreme responses are not the same as the rate of growth of the penetration due to the contact force obtained from FE analysis. Therefore, P_1 has to be multiplied by a factor and P_2 has to be divided by a factor before the averaging of the two factored equation is carried out to arrive at the response similar to the one shown by the FE results.

In order to bring the curves to correspond to the FE results, the factors α and γ are found empirically have values of *3.18* and *2.25* respectively. The resultant force is then found by using equation (4.68), and is shown in the following figure.

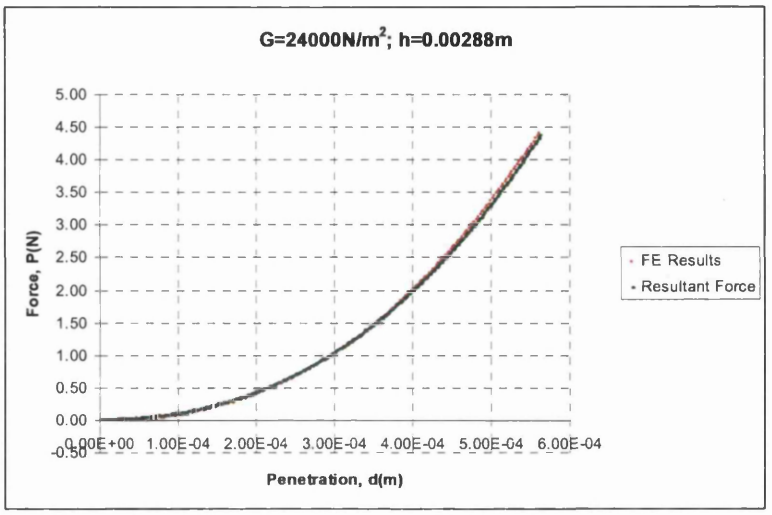

Figure 4.19: Comparison between the FE results and resultant force found after applying the factors.

From observations, the values of α and γ are found to be independent of the coating thickness but dependent on the shear modulus of the coating. Therefore, for a coating of any thickness, the value of α and γ can be determined by linear interpolation with respect to the shear modulus. The values of α and γ for some of the shear modulus are shown in the following table.

Table 4. 1: The values of α and γ for different shear modulus.

Shear Modulus, G (N/m²)	α	γ
24000	*3.18*	*2.25*
30000	*3.185*	*2.308*
50000	*3.2*	*2.5*
60000	*3.208*	*2.596*
70000	*3.215*	*2.692*
89000	*3.23*	*2.875*
100000	*3.238*	*2.981*

4.5 Comparison between the Modified Equation and the Finite Element Results

In order to assess the ability of the modified equation to approximate the contact forces to a reasonable accuracy, the cases that are analysed in section 4.3.1 are presented again in this section. The contact force obtained from the modified equation and the one obtained by Matthewson are plotted together with the results obtained from the FE analysis. The FE results are plotted in red dots, while Matthewson's and the modified equation results are represented by the black solid curve and the blue dashed curve respectively.

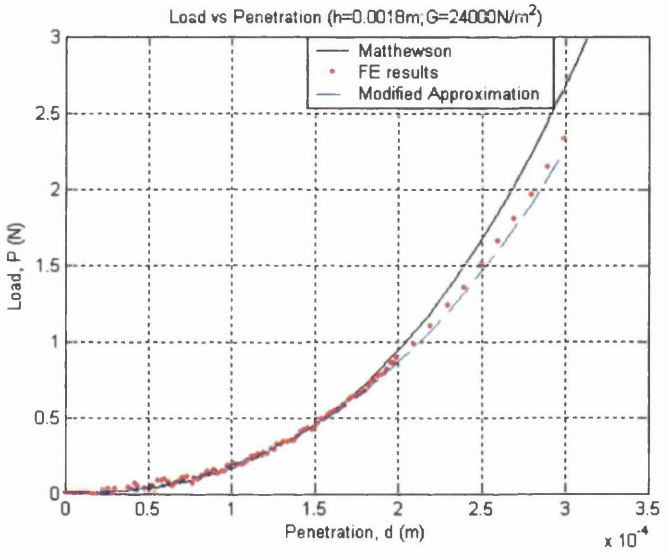

Figure 4.20: P-d graph showing contact force found from FE analysis, Matthewson's equation and modified equation for $G=24000N/m^2$ and $h=0.0018m$.

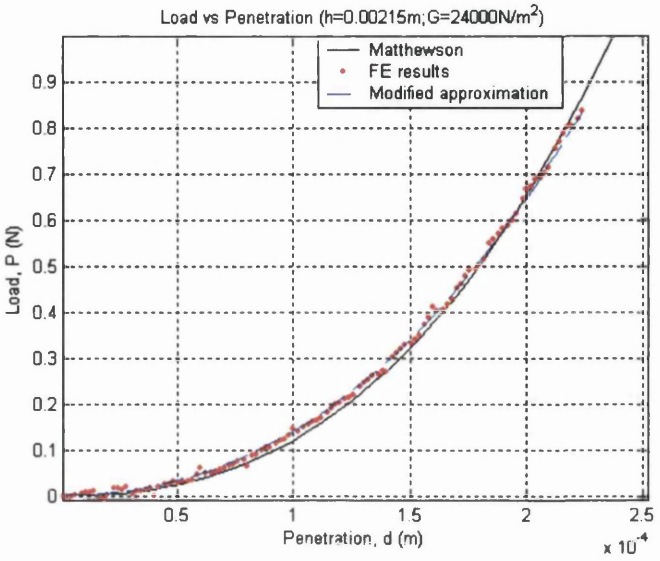

Figure 4.21: P-d graph showing contact force found from FE analysis, Matthewson's equation and modified equation for $G=24000N/m^2$ and $h=0.00215m$.

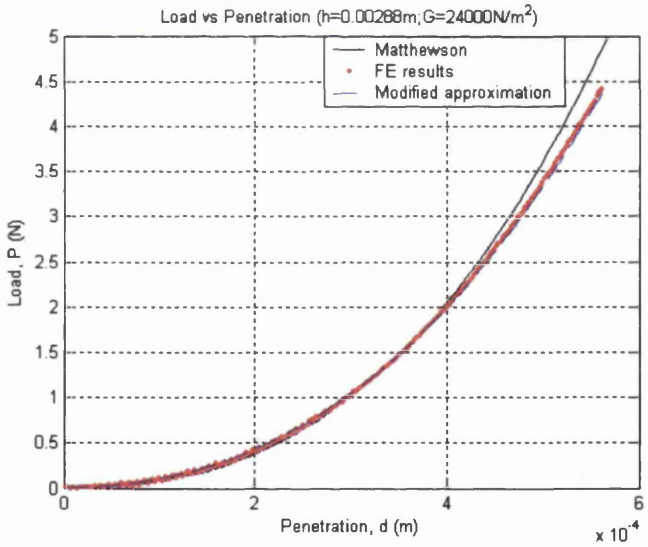

Figure 4.22: P-d graph showing contact force found from FE analysis, Matthewson's equation and modified equation for $G=24000N/m^2$ and $h=0.00288m$.

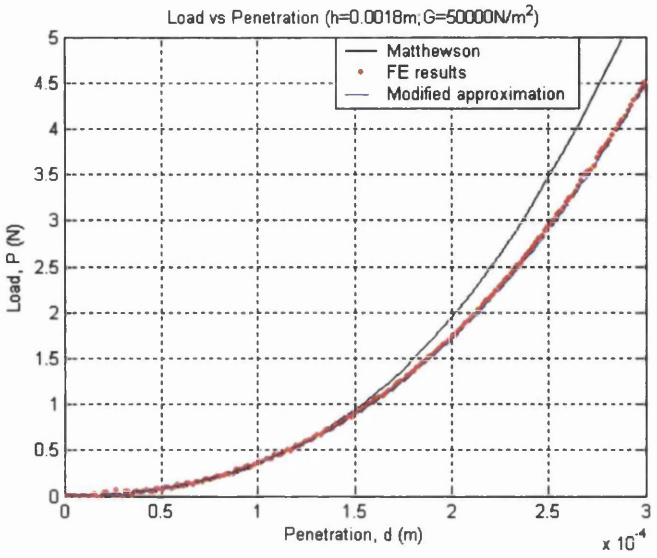

Figure 4.23: P-d graph showing contact force found from FE analysis, Matthewson's equation and modified equation for $G=50000N/m^2$ and $h=0.0018m$.

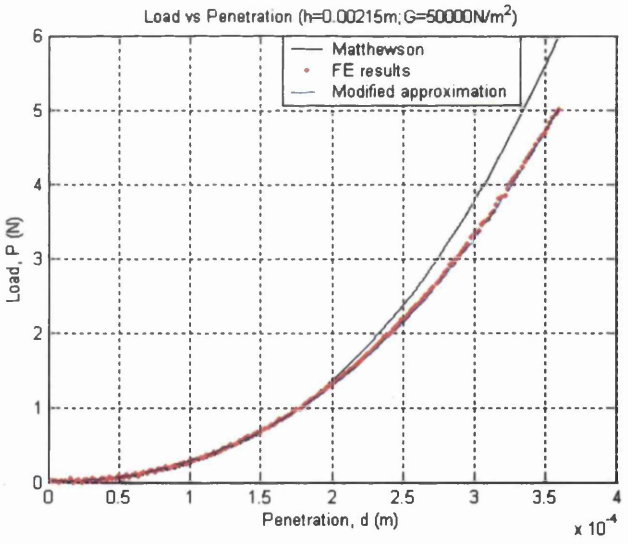

Figure 4.24: P-d graph showing contact force found from FE analysis, Matthewson's equation and modified equation for $G=50000N/m^2$ and $h=0.00215m$.

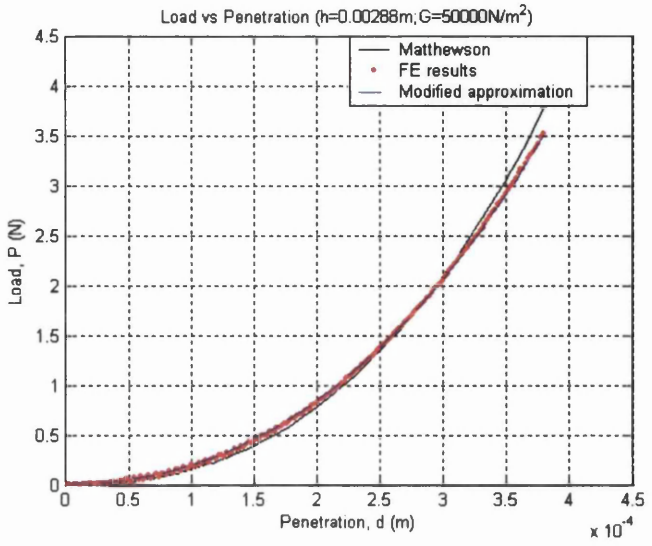

Figure 4.25: P-d graph showing contact force found from FE analysis, Matthewson's equation and modified equation for $G=50000N/m^2$ and $h=0.00288m$.

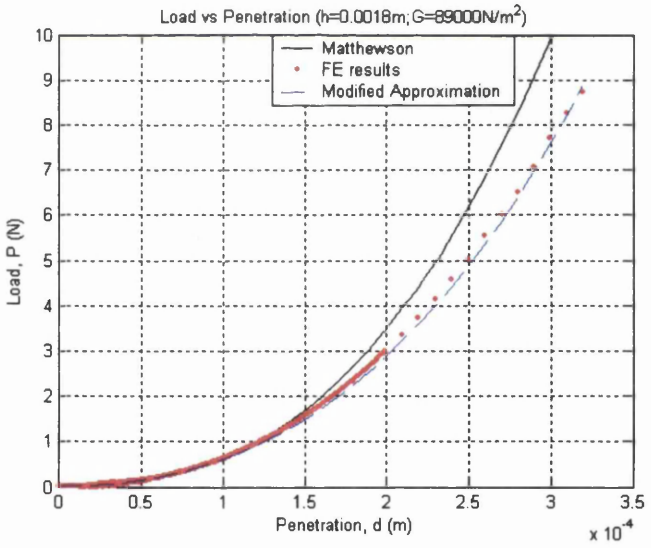

Figure 4.26: P-d graph showing contact force found from FE analysis, Matthewson's equation and modified equation for $G=89000N/m^2$ and $h=0.0018m$.

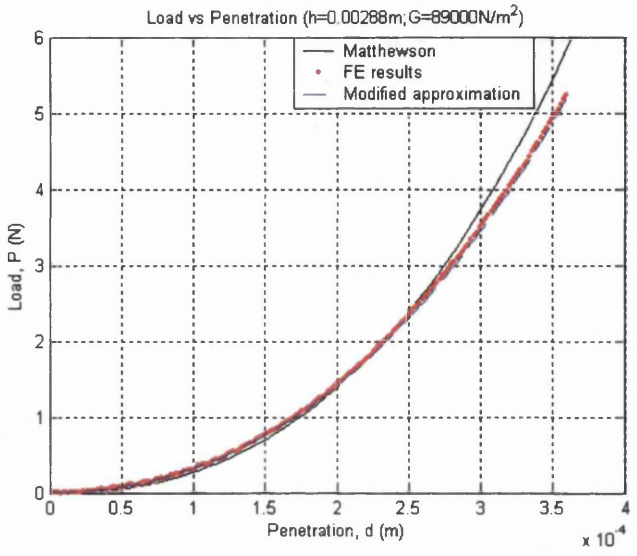

Figure 4.27: P-d graph showing contact force found from FE analysis, Matthewson's equation and modified equation for $G=89000N/m^2$ and $h=0.00288m$.

Also, case studies have been carried out by choosing 5 random combinations of the coating thickness h and shear modulus G, while keeping the radius of the indenter as previously used. The outcome of these results are shown in the following figures.

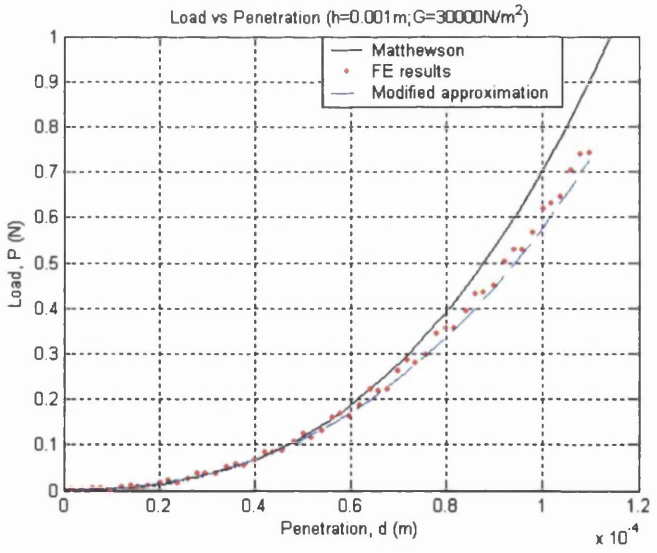

Figure 4.28: P-d graph showing contact force found from FE analysis, Matthewson's equation and modified equation for $G=30000N/m^2$ and $h=0.001m$.

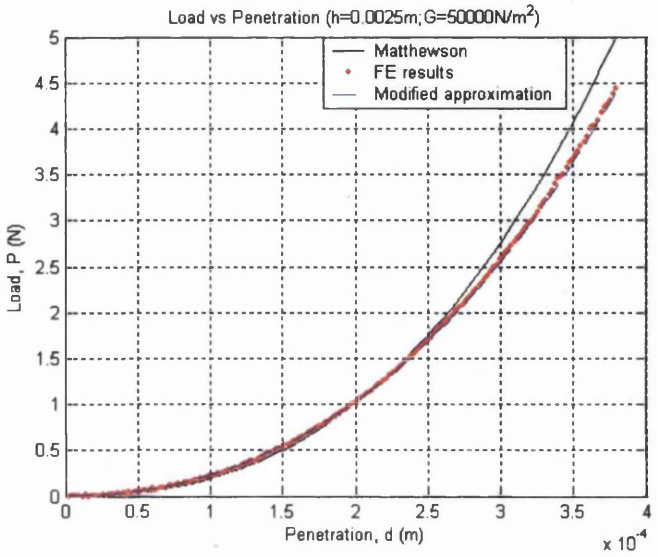

Figure 4.29: P-d graph showing contact force found from FE analysis, Matthewson's equation and modified equation for $G=50000N/m^2$ and $h=0.0025m$.

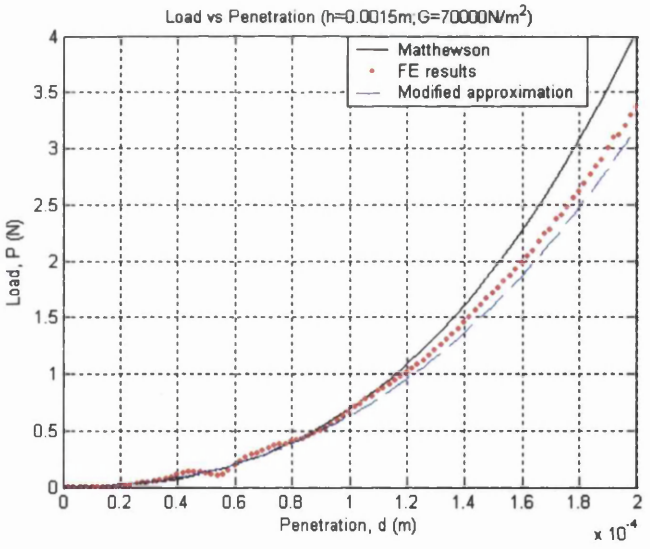

Figure 4.30: P-d graph showing contact force found from FE analysis, Matthewson's equation and modified equation for $G=70000N/m^2$ and $h=0.0015m$.

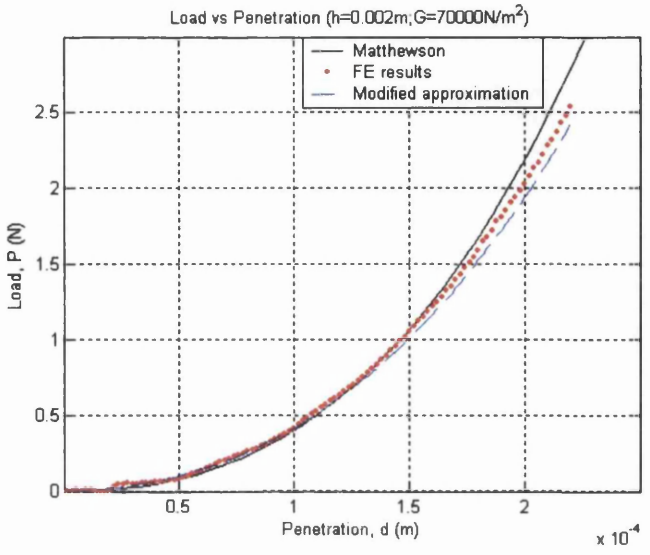

Figure 4.31: P-d graph showing contact force found from FE analysis, Matthewson's equation and modified equation for $G=70000N/\text{m}^2$ and $h=0.002m$.

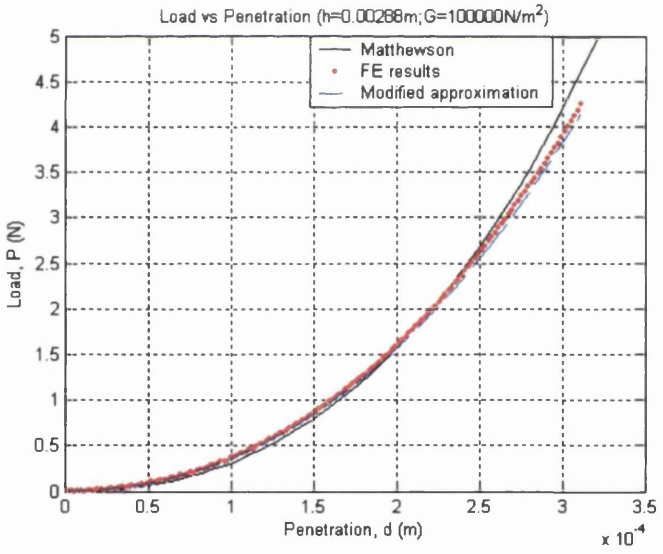

Figure 4.32: P-d graph showing contact force found from FE analysis, Matthewson's equation and modified equation for $G=100000N/\text{m}^2$ and $h=0.00288m$.

It can be seen from Figure 4.20 to Figure 4.32 that the modified equation gives a better approximation than the one presented by Matthewson. Although the initial formulation to this problem was not altered (i.e. based on linear elasticity), with additional assumptions to the radial and circumferential strain, and with the application of factors to the equations, the modified equation reasonably approximates the contact forces.

In the modification process, two assumptions were made for the strains at the contact: a) the radial strain is zero, and b) the circumferential strain is zero. Each of these assumptions gives rise to a force-penetration relation that does not require the use of Bessel Functions. When these two relations are factored with appropriate values, and an average value is obtained, the final force-penetration relation is able to approximate the axi-symmetry compression of an incompressible elastic layer with reasonable accuracy.

The analysis of the contact of elastic coating shows that the contact law for coated particles depends strongly on i) the thickness of the coating, and ii) the material properties of the coating. This forms the principle idea in the exploration of the contact law for elastic-plastic coating and also for adhesive contact in the following chapters, where material factor will be employed to separate the influence of the coating material, leaving the determination of the magnitude of other parameters that need to be incorporated into the contact law depending solely on the coating thickness.

Chapter 5

Axi-symmetric Contact of Elastic-Plastic Layer

The contact between elastic-plastic particles and the work of some researchers in this area are mentioned briefly in the beginning of this chapter to provide a background to the study of the contact between plastically coated particles. Finite element analyses of the contact between particles that are coated with a plastic coating are then presented, from which a simple contact law (force-penetration relation) was derived semi-empirically. To asses the accuracy of the contact law, a comparison between the contact law and the finite element analysis results is also presented.

5.1 Elastic-Plastic Contact

The contact between elastic bodies, based on Hertz theory, and the contact between a rigid body and an elastic layer have been discussed in the previous chapters. These bodies regain their original shape after decompression and hence the formulation of the problem is applicable to both the loading and unloading stages. However, for plastic materials, this is not the case as they involve permanent deformation if they are loaded beyond the elastic limit, i.e. beyond the yielding of the material. Therefore, the solution of the problems for both the loading and unloading process requires two separate formulations. Examples of pictorial and graphical representation for these is shown in the following figure.

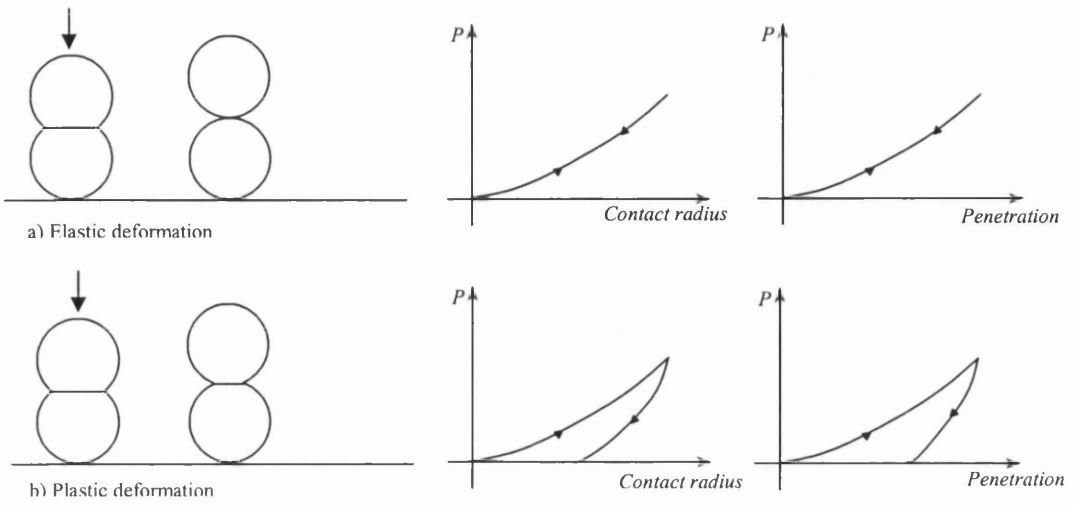

Figure 5.1: Example of elastic deformation and plastic deformation.

The analysis of contact between plastic materials has been difficult in the past due to the complex behaviour of materials which frequently change shape and size during loading [10]. As a result, the development of contact analysis for plastic materials has been slow until the recent boom in computer technology.

In recent years, Mesarovic and Fleck [63] established a contact law between elastic-plastic spheres of dissimilar size semi-empirically with the aid of the finite element method. In the analysis, they took into account the relative size, relative yield strength and the rate of strain hardening of the bodies. Also, Vu-Quoc *et al.* [64,65,66] predicted the force-displacement relations for the contact between elastoplastic materials via the finite element method. In their work, they made use of the additive decomposition of the elastoplastic contact radius into elastic and plastic components, and considered the change of particle radius due to plastic flow at the contact. The prediction was found to be in good agreement with the finite element results. In addition, Kogut and Etsion [67] had also carried out accurate finite element analysis of the contact between an elastoplastic sphere and a rigid flat plate. The results were compared to some analytical solutions and a great difference between these was observed. The reason given was due to the unrealistic assumptions made regarding the contact pressure distribution used in the analytical models.

Hu and Lawn [68], on the other hand, formulated a stress-strain relation using an empirical power-law for the contact between a bilayer and a rigid sphere with the help of

the finite element method. The purpose of this was to eliminate the need for a lengthy numerical computation to solve for the complex stress-strain behaviour for the composite material. In the formulation, they made use of the material factor E_c/E_s, where c and s represent coating and substrate respectively.

Although the contact laws for elastoplastic solids are plentiful, the studies of the contact between coated/layered systems still remain a new topic and the literature available to date is limited. Therefore, the following sections in this chapter aim to study the contact behaviour of coated particles and to develop a contact law that is able to predict the force-penetration relation for the contact between a pair of coated particles. As Hertz theory is readily available, the formulation of the contact relation between coated particles in the following sections are modified from Hertz formula with the use of material ratio to uncouple the influence of the material properties from the coating and the particle.

Due to the complex behaviour of plastic layered materials, the solution of such contact problems using analytical methods is extremely difficult. Thus, a finite element simulation is utilised here to study the contact behaviour of coated particles. From the observed response, a general relation between the contact force and penetration for both the loading and unloading stages is formulated, taking into account some important parameters for contact analyses such as the coating material and thickness. A comparison between the formulated relation and the finite element results will also be carried out to assess the accuracy.

5.2 Finite Element Investigation of the Contact between Coated Particles

A few assumptions were made regarding the model used in the finite element analysis. The coating was assumed to be fully bonded to the hard substrate/particle and may be modelled by assigning a relatively high value of Young's modulus to the particle. In addition, the contact between the coated particles was assumed to be frictionless and only the normal pressure is transmitted through the contact. The yielding of the coating is

assumed to occur when the strain reaches 0.01, and a von-Mises yield criterion was used with no hardening. The stress-strain relation for this is shown in the following figure.

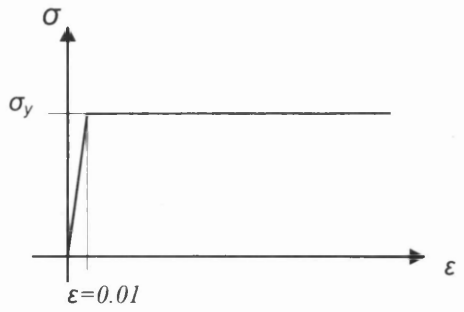

Figure 5.2: Stress-strain graph.

The geometry of the model used in the simulation is shown in Figure 5.3, where the two particles are in contact at a point prior to loading. The spherical shape of the particles is modelled using an axi-symmetry analysis along the common normal of the two particles. The particles are constrained in the radial direction along the axis of symmetry to represent a solid of revolution and in the vertical direction along the bottom of the model to avoid the system from moving under the application of load. These constraints are shown as red and green markers respectively in the figure.

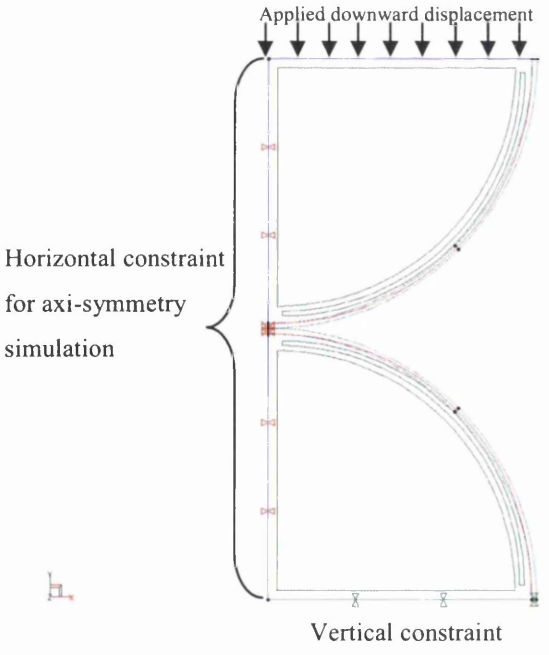

Figure 5.3: The geometry of the model with the applied constraints used in the analysis.

As the deformation in the coating is significant, therefore an adaptive mesh refinement is used where the frequency for mesh quality assessment and mesh refinement requirement were mentioned earlier in Chapter 3. The initial mesh used in the analysis is shown in the following figure.

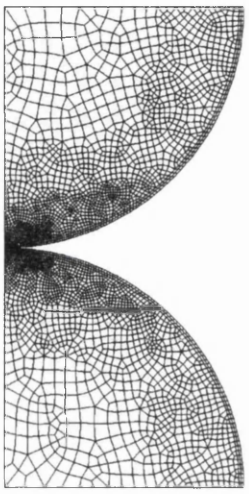

Figure 5.4: The geometry of the model with the initial mesh used in the analysis.

In the analysis, to have a complete understanding of the behaviour of the plastic coatings in contact, the system is loaded to a certain displacement and then unloaded to the point of detachment, i.e. zero contact force. A downward displacement was applied along the top of the model with a speed of $0.00001m/s$ for $1s$ which then reverses in direction for unloading with a speed of $8.33x10^{-6}m/s$.

Two coating thickness, h, were investigated i.e., $\frac{1}{50}R$ and $\frac{1}{10}R$, where R is the radius of the particles which was kept constant at $0.001m$ for all cases. For each of the coating thickness, three different Young's moduli with a Poisson's ratio of 0.3 were used, and there are listed in the table below.

Table 5.1: Material properties used in the analysis.

Coating Thickness, h	***Young's Modulus, E(N/m^2)***	***Particle's Young's Modulus, E(N/m^2)***
$\frac{1}{50}R$ *and* $\frac{1}{10}R$	10^2	10^9
$\frac{1}{50}R$ *and* $\frac{1}{10}R$	10^4	10^9
$\frac{1}{50}R$ *and* $\frac{1}{10}R$	10^6	10^9

5.2.1 Finite Element Results and Observation

Figure 5.5 shows the typical distribution of vertical stress across the contact between the coated particles. The stress contours are obtained for the case of $h = \frac{1}{50}R$ and $E_{coating} = 10^4 N/m^2$. It can be seen that the stress distribution is discontinuous across the boundary between the coating and the particle which further proves that the stress behaviour for coated/layered systems is complex, and not easily solved for, [68]. Furthermore, the computational time for this kind of contact problem is very extensive and took an average of 6 days CPU time to complete the simulation for each case.

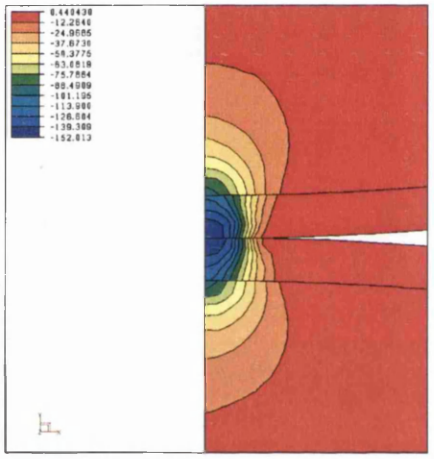

a) $t=0.05s$

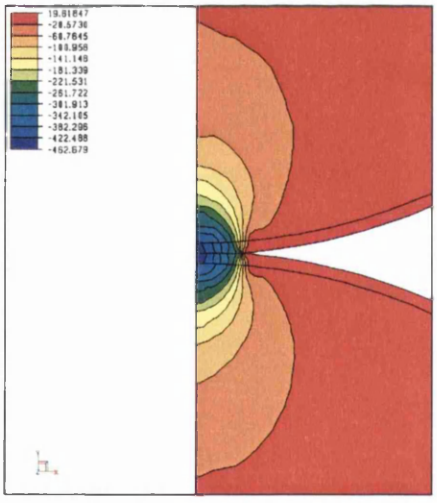

b) $t=0.5s$

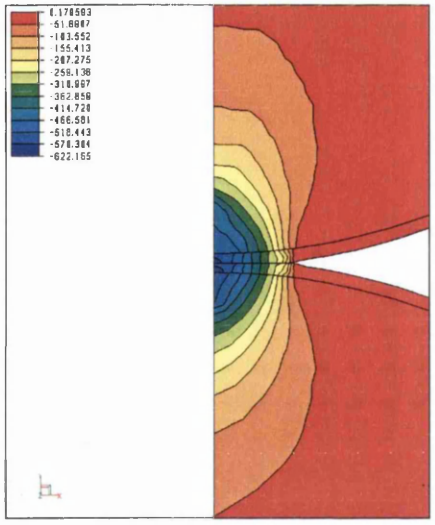

c) $t=1.0s$, when fully loaded to the maximum displacement of $0.00001m$.

Figure 5.5: Typical distribution of vertical stress across the contact.

When the particles are fully unloaded to zero pressure, a permanent deformation in the coating is observed with the contact width of the coating representing the residual contact radius. The amount of penetration at this point is the residual penetration. If the unloading process continues, the residual contact radius remains constant, and a gap appears between the particles, representing total detachment due to the absence of adhesion at the contact. This can be seen in the following figure.

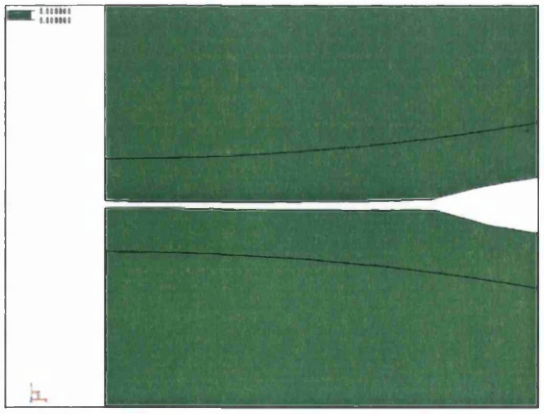

Figure 5.6: Permanent deformation in the coating after unloading.

Graphs of force-penetration relation for the various cases obtained from the finite element analysis are shown in Figure 5.7 and Figure 5.8.

a)

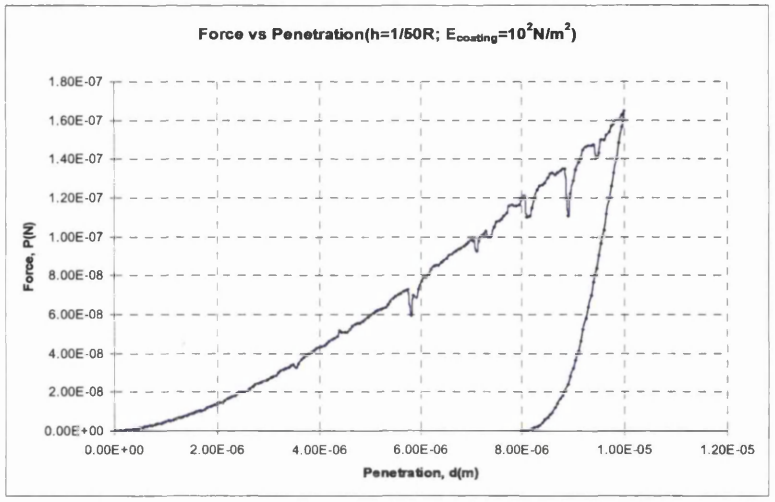

b)

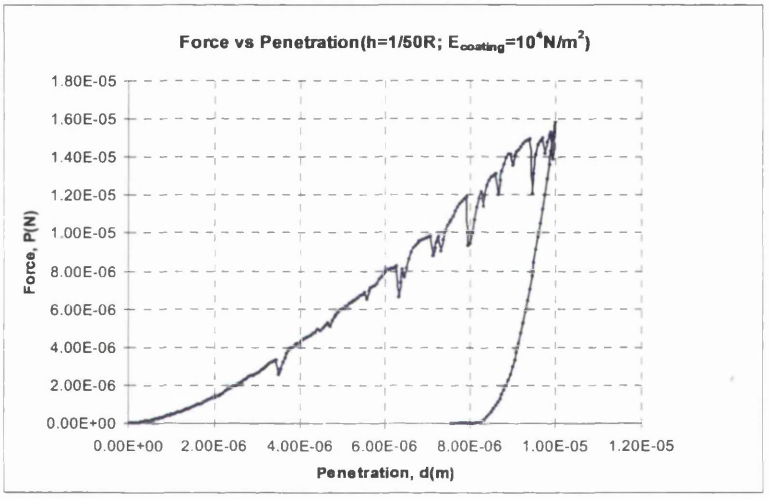

c)

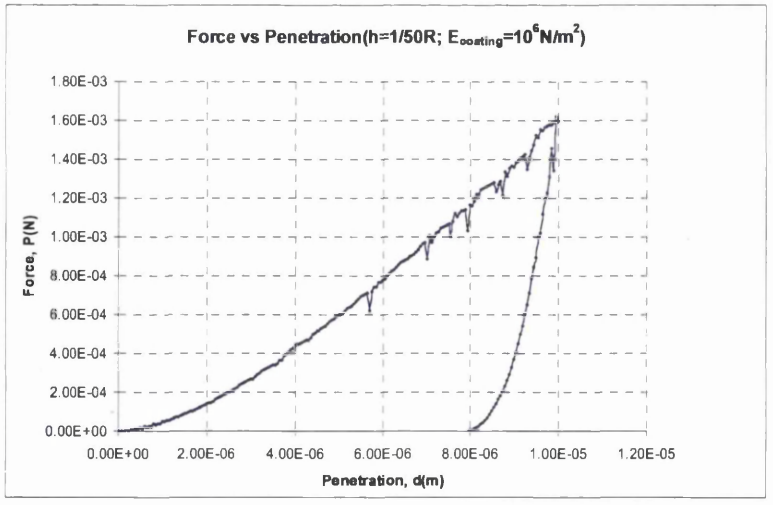

Figure 5.7: Force-penetration relation for $h = \frac{1}{50} R$.

a)

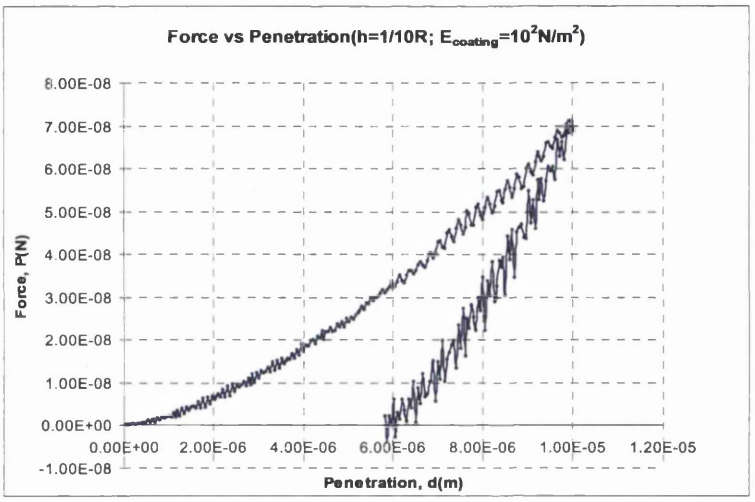

b)

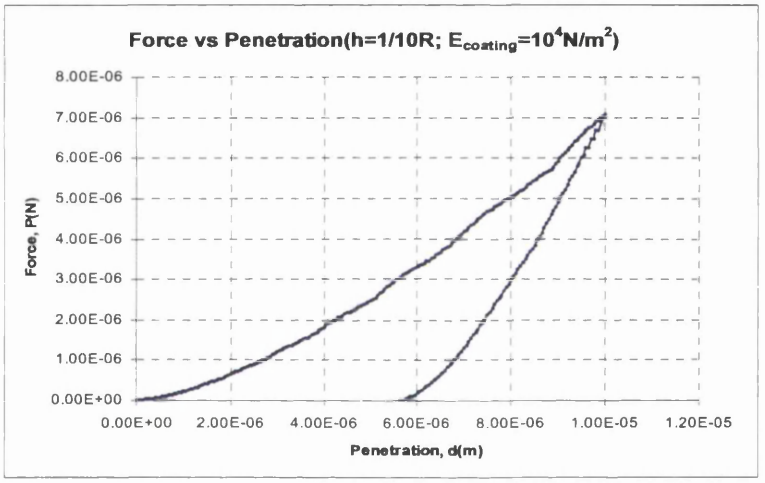

c)

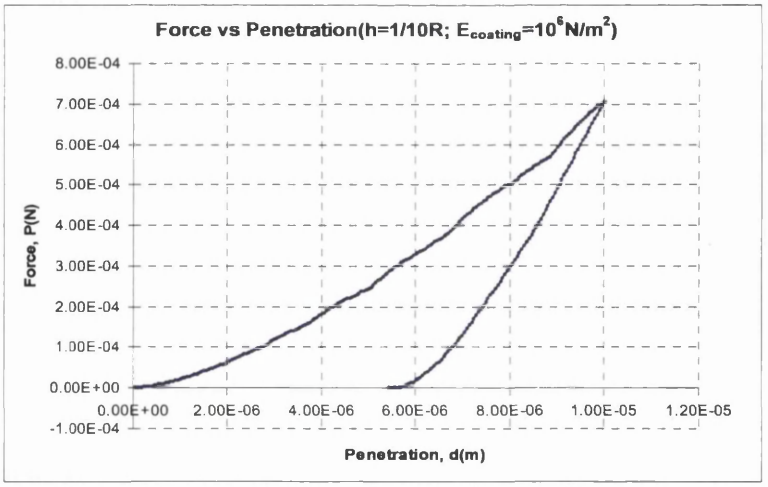

Figure 5.8: Force-penetration relation for $h = \frac{1}{10}R$.

It can be seen from Figure 5.7 and Figure 5.8 that, for a particular coating material, the contact force produced is higher when the thickness of the coating decreases. When the coating is softer, the contact force produced is also smaller for a particular coating thickness. The difference between the maximum penetration and the residual penetration, after unloading, ($d_{\max} - d_{res}$), are the same for a particular coating thickness regardless of the coating material. Furthermore, a thinner coating was found to produce greater permanent deformation.

Some oscillations in the force values were observed along the loading path as shown in Figure 5.7. This was due to the change of boundary after re-meshing took place. The force values, however, return to the loading path after a few iterations. Also, the graph for $E_{coating} = 10^2 N/m^2$, when $h = \frac{1}{10}R$, in Figure 5.8(a) was found to oscillate more as compared to the same material used for $h = \frac{1}{50}R$ in Figure 5.7(a). This is anticipated to be due to the instability produced in the soft material when subjected to loading, whereas the substrate has a 'support' effect against the shock produced from loading when the coating is thinner. It is also worth mentioning that by slowing down the rate of load application and load reversal (i.e. using a longer time), the problems of oscillation can be reduced. Unfortunately, as explicit analysis is used here, and the time step size is determined by the critical time step which is evaluated based on the smallest element size, an enormous simulation time is needed to complete the analysis. However, the graph in Figure 5.8(a) does follow the general trend as produced by other coating material and thickness.

5.3 Contact Law for Coated Particles

By looking at the loading trend of the coated particles obtained from the FE simulations, the P-d relation for the models was found to follow the form derived by the Hertz theory, i.e. $P \propto d^{\frac{3}{2}}$. Similar to the method used in deriving the contact law for elastic coating in Chapter 4, the Hertz model is modified using a material factor that measures the ratio between the coating's material properties and the particle's material properties. By doing

so, the well known and straight forward Hertz law can be transformed into an equation that takes into account the influence of the coating material on the whole system. Furthermore, the application of material factor on the equation also allows the determination of other parameters to be related to the coating thickness only, which simplifies the derivation process. Therefore, in order to further transform the 'Hertz like' equation to the one that is suitable for approximating the contact between coated particles, the modified equation can be further modified by multiplication with factor that is determined from the thickness of coating. This enables the resulting equation to approximate the response by taking into account the influence of both the material and the thickness of the coating.

It is also worth mentioning that Hertz model is chosen for the modification as it is developed based on the contact between elastic solids (which is what is used for the underlying particles in this research). Also, the thin coating that is being analysed in this research makes it possible to utilise the Hertz model as it is expected that the solid particles underneath the thin coating will react to the load application to a certain extend. Hence, the modified Hertz model will be suitable for the coated system, as long as the coating thickness remains a small value.

5.3.1 Elastic-Plastic Loading

As the yielding of the materials occurs relatively early during the compression process, the formulation of the relation considers that the material has already yielded during the load application. According to Hertz theory, the force, P, and penetration, d, relation is written as:

$$P = \frac{4}{3} E^* R^{*\frac{1}{2}} d^{\frac{3}{2}} \tag{5.1}$$

where E^* and R^* are the effective modulus and relative curvature respectively.
For the case where the particles in contact are of similar size and are covered with a thin coating, the material properties used for the relation in equation (5.1) are,

$$E_p^* = \left[\frac{\left(1 - \nu_p^2\right)}{E_p} \right]^{-1} \tag{5.2}$$

and the relative curvature is

$$R^* = R_p \tag{5.3}$$

where the subscript p represents the values associated with the particle.

It is worth mentioning that the values in (5.2) and (5.3) are not averaged between the two particles because they are not in direct contact and thus only the values from one side of the contact is adopted.

By substituting the values from (5.2) and (5.3) into equation (5.1), the relation becomes

$$P = \frac{4}{3}\frac{E_p R_p^{\frac{1}{2}}}{\left(1-\nu_p^2\right)} d^{\frac{3}{2}} \tag{5.4}$$

Having modified the Hertz formula with the values for E^* and R^*, equation (5.4) is then scaled with a factored ratio between the material properties of the coating and the material properties of the particle to give

$$P_{loading} = \xi m \frac{4}{3}\frac{E_p R_p^{\frac{1}{2}}}{\left(1-\nu_p^2\right)} d^{\frac{3}{2}} \tag{5.5}$$

where ξ is a factor to be determined empirically and the material ratio m has the form

$$\begin{aligned} m &= \frac{E_c^*}{E_p^*} \\ &= \frac{E_c\left(1-\nu_p^2\right)}{E_p\left(1-\nu_c^2\right)} \end{aligned} \tag{5.6}$$

where E_c^* and E_p^* are the material properties for the coating and particle respectively. The reason for applying a material ratio in the equation is to modify the contact law to only dependent on the coating thickness so that other parameters can be determined without considering the material properties of both the coating and the particle. However, the use of this ratio is only for the contact between coated particles of similar size, coating thickness and material properties, as can be seen in the works in this chapter and Chapter 6. The use of material ratio for the contact of dissimilar particles will have to be testified beforehand, and is not the subject of this thesis.

By comparing the values obtained in (5.5) to the finite element results, the value of ξ is found to be dependent on $\frac{h}{R}$, and is not affected by the material properties. When

$\frac{h}{R}$ increases, the value of ξ decreases. The reason for this could be that the influence from the underlying hard particle on the compression of the coated particles reduced when the coating thickness increases. Hence, more soft material responds to the compression giving a lower contact force.

From the finite element results, it was found that the values of ξ equal to *1.13* and *0.476* fit the loading curve closely for $\frac{h}{R} = 0.02$ and 0.1 respectively. By assuming a linear relation between ξ and $\frac{h}{R}$, the following equation was obtained for ξ:

$$\xi = -8.175\frac{h}{R} + 1.2935 \tag{5.7}$$

A graph of the ξ-$\frac{h}{R}$ relation is plotted in the following figure.

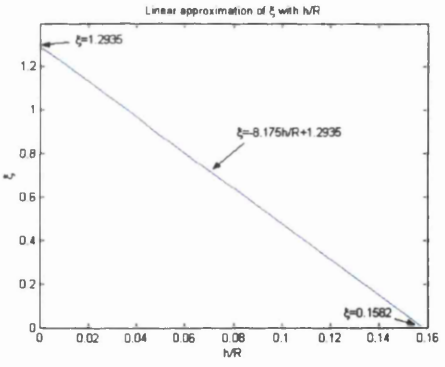

Figure 5.9: Graph of ξ-$\frac{h}{R}$ relation.

It can be seen from Figure 5.9 that when $\frac{h}{R}$=0, ξ=1.2935; and when $\frac{h}{R}$=0.1582, ξ=0, which are not realistic. As $h \to 0$, the situation is similar to the Hertz condition and the value for ξ should approach $\frac{1}{2\sqrt{2}}\frac{1}{m}$ for similar particles in contact. When the coating is relatively thick, for which the definition of 'thick' is a subjective matter

($\frac{h}{R} = 0.1$ is treated as thick in this study), the value for ξ is uncertain, and the coating should be treated using other approach, depending on the condition.

The following figure shows the values of ξ around the origin of the $\frac{h}{R}$ axis for different values of m. When $\frac{h}{R}$ is close to zero, the value for ξ is uncertain for a particular $\frac{h}{R}$, and varies with different values of m. Hence, the linear approximation does not guarantee an accurate approximation for the compression of the coated particles when the coatings are close to this region.

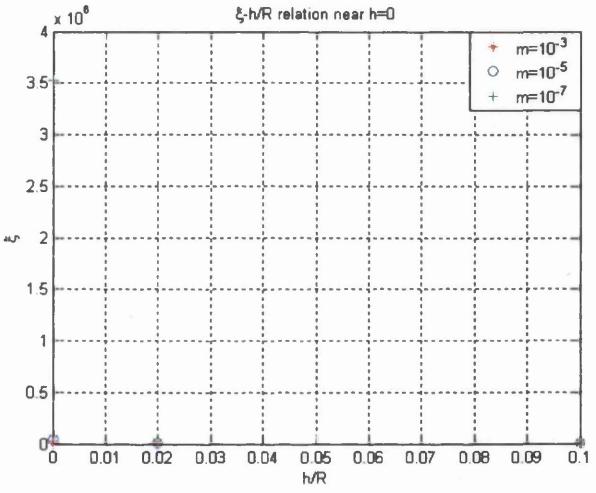

Figure 5.10: Graph of ξ - $\frac{h}{R}$ relation considering the limits.

However, as the range of coating thickness in this research is well away from the range of uncertainty, a linear variation of ξ with respect to $\frac{h}{R}$ is sufficient for the analysis.

5.3.2 Unloading Process

The determination of residual penetration:

From the finite element results, it can be seen in the unloading stage that the difference between the maximum penetration and the residual penetration after unloading,

($d_{\max} - d_{res}$), increases with increasing $\frac{h}{R}$, regardless of the coating properties. It was found that $d_{\max} - d_{res}$=0.0000018 for $\frac{h}{R}$=0.02, and $d_{\max} - d_{res}$=0.0000044 for $\frac{h}{R}$=0.1. Hence, by assuming a linear relation between ($d_{\max} - d_{res}$) and $\frac{h}{R}$, a linear equation can be formulated as

$$d_{\max} - d_{res} = 3.25 \times 10^{-5} \frac{h}{R} + 1.15 \times 10^{-6} \tag{5.8}$$

The ($d_{\max} - d_{res}$) and $\frac{h}{R}$ relation can be plotted as shown in the following figure.

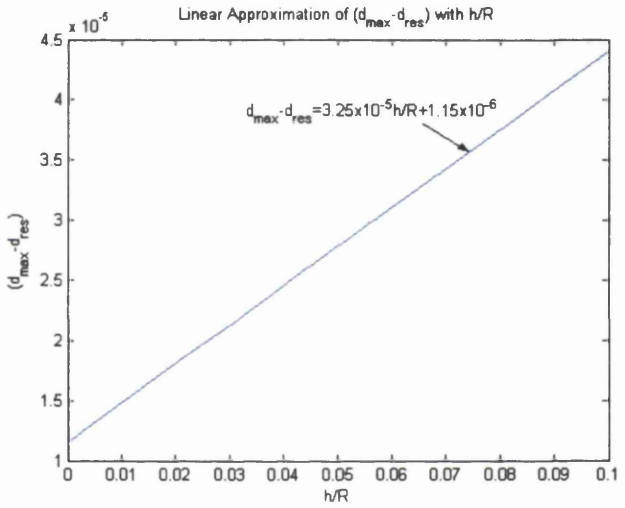

Figure 5.11: Graph showing the relation between ($d_{\max} - d_{res}$) and $\frac{h}{R}$.

The determination of unloading factor η*:*

Having found the residual penetration d_{res}, equation (5.4) is once again multiplied by the material ratio m as determined in (5.6). A factor η is then applied to the equation to represent the unloading path for the decompression of the coated particles.

The un-factored maximum unloading force, $P_{unloading}$, in the beginning of the unloading process (at $d_{\max}$) is calculated as

$$P_{unloading}(d_{\max}) = m\frac{4}{3}\frac{E_p R_p^{\frac{1}{2}}}{(1-\nu_p^2)}(d_{\max} - d_{res})^{\frac{3}{2}} \tag{5.9}$$

On the other hand, the maximum loading force, $P_{loading}$, at the end of the loading stage (at $d_{\max}$) is written as

$$P_{loading}(d_{\max}) = m\xi\frac{4}{3}\frac{E_p R_p^{\frac{1}{2}}}{(1-\nu_p^2)}(d_{\max})^{\frac{3}{2}} \tag{5.10}$$

Therefore, the factor η can be obtained from the ratio between the two maximum forces in (5.9) and (5.10) as

$$\begin{aligned}\eta &= \frac{P_{loading}(d_{\max})}{P_{unloading}(d_{\max})} \\ &= \frac{m\xi\frac{4}{3}\frac{E_p R_p^{\frac{1}{2}}}{(1-\nu_p^2)}(d_{\max})^{\frac{3}{2}}}{m\frac{4}{3}\frac{E_p R_p^{\frac{1}{2}}}{(1-\nu_p^2)}(d_{\max} - d_{res})^{\frac{3}{2}}} \\ &= \xi\left(\frac{d_{\max}}{d_{\max} - d_{res}}\right)^{\frac{3}{2}}\end{aligned} \tag{5.11}$$

As ξ and $(d_{\max} - d_{res})$ are only dependent on $\frac{h}{R}$, the value of η is also dependent on $\frac{h}{R}$, and only changes with $d_{\max}$ at a particular $\frac{h}{R}$. Therefore, if $d_{\max}$ is varied and the other parameter are constants, the factor η can also be determined using the ratio

$$\begin{aligned}\frac{\eta_{new}}{\eta_{old}} &= \left(\frac{d_{\max(new)}}{d_{\max(old)}}\right)^{\frac{3}{2}} \\ \eta_{new} &= \eta_{old}\left(\frac{d_{\max(new)}}{d_{\max(old)}}\right)^{\frac{3}{2}}\end{aligned} \tag{5.12}$$

For example, when $d_{\max}$=*0.00001m*, η=*14.8*. Hence, the value for η when $d_{\max}$=*0.000005m* can be calculated as

$$\eta_{new} = \eta_{old}\left(\frac{d_{\max(new)}}{d_{\max(old)}}\right)^{\frac{3}{2}}$$

$$= 14.8\left(\frac{0.000005}{0.00001}\right)^{\frac{3}{2}}$$

$$= 5.23$$

Also, from observation, as $\left(\frac{d_{\max}}{d_{\max} - d_{res}}\right)^{\frac{3}{2}}$ is greater than 1, the value of η is also greater than ξ during the unloading process.

Having found the value of η for each unloading case, the unloading force can be determined as

$$P_{unloading} = \eta m \frac{4}{3}\frac{E_p R_p^{\frac{1}{2}}}{\left(1-\nu_p^2\right)}\left(d - d_{res}\right)^{\frac{3}{2}} \tag{5.13}$$

The use of the material ratio m in the contact law for the approximation of the force-penetration relation during both the loading and unloading processes is useful in determining other parameters, such as ξ and η. The values of ξ and η are uncoupled from the material properties, and hence can be evaluated easily based on the relation with coating thickness $\frac{h}{R}$.

5.4 Comparison between the P-d Relation and the Finite Element Results

To assess the accuracy of the contact law (P-d relation) formulated in section 5.3, the finite element results obtained in section 5.2 are plotted in companion with the contact law. These are shown in the following figures.

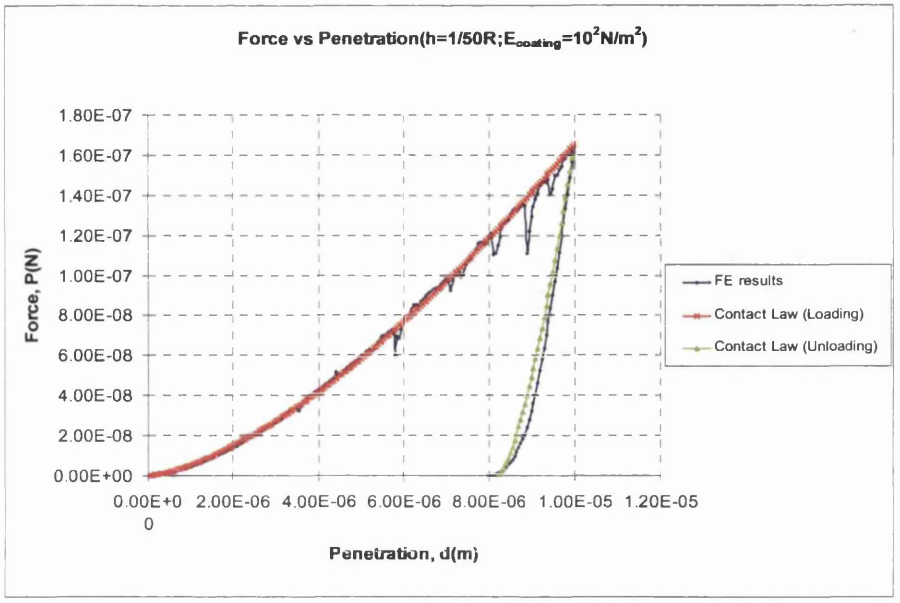
Force vs Penetration(h=1/50R;E$_{coating}$=10^{2}N/m^2)
Force, P(N)
1.80E-07
1.60E-07
1.40E-07
1.20E-07
1.00E-07
8.00E-08
6.00E-08
4.00E-08
2.00E-08
0.00E+00
0.00E+0 2.00E-06 4.00E-06 6.00E-06 8.00E-06 1.00E-05 1.20E-05
0
Penetration, d(m)
FE results
Contact Law (Loading)
Contact Law (Unloading)

a)

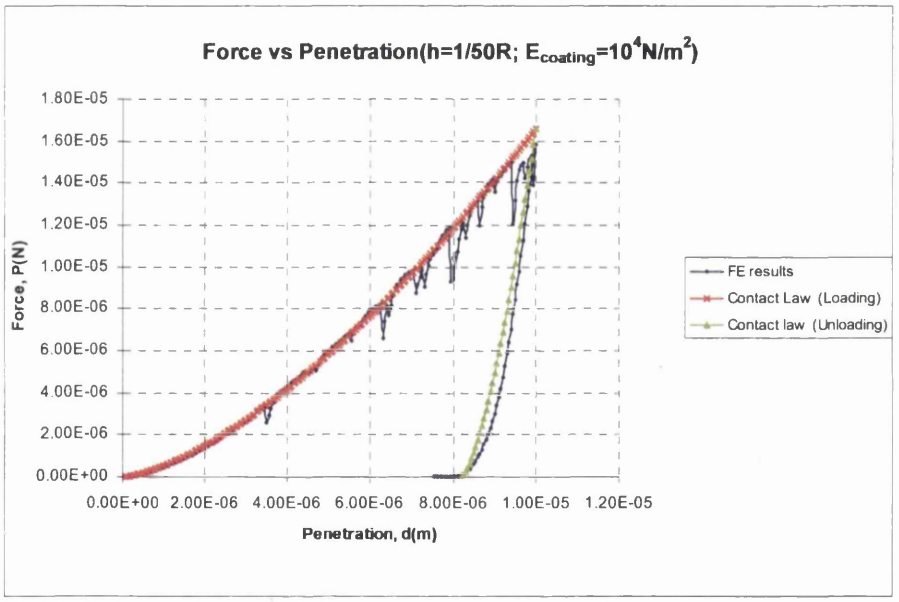
Force vs Penetration(h=1/50R; E$_{coating}$=10^{4}N/m^2)
Force, P(N)
1.80E-05
1.60E-05
1.40E-05
1.20E-05
1.00E-05
8.00E-06
6.00E-06
4.00E-06
2.00E-06
0.00E+00
0.00E+00 2.00E-06 4.00E-06 6.00E-06 8.00E-06 1.00E-05 1.20E-05
Penetration, d(m)
FE results
Contact Law (Loading)
Contact law (Unloading)

b)

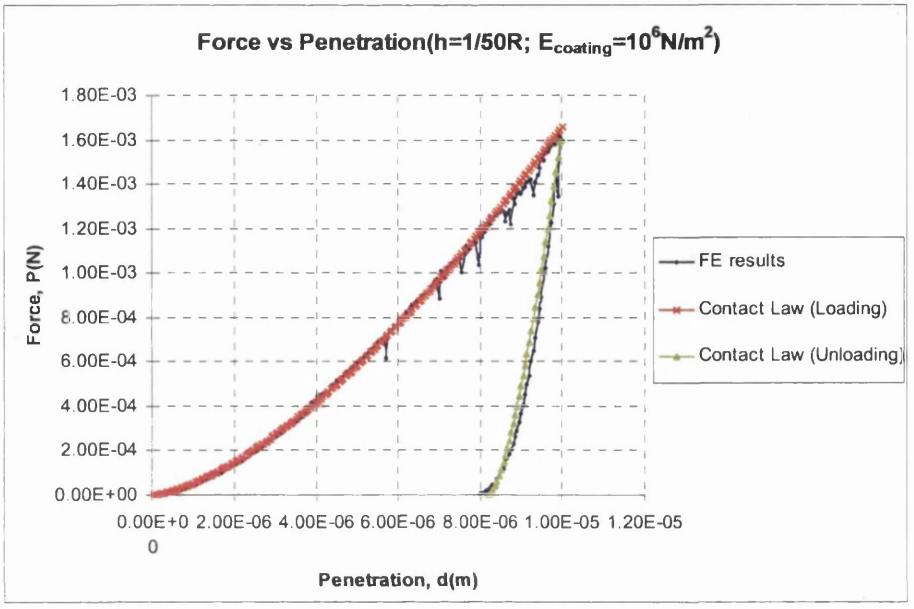

c)

Figure 5.12: Comparison between the contact law and the finite element results for $h = \frac{1}{50} R$.

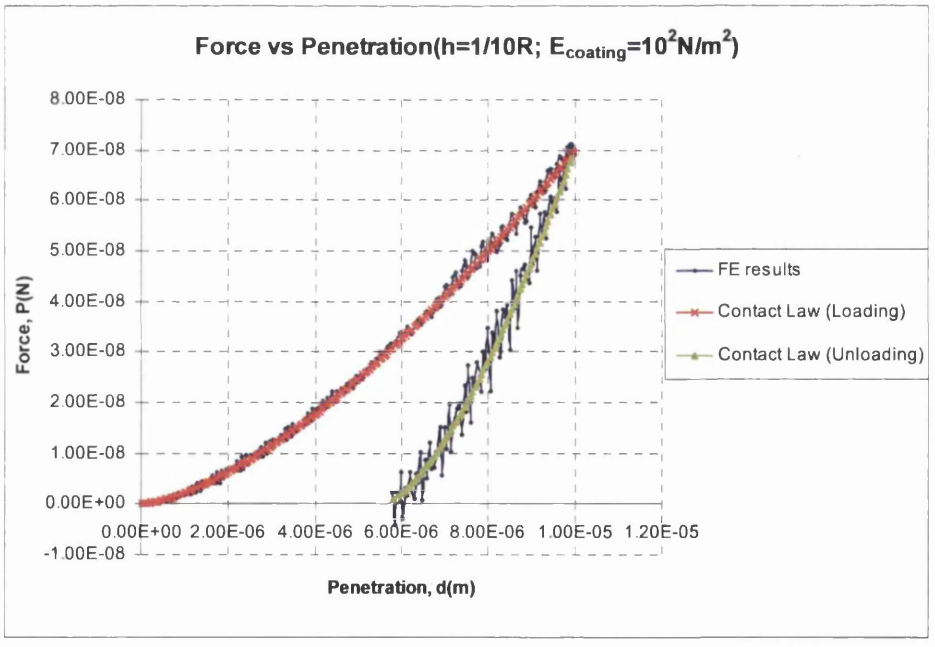

a)

b)

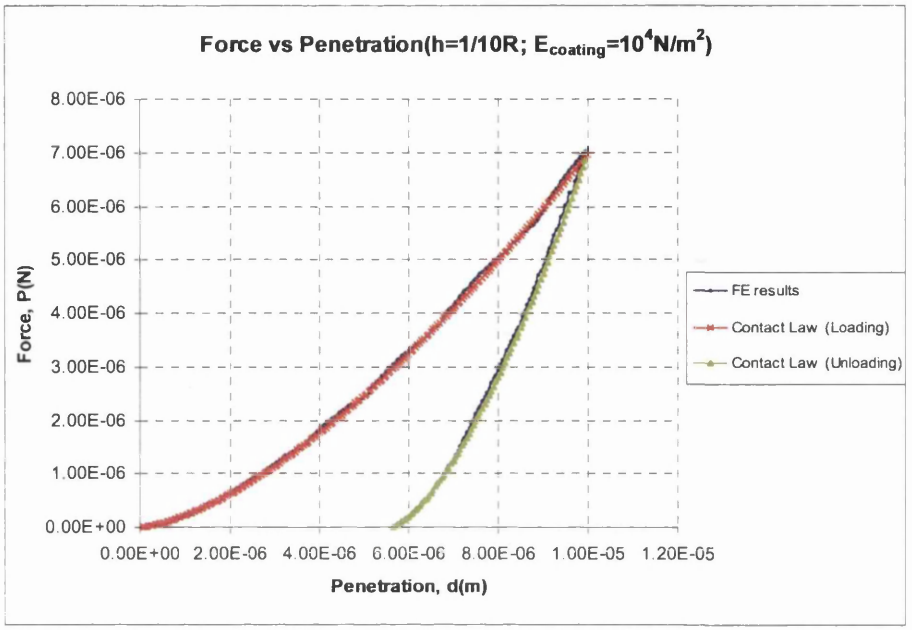

c)

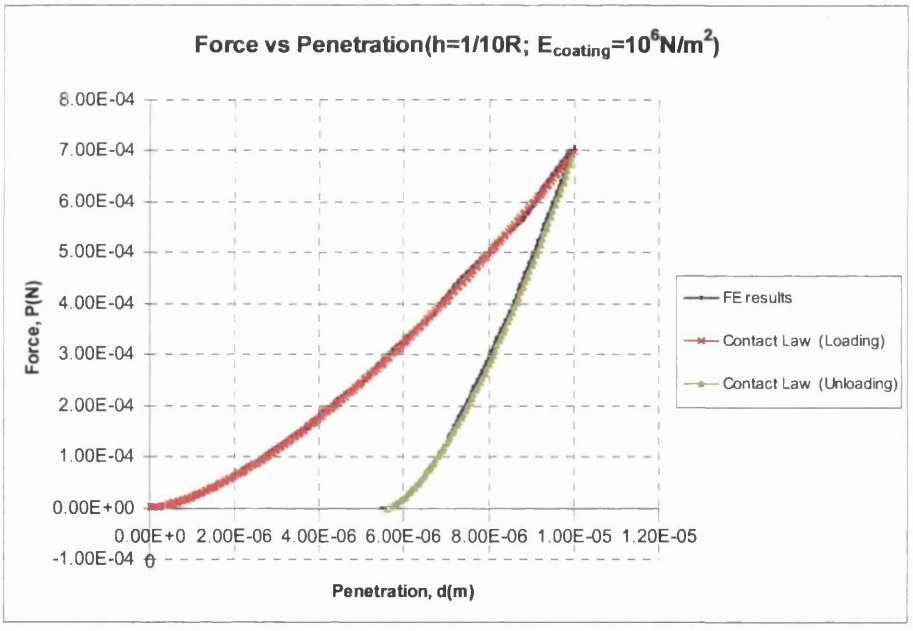

Figure 5.13: Comparison between the contact law and the finite element results for $h = \frac{1}{10}R$.

To have a further check on the accuracy of the contact law, an analysis was carried out by loading the coated particles up to half of the original maximum penetration, i.e. $d_{\max} = 0.000005m$, and unloading to zero force. A coating thickness of

$h = \frac{1}{50}R$ and a Young's modulus of $10^6 N/m^2$ were used is this case. A graph comparing the forces approximated by the contact law and the finite elements results is shown in the following figure.

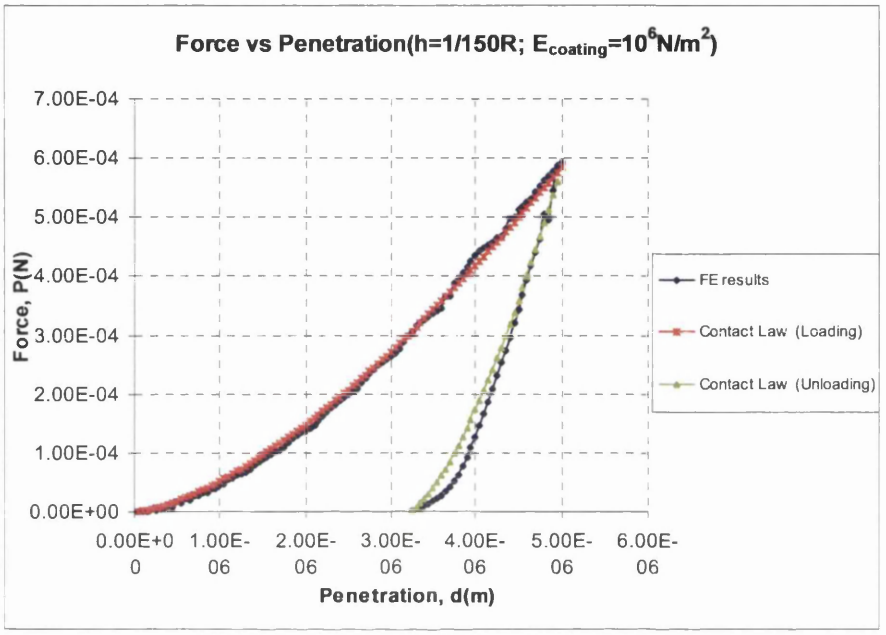

Figure 5.14: Comparison between the contact law and the finite element results for $h = \frac{1}{50}R$ when $d_{max} = 0.000005m$.

By comparing the forces predicted by the contact law with the finite element analysis results, it can be seen that the contact law is able to approximate the force-penetration relation very well. Although there is a slight deviation in the unloading curve for the case shown in Figure 5.14, the contact law is, however, able to predict the residual penetration d_{res} at the end of the unloading process. Furthermore, the time spent on evaluating the forces, using this simple contact law, is only a tiny fraction of the time spent in carrying out a finite element analysis.

Chapter 6

Axi-symmetric Contact of Adhesive Elastic-Plastic Layer

In the previous chapter, the compressed coated particles experience a total detachment at the contact when they are unloaded to zero force. In this chapter, the influence of adhesion is included at the contact, and the particles are assumed to adhere together when they are unloaded to zero force, so that a state of tension was created if the unloading process continues. A numerical adhesive model, similar to a notch extension as mentioned later in this chapter, is set up to analyse this behaviour. Also, a contact law which included adhesion at the contact is formulated, based on observations from the analyses. Finally, the accuracy of the contact law is assessed by comparison with the finite element results.

6.1 Existing Work on Adhesive Contact

As mentioned earlier in Chapter 1, the force that exists between two surfaces when brought into close contact is termed the adhesion force. This force is related to the work of adhesion, which is defined as the free energy change required to separate unit areas of the two surfaces from contact to infinity in a vacuum, and can be measured from experiments.

Many experiments have been carried out to derive theories for modelling contact adhesion. The most popular theories are the Johnson-Kendall-Roberts theory (JKR) and the Deryaguin-Müller-Toporov theory (DMT), which are modified from Hertz theory, which does not consider the attractive forces at the contact under external applied loads [3,16]. However, these two theories are in contradiction, and are in fact two extreme situations, as shown later by Maugis's 'Dugdale model' that is able to model the transition between these models [3]. Johnson and Greenwood [69], on the other hand, have also constructed an adhesion map which shows the transition between the various models, and this is shown in the following figure. The adhesion map is constructed using Maugis-Dugdale theory that assumed the surface traction is built up from two terms:

i) Hertz pressure within contact radius of a;

ii) Adhesive (Dugdale) stress that has the form:

$$p_a = \begin{cases} -(\sigma_0/\pi)\cos^{-1}\left\{\dfrac{2a^2 - c^2 - r^2}{c^2 - r^2}\right\}, & r \le a \\ -\sigma_0, & a \le r \le c \end{cases} \tag{6.1}$$

The distribution of the surface traction based on this theory is shown in Figure 6.2.

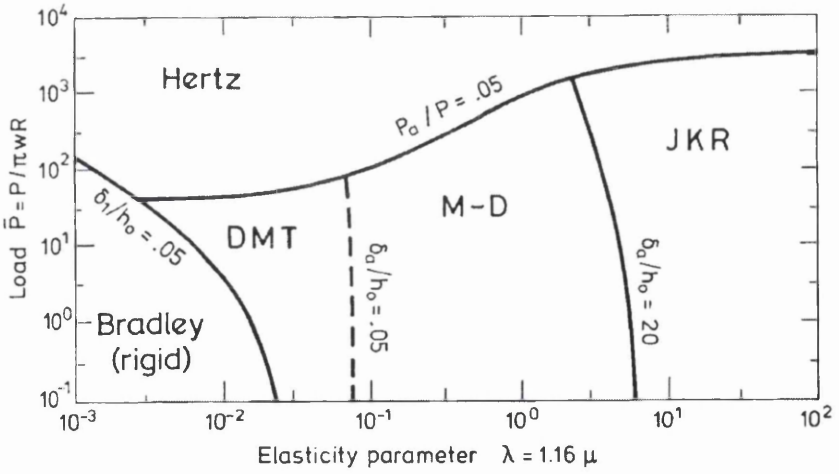

Figure 6.1: Adhesion map (*obtained from [69]*).

Referring to the above graph:

$$P_a = \frac{8\pi wR}{3}\left[\frac{1}{4}\left(\frac{z}{z_0}\right)^{-8} - \left(\frac{z}{z_0}\right)^{-2}\right] \tag{6.2}$$

is the surface force, R is the effective radius of the spheres, z is the separation between the surfaces, z_0 is the equilibrium separation, and w is the work of adhesion.

Also,
$$\mu \equiv \left(\frac{Rw^2}{E^{*2}z_0^3}\right)^{1/3} \tag{6.3}$$

is the ratio of the elastic displacement of the surfaces at the point of separation to the effective range of the surface forces characterised by z_0, and E^* is the combined elastic modulus of the spheres. Hence, as it is related to the Young's modulus of the particles, the smaller the value it is, the stiffer the material is, as can be seen from the equation above.

$$P = P_1 + P_a \tag{6.4}$$

is the net contact force due to Hertz P_1 and adhesion P_a.

$$\begin{aligned}\overline{P} &= \overline{P_1} + \overline{P_a} \\ &= \frac{P}{\pi wR}\end{aligned} \tag{6.5}$$

is the non-dimensional net contact force, which is also the ratio of the applied load to the adhesive force.

$$\delta_1 = \frac{a^2}{R} \tag{6.6}$$

is the elastic compression due to Hertz pressure.

$$\delta_a = -\left(\frac{2\sigma_0}{E^*}\right)\sqrt{c^2 - a^2} \tag{6.7}$$

is the compression due to adhesive force. σ_0 is the intensity of the adhesive force at the extended contact radius c as shown in Figure 6.2, and h_0 is the separation between the surfaces at c.

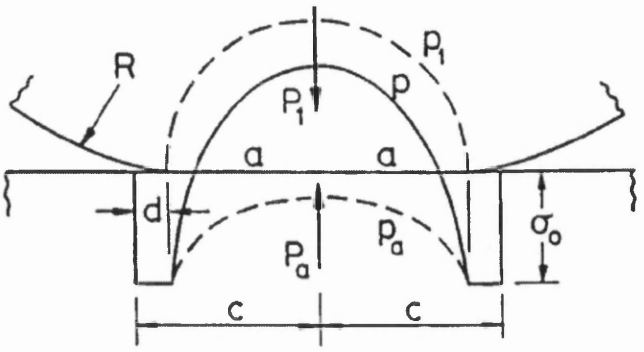

Figure 6.2: The distribution of surface traction according to Maugis-Dugdale theory. (*obtained from [69]*).

As mentioned in Section 1.5 of Chapter 1, JKR model is ,pre suited for large and soft spheres, and the region for this model lies in the higher end of the λ axis on the adhesion map. The elastic deformation caused by the adhesive force is huge compared to the range of action h_0, and hence the boundary for JKR zone can be drawn by writing $\delta_a / h_0 > \eta$, where η much greater than 1 [69]. For the boundary shown in the adhesion map, $\eta = 20$ is used.

The DMT theory, on the other hand, works well for small and stiff particles, and hence the region for this model lies in the lower end of λ axis on the adhesion map. The elastic deformation due to surface force is small compared to the range of action, and the boundary for this model can be drawn by writing $\delta_a / h_0 < \eta$, where η much smaller than 1 [69]. For the adhesion map shown, $\eta = 0.05$ is adopted.

It can be seen that a broken line is used to draw up the boundary between DMT zone and MD zone. This is because DMT theory assumed that the elastic deformation is entirely due to Hertz pressure within the contact, and adhesive force is confined to the outer zone, i.e. $r > a$. However, Maugis' analysis showed that adhesive force also present within the contact, and hence a correction to DMT model was made that becomes a 'transition' model between DMT and JKR model [69].

When solids of high stiffness (i.e. rigid solids) are in contact, the elastic deformation at sufficiently light load becomes small compared to the range of surface

forces [69]. The contact condition will have to satisfy not only $\delta_a/h_0 < \eta$, but also $\delta_1/h_0 < \xi$, where δ_1 is the elastic compression due to Hertz pressure, and ξ is much smaller than 1 [69]. For the adhesion map shown, $\xi = 0.05$ is used.

When a compressive load is sufficiently high, the adhesive force can be neglected, and Hertz theory becomes applicable [69]. This makes the Hertz zone lies in the upper part of the $\overline{P}$ axis, where the applied force is relatively huge compared to the adhesive force. The boundary for this zone can be drawn by writing $P_a/P < \xi$, where ξ is much less than 1 [69]. For the adhesion map shown, $\xi = 0.05$ is used.

It is worth mentioning that the adhesion map shown is referred to the contact between perfectly elastic spheres only. Also, the JKR theory is found to work well for elastomeric materials (due to the low modulus of the materials), but found to be inconsistent with the layered structured studied using the surface force apparatus in the experiments[69].

Pollock et al [70] have also carried out experiments to measure the adhesion between a curved metal and a flat surface (single-asperity experiments), and performed the calculation of the work of adhesion based on these results [71]. In the calculation, plastic deformation was assumed to take place at the instant of contact (even at zero applied load), and hence the geometry of the deformed but unstressed surface is assumed to look like the one shown in Figure 6.3 after initial contact. The initial radius of curvature r is modified to r_f that gives the surface radius of a_f.

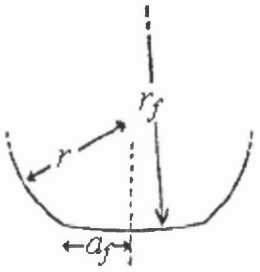

Figure 6.3: The geometry of the modified surface (*obtained from [71]*).

The geometry of the contact between the two surfaces, under an applied load P_0, is then assumed to be of the form shown in the following figure.

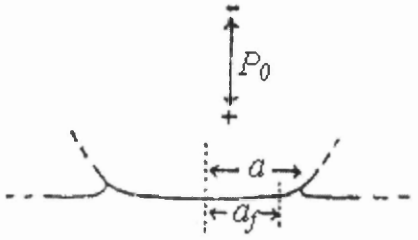

Figure 6.4: The contact between surfaces under applied load P_0 (*obtained from [71]*).

When a negative force is applied, i.e. when the surfaces are pulled apart, there are four possible modes of separation that will occur at the contact, and these are outlined below:

I) The behaviour at the contact corresponds to a ductile extension of a deep notch. The yield stress applied during extension is assumed to be the same as the one applied during compression. The 'notch extension force' P_n is given by

$$-P_n = P_f \tag{6.8}$$

where $P_f = \dfrac{Ka_f^3}{r_f}$ is the apparent plastic load that produces a plastic contact radius a_f in the absence of surface energy, and $K = \dfrac{4}{3}\left(\dfrac{1-\nu_1^2}{E_1} + \dfrac{1-\nu_2^2}{E_2}\right)^{-1}$ is an elastic constant for materials 1 and 2.

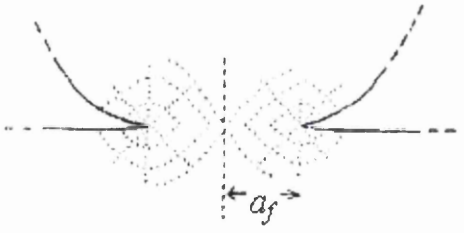

Figure 6.5: Deep notch extension at $a = a_f$ (*obtained from [71]*).

II) If failure occurs within the bulk of one of the materials, then ductile extension will occur when the load reaches P_b.

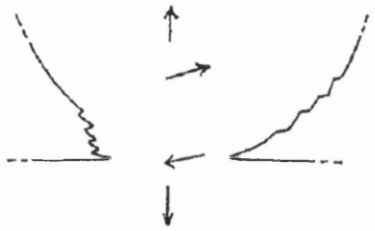

Figure 6.6: Ductile failure within the bulk of one material (*obtained from [71]*).

III) Brittle failure at the contact $a < a_f$ with a force given by

$$-P_c = 1.5\pi\Delta\gamma r_f \tag{6.9}$$

where $\Delta\gamma$ is the work of adhesion per unit area.

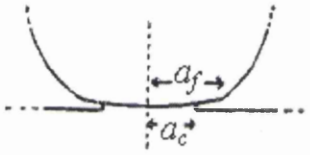

Figure 6.7: Brittle separation at $a < a_f$ (*obtained from [71]*).

IV) Brittle failure at the contact $a = a_f$ with a force given by

$$-P_m = 2\left(1.5\pi\Delta\gamma K a_f^3\right)^{1/2} - P_f \tag{6.10}$$

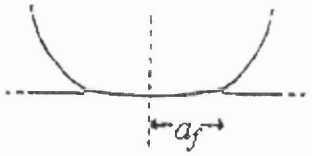

Figure 6.8: Brittle separation at $a = a_f$ (*obtained from [71]*).

As the experiments carried out by Pollock [71] only involved the separation at the interface, separation mode (ii) was not considered in the calculation of the work of adhesion. The measured adhesion force ΔP, which is also the greatest negative value of the applied load P_0 in the experiment, is hence assumed to be

$$|\Delta P| = |P_n| = |P_c| = |P_m| \quad \text{if } P_f = |F|_{P_0=0} \tag{6.11}$$

where F is the compressive reaction force between the surfaces which is equal and opposite to the combined applied load P_0 and the force of attraction F_s, i.e.

$$0 = -F + P_0 + F_s \tag{6.12}$$

and at zero load,

$$[F]_{P_0=0} = [F_s]_{P_0=0} = \left(1.5\pi\Delta\gamma K a_f^3\right)^{1/2} = P_f \tag{6.13}$$

Pollock [71] concluded that $|P_n|$, $|P_c|$ and $|P_m|$ are each roughly equal to the force of adhesion:

$$\begin{aligned}\left(1.5\pi\Delta\gamma K a_f^3\right)^{1/2} = [F]_{P_0=0} \approx P_f = \frac{K a_f^3}{r_f} = |P_n| \approx |P_m| \\ \approx \Delta P = |P_c| = 1.5\pi\Delta\gamma r_f\end{aligned} \tag{6.14}$$

Mesarovic and Johnson [72], on the other hand, examined the process of decohesion of two adhering elastic-plastic particles that have been loaded beyond the elastic limit. In the analysis, the pressure distribution at the beginning of the unloading process was assumed to be uniform, and the unloading process is assumed to be elastic. The solution to the adhesive contact was then obtained firstly by deriving the contact pressure in the absence of adhesion, and secondly by adding the appropriate adhesive tension that must satisfy the condition that the normal displacement in the contact area is uniform, so that the net force acting at the contact will be

$$P = P_1 + P_2 \tag{6.15}$$

where P_1 is the force without adhesion, and P_2 is the force caused by adhesion.

In the absence of adhesion, the variation of contact radius a with load P_1 was found based on the method of rigid punch decomposition to give

$$\frac{P_1}{P_0} = \frac{P_1}{\pi a_0^2 p_0^2} = \frac{2}{\pi}\left[\arcsin\left(\frac{a}{a_0}\right) - \left(\frac{a}{a_0}\right)\sqrt{1-\left(\frac{a}{a_0}\right)^2}\right] \tag{6.16}$$

where P_0 is the initial load during the unloading process.

The adhesive traction at the contact was then found in two ways. The first method assumed a singular traction distribution, where the adhesive traction is equal to

$$p_2(r,a) = -\sqrt{\frac{a}{\pi}}\frac{K}{\sqrt{a^2 - r^2}} \tag{6.17}$$

which correspond to the adhesive load of

$$P_2 = 2\kappa\pi^{1/2}a^{3/2} \tag{6.18}$$

where $\kappa = \sqrt{2\Delta\gamma E^*}$ is the stress intensity factor.

The second method used in determining the adhesive traction is the cohesive zone solution, where the surfaces are assumed to separate slightly around the ring of contact $(a < r < c)$. A constant adhesive stress is assumed to act in this region as shown in Figure 6.9.

The adhesive traction is assumed to have the form

$$\sigma = \begin{cases} \sigma_0 & \text{for } \delta \le \delta_0 \\ 0 & \text{for } \delta > \delta_0 \end{cases} \tag{6.19}$$

and the adhesive traction over the whole contact area is given by

$$p_2(r,a,c) = \begin{cases} -\dfrac{2\sigma_0}{\pi}\arctan\dfrac{\sqrt{c^2 - r^2}}{\sqrt{a^2 - r^2}}, & r < a \\ -\sigma_0, & a < r \le c \end{cases} \tag{6.20}$$

which gives the adhesive force of

$$P_2 = \pi\sigma_0\left\{ca_0\arccos\frac{a}{c} + a\sqrt{c^2 - a^2}\right\} \tag{6.21}$$

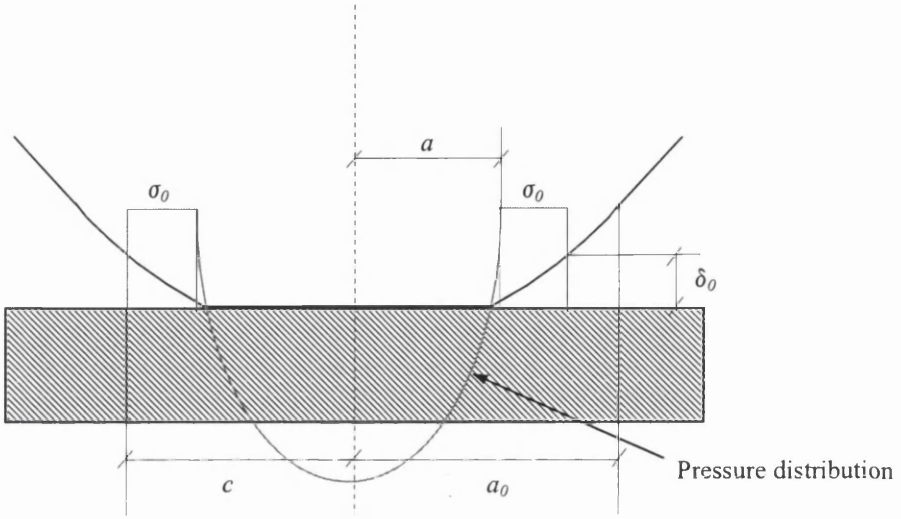

Figure 6.9: Pressure distribution at the adhesive contact.

The adhesive contact model derived by Mesarovic and Johnson [72] was applied via the Discrete Element Method by Martin [73] to calculate the resulting springback in the powder compact in an attempt to examine the unloading of an agglomerate of perfectly plastic spherical particles which had been compacted beyond the elastic limit and which had some adhesion. It was shown that the springback in the powder compact was dependent on the material parameters of the powders, and the adhesion at the contact also has an important effect, apart from the elastic recovery, during unloading.

As well as analysing adhesion between elastic particles and between elastic-plastic particles, some researchers have also studied the adhesion of a thin compliant film. Many have found that although the JKR model is able to model the adhesive contact for a wide range of particles' parameters, the model is however inappropriate for the contact between thin films as they cannot be treated as a semi-infinite elastic half-space [69,74,75].

Yang [74] presented analyses of adhesive contact between an incompressible elastic thin film of thickness h and a rigid axisymmetric indenter of spherical and conical shape. The interface between the film and the substrate was assumed to be either frictionless or perfectly bonded. Load-displacement relationships, taking into account the adhesion energy $\Delta\gamma$, were established using a thermodynamic method and asymptotic

analysis, from where the pull-off force P_c (equivalent to the force of adhesion) for different indenter geometries and film-substrate interface conditions was found as follows:

- For a spherical indenter with a radius R:
  - For frictionless contact between the film and the substrate:

$$P_c = -2\pi\Delta\gamma R \tag{6.22}$$

  - For perfect bonding between the film and the substrate:

$$P_c = -3\pi\Delta\gamma R \tag{6.23}$$

- For a conical indeneter with an angle ϑ:
  - For frictionless contact between the film and the substrate:

$$P_c = -\frac{4\pi\Delta\gamma \tan^2\vartheta}{3}\sqrt{\frac{2\Delta\gamma h}{G}} \tag{6.24}$$

    , where G is the shear modulus of the thin film.
  - For perfect bonding between the film and the substrate:

$$P_c = -\frac{9\pi h\Delta\gamma \tan^{3/2}\vartheta}{5}\left(\frac{54\Delta\gamma}{Gh}\right)^{1/4} \tag{6.25}$$

Also, Sridhar et al [75] investigated the adhesion mechanics between a compliant elastic coating and a spherical indenter using the finite element method, from which an empirical expression for the adhesion load was obtained. From the analysis, it was found that the compliance system was a function of the contact radius a, and the relation between the contact radius and the film thickness h is an important parameter that represents the significance of the confinement effects on the elastic and adhesive properties of the thin film. Assuming frictionless contact between the indenter and the film and perfect bonding between the film and substrate, the Hertz load is expressed as

$$\frac{4}{3}\frac{P_1 R}{E_1' a^3} = F\left(\frac{a}{h}, \frac{E_2'}{E_1'}\right) \equiv F(x,k) \tag{6.26}$$

while the adhesive load has the form

$$\frac{P_a}{\sqrt{8\pi\Delta\gamma E_1' a^3}} = H\left(\frac{a}{h}, \frac{E_2'}{E_1'}\right) \equiv H(x,k) \tag{6.27}$$

where $E_i' = \frac{E_i}{\left(1-\nu_i^2\right)}$, $i = 1,2$ are the moduli of the film and substrate respectively, and $F(x,k)$ and $H(x,k)$ are fitted functions from the FE analysis.

The net load P acting on the system is then written as

$$\begin{aligned}\frac{PR}{E_1' h^3} &= \frac{P_1 R}{E_1' h^3} - \frac{P_a R}{E_1' h^3} \\ &= \frac{4}{3}x^3 F(x,k) - \frac{\sqrt{8\pi\Delta\gamma R^2}}{E_1' h^3} x^{3/2} H(x,k)\end{aligned} \tag{6.28}$$

However, from the results, it was found that it was not possible to have a general empirical equation for $F(x,k)$ and $H(x,k)$ which covered the entire film-substrate system, and separate formulas were needed for different situations such as:

- For an incompressible film on a rigid substrate:

$$\begin{aligned}F(x,k) &= 1 + \left[\frac{8}{x(1+x)^{1.5}} + \frac{6.8(1-2\nu_1)}{x}\right]^{-1} \\ H(x,k) &= 1 + \left[\frac{3.8}{x\sqrt{1+x}} + \frac{2.1\sqrt{1-2\nu_1}}{\sqrt{x}}\right]^{-1}\end{aligned} \tag{6.29}$$

- For an incompressible film on an elastic substrate:

$$\begin{aligned}\log F(x,k) &= \frac{k'}{2}\{\tanh[A'(\log x + B')] + 1\} \\ \log H(x,k) &= \frac{k''}{2}\{\tanh[A''(\log x + B'')] + 1\}\end{aligned} \tag{6.30}$$

, where $A' = 0.1006k'^2 - 0.7204k' + 2.7366$,

$B' = 0.0253k'^2 - 0.3404k' - 0.1276$,

$A'' = 0.3280k''^2 - 1.3439k'' + 2.7903$,

$B'' = 0.1160k''^2 - 0.7397k'' - 0.0291$,

$k' = \log k$, $k'' = \log\sqrt{k}$

- For a compressible film on an elastic substrate:

$$\log F(x,k) = \frac{k'}{2}\{\tanh[A'(\log x + 0.60)] + 1\}^8$$
$$\log H(x,k) = \frac{k''}{2}\{\tanh[A''(\log x + 0.75)] + 1\}^8 \quad (6.31)$$

, where $A' = 0.037k'^2 - 0.33k' + 1.2$,

$A'' = 0.18k''^2 - 0.70k'' + 1.2$,

$k' = \log k$, $k'' = \log\sqrt{k}$

Similar to the work of Yang and Sridhar et al[74,75] the following sections in this chapter aim to study the contact adhesion between coated particles. Finite element analyses are carried out to examine the behaviour at the adhered contact when subjected to pulling, and a simple load-penetration (P-d) relation that is modified from Hertz formula will be formulated empirically based on observations. Also, as the adhesion between coated particles can not be treated as semi-infinite elastic half-space, comparison to the adhesion map shown in Figure 6.1 can not be made.

6.2 Finite Element Investigation of Adhesive Contact between Coated Particles

6.2.1 The Model for Contact Adhesion

The analysis in this chapter is an extension from the work that has been discussed in Chapter 4, where the coated particles show a complete detachment when pulled further than the residual penetration d_{res}, as shown in Figure 6.10(d). The particles are now assumed to adhere (fused) together when unloaded to zero force with a permanent deformation that forms a residual contact radius a_{res} as shown in Figure 6.10(c). The adhesion between the particles will start to take effect at this point if the unloading process continues. This is similar to the ductile extension of a deep notch as proposed by Pollock [71] and shown in Figure 6.5. After a period of unloading, the geometry at the contact is expected to have the form as shown in Figure 6.10(e), which is similar to the necking behaviour observed in a tensile test.

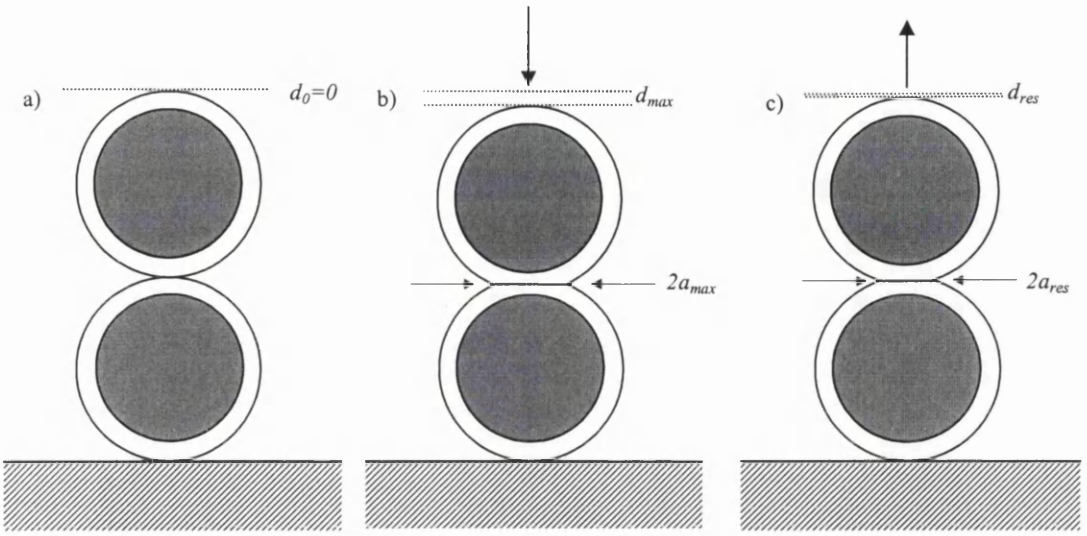

Two particles are initially at rest and in contact.

The top particle is compressed to a maximum displacement, d_{max}, forming $2a_{max}$ at the contact.

The top particle is de-compressed, a permanent deformation, $2a_{res}$, is formed at the contact, giving a permanent displacement, d_{res}.

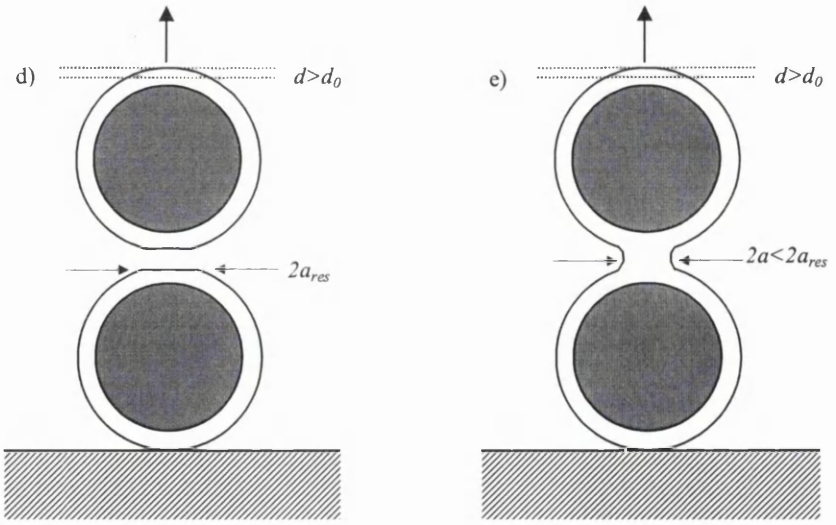

With no adhesion at the contact, detachment will occur if the top particle is pulled beyond d_{res}.

With adhesion at the contact, the contact will be in tension if the top particle is pulled beyond d_{res}. A behaviour that is analogous to the tensile test is observed.

Figure 6.10: The process of compression and decompression of two coated particles with and without adhesion at the contact.

In order to simulate the spherical nature of the particles, an axi-symmetric finite element analysis was carried out. The residual contact radius and penetration at the end of unloading (at zero force and without adhesion) is measured, and the contact model between the two particles at that instant is replaced with a continuum model with a contact width of $2a_{res}$, shown in Figure 6.11. The model is restrained from vertical movement by vertical constraints along the bottom of the bottom particle (represented by green markers) and from radial movement by horizontal constraints along the common normal of the particles (represented by red markers). An upward displacement is applied along the top of the model with a speed of $1.5\times10^{-5}\ m/s$ so that the contact area is in a state of tension.

As the contact area between the particles will exhibit high stresses, the mesh around this region is denser in order to have a more accurate analysis (Figure 6.12). Also, to avoid inaccurate results caused by mesh distortion, an adaptive mesh refinement is utilised as mentioned previously.

As an extension to the previous work, the dimension and material properties used in the analyses in this chapter are similar to those shown in Table 4.1 in Chapter 4.

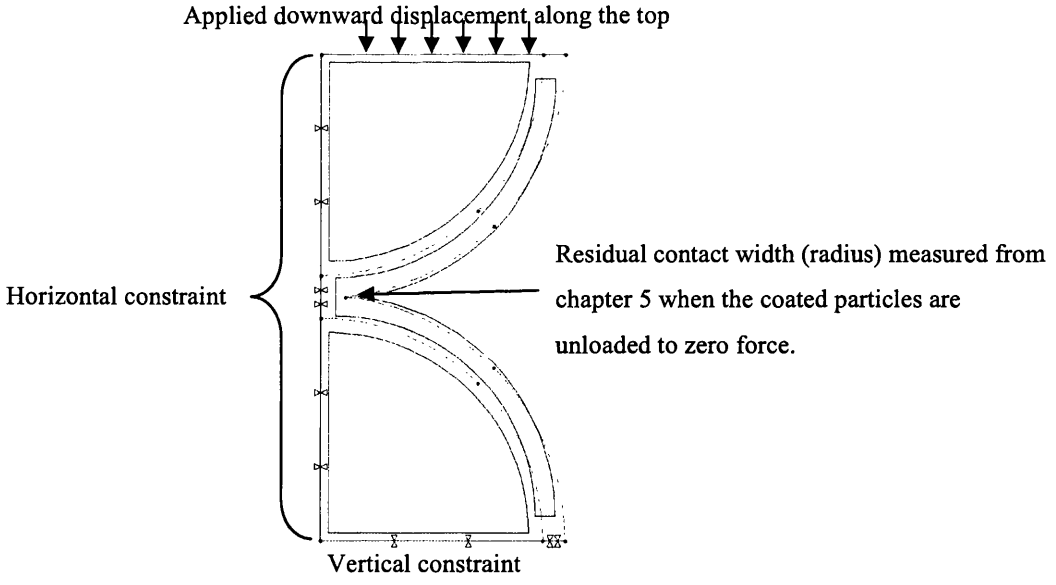

Figure 6.11: A continuum model for the contact between two coated particles with applied boundary constraints.

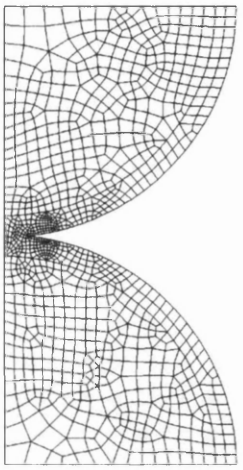

Figure 6.12: Initial mesh assignment on the contact model.

6.2.2 Finite Element Results and Discussions

The force-penetration relation for different coating thicknesses and material properties as obtained from the finite element simulation are shown in the following figures, where the negative values indicate tension in the system. The geometry of the contact and the effective stress distribution around the contact are also shown for each case at the point of maximum tensile force and at the end of the pulling-apart process.

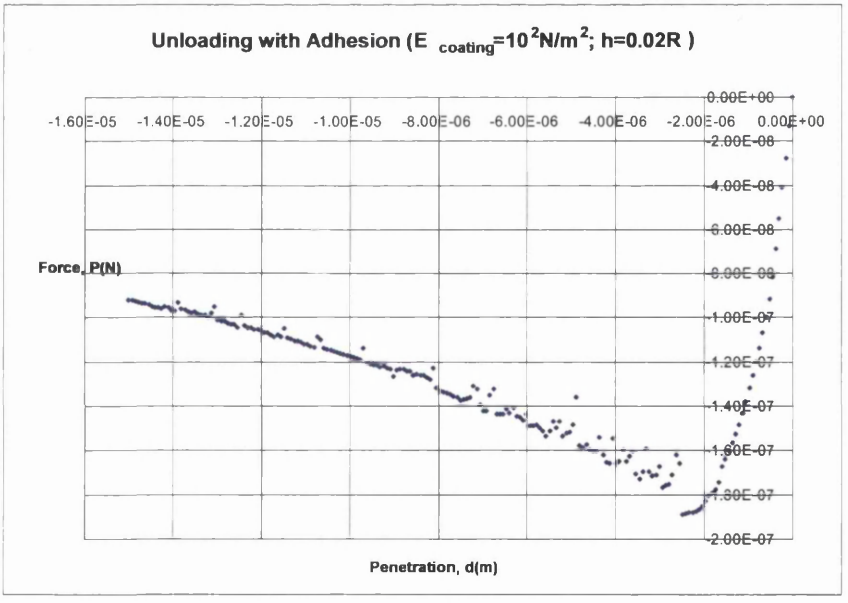

Figure 6.13: Force-penetration relation for $E_{coating} = 10^2 N/m^2$ and $h = 0.02R$.

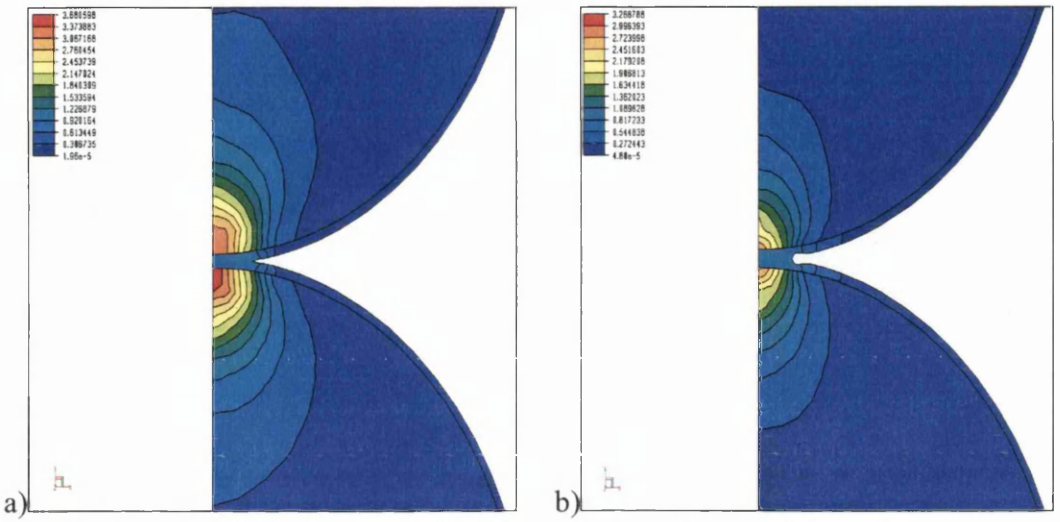

Figure 6.14: The geometry and effective stress distribution at the contact a) at maximum tensile force; b) at the end of pulling-apart process for $E_{coating} = 10^2 N/m^2$ and $h = 0.02R$.

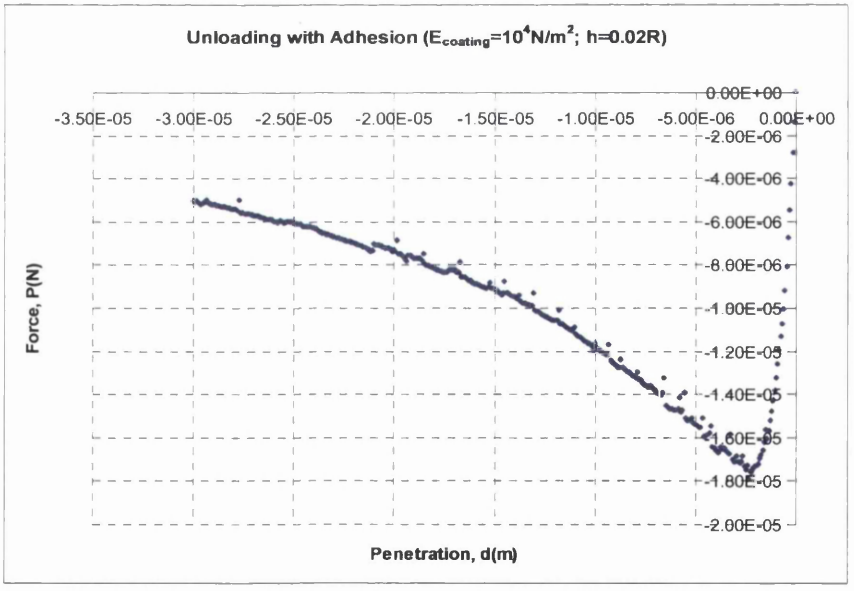

Figure 6.15: Force-penetration relation for $E_{coating} = 10^4 N/m^2$ and $h = 0.02R$.

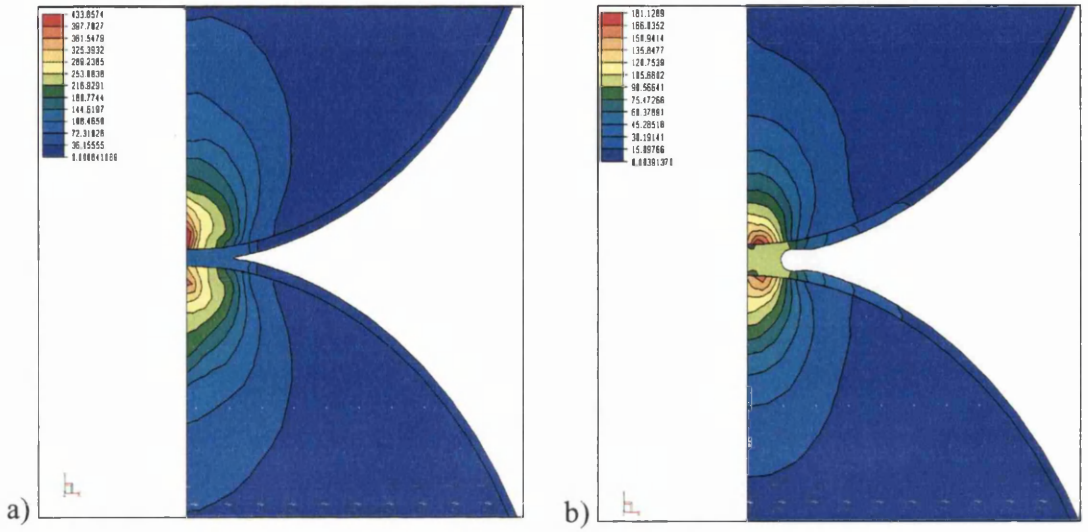

Figure 6.16: The geometry and effective stress distribution at the contact a) at maximum tensile force; b) at the end of pulling-apart process for $E_{coating} = 10^4 N/m^2$ and $h = 0.02R$.

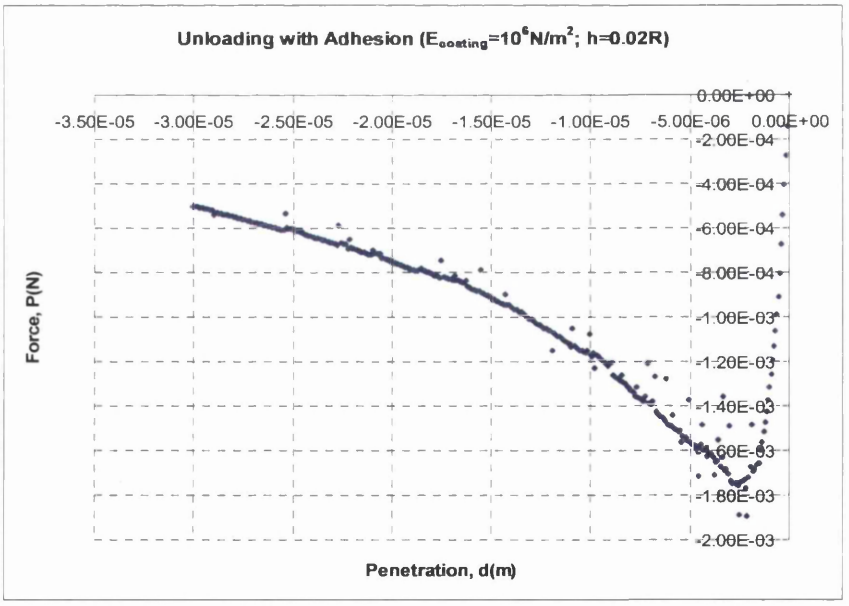

Figure 6.17: Force-penetration relation for $E_{coating} = 10^6 N/m^2$ and $h = 0.02R$.

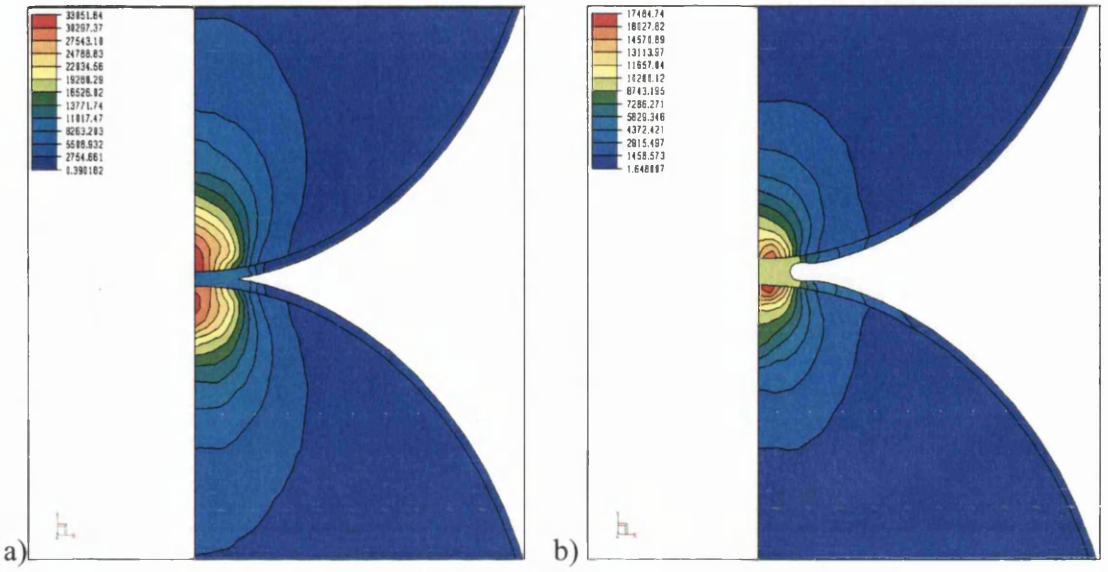

Figure 6.18: The geometry and effective stress distribution at the contact a) at maximum tensile force; b) at the end of pulling-apart process for $E_{coating} = 10^6 N/m^2$ and $h = 0.02R$.

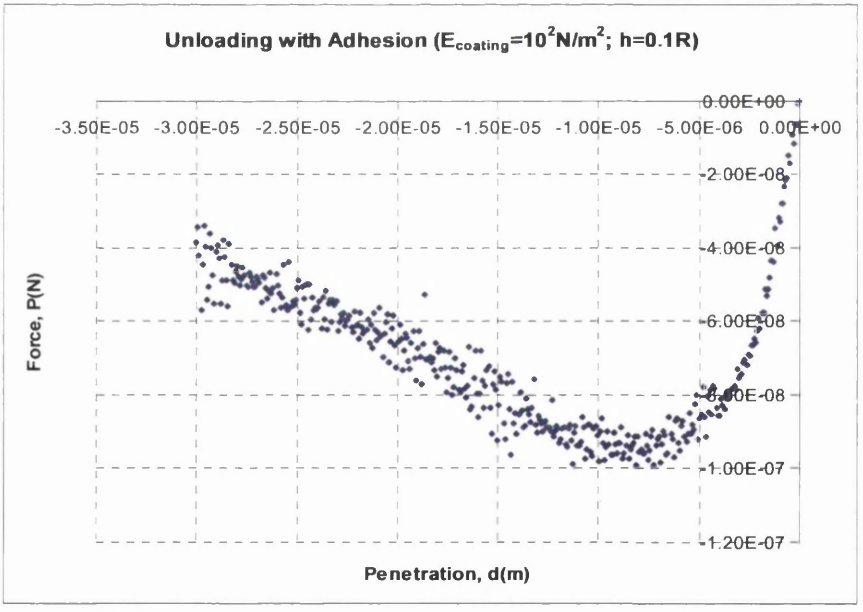

Figure 6.19: Force-penetration relation for $E_{coating} = 10^2 N/m^2$ and $h = 0.1R$.

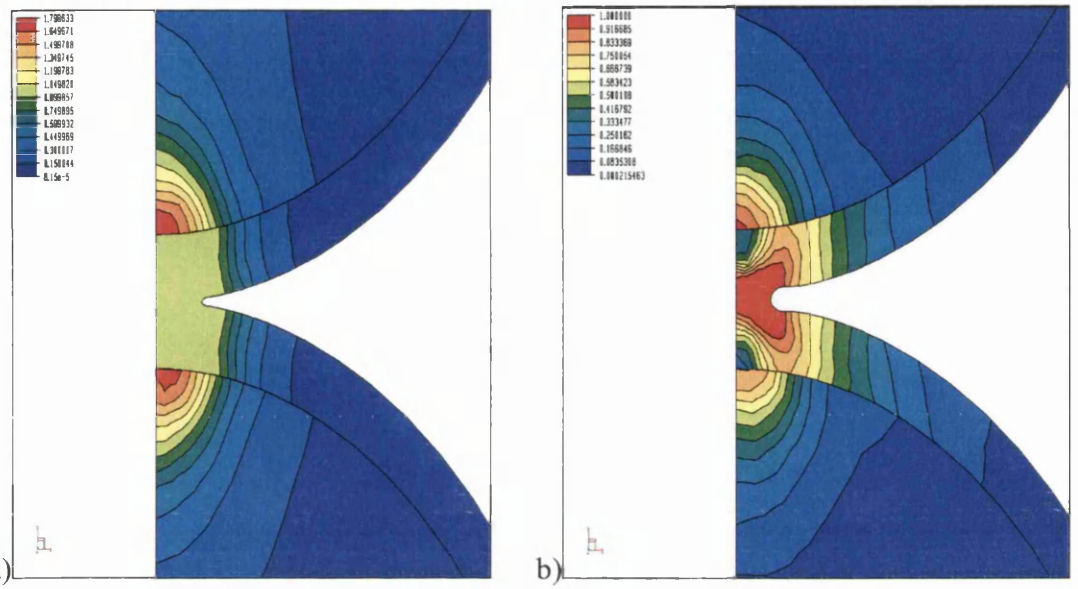

Figure 6.20: The geometry and effective stress distribution at the contact a) at maximum tensile force; b) at the end of pulling-apart process for $E_{coating} = 10^2 N/m^2$ and $h = 0.1R$.

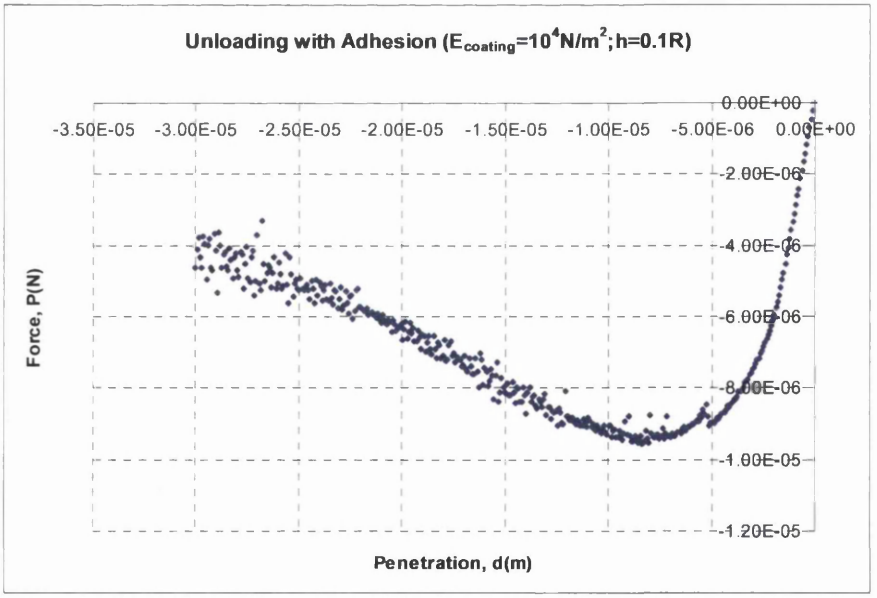

Figure 6.21: Force-penetration relation for $E_{coating} = 10^4 N/m^2$ and $h = 0.1R$.

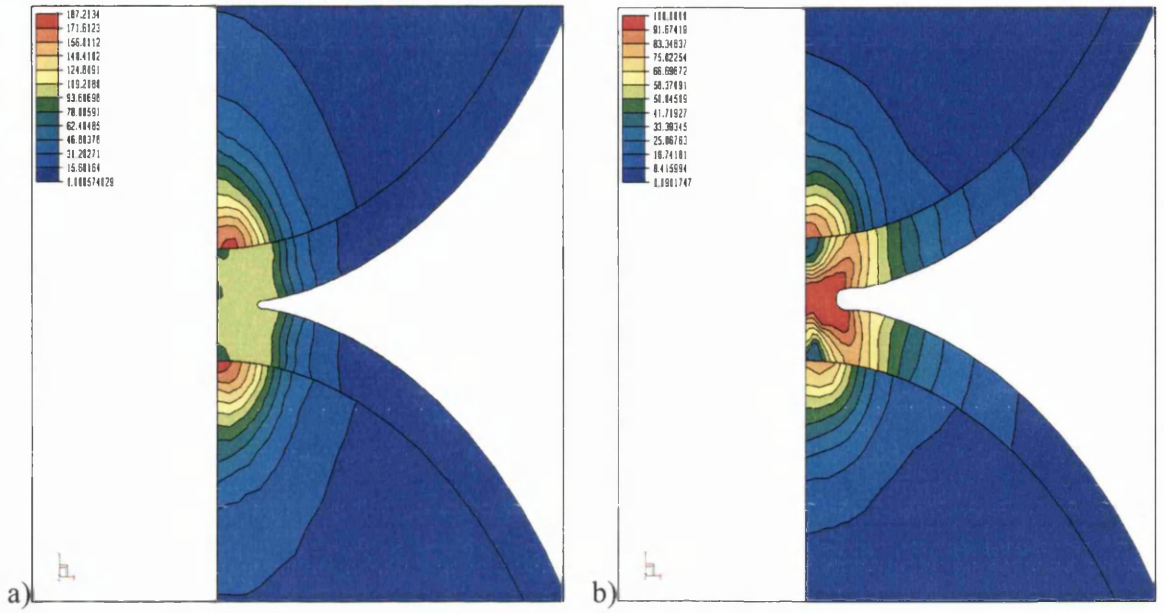

Figure 6.22: The geometry and effective stress distribution at the contact a) at maximum tensile force; b) at the end of pulling-apart process for $E_{coating} = 10^4 N/m^2$ and $h = 0.1R$.

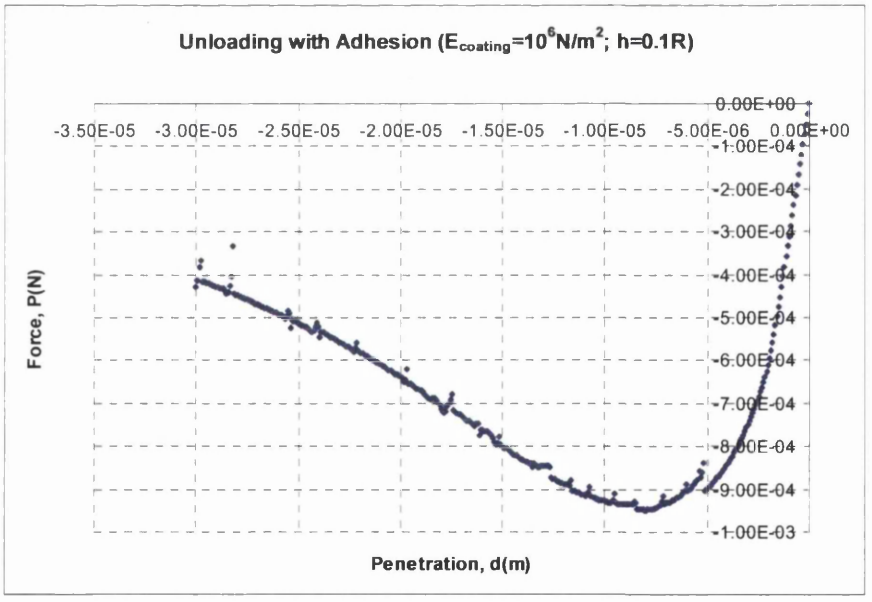

Figure 6.23: Force-penetration relation for $E_{coating} = 10^6 N/m^2$ and $h = 0.1R$.

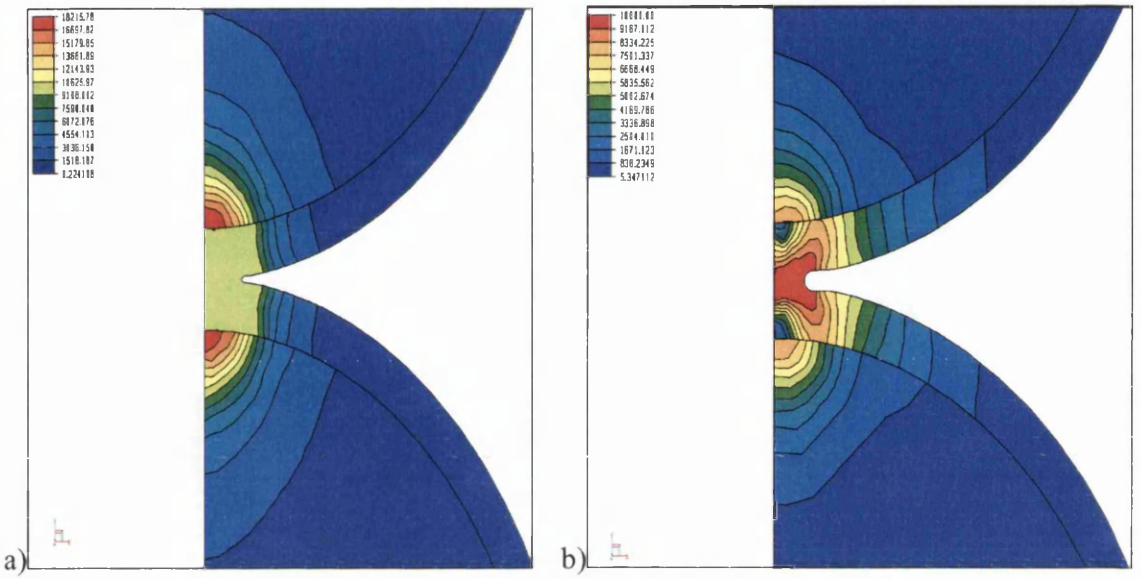

Figure 6.24: The geometry and effective stress distribution at the contact a) at maximum tensile force; b) at the end of pulling-apart process for $E_{coating} = 10^6 N/m^2$ and $h = 0.1R$.

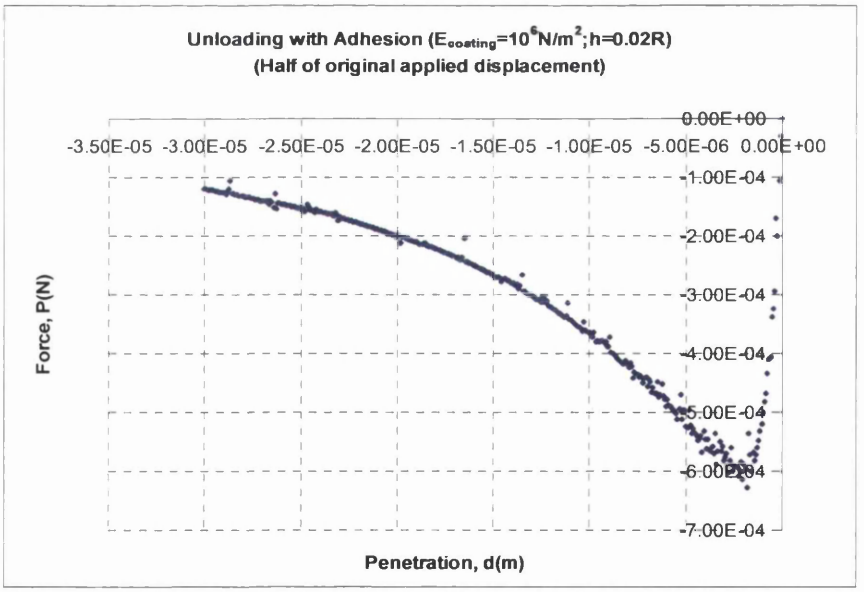

Figure 6.25: Force-penetration relation for $E_{coating} = 10^6 N/m^2$ and $h = 0.02R$.

(Unloaded from half of the original applied maximum displacement)

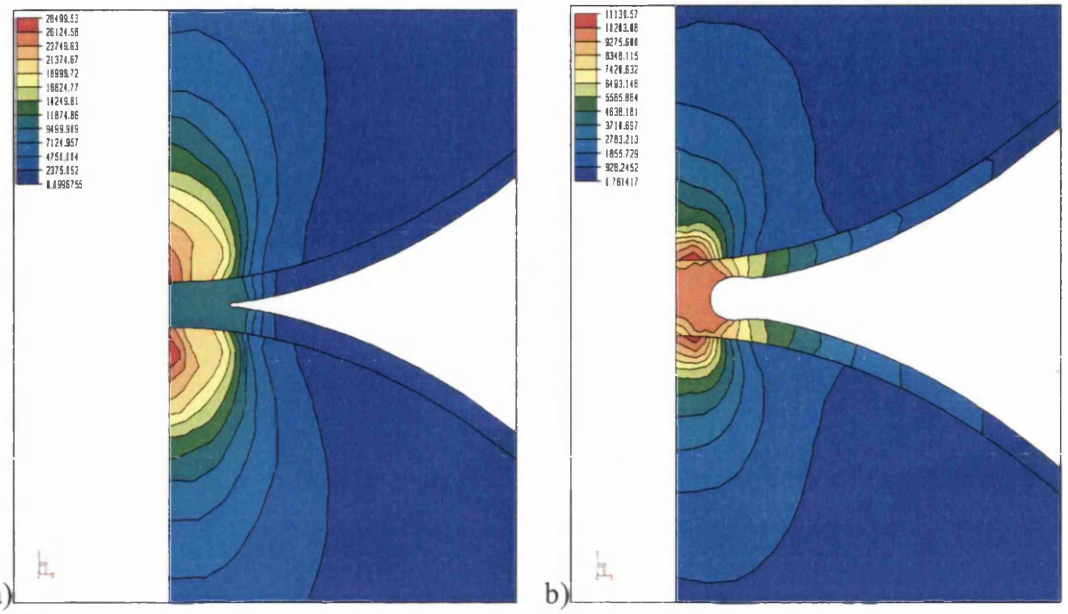

Figure 6.26: The geometry and effective stress distribution at the contact a) at maximum tensile force; b) at the end of pulling-apart process for $E_{coating} = 10^6 N/m^2$ and $h = 0.1R$. (Unloaded from half of the original applied displacement)

As can be seen in Figure 6.13 to Figure 6.25, when the particles are pulled apart, a tensile (negative) force is exerted at the contact in order to hold the two surfaces together. However, this phenomenon is inelastic and a maximum tensile force is observed at a certain stage of the process. After the maximum tensile force is reached, the contact starts to soften under the 'pulling-apart' process, and causes necking at the contact as observed in Figure 6.14, Figure 6.16, Figure 6.18, Figure 6.20, Figure 6.22, Figure 6.24 and Figure 6.26, and hence a reduction in the tensile force.

Also, it can be seen from Figure 6.14(a), Figure 6.16(a), Figure 6.18(a), Figure 6.20(a), Figure 6.22(a), Figure 6.24(a) and Figure 6.26(a) that at the maximum tensile force, the coating has yielded throughout the thickness. As the pulling persists, the tensile stress at the interface between the coating and the particle shows a reduction in magnitude. However, the high tensile stress starts to form a ring and concentrates around the junction between the coatings (which is obvious for the cases of $h = 0.1R$) and this

could be the reason for the contact to start to fail and break-up. However, the reduction in the magnitude of the tensile stress at the interface between the coating and the particle could suggest that failure would have occurred previously by the detachment of the coating from the particle.

A comparison between the force-displacement relation between $h = 0.1R$ and $0.02R$ for a particular coating material can be seen in Figure 6.27, Figure 6.28 and Figure 6.29. In general, for a particular coating material, the maximum tensile force produced is greater when the coating is thinner (i.e. $h = 0.02R$). Also, the P-d curve exhibits a sharp drop of force from zero to a maximum tensile force for $h = 0.02R$ while the change in force is less for $h = 0.1R$. The difference between the penetration at maximum tensile force and the penetration at zero force $(d_{\min} - d_0)$ is also found to vary with the coating thickness, but is unaffected by the coating material, where a thicker coating shows greater difference in $(d_{\min} - d_0)$. As the particles are pulled further from the point of maximum tensile force, the tensile force reduces in magnitude and both curves (for $h = 0.1R$ and $0.02R$) converge towards roughly the same path.

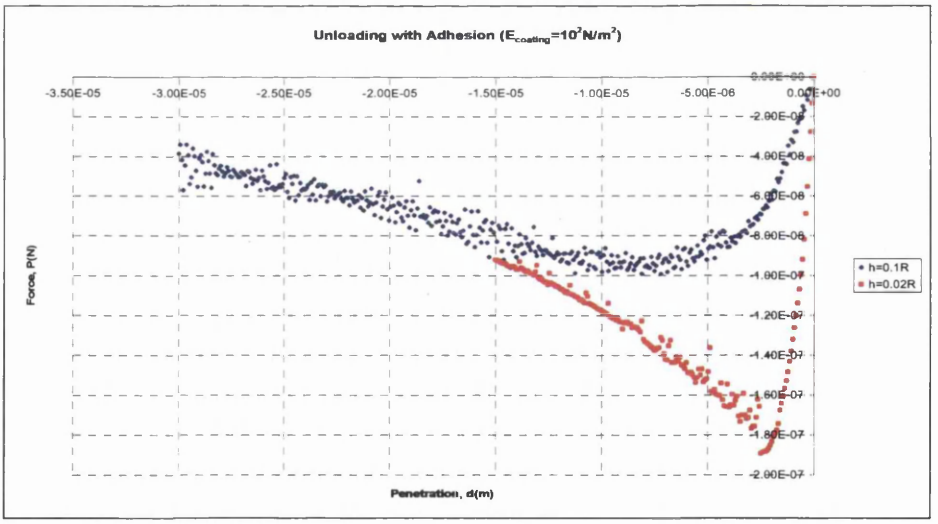

Figure 6.27: Comparison of force-penetration relation between $h = 0.1R$ and $0.02R$ with $E_{coating} = 10^2 N/m^2$.

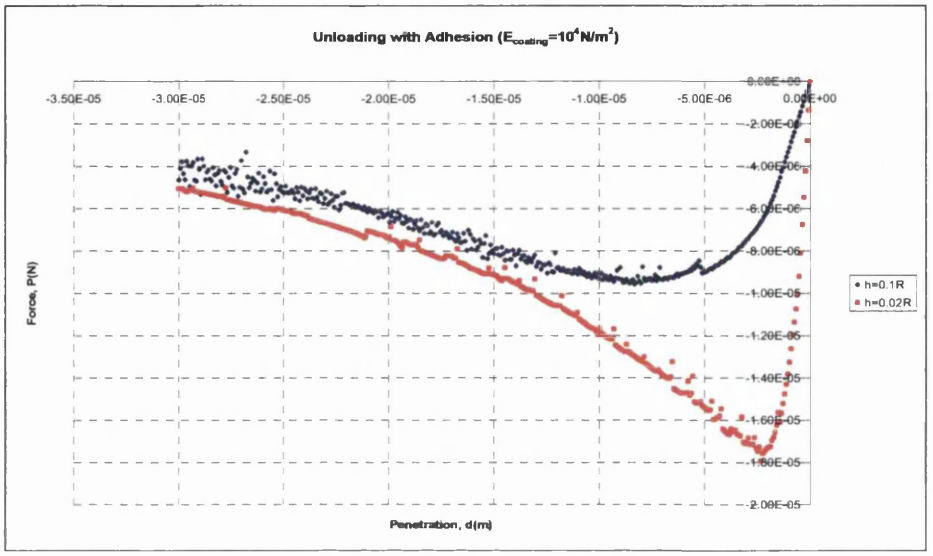

Figure 6.28: Comparison of force-penetration relation between $h = 0.1R$ and $0.02R$ with $E_{coating} = 10^4 N/m^2$.

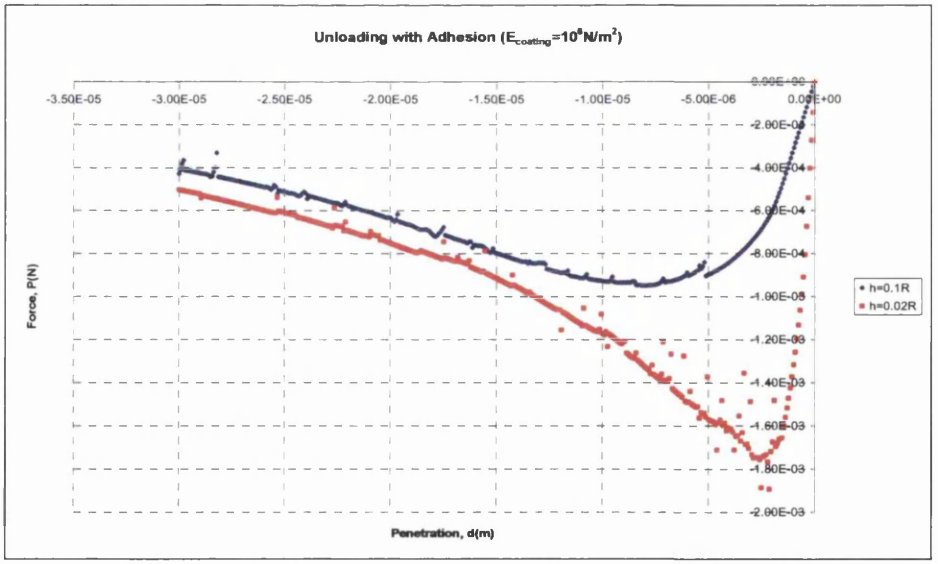

Figure 6.29: Comparison of force-penetration relation between $h = 0.1R$ and $0.02R$ with $E_{coating} = 10^6 N/m^2$.

In order to obtain the P-d relation for the unloading of the adhesive coated particles from the maximum penetration to the residual penetration and beyond, the P-d curves obtained in Chapter 4 are now combined with the P-d curves obtained in this section at the residual penetration d_{res} (i.e. at the point of zero force). These are shown in the following figures with the green curves representing the unloading from the maximum penetration to the residual penetration and the blue curves represent the unloading from the residual penetration with adhesion at the contact.

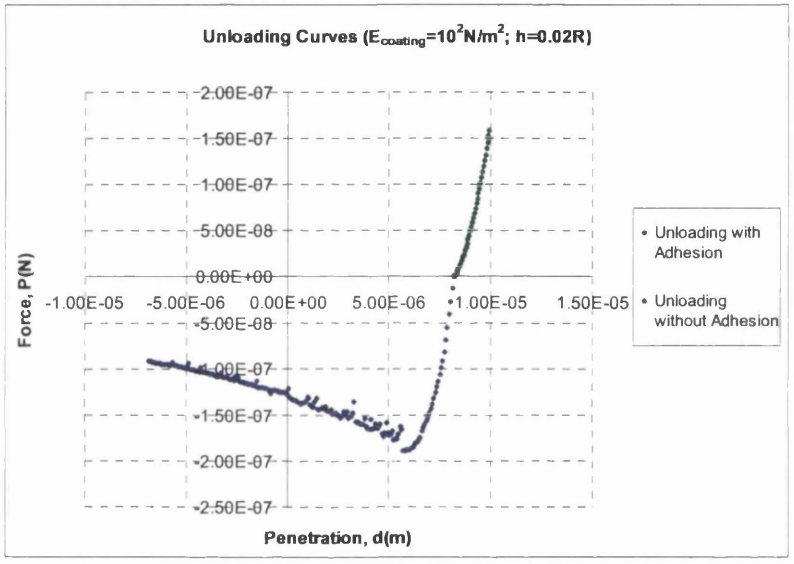

Figure 6.30: P-d relation for the unloading of the particles with adhesion at the contact at d_{res}. ($E_{coating} = 10^2 N/m^2$; $h = 0.02R$)

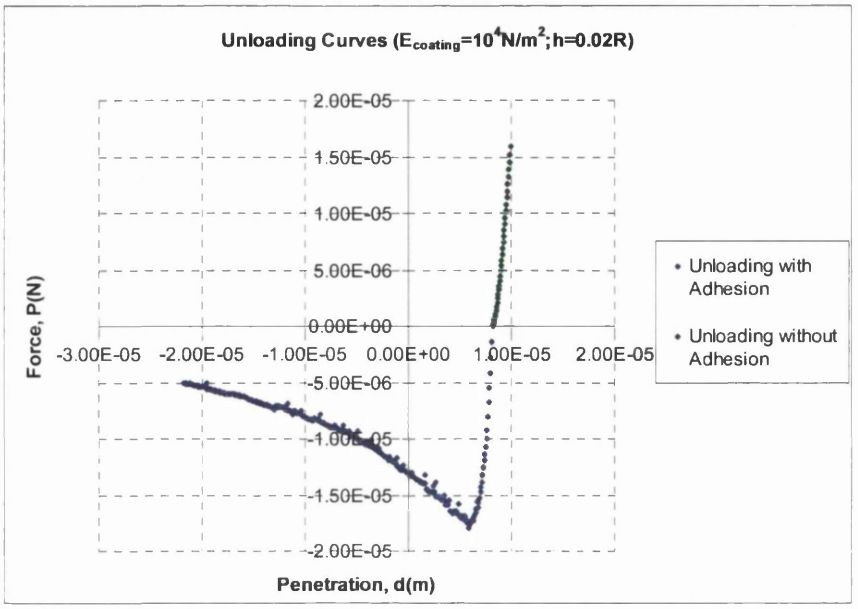

Figure 6.31: P-d relation for the unloading of the particles with adhesion at the contact at d_{res}. ($E_{coating} = 10^4 N/m^2$; $h = 0.02R$)

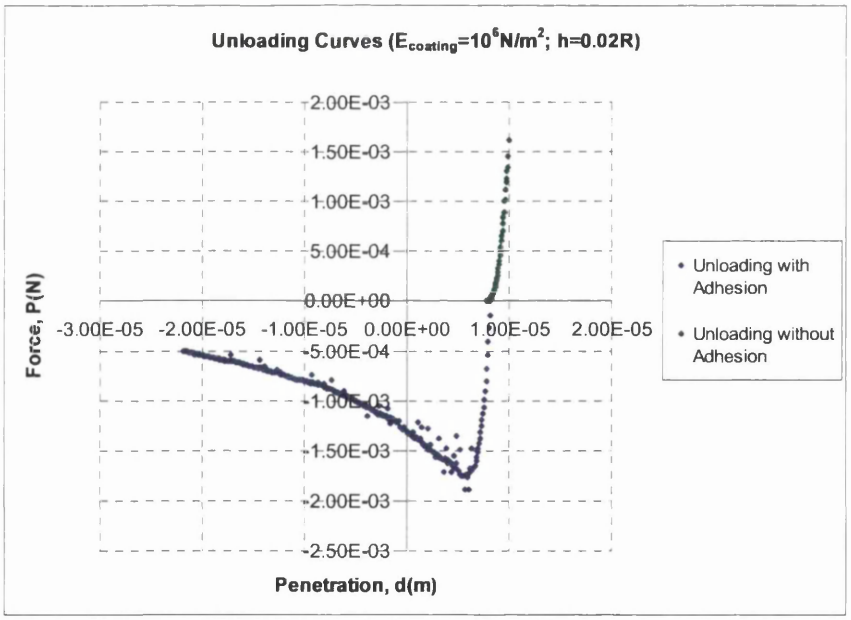

Figure 6.32: P-d relation for the unloading of the particles with adhesion at the contact at d_{res}. ($E_{coating} = 10^6 N/m^2$; $h = 0.02R$)

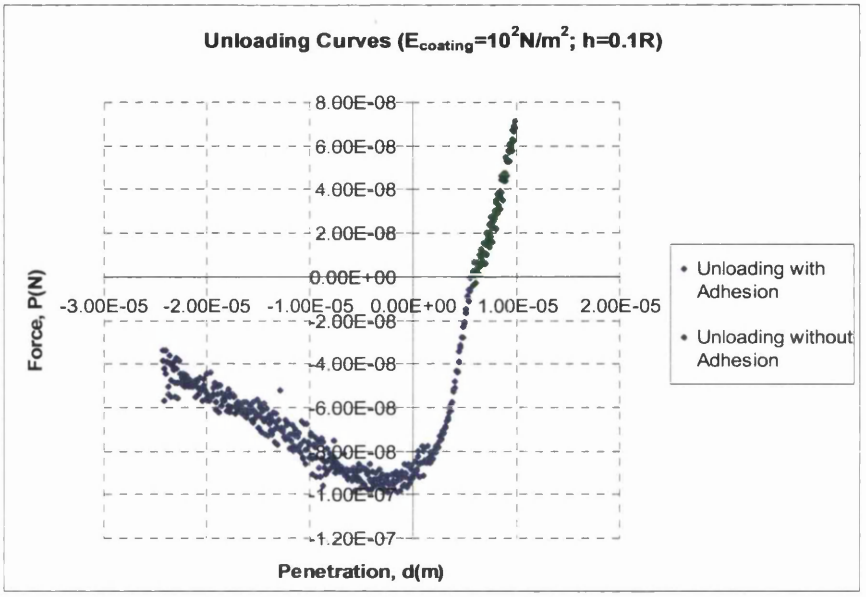

Figure 6.33: P-d relation for the unloading of the particles with adhesion at the contact at d_{res}. ($E_{coating} = 10^2 N/m^2$; $h = 0.1R$)

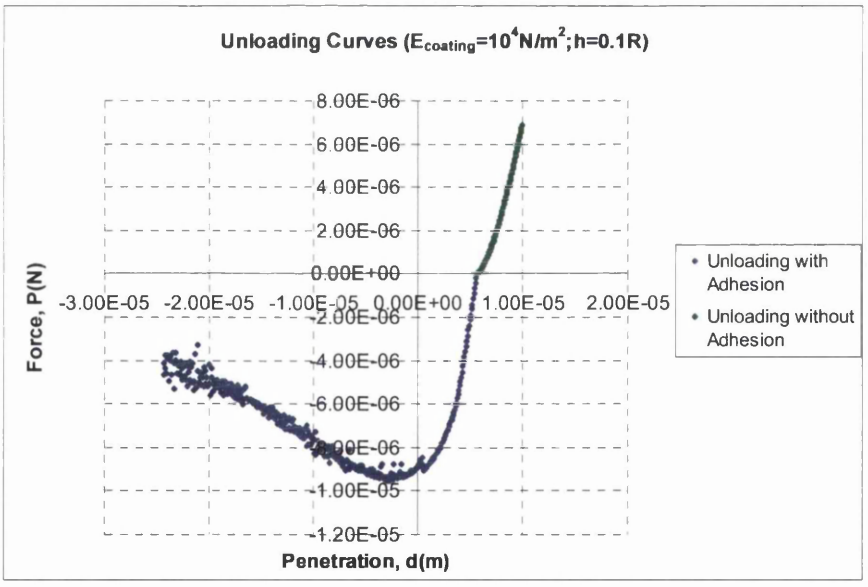

Figure 6.34: P-d relation for the unloading of the particles with adhesion at the contact at d_{res}. ($E_{coating} = 10^4 N/m^2$; $h = 0.1R$)

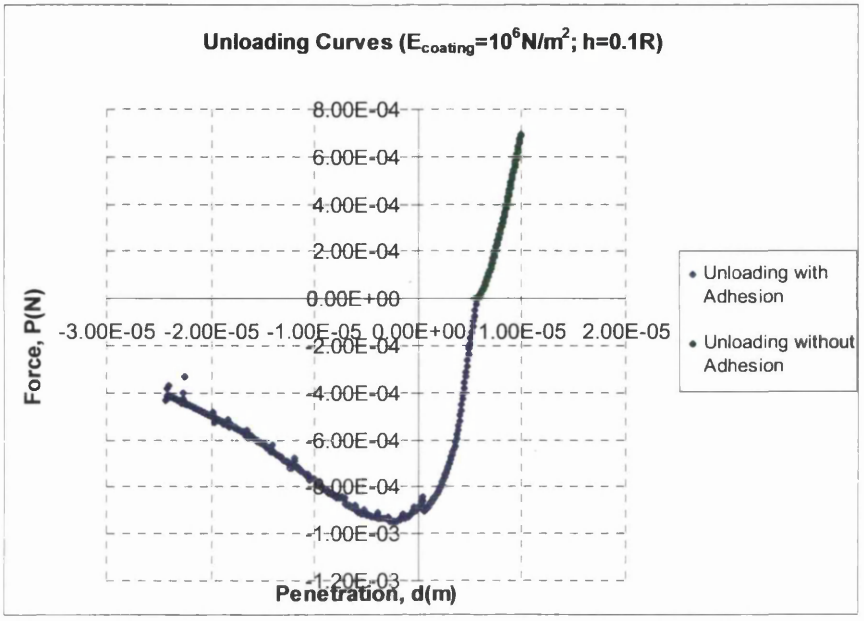

Figure 6.35: P-d relation for the unloading of the particles with adhesion at the contact at d_{res}. ($E_{coating} = 10^6 N/m^2$; $h = 0.1R$)

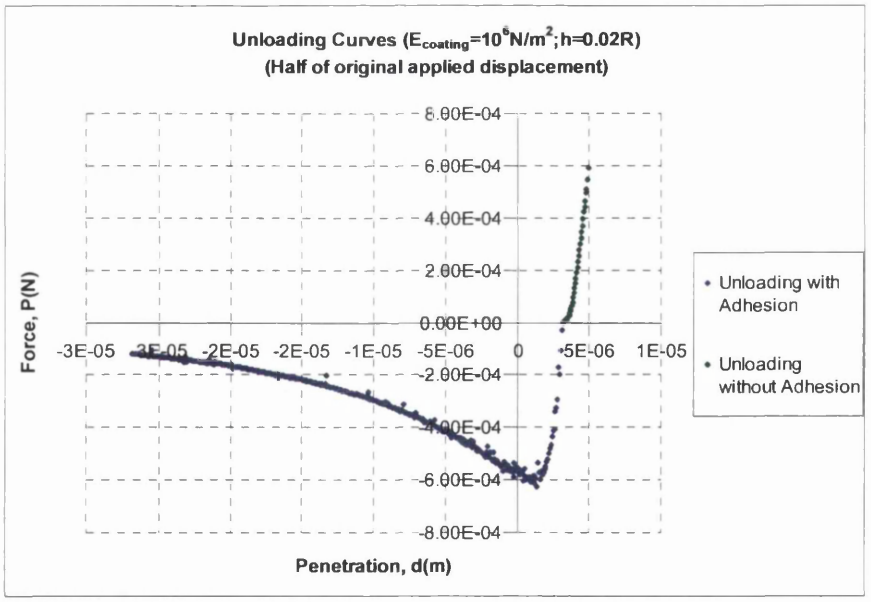

Figure 6.36: P-d relation for the unloading of the particles with adhesion at the contact at d_{res}. ($E_{coating} = 10^6 N/m^2$; $h = 0.02R$, Unloaded from half of the original applied maximum displacement)

From Figure 6.30 to Figure 6.36, it can be seen that the two curves join quite well at the contact, especially for the thin coating ($h = 0.02R$), where the unloading path through the residual penetration d_{res} resembles a smooth and continuous curve from the maximum penetration.

6.3 Contact Law for Coated Particles with Adhesion at the Contact

From the results obtained in section 6.2.2, it can be seen that the unloading of the coated particles with adhesion at the contact follows a trend that allows the generalisation of the contact behaviour with respect to the material and geometry parameters to form a simple contact law. Relations for $P_{\min}$ (or maximum tensile force) and $d_{\min}$ at maximum tensile force can both be formulated based on observations as follows,

6.3.1 Determination of $d_{\min}$

From the finite element analysis results, it can be seen that for the same coating material, the unloading curve follows the trend as shown in Figure 6.37. The difference between $d_{\max}$ and $d_{\min}$, $(d_{\max} - d_{\min})$, was found to increase with increasing $\frac{h}{R}$, and is not affected by the Young's Modulus of the coating material. From the FE simulations, the value of $d_{\min}$ for the two coating thickness is as follow:

$$d_{\min} = 5.725 \times 10^{-6} \quad \text{at} \frac{h}{R} = 0.02$$

$$d_{\min} = -3.425 \times 10^{-6} \quad \text{at} \frac{h}{R} = 0.1$$

Hence, the difference between $d_{\max}$ and $d_{\min}$ is:

$$d_{\max} - d_{\min} = 4.275 \times 10^{-6} \quad \text{at} \frac{h}{R} = 0.02$$

$$d_{\max} - d_{\min} = 1.3425 \times 10^{-5} \quad \text{at} \frac{h}{R} = 0.1$$

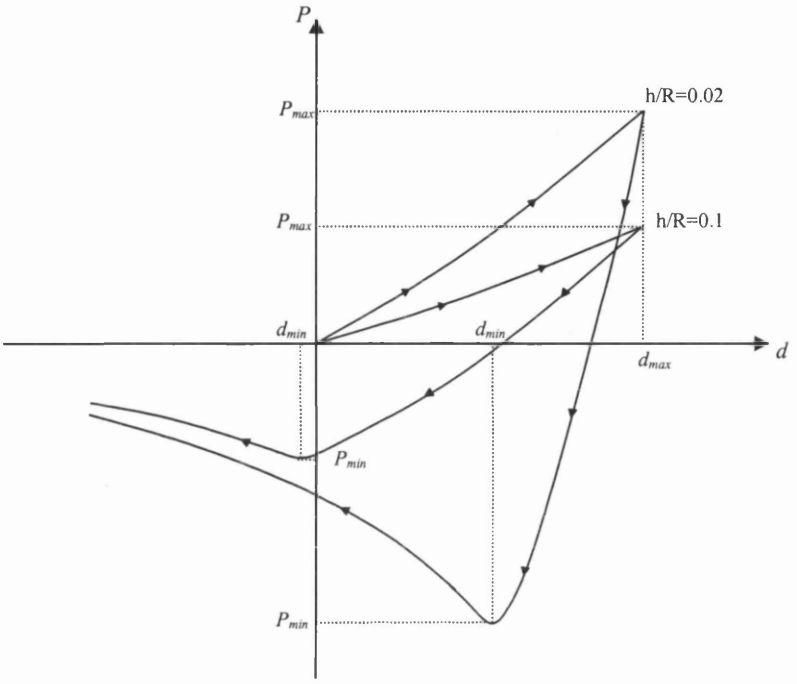

Figure 6.37: The loading and unloading paths for different coating thickness with the same coating material, in the presence of adhesion at the contact.

By assuming a linear relation between $(d_{\max} - d_{\min})$ and $\frac{h}{R}$, the following linear equation can be used to represent the change of $(d_{\max} - d_{\min})$ with respect to $\frac{h}{R}$ as shown in Figure 6.38. The equation is written as:

$$(d_{\max} - d_{\min}) = 1.14375 \times 10^{-6} \frac{h}{R} + 1.9875 \times 10^{-6} \tag{6.32}$$

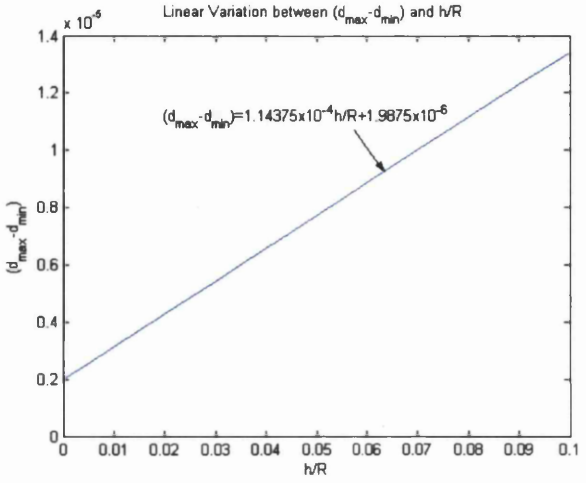

Figure 6.38: The linear variation of $(d_{\max} - d_{\min})$ with respect to $\frac{h}{R}$.

6.3.2 Determination of $P_{\min}$, the Maximum Tensile Force

Also, from observations, the ratio $\frac{P_{\max}}{P_{\min}}$ is found to vary with $\frac{h}{R}$, but is not affected by the value of the coating material. From the results shown, the $\frac{P_{\max}}{P_{\min}}$ ratios are obtained as follows,

$$\frac{P_{\max}}{P_{\min}} = -0.946 \quad \text{at} \frac{h}{R} = 0.02$$

$$\frac{P_{\max}}{P_{\min}} = -0.75 \quad \text{at} \frac{h}{R} = 0.1$$

The value of $\frac{P_{\max}}{P_{\min}}$ is found to reduce with increase $\frac{h}{R}$, which indicates that the value of $P_{\min}$ is greater than $-P_{\max}$, and the difference is greater when $\frac{h}{R}$ is greater. Thus, using a linear approximation, the relation between $\frac{P_{\max}}{P_{\min}}$ and $\frac{h}{R}$ can be written as

$$\frac{P_{\max}}{P_{\min}} = 2.45\frac{h}{R} - 0.995 \tag{6.33}$$

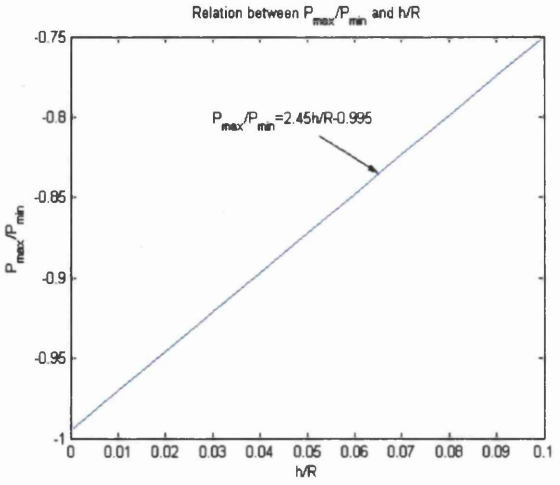

Figure 6.39: The linear variation of $\frac{P_{\max}}{P_{\min}}$ with respect to $\frac{h}{R}$.

From equation (6.8), the value of the 'notch extension force' P_n is said to be equal to the negative apparent plastic load P_f which produces a plastic contact radius a_f and modified radius r_f in the absence of surface energy. The relation for P_f is written as

$$P_f = \frac{Ka_f^3}{r_f} \tag{6.34}$$

which can also be written as

$$P_f = \frac{4}{3}E^* r_f^{1/2} d_f^{3/2} \tag{6.35}$$

as $K = \frac{4}{3}\left(\frac{1-\nu_1^2}{E_1} + \frac{1-\nu_2^2}{E_2}\right)^{-1}$ and d_f is the penetration caused by the apparent plastic load at contact radius a_f.

For contact between particles which are coated with a plastic coating, it was found in Chapter 5 that the P-d relation for the contact can be written as

$$P_{\max} = \xi m \frac{4}{3}\frac{E_p R_p^{\frac{1}{2}}}{\left(1-\nu_p^2\right)} d_{\max}^{\frac{3}{2}} \tag{6.36}$$

where ξ is a factor determined empirically and m is a material ratio between the coating and the particle. By comparing equation (6.35) with (6.36), it can be seen that they are of

similar form, and the ratio $\frac{P_{max}}{P_{min}}$ found from the observations is said to follow the condition mentioned in [71] for deep notch extension. If P_{max} is equivalent to P_f, in the limit where the particles are not coated, i.e. $\frac{h}{R} \to 0$, then the ratio $\frac{P_{max}}{P_{min}}$ has to be close to -1, as suggested in equation (6.8) by Pollock [71]. As can be seen from equation (6.33), as $\frac{h}{R} \to 0$, $\frac{P_{max}}{P_{min}} = -0.995$, which is close to -1 to conform with the situation of a 'deep notch extension'.

To explore to limitation of equation (6.33), the ratio $\frac{P_{max}}{P_{min}}$ was made equal to or less than zero in order to make sure that P_{min} is always a negative value (a tensile force), i.e. $\frac{P_{max}}{P_{min}} \le 0$. Hence, from equation (6.33),

$$2.45\frac{h}{R} - 0.995 \le 0$$
$$\frac{h}{R} \le 0.406 \tag{6.37}$$

which means that the equation will not be applicable when h is greater than $0.406R$. However, the P-d relation formulated in the previous chapter for the contact between coated particles might not be applicable for coatings of this thickness. The analyses carried out in this research are intended for coating thickness ranging from $0.02R$ to $0.1R$.

6.3.3 Force-Penetration Contact Law for Unloading with Adhesion

In Chapter 4, the unloading force is found to be

$$P_{unloading} = \eta m \frac{4}{3}\frac{E_p R^{\frac{1}{2}}}{\left(1-\nu_p^2\right)}\left(d - d_{res}\right)^{\frac{3}{2}}$$

, where $m = \frac{E_c}{E_p}\frac{2\left(1-\nu_p^2\right)}{2\left(1-\nu_c^2\right)}$, $\eta = \xi\left(\frac{d_{max}}{d_{max} - d_{res}}\right)^{\frac{3}{2}}$ and $\xi = -8.175\frac{t}{R} + 1.2935$.

For the case where adhesion is present at the contact, the unloading force $P^*_{unloading}$, up to the maximum tensile force $P_{\min}$, can be represented by the summation of the adhesive force and the non-adhesive force as:

$$\left(P^*_{unloading}\right)_n = P_{\min} + \left(P_{unloading}\right)_n$$

$$= \frac{P_{\max}}{\left(2.45\frac{h}{R} - 0.995\right)} + \theta m \frac{4}{3}\frac{E_p R^{\frac{1}{2}}}{\left(1-\nu_p^2\right)}\left(d_n - d_{\min}\right)^{\frac{3}{2}} \tag{6.38}$$

where θ can be found by relating $P^*_{unloading}$ to the maximum force $P_{\max}$ achieved during the loading stage, and $d_{\min}$ is obtained from section 6.3.1. Therefore, at maximum load,

$$\xi m \frac{4}{3}\frac{E_p R^{\frac{1}{2}}}{\left(1-\nu_p^2\right)} d_{\max}^{\frac{3}{2}} = P^*_{unloading}$$

$$\xi m \frac{4}{3}\frac{E_p R^{\frac{1}{2}}}{\left(1-\nu_p^2\right)} d_{\max}^{\frac{3}{2}} = \frac{P_{\max}}{\left(2.45\frac{h}{R} - 0.995\right)} + \theta m \frac{4}{3}\frac{E_p R^{\frac{1}{2}}}{\left(1-\nu_p^2\right)}\left(d_{\max} - d_{\min}\right)^{\frac{3}{2}} \tag{6.39}$$

$$\xi m \frac{4}{3}\frac{E_p R^{\frac{1}{2}}}{\left(1-\nu_p^2\right)} d_{\max}^{\frac{3}{2}} = \frac{\xi m \frac{4}{3}\frac{E_p R^{\frac{1}{2}}}{\left(1-\nu_p^2\right)} d_{\max}^{\frac{3}{2}}}{\left(2.45\frac{h}{R} - 0.995\right)} + \theta m \frac{4}{3}\frac{E_p R^{\frac{1}{2}}}{\left(1-\nu_p^2\right)}\left(d_{\max} - d_{\min}\right)^{\frac{3}{2}}$$

By rearranging the terms, θ is thus written as

$$\theta = \xi\left(\frac{d_{\max}}{\left(d_{\max} - d_{\min}\right)}\right)^{\frac{3}{2}}\left(1 - \frac{1}{\left(2.45\frac{h}{R} - 0.995\right)}\right) \tag{6.40}$$

Again, from the equation above, it can be seen that the value of θ is only related to $\frac{h}{R}$, and is not affected by the material properties of the coating. Also, similar to equation (6.33), this equation will be invalid when h is greater than $0.406R$, as θ will be a negative value, which is undesirable.

Some of the θ values used in the study with respect to d_{max} and $\frac{h}{R}$ are shown in the table below:

Table 6.1: Some of the θ values used in the study.

$\frac{h}{R}$	d_{max} (m)	θ
0.02	0.00001	8.32
0.02	0.000005	2.94
0.1	0.00001	0.71

6.3.4 Material Softening

As mentioned earlier in section 6.2.2, the particle coating yielded throughout the contact when the maximum tensile force was reached. As the process of pulling-apart continues, the magnitude of the tensile force is reduced, which indicates a phenomenon of material softening that causes necking at the contact.

From the point of maximum tensile force (minimum force), the contact radius a was found to decrease linearly with penetration d as the unloading process continues. The relation between a and d as obtained from the finite element analyses, were curve fitted as shown in the following tables.

Table 6.2: Curve fitted $a-d$ relation for $\frac{h}{R}=0.02$.

$\sigma_{coating}(N/m^2)$	$\sigma_{yield}(N/m^2)$	$d_{max}(m)$	$a-d$ relation
100	1	0.00001	$a_n=\kappa(d_n-d_{min})+a_{min}$ $=1.591353(d_n-d_{min})+0.000128$
10000	100	0.00001	$a_n=1.45534(d_n-d_{min})+0.000128$
1000000	10000	0.00001	$a_n=1.475932(d_n-d_{min})+0.000127$
1000000	10000	0.000005	$a_n=1.24523(d_n-d_{min})+0.00008$

Table 6.3: Curve fitted $a-d$ relation for $\frac{h}{R}=0.1$.

$\sigma_{coating}(N/m^2)$	$\sigma_{yield}(N/m^2)$	$d_{\max}(m)$	$a-d$ relation
100	1	0.00001	$a_n=1.297913(d_n-d_{\min})+0.000109$
10000	100	0.00001	$a_n=1.27305(d_n-d_{\min})+0.00011$
1000000	10000	0.00001	$a_n=1.317935(d_n-d_{\min})+0.000108$

By averaging the factor κ, the $a-d$ relation can be simplified to

$$\begin{aligned} a_n &= \kappa(d_n-d_{\min})+a_{\min} \\ &= 1.38(d_n-d_{\min})+a_{\min} \end{aligned} \tag{6.41}$$

, where $d_n \le d_{\min}$, and $a_{\min}$ can be related to the average vertical stress $\bar{\sigma}_z$ and maximum tensile force $P_{\min}$ by

$$a_{\min}=\sqrt{\frac{|P_{\min}|}{\pi\bar{\sigma}_z}} \tag{6.42}$$

The reason that an average value is adopted for the vertical stress in this relation is that the stress distribution at the contact is normally non-uniform and requires integration throughout the whole contact area, which sometimes involves complex mathematical procedures. Therefore, the average vertical stresses at the contact as observed from the finite element results are curve fitted with respect to the penetration in order to find a general relation that is able to approximate the average vertical stresses. The curve-fitted $\bar{\sigma}_z-d$ relations are shown in the following tables.

Table 6.4: Curve fitted $\bar{\sigma}_z-d$ relation for $\frac{h}{R}=0.02$.

$E_c(N/m^2)$	$\sigma_y(N/m^2)$	$d_{\max}(m)$	$\bar{\sigma}_z-d$ relation
100	1	0.00001	$(\bar{\sigma}_z)_n=-7.1\times10^4(d_n-d_{\min})-3.3166$
10000	100	0.00001	$(\bar{\sigma}_z)_n=-5.0\times10^6(d_n-d_{\min})-324.97$
1000000	10000	0.00001	$(\bar{\sigma}_z)_n=-5.0\times10^8(d_n-d_{\min})-32502$
1000000	10000	0.000005	$(\bar{\sigma}_z)_n=-5.0\times10^8(d_n-d_{\min})-29118$

Table 6.5: Curve fitted $\bar{\sigma}_z - d$ relation for $\frac{h}{R} = 0.1$.

$E_c(N/m^2)$	$\sigma_y(N/m^2)$	$d_{\max}(m)$	$\bar{\sigma}_z - d$ relation
100	1	0.00001	$(\bar{\sigma}_z)_n = -3.4\times10^4(d_n - d_{\min}) - 2.7689$
10000	100	0.00001	$(\bar{\sigma}_z)_n = -3.0\times10^6(d_n - d_{\min}) - 262.54$
1000000	10000	0.00001	$(\bar{\sigma}_z)_n = -3.0\times10^8(d_n - d_{\min}) - 26066$

From observations, the $\bar{\sigma}_z - d$ relation can be simplified to the following form

$$\bar{\sigma}_z = -\sigma_y[\chi(d_n - d_{\min}) + 3] \tag{6.43}$$

where χ is assumed to vary inversely linearly with $\frac{h}{R}$ and is found to be unaffected by the material properties of the coating. For $\frac{h}{R} = 0.02$, χ is equal to 50000, and for $\frac{h}{R} = 0.1$, $\chi = 30000$.

Also, it can be seen that the second term in equation (6.43) is equivalent to the hardness of the materials which obey the von Mises criterion, $H \approx 3\sigma_y$ [9]. Hence, at a maximum tensile force (i.e. at $a_{\min}$ and thus $d_{\min}$), the average vertical stress $\bar{\sigma}_z$ is approximately equivalent to $-3\sigma_y$, which is the hardness of the coating material. In addition, the contact radius at a maximum tensile force $a_{\min}$ as calculated from equation (6.42) using the stress approximation in (6.43)was also found to be in good agreement with the curve-fitted $a_{\min}$. This is shown in the second term of the $a - d$ relations in Table 6.2 and Table 6.3, with an average percentage error of less than 10%.

Finally, having found the variation of contact radius and average vertical stress as the pulling process continues after the point of maximum tensile force, the force can be calculated using the relation

$$(P_{softening})_n = \pi a_n^2 \bar{\sigma}_z \tag{6.44}$$

6.4 Comparison between the Adhesive Contact Law with the Finite Element Results

The formulated contact law that takes into account the adhesion at the contact is then compared with the finite element analyses results in this section for different coating thicknesses and coating material. The comparisons are shown in the graphs in the following figures, with the approximated unloading path $P^{*}_{unloading}$ and material softening path $P_{softening}$ represented by red and pink curves.

a)

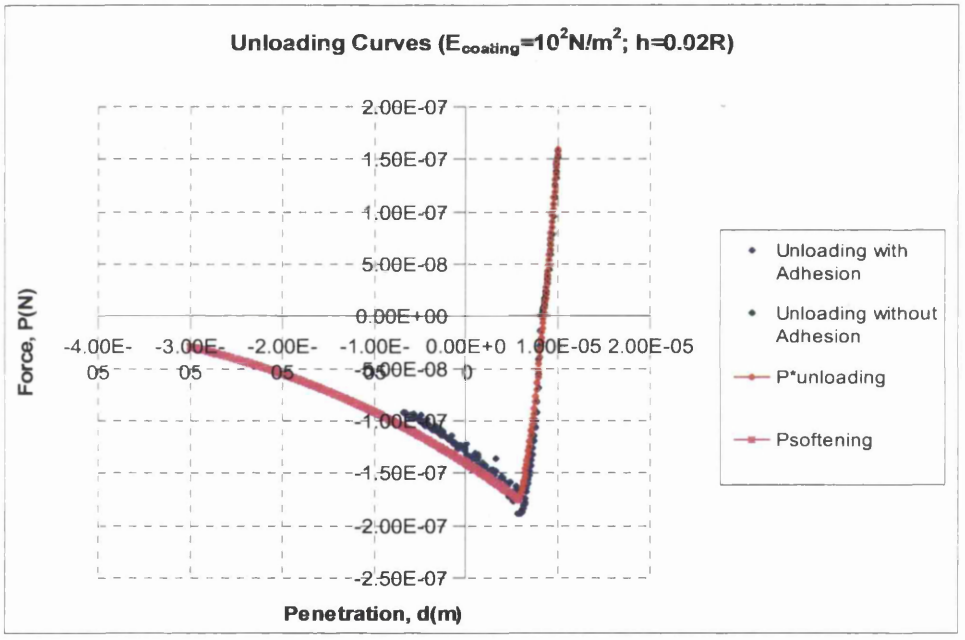

b)

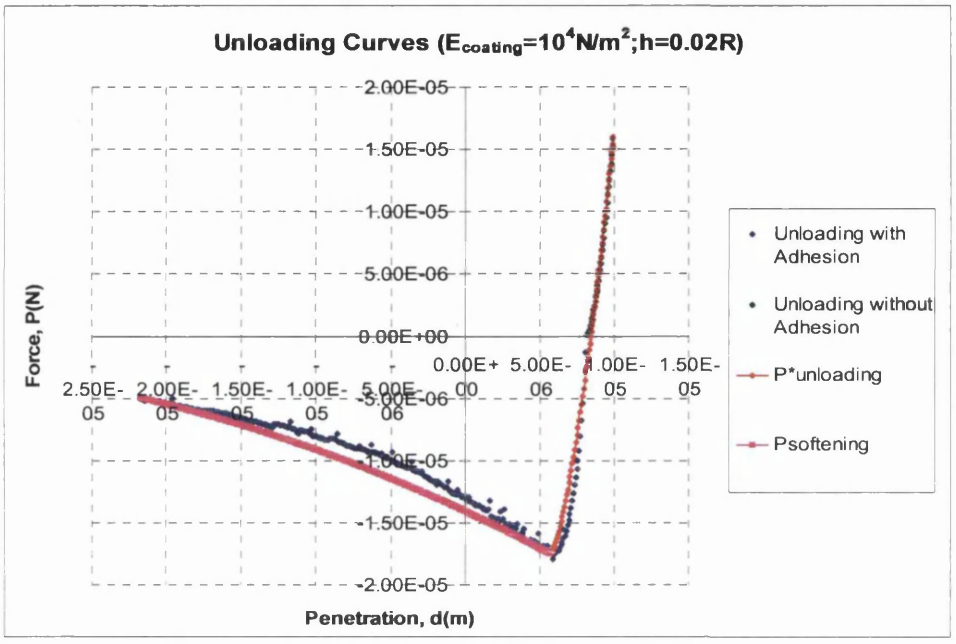

c)

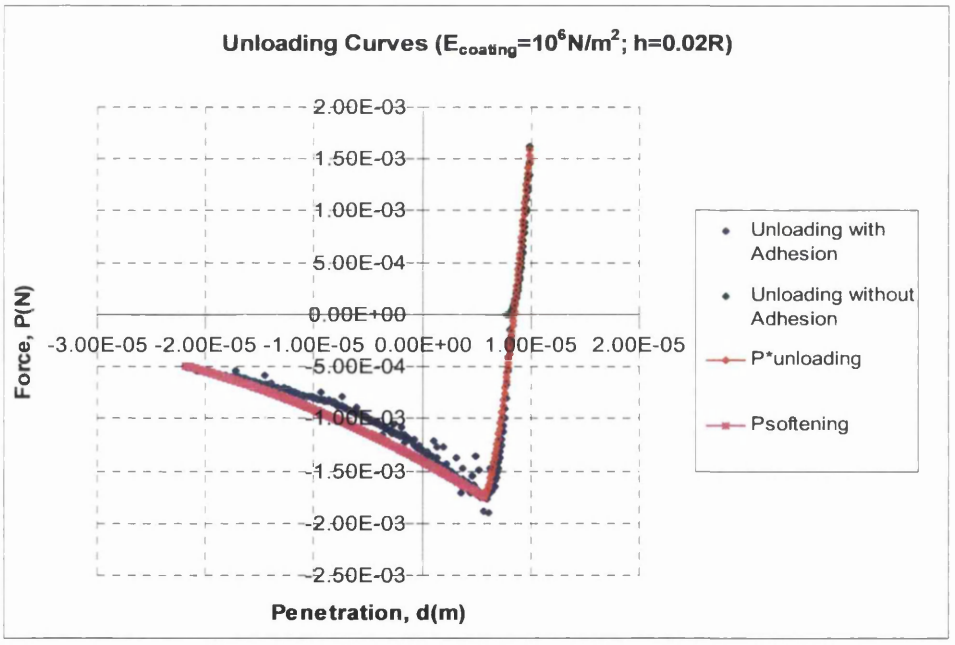

Figure 6.40: Comparison between the contact law and the finite element results for $h = 0.02R$.

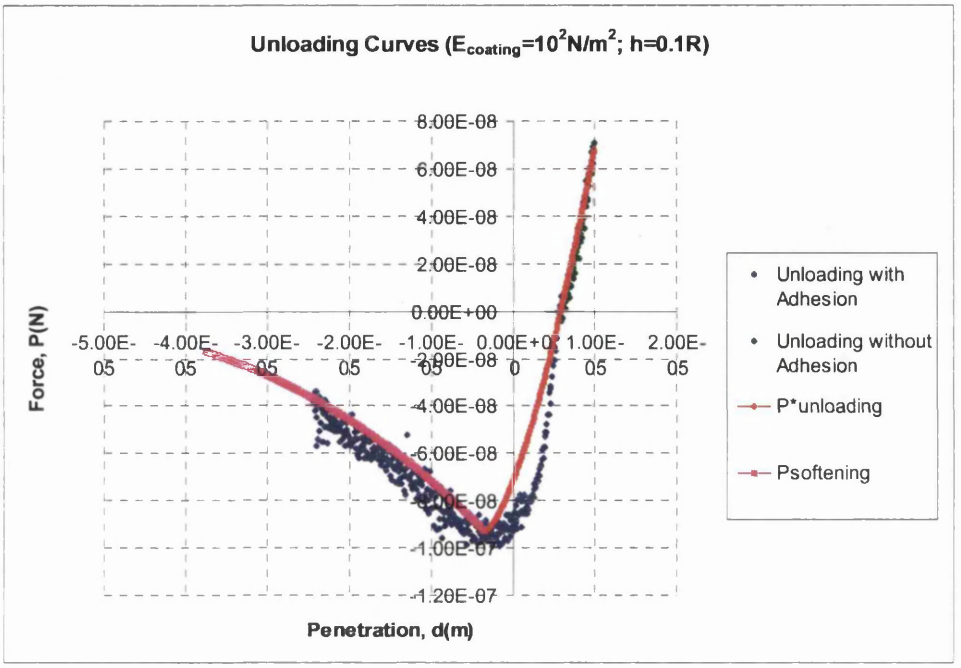
Unloading Curves ($E_{coating}=10^2 N/m^2$; h=0.1R)
8.00E-08
6.00E-08
4.00E-08
2.00E-08
0.00E+00
-2.00E-08
-4.00E-08
-6.00E-08
-1.00E-07
-1.20E-07
-5.00E-05
-4.00E-05
-3.00E-05
-2.00E-05
-1.00E-05
0.00E+0
1.00E-05
2.00E-05
Force, P(N)
Penetration, d(m)
Unloading with Adhesion
Unloading without Adhesion
P*unloading
Psoftening

a)

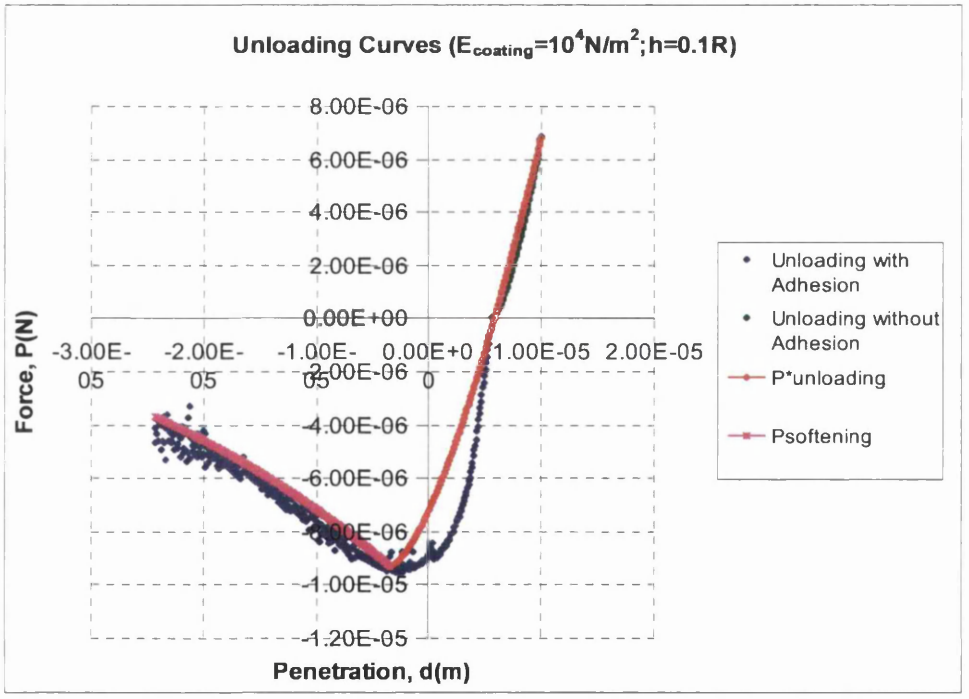
Unloading Curves ($E_{coating}=10^4 N/m^2$;h=0.1R)
8.00E-06
6.00E-06
4.00E-06
2.00E-06
0.00E+00
-2.00E-06
-4.00E-06
-6.00E-06
-1.00E-05
-1.20E-05
-3.00E-05
-2.00E-05
-1.00E-05
0.00E+0
1.00E-05
2.00E-05
Force, P(N)
Penetration, d(m)
Unloading with Adhesion
Unloading without Adhesion
P*unloading
Psoftening

b)

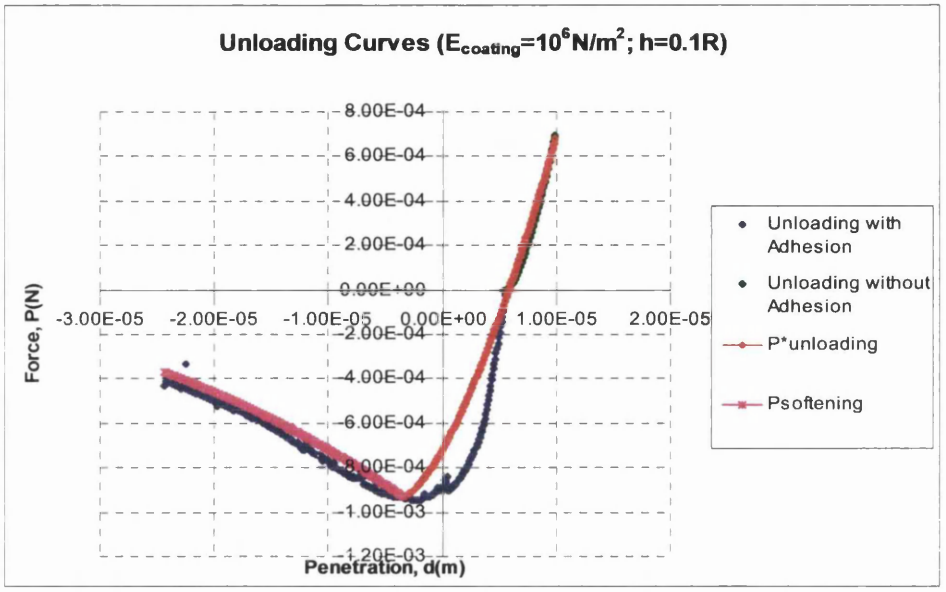

c)

Figure 6.41: Comparison between the contact law and the finite element results for $h = 0.1R$.

For the case where the particles with a coating thickness of $h = 0.02R$ and a Young's modulus of $10^6 N/m^2$ were loaded to half of the original maximum penetration, i.e. $d_{\max} = 0.000005m$, and then unloaded with adhesion at the contact. The comparison between the contact law and the finite element analysis is shown in the following figure.

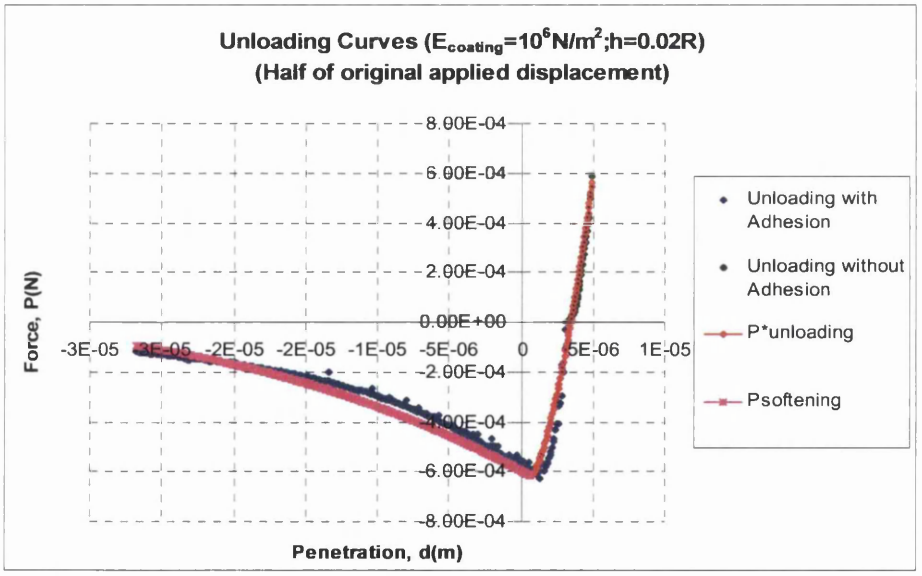

Figure 6.42: Comparison between the contact law and the finite element results for $h = 0.02R$ when $d_{\max} = 0.000005m$.

From Figure 6.40 and Figure 6.42, it can be seen that the unloading ($P^*_{unloading}$) and softening ($P_{softening}$) curves are able to match closely with the finite element results, with a slight deviation from the finite element results in the material softening part.

For the case where $h = 0.1R$, the $P^*_{unloading}$ curve was able to match the finite element results closely in the region between the maximum force and the zero force, but shows a deviation from the finite element results when adhesion takes place in a state of tension down to the maximum tensile force as shown in Figure 6.41. This is because the curve in these two regions is not continuous (which could be due to the approximation of the model used in the numerical analysis), and hence it is impossible for the approximated $P^*_{unloading}$ to match these two parts exactly. However, the $P_{softening}$ curve is a close match with the analyses results.

In general, the contact law was able to approximate the maximum tensile force for all cases quite accurately, which was the main purpose for the adhesion analysis.

Chapter 7

Concluding Remark

7.1 Conclusions

The contact between a rigid spherical indenter and an elastic incompressible layer and the contact between coated spherical particles, where the coatings behave elastic-plastically and are highly elastic, have been analysed using the finite element method. The Young's moduli values for the coatings were varied, and different coating thickness were analysed.

In general, when the coating material properties are the same, the contact forces increase with a reduction in coating thickness. Whereas, when the coating thickness is the same, the contact forces increase with an increase of the coating material properties.

For the case where the coatings behave elastic-plastically, the difference between the maximum penetration achieved during loading and the residual penetration obtained when the unloading process has reached zero force, $(d_{\max} - d_{res})$, only changes with different coating thicknesses, and is not affected by a change of the coating material properties. The stress distribution across the boundary between the coating and the particles is discontinuous and complex. Also, as adhesion is absent at the contact, the particles experience a total detachment with a deformed contact radius a_{res}, when the unloading process reaches zero force.

For the case where the elastic-plastic coatings are assumed to adhere together with contact width of $2a_{res}$ when the unloading process reaches zero force, a tensile force is exerted at the contact as the unloading process continues. The adhesion behaviour at the

contact was successfully modelled by treating the two coated particles as a continuum model with the coatings initially connected at the contact that has contact width of $2a_{res}$. The unloading process behaves inelastically and a maximum tensile force $P_{\min}$, which is regarded as the adhesion force, is observed. When $P_{\min}$ is reached, the coatings yielded throughout, producing a vertical stress that is equivalent to the hardness of the coating material $\left(H \approx 3\sigma_y\right)$. For the same coating thickness, the magnitude of $P_{\min}$ increases with an increase in the coating material properties. While for the same material properties, the magnitude of $P_{\min}$ increases with a reduction in the coating thickness. The difference between the maximum penetration and the penetration when the tensile force reaches $P_{\min}$, $\left(d_{\max} - d_{\min}\right)$, only changes with different coating thickness but is not affected by the change of coating material properties. Furthermore, the softening of the coating material from the point of $P_{\min}$ as the unloading process continues indicates that material failure occurs at and beyond $P_{\min}$.

Also, from the finite element investigations of the contact between coated particles, simple contact laws (force-penetration relations) have been formulated semi-empirically without the need of complex mathematical relations/functions and these match the finite elements results closely for coating thicknesses in the range $h = 0.02R$ to $h = 0.1R$. The Hertz formula was successfully modified with the use of coefficients determined empirically for the formulation of the contact laws for the coated particles, and a material factor m was utilised to effectively uncouple the influence of the material properties of the coatings from the determination of other parameters. Hence, a straightforward formulation which relates the contact force and the penetration was made possible. In addition, not only is the contact law able to approximate the relation between the contact force and the penetration for the process of loading and unloading, it was also able to approximate the response when adhesion is present at the contact.

In general, for contact between two coated particles where the coatings are plastic, the following modified Hertz formula can be used

$$P_{loading} = \xi m \frac{4}{3} \frac{E_p R_p^{\frac{1}{2}}}{\left(1-\nu_p^2\right)} d^{\frac{3}{2}}$$

where m is the material factor, ξ is the coefficient determined empirically that takes into account the effect of coating thickness and the subscript p stands for the particle. For unloading without contact adhesion, the following equation can be used

$$P_{unloading} = \eta m \frac{4}{3}\frac{E_p R_p^{\frac{1}{2}}}{\left(1-\nu_p^2\right)}\left(d-d_{res}\right)^{\frac{3}{2}}$$

where the residual penetration d_{res} is obtained by taking into account the effect of the coating thickness, and the coefficient η is obtained using the relation

$$\eta = \xi\left(\frac{d_{\max}}{d_{\max}-d_{res}}\right)^{\frac{3}{2}}$$

where $d_{\max}$ is the amount of penetration at maximum loading.

For unloading, with adhesion at the contact, the equation can be written as the summation of the adhesion force (maximum tensile force) and the unloading force as

$$P^*_{unloading} = P_{\min} + P_{unloading}$$

$$= \frac{P_{\max}}{\left(2.45\frac{h}{R}-0.995\right)} + \theta m \frac{4}{3}\frac{E_p R^{\frac{1}{2}}}{\left(1-\nu_p^2\right)}\left(d-d_{\min}\right)^{\frac{3}{2}}$$

where $P_{\min}$ (maximum tensile force) and $d_{\min}$ (the amount of penetration at maximum tensile force) are both found to be related to the coating thickness and θ is obtained from

$$\theta = \xi\left(\frac{d_{\max}}{\left(d_{\max}-d_{\min}\right)}\right)^{\frac{3}{2}}\left(1-\frac{P_{\min}}{P_{\max}}\right)$$

where $P_{\max}$ is the contact force at maximum penetration. After the point of maximum tensile force, the contact between the coated particles experience a material softening that is approximated by

$$P_{softening} = \pi a^2 \bar{\sigma}_z$$

where the contact radius a and the average stress $\bar{\sigma}_z$ are related to $d_{\min}$. At maximum tensile force, the average stress $\bar{\sigma}_z$ was found approximately to be equivalent to three

times the yield stress of the coating material, $-3\sigma_y$, which is the hardness of the coating material.

A complete picture of the force-penetration relation for loading and unloading with adhesion at the contact is shown in Figure 7.1.

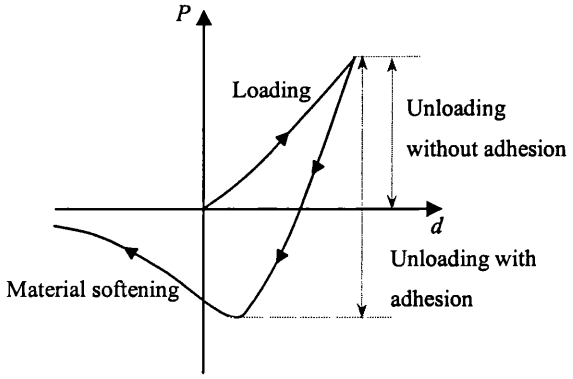

Figure 7.1: Force-penetration relation for loading and unloading with adhesion at the contact.

7.2 Suggestion for Further Works

The analyses conducted so far in this research only focus on the contact between highly elastic particles which are coated with coatings of different material behaviour, and hence the formulated force-penetration (P-d) relation is only valid for this coating-substrate system. As the thickness of the coating was reduced, the influence from the underlying particles towards the contact behaviour increases. Therefore, further finite element investigations should be carried out on the contact between particles of different materials which are coated with thin coatings. As mentioned by Sridhar et al [75] it is not possible to obtain a general empirical relation for the entire film-substrate systems, especially when adhesion is taken into account.

Also, the formulated P-d relation is only intended for coating thicknesses within the range $h = 0.02R$ to $h = 0.1R$, and hence may break down at some point outside this range. In addition, the P-d relations are formulated based on the contact between coated particles of similar size and hence is not valid for the case where the coated particles are of dissimilar size or material. Besides, as the derived simplified contact laws are only for normal contact, tangential friction and rolling effect should also be considered for a more

realistic contact behaviour between coated particles within a powder compact. Thus, further analyses on the limits of the validity of this relation is suggested.

Finally, as published literature on contact analyses of coated particles is limited, it is suggested that laboratory experiments should be carried out so that comparisons can be made against finite element analyses and the formulated P-d relation.

References

1. Royal Pharmaceutical Society of Great Britain, Information Sheet 9: *Capsules and Tablets.*
2. Wu C-Y. et al. *Numerical and experimental investigation of capping mechanisms during pharmaceutical tablet compaction.* Paper prepared for Powder Technology via "Particulate Processes in the Pharmaceutical Industry", June 26-30, 2005, Montreal.
3. Podczeck F. *Particle-particle Adhesion in Pharmaceutical Powder Handling.* Imperial College Press, 1998.
4. Sunil Jain. (1999) *Mechanical properties of powders for compaction and tableting: an overview.* PSTT **2**(1), 20-31.
5. Rowe R.C. and Roberts R.J. *Mechanical Properties.* Pharmaceutical Powder Compaction Technology (Editors: Alderborn G. and Nystrom C.), Marcel Dekker Inc., 1996, 283-322.
6. Nystrom C. and Karehill P. *The Importance of Intermolecular Bonding Forces and the Concept of Bonding Surface Area.* Pharmaceutical Powder Compaction Technology (Editors: Alderborn G. and Nystrom C.), Marcel Dekker Inc., 1996, 17-53.
7. Alebiowu G. and Itiola O.A. (2003) *The effects of starches on mechanical properties of paracetamol tablet formulations. I. Pregelatinization of starch binders.* Acta Pharm, **53**, 231-237.
8. German R.M. *Powder Metallurgy Science.* 2nd Edition, Princeton, N.J: Metal Powder Industries Federation, 1994, 192-237.
9. Hiestand E.N. (1997) *Mechanical properties of compacts and particles that control tableting success.* Journal of Pharmaceutical Sciences, **86**(9), 985-990.
10. Mendelson A. *Plasticity: Theory and Application.* The MacMillan Company, 1968.
11. Ragnarsson G. *Force-displacement and Network Measurement.* Pharmaceutical

Powder Compaction Technology (Editors: Alderborn G. and Nystrom C.), Marcel Dekker Inc., 1996, 77-96.

12. Pfeffer R. et al (2001) *Synthesis of engineered particulates with tailored properties using dry particle coating.* Powder Technology, **117**, 40-67.
13. Mattsson S. *Pharmaceutical Binders and Their Function in Directly Compressed Tablets: Mechanistic Studies on the Effect of Dry Binders on Mechanical Strength, Pore Structure and Disintegration of Tablets.* Acta Universitatis Upsaliensis, 2000.
14. Johnson K.L. *Contact Mechanics.* Cambridge University Press, 2001.
15. Israelachvili J.N. (2005) *Skimming the surface.* Nature, **435**(16), 893-895.
16. Heim L.O. and Blum J. (1999) *Adhesion and friction forces between spherical micrometer-sized particles.* Physical Review Letters, **83**(16), 3328-3331.
17. Greenwood J.A. (1997) *Adhesion of elastic spheres.* Proc. R. Soc. Lond. A. **453**, 1277-1297.
18. Coube O. and Riedel H. (2000) *Numerical simulation of metal powder die compaction with special consideration of cracking.* Powder Metallurgy **43** (2), 123-131.
19. Lewis R.W. and Khoei A.R. (1998) *Numerical modelling of large deformation in metal powder forming. Comput.* Methods Appl. Mech. Engrg. **159**, 291-328.
20. Khoei A.R., Lewis R.W. (1998) *Finite element simulation for dynamic large elastoplastic deformation in metal powder forming.* Finite Elements in Analysis and Design **30**, 335-352.
21. Khoei A.R. (2002) *Numerical simulation of powder compaction process using an inelastic finite element analysis.* Materials and Design **23**, 523-529.
22. Cunningham J.C., Sinka I.C. and Zavaliangos A. (2004) *Analysis of tablet compaction. I. Characterization of mechanical behaviour of powder and powder/tooling friction.* Journal of Pharmaceutical Sciences **93** (8), 2022-2039.
23. Sinka I.C., Cunningham J.C. and Zavaliangos A. (2004) *Analysis of tablet compaction. II. Finite element analysis of density distributions in convex tablets.* Journal of Pharmaceutical Sciences **93** (8), 2040-2053.
24. Michrafy A., Ringenbacher D. and Tchoreloff P. (2002) *Modelling the*

compaction behaviour of powders: application to pharmaceutical powders. Powder Technology **127**, 257-266.

25. Gethin D.T., Lewis R.W. and Ransing R.S. (2003) *A discrete deformable element approach for the compaction of powder systems.* Modelling Simul. Mater. Sci. Eng. **11**, 101-114.
26. Cundall P.A. & Strack O.D.L. (1979) *A discrete numerical model for granular assemblies.* Geotechnique **29**(1), 47-65.
27. Cundall P.A. (2000) *A discontinuous future for numerical modelling in geomechanics?* Proceedings of the Institute of Civil Engineers, Geotechnical Engineering, **149**(1), 41-47.
28. Munjiza A., Owen D.R.J. and Bicanic N. (1995) *A combined finite-discrete element method in transient dynamics of fracturing solids.* Eng. Comput. **12**, 145-174.
29. Rendanz P. and Fleck N.A. (2001) *The compaction of a random distribution of metal cylinders by the discrete element method.* Acta Materialia, **49**, 4325-4335.
30. Munjiza, A. and Andrews K.R.F. (2000) *Penalty function method for combined finite-discrete element systems comprising large number of separate bodies.* Int. J. Numer. Meth. Engng, **49**, 1377-1396.
31. Ransing R.S., Gethin D.T., Khoei A.R., Mosbah P. and Lewis R.W. (2000) *Powder compaction modelling via the discrete and finite element method.* Materials and Design **21**, 263-269.
32. Gethin D.T., Ransing R.S., Lewis R.W., Dutko M. and Crook A.J.L. (2001) *Numerical comparison of a deformable discrete element model and an equivalent continuum analysis for the compaction of ductile porous material.* Computers and Structures **79**, 1287-1294.
33. Cameron I.M. and Gethin D.T. (2001) *Exploration of die wall friction for powder compaction using a discrete finite element modelling technique.* Modelling Simul. Mater. Sci. Eng. **9**, 289-307.
34. Owen D.R.J and Feng Y.T. (2001) *Parallelised finite/discrete element simulation of multi-fracturing solids and discrete systems.* Engineering Computations, **18**(3/4), 557-576.

35. Liu X.L. and Lemos J.V. (2001) *Procedure for contact detection in discrete element analysis.* Advances in Engineering Software, **32**, 409-415.

36. Perkins E. and Williams J.R. (2001) *A fast contact detection algorithm insensitive to object sizes.* Engineering Computations, **18**(1/2), 48-62.

37. Hogue C. (1998) *Shape representation and contact detection for discrete element simulations of arbitrary geometries.* Engineering Computations, **15**(3), 374-390.

38. Yang X.S., Lewis R.W., Gething D.T., Ransing R.S. and Rowe R.C. *Discrete-finite element modelling of pharmaceutical powder compaction: A two-stage contact detection algorithm for non-spherical particles.* DEM Numerical Modelling of Discontinua (Geotechnical Special Publication No. 117) 74-78.

39. Lewis R.W., Gethin D.T., Yang X.S. and Rowe R.C. (2005) *A combined finite – discrete element method for simulating pharmaceutical powder tableting.* Int. J. Numer. Meth. Engng. **62**, 853-869.

40. Zienkiewicz O.C. and Taylor R.L. *The Finite Element Method. Vol 1: Basic Formulation and Linear Problems.* 4th Edition, McGrawhill Book Company, 1989.

41. Bathe K. J. *Finite Element Procedures.* Pretince Hall, 1996.

42. Cook R.D., Malkus D.S. and Plesha M.E. *Concepts and Applications of Finite Element Analysis.* 3rd Edition, John Wiley & Sons, 1989.

43. Belytschko T., Liu W.K. and Moran B. *Nonlinear Finite Elements for Continua and Structures.* John Wiley & Sons, 2001.

44. Peric D. M.Sc. Computational Plasticity lecture notes, University of Wales Swansea, 2003.

45. http://www.flow3d.com/Cfd-101/impvexp.htm

46. Peric D. and Owen D.R.J. (1998) *Finite-element applications to the nonlinear mechanics of solids.* Rep. Prog. Phys. **61**, 1495-1574.

47. Wu X., Downes M.S., Goktekin T. and Tendick F. (2001) *Adaptive nonlinear finite elements for deformable body simulation using dynamic progressive meshes.* Eurographics, **20**(3).

48. De Araujo T.D., Roehl D. and Martha L.F. *An adaptive strategy for elastic-plastic two-dimensional finite element analysis.* European Congress on Computational

Methods in Applied Sciences and Engineering, Barcelona, 11th-14th September 2000.

49. Feng Y.T., Han K. and Owen D.R.J. (2004) *Discrete element simulation of the dynamics of high energy planetary ball milling processes.* Materials Science and Engineering A. **375-377**, 815-819.
50. Feng Y.T. and Owen D.R.J. (2002) *An augmented spatial digital tree algorithm for contact detection in computational mechanics.* Int. J. Numer. Meth. Engng, **55**, 159-176.
51. Munjiza A. and Andrews K.R.F. (1998) *NBS contact detection algorithm for bodies of similar size.* Int. J. Numer. Meth. Engng., **43**, 131-149.
52. Feng Y.T. and Owen D.R.J. (2004) *A 2D polygon/polygon contact model: algorithmic aspects.* Engineering Computations, **21**(2/3/4), 265-277.
53. Han K., Feng Y.T. and Owen D.R.J. (2006) *Polygon-based contact resolution for superquadrics.* Int. J. Numer. Meth. Engng., **66**, 485-501.
54. Williams J.R. and O'Connor R. (1995) *A linear complexity intersection algorithm for discrete element simulation of arbitrary geometries.* Engineering Computations, **12**(2), 99-201.
55. Hogue C. and Newland D. (1994) *Efficient computer simulation of moving granular particles.* Powder Technology, **78**(1), 51-66.
56. Timoshenko S.P. and Goodier J.N. *Theory of Elasticity.* 3rd Edition, McGraw-Hill, 1970.
57. Matthewson M.J. (1981) *Axi-symmetry contact on thin compliant coatings.* J. Mech. Phys. Solids **29**(2), 89-113.
58. Aleksandrov V.M. (1968) *Asymptotic methods in contact problems of elasticity theory.* PMM **32**(4), 672-683.
59. Aleksandrov V.M. (1969) *Asymptotic solution of the contact problem for a thin elastic layer.* PMM **33**(1), 61-73.
60. Conway H.D. and Engel P.A. (1969) *Contact stresses in slabs due to round rough indenters.* Int. J. mech. Sci. **11**, 709-722.
61. Ogilvy J.A. (1993) *A parametric elastic model for indentation testing of thin films.* J. Phys. D: Appl. Phys. 26, 2123-2131.

62. Abramowitz M. and Stegun I.A. *Handbook of Mathematical Functions.* Applied Mathematics Series Vol. 55, Washington: National Bureau of Standards, 1964.

63. Mesarovic S.D. and Fleck N.A. (2000) *Frictionless indentation of dissimilar elastic-plastic spheres.* International Journal of Solids and Structures, **37**, 7071-7091.

64. Vu-Quoc L. and Zhang X. (1999) *An elastoplastic contact force-displacement model in the normal direction: displacement-driven version.* Proc. R. Soc. Lond. A, **455**, 4013-4044.

65. Vu-Quoc, Zhang X. and Lesburg L. (2000) *A normal force-displacement model for contacting spheres accounting for plastic deformation: force-driven formulation.* Journal of Applied Mechanics, **67**, 363-371.

66. Vu-Quoc, Zhang X. and Lesburg L. (2001) *Normal and tangential force-displacement relations for frictional elasto-plastic contact of spheres.* International Journal of Solids and Structures, **38**, 6455-6489.

67. Kogut L. and Etsion I. (2002) *Elastic-plastic contact analysis of a sphere and a rigid flat.* Journal of Applied Mechanics, **69**, 657-662.

68. Hu X.Z. and Lawn B.R. (1998) *A simple indentation stress-strain relation for contacts with spheres on bilayer structures.* Thin Solid Films, **322**, 225-232.

69. Johnson K.L. and Greenwood J.A. (1997) *An adhesion map for the contact of elastic spheres.* Journal of Colloid and Interface Science, **192**, 326-333.

70. Pollock H.M., Shufflebottom P. and Skinner J. (1977) *Contact adhesion between solids in vacuum: I. Single-asperity experiments.* J. Phys. D: Appl. Phys., **10**, 127-138.

71. Pollock H.M. (1978) *Contact adhesion between solids in vacuum: II. Deformation and interfacial energy.* J. Phys. D: Appl. Phys., **11**, 39-54.

72. Mesarovic S.Dj. and Johnson K.L. (2000) *Adhesive contact of elastic-plastic spheres.* J. Mech. Phys. Solids, **48**, 2009-2033.

73. Martin C.L. (2003) *Unloading of powder compacts and their resulting tensile strength.* Acta Materialia, **51**, 4589-4602.

74. Yang F. (2002) *Adhesive contact between a rigid axisymmetric indenter and an incompressible elastic thin film.* J. Phys. D: Appl. Phys., **35**, 2614-2620.

75. Sridhar I., Zheng Z.W. and Johnson K.L. (2004) *A detailed analysis of adhesion mechanics between a compliant elastic coating and a spherical probe.* J. Phys. D: Appl. Phys., **37**, 2886-2895.